Two Proton Knockout From Carbon Using Linearly Polarised Photons

Jamie Robinson

A thesis presented for the degree of
Doctor of Philosophy

Nuclear Physics Experimental Research Group
Department of Physics & Astronomy
University of Glasgow
Scotland

June 2010

This thesis is dedicated to my nana, Theresa Robinson

Two Proton Knockout From Carbon Using Linearly Polarised Photons

Jamie Robinson

Submitted for the degree of Doctor of Philosophy
June 2010

Abstract

The $^{12}C(\overrightarrow{\gamma}$,pp) reaction has been studied in the photon energy range E_γ=200-450 MeV at the Mainz microtron MAMI. The linearly polarised photon beam was produced via the coherent bremsstrahlung technique with a diamond radiator and tagged with the Glasgow Tagging Spectrometer. The beam was incident on a ^{12}C target and the reaction products were detected in the $\sim 4\pi$ Crystal Ball detector. The experimental study examines the photon asymmetry Σ over a wider photon energy range than previous measurements and presents the first measurement of the angular dependence of Σ.

The photon asymmetry has a negative magnitude for missing energies $E_m <$ 70 MeV where direct emission of nucleon pairs is expected. A strong peak at low E_m is observed in $\Sigma_{(\gamma,pp)}$ for photon energies above and below Δ resonance energies. The asymmetry is studied in two missing energy regions E_m <40 MeV and E_m=40-70 MeV where direct knockout from $(1p)^2$ and (1s)(1p) shells is expected. For both missing energy regions the photon energy dependence of Σ is rather flat, and the magnitude of $\Sigma_{(\gamma,pp)}$ generally exceeds $\Sigma_{(\gamma,pn)}$ for photon energies below 300 MeV. Similar values are observed for $E_\gamma > 300\,MeV$. At low E_m and $E_\gamma < 300\,MeV$, the results suggest that different mechanisms contribute to $^{12}C(\gamma$,pp) and $^{12}C(\gamma$,pn) reactions. The similarity in Σ above $E_\gamma \sim$300 MeV suggests that both channels are dominated by contributions from isobaric currents. A strong angular dependence of Σ is presented which follows a trend remarkably similar to deuteron photodisintegration. Theoretical calculations using an unfactorised distorted wave treatment of

direct two-nucleon emission do not agree with the magnitude of the photon asymmetry. For E_m above 100 MeV and $E_\gamma > 300$ MeV, Σ has a substantially negative value which is attributed to two-step reactions following initial quasifree pion production.

Declaration

The work in this thesis is based on research carried out at the Nuclear Physics Experimental Research Group, Department of Physics & Astronomy, University of Glasgow, Scotland. No part of this thesis has been submitted elsewhere for any other degree or qualification and it is all my own work unless referenced to the contrary in the text.

Acknowledgements

The completion of this thesis would not have been possible without the help of many people throughout the last 4 years. Firstly, I would like to thank Guenther Rosner for giving me the opportunity to undertake a PhD in the Glasgow NPE group. Special mention must go to my two supervisors, Douglas MacGregor and Ken Livingston. Douglas deserves thanks for the many helpful suggestions he has made during my time in the group and for taking the time to carefully and critically read this thesis. I am particularly indebted to Ken for all the assistance in the many computing issues I've had over the years (and there have been many) and the interesting discussions we've had on coherent bremsstrahlung and photon polarisation. One day I will understand the Stonehenge Technique. Derek Glazier and David Hamilton also deserve enormous thanks for going beyond the call of duty in helping me with various data analysis problems, my PhD would have be a more painful experience without your assistance. I am also much obliged to John Annand, Cameron McGeorge and Bob Owens for their helpful contributions during our weekly Mainz analysis meeting. Bob deserves a special mention for his efforts in recent weeks in critically examining the work. Thanks are also due to the A2 collaboration for allowing me to contribute to the series of CB@MAMI experiments, whether in shift taking, calibration or data analysis.

In the Glasgow Nuclear Physics Group, I would like to thank the many students and staff who have made my time in the group such an enjoyable experience. In particular, Richard Codling, Eilidh McNicoll, Joe Mancell and David "The Burger" Howdle for being great company both in Glasgow and on our many trips to the Zeitungs Ente and Bavaria in Mainz. The Edinburgh Mainzers - Tom Jude, Mark Sikora and Pauline Hall Barrientos - also deserve thanks for the excellent nights

we shared in Mainz. When in Glasgow, it has been a pleasure to spend time in the company of the numerous office dwellers and Ashoka devotees. These include Craig Paterson, Russell Johnstone, Neil Hassall, Stuart Fegan, Gordon Hill, Neil Thompson, Seian Al Jebali, Jonathan Burns, Gary Smith and my old primary school friend David Mahon. Thanks for all the non physics related laughs we have shared over the years, from quizzes to limericks and Newcastle to rotten fruit. I would also like to acknowledge the daily renditions of 'The Arbiter' and the general antics of 415, they were welcome distractions when I needed a break from analysis and thesis writing.

A final thank you to my parents, brothers and Heather for their support and patience throughout my PhD.

"Head Up Dear, The Rabbit Might Die" - The Twilight Sad

Contents

List of Figures

List of Tables

Chapter 1

Introduction

Understanding the detailed properties and structure of nuclei based on realistic interactions between their constituent particles is a fundamental goal of nuclear physics. A good knowledge of the interaction between nucleons at high relative momenta underpins the basic nucleon-nucleon potential and is central to constructing such theories. Despite the fact that nucleons interact strongly, theories of nuclei derived from independent particle models (IPM) [1, 2] have been largely successful in their description of nuclear properties. The Nuclear Shell Model describes the nucleus as a system of non-colliding independent nucleons moving in a mean field generated by all other nucleons, with protons and neutrons inhabiting separate energy levels (shells) within the nucleus. Hartree-Fock calculations based on effective nucleon-nucleon interactions with the important addition of spin-orbit interactions explain the existence of magic nuclei with stable shell configurations [3, 4] and successfully predict the spin and parity of many nuclear ground states. This success is largely due to the suppression of collisions by Pauli exclusion which constrains the number of final states that nucleons can scatter into. Unfortunately, the model fails to adequately describe nuclear binding energies when potentials derived from realistic NN-interactions are applied. This failure stems from 3N forces and the strong repulsive nature of the nuclear force at short internucleon distances which introduce to the nuclear wave function correlated behaviour beyond the mean field description. Before a description of nuclear properties in terms of a realistic NN-interaction can be achieved, a detailed study of short-range correlations (due to this

short-range repulsive force) and the interaction of hadrons in the nuclear medium must be undertaken.

Following discoveries in the 1950s that nuclear absorption of a high energy photon frequently results in the emission of nucleon pairs [5], electromagnetically induced two-nucleon knockout has been considered one of the most promising and direct tools for exploring the properties of nucleon pairs within nuclei and their interaction at short distance [6, 7, 8]. Electromagnetically induced two-nucleon knockout was initially thought to be a good tool for studying short-range correlations (SRC), if it is assumed that the photon is absorbed by either nucleon of a correlated pair, resulting in both nucleons being ejected from the nucleus. However, it was quickly realised that two-nucleon knockout reactions, following the absorption of a photon by a nucleon-pair, can also proceed via several competing mechanisms - with contributions from two-body meson exchange currents (MEC) and isobar currents (IC). Final state interactions (FSI) between the outgoing nucleons and the residual nucleus, which makes it difficult to extract information about the initial state of the nucleon pair, also affect the measured reaction cross section. The importance of the different mechanisms and their contribution to the measured cross section depends on the reaction channel and the kinematics studied. Hence, to fully understand the different reaction mechanisms involved and to extract interesting information on nuclear structure, a detailed study of the 4 possible NN-knockout channels - (e,$e^{'}$pn), (e,$e^{'}$pp), (γ,pn) and (γ,pp) - over a wide range of photon energies and kinematics is necessary. In addition, a reliable theoretical treatment of these mechanisms are essential before one can draw definite conclusions from comparisons with data.

Described in this thesis is a study of the ($\overrightarrow{\gamma}$,pp) reaction using linearly polarised photons. The kinematics of the reaction is illustrated in figure 1.1, with the incident photon with momentum P_{γ} absorbed by a proton pair with initial momentum P_{pair}, with the residual nucleus spectating. In the spectator approximation and in the absence of FSI, the magnitude of the recoil momentum of the residual nucleus is equal to P_{pair}. Theoretical models [6, 9, 10] predict that photoinduced two-nucleon knockout reactions are sensitive to mechanisms involving two-body currents (MEC and IC) and also contain information about the different possible pair configurations which

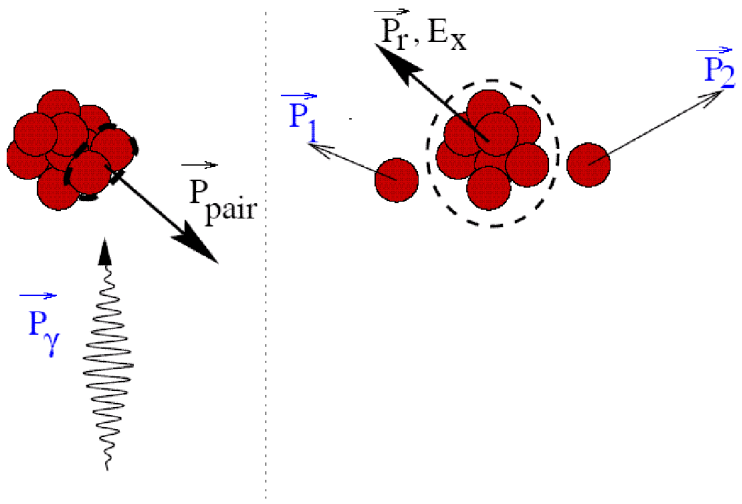

Figure 1.1: Photon with momentum P_γ is absorbed by a proton pair with initial momentum P_{pair}. In the lab frame the nucleon pair are ejected non-coplanar (right hand side). In the spectator approximation and in the absence of FSI, the magnitude of the recoil momentum of the residual nucleus, P_r is equal to P_{pair}. P_1 and P_2 are the momentum of the outgoing nucleons and E_x is the excitation of the residual nucleus.

exist in the nucleus and their relative populations. Furthermore, measurements of photonuclear reactions with polarised photons provide unique access to observables which are sensitive to the details of the reaction process which may be negligible when averaged over the total response [6,9,10]. Cross sections for reactions in which the polarisation of the incident photon is either parallel ($\sigma_\parallel$) or perpendicular ($\sigma_\perp$) to the reaction plane have different sensitivity to the various reaction mechanisms which contribute. This difference is emphasised through the photon asymmetry, $\Sigma = \frac{\sigma_\parallel - \sigma_\perp}{\sigma_\parallel + \sigma_\perp}$. Therefore, polarised photon measurements provide a unique tool to investigate any differences between (γ,pn) and (γ,pp) reaction mechanisms. They also provide an extra degree of freedom which offers an independent test of photonuclear reaction models.

The remainder of this thesis is as follows. The next chapter explores in more detail some of the ideas discussed in this section, providing some theoretical back-

ground and outlining the motivation behind the experiment. Chapter 3 describes the detector systems and apparatus used in the experiment, with chapter 4 outlining the various detector calibrations carried out together with basic event selection. Chapter 5 gives a detailed account of the methods used to extract the photon polarisation while the $\Sigma_{(\gamma,pp)}$ results and their interpretation are presented in chapter 6. Finally, chapter 7 draws conclusions from the present work and makes some suggestions for future study.

Chapter 2

Theory and Motivation

This chapter provides the motivation for the analysis and the extraction of Σ for (γ,pp) reactions. Outlined below is a brief overview of the nucleon-nucleon interaction, the study of nuclei using energetic photons and a review of previous two-nucleon knockout measurements with unpolarised photons. A review of the various theoretical models describing (γ,NN) is discussed with emphasis on work with polarised photons. A review of previous measurements using polarised photons is provided. The chapter concludes with a summary and outline of the aims of the present experiment.

2.1 Nucleon-Nucleon Potential

As discussed in the introduction, one of the defining goals of nuclear physics is to construct a theory of nuclear structure based on realistic NN-interactions. A model describing the basic NN-interaction is the common starting point. This model could be derived from Quantum Chromodynamics (QCD), meson exchange or purely phenomenological [11]. The NN-interaction is considered realistic if the parameters of the model can be adjusted to provide a good fit to NN-scattering data and to properties of the deuteron. The second step involves the solution of a many body problem with A nucleons interacting in terms of this realistic NN-interaction. The simplest approach uses the independent particle model (IPM), treating the nucleus as a group of independent nucleons moving in a mean potential generated by all

other nucleons. Mean field calculations employing realistic interactions fail - predicting unbound nuclei [11]. This failure is a consequence of repulsive short-range components of the NN-interaction (and 3N forces) necessary to describe NN scattering data. A careful treatment of two-body short-range correlations beyond the mean field approximation is therefore essential to describe the structure of nuclei in terms of realistic NN-interactions.

Correlated NN-interactions have two main components, the first a central scalar term - the SRCs - is a phenomenological repulsive force at small internucleon separation thought to arise from the dominance of quark/gluon degrees of freedom [12]. Evidence of correlated behaviour beyond the mean field description of the nucleus is provided from the study of electromagnetically induced one nucleon emission from complex nuclei (A $>$ 4). Through measurement of the energy of the outgoing proton and scattered electron in an (e,e'p) reaction, the spectroscopic strength [6], a measure of the occupancy of the energy levels below the Fermi level, can be accessed. The left panel of figure 2.1 plots the spectroscopic factor relative to shell-model multiplicity for valence protons of several nuclei as a function of target mass. The average value of the spectroscopic strength for the nuclei studied was found to be $\sim$65% of that predicted by IPMs [13]. Much of the observed depletion of the Fermi sea is thought to arise from the influence of SRC with nucleons undergoing violent short-range interactions which push the nucleon pair into an excited state. The depletion of levels below the Fermi surface is counterbalanced by an increase in the population of highly excited orbitals which are predicted to be empty in Shell Model calculations. There is clear evidence of this in right panel of figure 2.1

This repulsive force was initially modelled by hard-core potentials which become infinitely repulsive for relative distances smaller than $\sim$0.4 fm. This is replaced in modern meson exchange models by a soft-core where the probability of finding two nucleons at relatively small separations diminishes the closer they get. There is also a tensor term which depends on the spin and spatial orientation of the nucleon pair, known as Tensor Correlations [14]. It is energetically more favourable for the alignment of the nucleon separation to be parallel to the direction of the total spin of the nucleons. The tensor force only acts on pn-pairs as like nucleon pairs in the

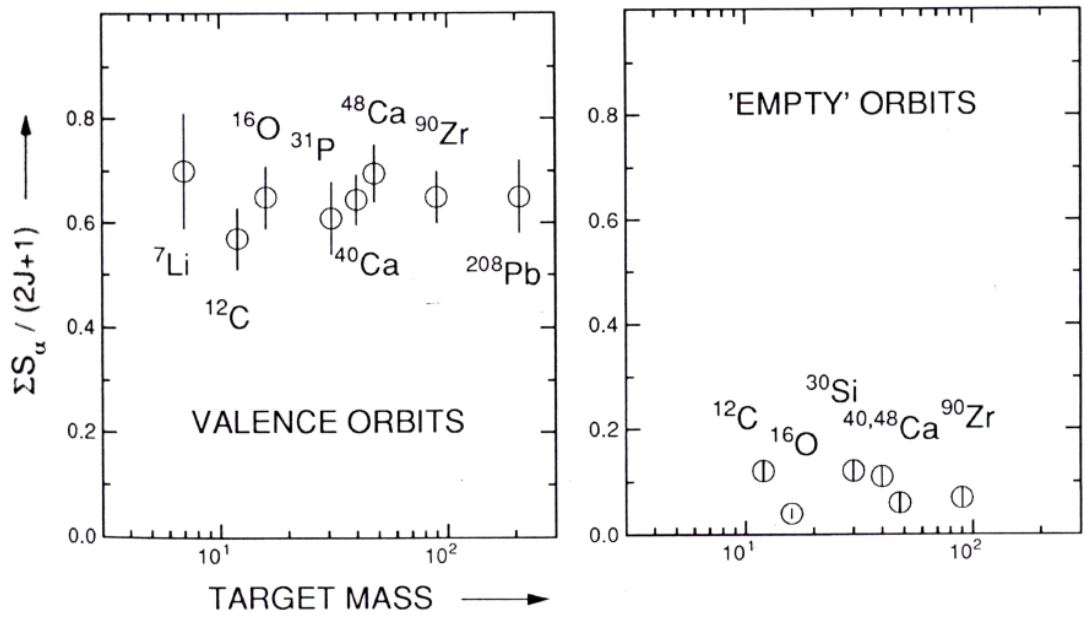

Figure 2.1: Quasi-particle strength for valence orbitals (left panel) and for states just above the Fermi level (right panel) observed in the (e,e'p) reaction as a function of the target mass [13].

same orbit can only be found in an S=0 state whereas pn-pairs can be found in an S=1 state which allows their relative spins to be aligned.

Meson exchange currents transmit the nuclear force between nucleons for all but the shortest NN-separations [15]. The lightest of the mesons, the π-meson is responsible for much of the long-range (1-1.5 fm) attractive part of the NN-potential. The pion exists in three charge states ($\pi^{\pm}$ and π^0) and to first order charged meson exchange only occurs between pn-pairs whereas neutral pions are exchanged between all NN combinations. At intermediate distances (0.5-1 fm) the nuclear potential is parameterised by σ-meson exchange which describes multiple pion exchange between nucleons and again is an attractive potential. At shorter separations (<0.25 fm) heavier ω and ρ-exchange may take place, which contributes to the repulsive force between nucleons [16]. To obtain sufficient repulsion at short internucleon distances a rather large ω coupling constant is used to describe strong ω exchange in one boson exchange (OBE) potentials. A possible reason for this large coupling constant may be that ω-exchange in OBE models contains an effective parameterisation of short range repulsion originating from quark effects [11].

Isobar currents also contribute to the NN-potential, with the absorbed meson exciting a nucleon into a baryon resonance [11]. The $\Delta(1232)$ resonance which decays $\Delta \rightarrow N\pi$ in $\sim 10^{-24}$ s is the most important of these resonances and it plays an important role at intermediate separations. Spontaneous occurrences of Δ-resonances in the nucleus are infrequent as additional energy is required to excite the nucleon and consequently isobar currents have a smaller contribution to the NN-potential than MECs. The mean field of IPMs take into account the average behaviour of all meson exchange and isobar currents when describing nuclear structure.

Several models have been developed to describe the NN-potential based on the exchange of mesons and also include the forces involved in correlated behaviour [16, 17, 18, 19]. One pion exchange describing the long range part of the interaction is common to each model though different parameterisations are used to account for intermediate and short range components. These models have been compared to NN-scattering data and typically have a χ^2 per datum of ~ 1. Figure 2.2 compares the phase shifts from proton-proton scattering at medium energies calculated using the charge dependent Bonn potential with the results from various pp phase shift analysis [20]. The change in the $^1S_0$-wave phase at about E_p=300 MeV shows that at these energies the incident nucleon is probing a repulsive core in the NN interaction.

2.2 Electromagnetic Probes

The key to understanding the structure and dynamics of hadronic matter is through its response to an external probe as a function of energy and momentum transfer. The electromagnetic probe, whether through electron scattering or photon absorption has long been established as one of the most powerful and direct tools to meet this aim. The photon (or virtual photon in the case of electron scattering) interacts with the nucleus via the electromagnetic interaction which is completely understood through Quantum Electrodynamics (QED). The electromagnetic contribution to the photonuclear or electron scattering cross section can be separated from the hadronic contribution allowing, in principle, access to relevant information about hadronic structure through the target response to the probe [6]. Due

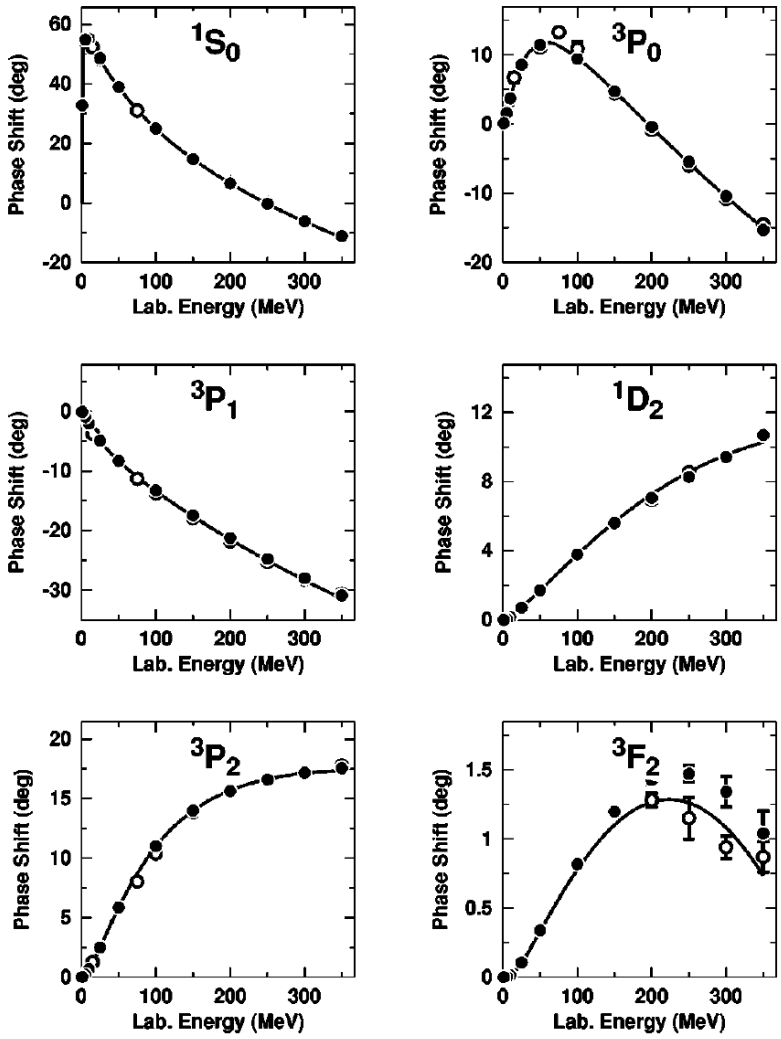

Figure 2.2: pp phase shift parameters in partial waves with J<4. The solid line represents the predictions by the CD-Bonn potential. The solid dots and open circles are the results from the Nijmegen multi-energy pp phase shift analysis and Virginia Polytechnic Institute pp-scattering analysis SM99, respectively. From [20] and references therein.

to its relatively weak interaction, the photon has a mean free path much longer an the target dimensions used here and is thus an ideal probe to explore the entire volume of the nucleus. Conversely, hadronic probes are frequently absorbed at the nuclear surface and have a high probability of undergoing Initial State Interactions with the incoming probe being perturbed by the nucleus. However, the weakness of the electromagnetic interaction has a large disadvantage in that the cross section for photoreactions and electron scattering are exceedingly small when compared to purely hadronic reactions.

Electron scattering has an advantage over the use of real photons in that it allows independent variation of energy and momentum transfer and of the (longitudinal and transverse) polarisation of the virtual photon. This flexibility is reflected in the cross sections involved which have a large number of structure functions, related to the different ways the target can absorb the virtual photon. Real photons are purely transverse and the cross sections involved depend only on the transverse structure function W_T [6]. For real photons, the energy and momentum transfer are equivalent. Experiments with real photons have the advantage of allowing measurements over a wide angular region and a wide photon energy range.

2.2.1 Absorption of Photons by Nuclei

The size of structure to which the photon will couple strongly depends on the wavelength and thus the energy of the probe. The total photon absorption cross section is a sum of many competing absorption mechanisms and depending on the explored excitation energy and momentum transfer, different degrees of freedom come into play. Figure 2.3 illustrates the total photon absorption cross section per nucleon for several nuclei [21]. The first notable feature in the nuclear response is the giant dipole resonance with the peak at $\sim$30 MeV corresponding to the photon coupling to the nucleus as a whole, inducing an oscillation of neutrons relative to protons.

At higher photon energies, the wavelength of the probe decreases and mechanisms more sensitive to nucleon and quark degrees of freedom become evident in the nuclear response. At excitation energies of $\sim$300 MeV the first nucleon excitation - the Δ-resonance, corresponding to a magnetic dipole transition that flips the spin of one

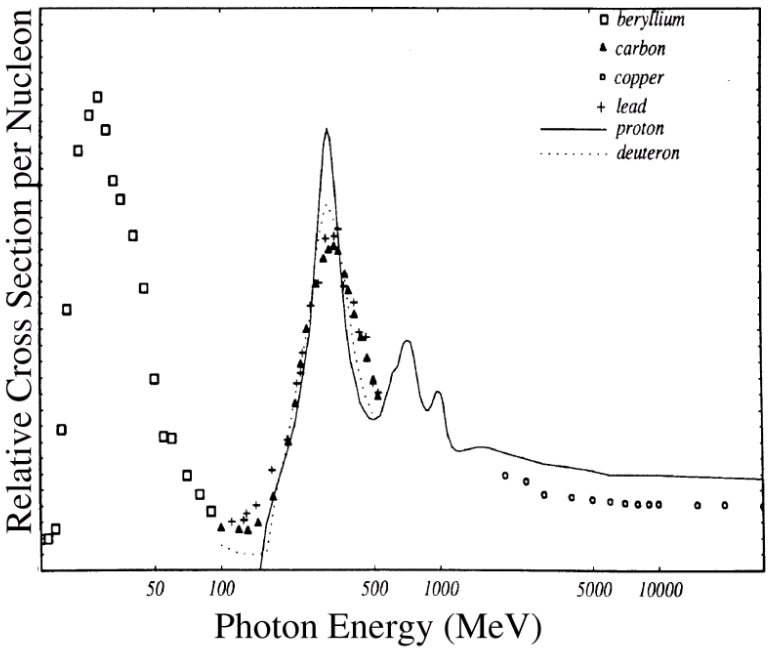

Figure 2.3: Total nuclear photon absorption cross section on different nuclei. Taken from reference [21].

of the constituent quarks - appears in the cross section. The Δ resonance is also evident in the photoexcitation spectrum of the free proton illustrated by the solid line in figure 2.3. The increasing width and position of the peak for heavier nuclei is due to Fermi motion. Other baryon resonances evident in the cross section for free nucleons at excitation energies above 500 MeV are suppressed in complex nuclei.

At intermediate photon energies between the peaks of the giant dipole and Δ resonances much of the cross section strength stems from photon absorption on nucleon pairs [8, 7]. At energies above 100 MeV one nucleon knockout reactions induced by photon absorption on a single nucleon are strongly suppressed due to the momentum mismatch between the ejected nucleon and incident photon, as the nucleon absorbs most of the photon energy. For two-nucleon knockout reactions, the nucleon pair share much of the photon energy and are emitted roughly back-to-back with the residual nucleus acting as a spectator with the extra degree of freedom allowing an exact momentum balance. Thus (γ,NN) reactions are promising tools for studying the interaction between nucleon pairs at short and medium range in

the nuclear environment.

2.2.2 (γ,NN) Knockout Mechanisms

Various reaction mechanisms lead to the ejection of two nucleons following the absorption of a photon by a nucleus. One-body currents compete with two-body MECs and ICs to account for the observed strength of the measured (γ,NN) cross section. Figure 2.4 shows the Feynman diagrams associated with each mechanism.

Meson Exchange Currents result from the photon coupling to a meson which is being exchanged between two nucleons as shown by figures 2.4(a) and (b). Figure 2.4(a) shows the pion-in-flight mechanism where the photon is absorbed by a pion as it is exchanged between both nucleons and figure 2.4(b) illustrates the pion-seagull mechanism where the photon is absorbed by the nucleon producing the pion which is subsequently absorbed by the second nucleon. Figures 2.4(c) and 2.4(d) show the mechanisms involving isobar currents. Figure 2.4(c) shows the Δ-excitation mechanism where the absorbed photon excites the nucleon into a Δ resonance. The Δ subsequently decays, $\Delta \rightarrow \pi N$ via an interaction with another nucleon. In figure 2.4(d) the photon is absorbed by a pre-existing Δ resonance within the nucleus. In figure 2.4(e) the photon is absorbed by either nucleon of a strongly correlated pair within the nucleus. Following a violent short-range interaction, the pair have a high relative momentum compared to other nucleons in the nucleus and both are subsequently ejected from the nucleus.

Each process has different sensitivity to kinematic variables such as energy transfer and particle emission angle. It is important to investigate both (γ,pn) and (γ, pp) reactions over a wide range of kinematic variables to obtain maximum information about the interaction between nucleons as the main mechanisms which contribute can be very different for both channels. A large part of the (γ,pn) cross section comes from absorption on pion-exchange currents [22,23]. The charge exchange part of the two-body currents are suppressed in (γ,pp) reactions as the photon will not couple to the exchanged neutral meson. As a result the (γ,pp) strength is relatively weak compared to (γ,pn). The (γ,pp) channel is expected to be more sensitive to intermediate Δ-isobar excitation and SRC, although the effects of SRC are thought to

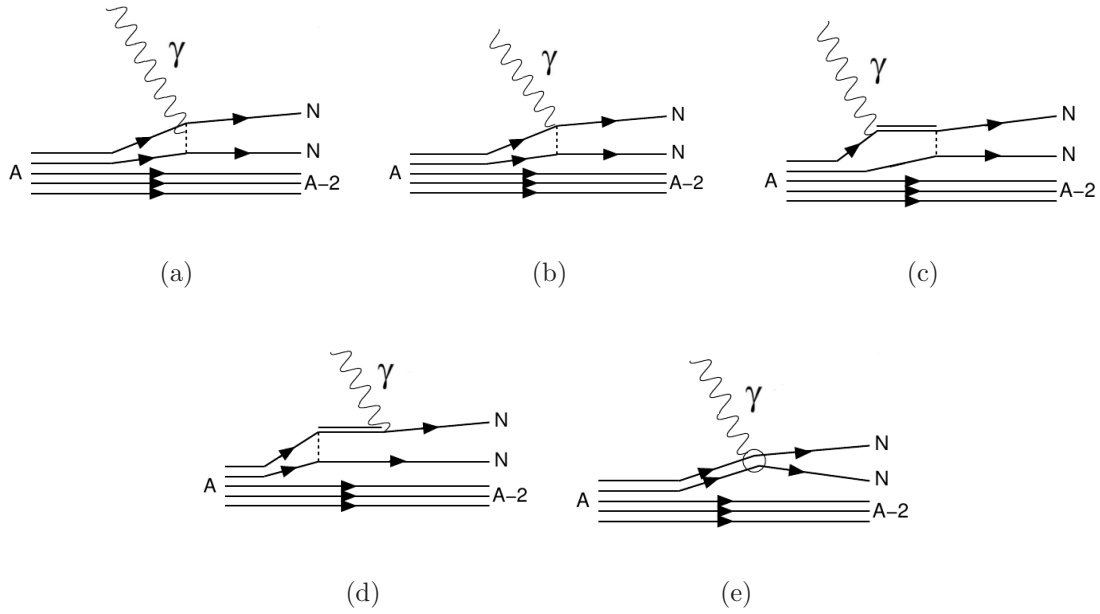

Figure 2.4: Mechanisms for real photon induced 2N knockout: (a) pion-in-flight; (b) pion seagull; (c) Δ-excitation; (d) Δ-de-excitation; (e) direct knockout of a correlated pair.

be small in photoreactions below ∼500 MeV [24].

It is also difficult to distinguish between direct two proton emission and multi-step processes which result from final state interactions (FSI) such as (π,2N) reactions following quasi-free pion production. There is also the possibility that some of the (γ,pp) strength could arise from (γ,pn) reactions followed by (n,p) scattering [25]. Theoretical models on two-nucleon photoabsorption require an accurate description of each direct mechanism plus an understanding of multi-step processes before any information on nuclear structure can be extracted in comparison with data.

2.3 Overview of Theoretical Models

2.3.1 Early Factorised Models

The simplest two-body photon absorption model is the quasideuteron model proposed by Levinger [8] in which the photon interacts with a correlated pn-pair, while the remainder of the nucleus acts as a spectator. The model parametrises the cross

section by:

$$\sigma_{QD} = L\frac{NZ}{A}\sigma_D \tag{2.1}$$

where the basic interaction with the proton-neutron pair is characterised by the free-deuteron photodisintegration cross section σ_D. The term NZ/A is proportional to the density of pn-pairs contributing to the reaction and the Levinger parameter L represents the relative probability of a pn pair being close enough in a complex nucleus, compared to the free deuteron and for ^{12}C, L$\sim$6. Although somewhat phenomenological and neglecting the effects of Fermi motion, Pauli blocking and FSI, the model contains the basic properties of two-body photon absorption and accounts in a general way for the main features of photoreaction data in the intermediate energy range, E_γ=150-500 MeV (section 2.4).

The basic ideas of Levinger were developed into a more sophisticated microscopic treatment by Gottfried [26] who applied several approximations to obtain an analytical solution. Gottfried expressed the correlated pair as the product of the pair function of the shell model ϱ_s, derived from a Slater determinant, and a Jastrow type correlation function g [27] which incorporates central short range correlations:

$$\varrho(r_1, r_2) = \varrho_s(r_1, r_2)|g(|r_1 - r_2|)|^2 \tag{2.2}$$

where ϱ_s describes the long-range properties of the nucleon wave function and g represents central correlations at small internucleon separations which can be considered a modification of the shell model picture. Two approximations are necessary for the (γ,NN) cross section to factorise. Firstly the effects of FSI are neglected and a plane-wave description for the outgoing nucleons is adopted. Gottfried also decoupled the centre-of-mass (COM) and relative (REL) motion of the nucleon pair using a "zero-range" approximation for the interaction. This restricts photoabsorption to pairs in relative S angular momentum states (l=0). Under these assumptions, the (γ,NN) cross section, σ, factorises and is a product of two terms:

$$\sigma \,\alpha\, F(P)S_{fi} \tag{2.3}$$

where F(P) is the probability of finding a pair in the nucleus at zero separation with total momentum $P = |k_1 + k_2 - \omega|$ where k_1 and k_2 are the momenta of the emitted

nucleons and ω the photon energy. The second term S_{fi} depends principally on the relative motion of the pair and contains all information on the dynamics of the process. Boato and Giannini [28] showed that this factorisation still held even when meson exchange currents were included in the calculation.

Previous works [29, 30] have shown that the role of the pair function F(P) in the (γ,pn) reaction is well described by harmonic oscillator wave functions at low residual excitation. This observation has led to increased confidence that information on the short-range interaction contained in the S_{fi} term could become accessible. It is more desirable to study these effects in (γ,pp) due to the suppression of charged MEC. However, the mechanism governing the reaction in this channel is less well understood compared with (γ,pn) and an improvement in the theoretical treatments describing the process is necessary. Significant theoretical progress has been made through the work of groups at Valencia, Pavia and Gent whose models offer a more refined theoretical approach which are outlined below. Additionally, the study of ($\overrightarrow{\gamma}$,NN) reactions provide an extra degree of freedom which further constrain theoretical models and is discussed in section 2.5.

2.3.2 Valencia Model

The most ambitious model is that of the Valencia group [31] who have developed a full microscopic treatment of photon-nucleus coupling at intermediate energies and include pion final state interactions. The model includes all (multi-) pion and (multi-) nucleon production processes in complex nuclei. The pion production processes include both resonant (Δ) and non-resonant terms and include the propagation and interaction of the Δ in the nuclear medium. Long and short-range correlations are contained within the model, with the latter included by using correlated wave functions. The products of these reactions are tracked through the nuclear medium, using a semi-classical approach to account for any further interactions in the nuclear medium. Nucleons produced from the initial reaction can be scattered by the medium, while pions can be scattered or reabsorbed in (π,NN) reactions. The model gives a good description of the (γ,pn) missing energy spectra (section 2.4) giving confidence that the different reaction processes are well understood.

The Valencia model represents a major theoretical advance, allowing the treatment of the full complexity of photonuclear reaction mechanisms. Unfortunately, this is at the expense of the nuclear structure aspects of the reaction. The model is based on a Fermi gas approach which, although related to real nuclei by a local density approximation, neglects binding effects and ignores nuclear shell structure. Nevertheless, the Valencia model gives a quantitative measure of the relevance of different mechanisms as a function of photon energy. A major conclusion drawn from the comparisons with (γ,NN) data is that for the reaction mechanism to be dominantly two-body, a restriction has to be made to the low energy part of the residual excitation spectra. At high missing energies, the Valencia calculations suggest much of the two-nucleon knockout strength is fed by initial pion production followed by FSI. Valencia model calculations compared to experimental missing energy distributions are plotted in section 2.4.

2.3.3 Pavia and Gent Models

The theoretical approaches of the Pavia [10, 22, 32] and Gent [9, 33, 34] models to (γ,NN) reactions concentrate on the direct two-nucleon knockout process (2N) leaving the residual nucleus in a low lying, bound state. They are less ambitious in terms of the number of reaction mechanisms included and do not include any description of the pion production processes. Instead, emphasis is placed on direct two-body photoabsorption and both models are restricted to the low missing energy part of two-nucleon knockout spectra. The models give a detailed description of the nuclear structure aspects of the 2N emission reaction process. A shell-model framework is the common starting point, accounting for nuclear structure in both models, with central Jastrow correlations describing correlation effects. Furthermore, both models provide a more refined, unfactorised theoretical treatment of two-nucleon emission by investigating the two assumptions which reduce the cross section to a factorised form: the zero range approximation and effects of final state interactions.

The coincidence cross section for the reaction induced by a photon with energy E_γ, with two nucleons with momenta $\mathbf{p}_1$ and $\mathbf{p}_2$ and energies E_1 and E_2 ejected

from a nucleus is directly proportional to the transverse structure function W_T [6]:

$$\frac{d^5\sigma}{dE_1 d\Omega_1 d\Omega_2} \alpha\, W_T \tag{2.4}$$

which is expressed in terms of components of the hadron tensor $W^{\mu\nu}$ with $W_T = W^{xx} + W^{yy}$. The hadron tensor is related to the transition amplitude between the initial state of the target A and the final nuclear state corresponding to a residual A-2 nucleus and two outgoing nucleons. The Pavia model describing the (γ,pp) reaction assumes a direct knockout mechanism leaving the spectating residual nucleus in a discrete state [22]. Under these assumptions the transition matrix contains three main ingredients: the two nucleon overlap integral ψ_i, the nuclear current **J** and the final state wave function ψ_f. The two nucleon overlap integral contains information on nuclear structure and the dynamics of the two-hole state in the initial nucleus. It allows the cross section to be written in terms of the two hole spectral function of equation 2.2. The nuclear current operator is a sum of one and two-body parts. As MEC are suppressed in (γ,pp) reactions, the two-body current only contains the isobar currents of figure 2.4. In the final state ψ_f, each of the outgoing nucleons interact with the residual nucleus while mutual interactions between the outgoing nucleons are neglected. A complex phenomenological optical potential containing central, Coulomb and spin-orbit terms account for FSI effects between the outgoing nucleons and the residual nucleus.

Pavia calculations for $^{16}O(\gamma,\mathrm{pp})$ and $^{16}O(\gamma,\mathrm{pn})$ have been carried out for photon energies E_γ=100-400 MeV [22]. The cross sections and asymmetries were found to have small contributions from one-body currents and the effects of SRC are generally very small. Different correlation functions derived from the Bonn-A [35] and Reid Soft-Core (RSC) potentials [36] were compared for $^{16}O(\gamma,\mathrm{pp})$ at E_γ=100 MeV, where Δ contributions are small and show reasonable agreement. One-body current contributions increase at higher E_γ, with the RSC potential predictions larger than Bonn-A. However, Δ contributions are much larger and completely dominate the cross section. Therefore, two-nucleon emission reactions may not be ideal for investigation of SRC but might be better suited to give information on the various terms of the nuclear current and on their behaviour in different kinematic conditions and in different states.

The approach of the Gent model differs from the Pavia calculations in some respects. Following the absorption of a photon by the target nucleus, two nucleons are excited from a bound state to a continuum eigenstate of a mean-field potential, derived from a Hartree-Fock calculation. The final state is given by the product of two shell model continuum state wave functions and distortion effects are treated using a partial wave expansion for each nucleon in a real mean-field potential. An energy dependence of the Δ width is included and the contributions of heavier meson exchange currents (ρ, σ and ω) were investigated. For the (γ,pn) reaction, contributions from ρ-exchange currents were found to be non-negligible. Isobaric currents are the dominant contributors to the (γ,pp) reaction, similar to the results found in the Pavia calculations.

2.4 Review of (γ,NN) Experiments

Early (γ,NN) experiments [5, 37, 38, 39] used continuous bremsstrahlung which necessitated assumptions about the residual nucleus to determine the incident photon energy. Despite the poor statistical accuracy of the results the evidence supported quasideuteron behaviour for the (γ,pn) reaction in complex nuclei. The experiments detected a pn pair in coincidence following photon absorption and the average opening angle was consistent with distributions seen in deuteron photodisintegration with some smearing due to initial Fermi motion of the pair. An early study of the (γ,pp) reaction was performed by Weinstein *et al.* [40] who argued that the results were consistent with initial pn absorption followed by a charge exchange FSI.

Little progress was made in understanding the reaction mechanisms which govern (γ,NN) processes until the advent of tagged photon facilities. Experiments using tagged photons at Bonn [41] and Tokyo [42], though lacking sufficient resolution to distinguish the initial shells of the emitted nucleons, provided useful data on the photon energy and angular dependence of the cross sections. The angular distributions of the emitted pn-pairs again supported the predictions of the quasideuteron model although this was not the case for pp-pairs which exhibited flat angular distributions. The rapid increase in the (γ,NN) cross section above the pion production

threshold suggested an increasing fraction of the photoabsorption strength originates from quasi-free pion production followed by a $\Delta N \rightarrow NN$ reaction.

The high resolution Glasgow-Edinburgh-Mainz photon tagging spectrometer [43] used with the 180 MeV MAMI-A electron beam provided the experimental resolution ($\sim$7 MeV) sufficient to resolve the shells of the emitted nucleons and allowed the reaction to be studied for all excitation energies of the residual nucleus. The reactions $^{12}C(\gamma,\mathrm{pn})$ [44, 29] and $^{16}O(\gamma,\mathrm{pn})$ [45] were studied over a photon energy range E_γ=80-150 MeV with the results showing a concentration of strength on states lying close to the ground state of the residual nucleus. The shapes of the residual spectra were simulated by folding single nucleon excitation energy distributions from (e,e'p) data. The experimental data for (γ,pn) at low excitation energy, E_x <30 MeV were in good agreement with calculated absorption strengths on $(1\mathrm{p})^2$ and (1p)(1s) nucleon pairs indicating the (γ,pn) reaction proceeds with the (A-2) residual nucleus acting as a spectator. The $^{12}C(\gamma,\mathrm{pp})$ strength was concentrated at higher missing energies and the lack of strength near threshold indicated that there is very little true absorption on pp-pairs [29]. Attempts to describe the missing energy in terms of folding together single nucleon knockout excitation spectra gave a poor description of the data. The strength at higher missing energies was a possible indication that much of the (γ,pp) strength are fed through FSI following initial pn-pair absorption.

The corresponding recoil momentum distributions, P_r, for low residual excitations were compared to a Monte Carlo model of the direct two-nucleon process, which simulates the measured pair momentum distribution on the basis of the Gottfried model assumptions. The (γ,pn) distributions were well described by direct absorption on $(1\mathrm{p})^2$ nucleon pairs at low excitation energies and (1s)(1p) absorption at higher excitation. Surprisingly for the (γ,pp) reaction, the observed distributions for low residual excitation were also reasonably close to the distribution expected for direct emission from $(1\mathrm{p})^2$ pairs. The recoil momentum distributions for (γ,pn) and (γ,pp) for E_γ=145-157 MeV for different nuclear excitation are shown in figure 2.5.

A significant energy upgrade of the MAMI accelerator and the installation of the Glasgow photon tagging spectrometer allowed high resolution studies of (γ,NN)

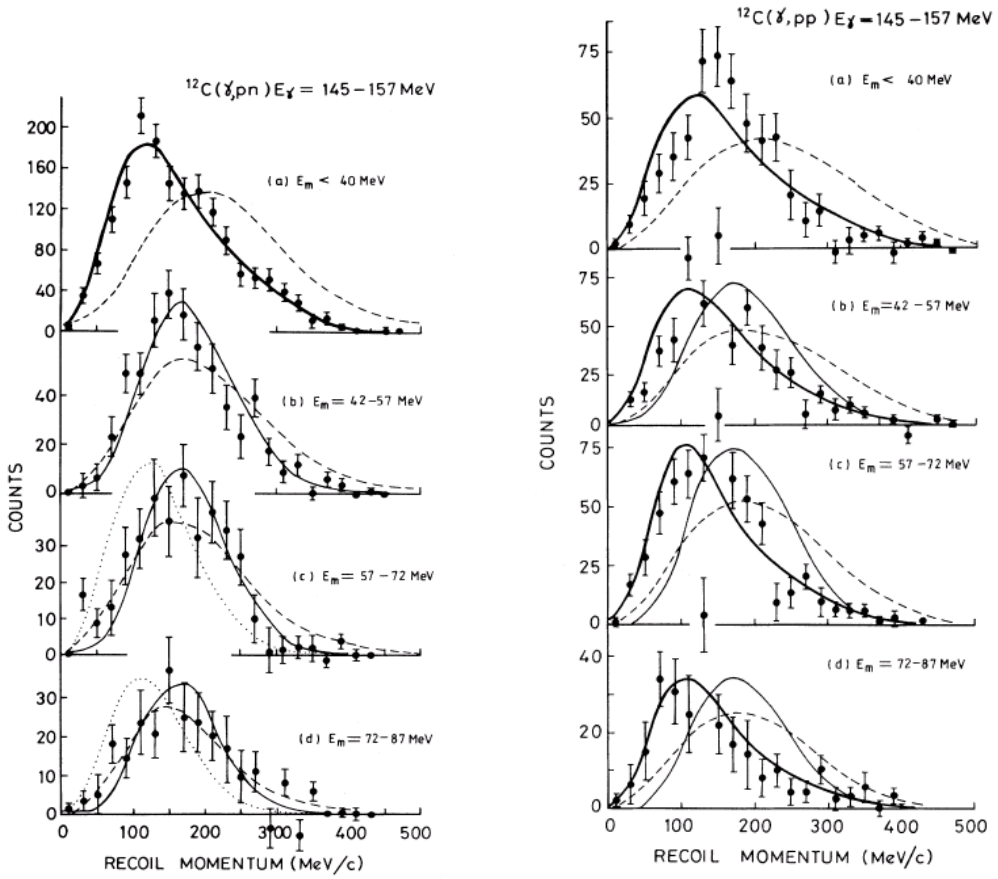

(a) (b)

Figure 2.5: The observed recoil momentum distributions for E_γ=145-157 MeV and different missing energy regions for (a)$^{12}C(\gamma,pn)$ and (b)$^{12}C(\gamma,pp)$. The thick, thin and dotted lines represent the direct 2N simulation with absorption on p-, sp- and s-shell nucleon pairs respectively. The dashed line corresponds to a simulation where the available energy is shared amongst the emitted nucleons and recoiling nucleus according to the phase space available [29].

reactions at Δ-resonance energies. Recoil momentum distributions for $^{12}C(\gamma,NN)$ reactions in the photon energy range E_γ=200-400 MeV were studied by Harty *et al.* [30]. Again, at low residual excitation (E_x <13 MeV) the (γ,pn) data was consistent with direct knockout of $(1p)^2$ pn-pairs. At higher residual excitation (E_x =13-43 MeV) dominant photoabsorption on (1s)(1p) pn-pairs occurs. Calculations based on the spectator approximation at low residual excitation for absorption on a $(1p)^2$ pp-pair were compared with (γ,pp) data, giving a slightly poorer description of

the recoil momentum distribution [29]. For residual excitation E_x =13-43 MeV appreciable deviations from the spectator model were observed for P_r >300 MeV/c, giving a probable indication of FSI. At higher residual excitation (E_x=73-173 MeV) the data extended to much larger recoil momenta than predicted by the direct two-nucleon knockout model confirming more complex mechanisms dominate. There was little difference in the recoil momentum distributions for the (γ,pn) and (γ,pp) reactions at high residual excitation implying similar reaction mechanisms account for both processes.

The angular distributions of both the ^{12}C(γ,pn) and ^{12}C(γ,pp) reactions were studied by MacGregor [46] and Yau [47] to achieve better understanding the reaction mechanisms. To emphasise direct emission of nucleon pairs the correlated nucleon detectors where placed back-to-back in the centre-of-mass of the photon and nucleon pair (quasideuteron kinematics) and covered a wide range of proton angles θ_p=23-152°. For E_x <13 MeV, large differences in the (γ,pp) and (γ,pn) angular distribution were noted for E_γ=150-200 MeV, 250-300 MeV and 350-400 MeV [46]. If charge exchange following initial absorption on a pn-pair were responsible for much of the (γ,pp) strength similar angular distributions would be expected for both channels. The dissimilar shapes were a direct indication that intrinsically different mechanisms are responsible for the (γ,pp) and (γ,pn) reactions at low excitation and that contributions from charge-exchange FSI are small. At higher E_x the angular distributions of the pn and pp channels showed more similar characteristics, suggesting that charge exchange FSI contribute to the (γ,pp) reaction. Calculations based on the Gent model had reasonable success in reproducing the general trends in the photon energy dependence of both channels and some of the distinctive features in the angular distributions but did not give an accurate description of the data, particularly for (γ,pp).

Angular distributions of ^{12}C(γ,pn) for E_γ=120-150 MeV and $E_x < 43$ MeV were compared with the differential cross section for ^{2}H(γ,p) [47]. The differences in angular distribution gave the first indication that (γ,pn) in complex nuclei is not a simple scaling of deuteron photodisintegration. The results were compared to Gent calculations which included effects due to ρ-exchange in their calculations. This

gave a better representation of the shape of the angular distribution.

The works of Lamparter [48] and Watts *et al.* [24] aimed to give a measure of the relevant strengths of different mechanisms for various kinematic regions, comparing the results to the microscopic code of the Valencia group. Valencia calculations, shown in figure 2.6, successfully described the shape of the (γ,NN) excitation spectra suggesting the dominant mechanisms are largely under control although the model overestimates the (γ,pp) cross section by a factor of $\sim$3.5 [48]. A study of the ^{12}C(γ,NN) reaction over a wide kinematic range covering back-to-back emission and more extreme kinematics which extend beyond quasideuteron regions and covering E_γ=200-700 MeV was made by Watts *et al.* [24]. In the measurements, protons were detected in a charged particle hodoscope (PiP) placed in a backward position covering the polar angular range $78^\circ - 158^\circ$. Region I, II and III in figures 2.6 and 2.7 correspond to different placements of ToF bars which detect the coincident nucleons. Region I sampled back-to-back QD kinematics and covered a polar angular range $36.7^\circ - 71.2^\circ$. Regions II and III sampled progressively more extreme kinematics with polar angle ranges of $78.8^\circ - 142.4^\circ$ for II and $13.7^\circ - 30.2^\circ$ (where both PiP and the ToF bars are on the same side of the photon beam). Studying two-nucleon emission away from back-to-back kinematics gives more sensitivity to distortions from FSI and multi-particle processes. The general features of ^{12}C(γ,pn) reaction were well described for all missing energy by the Valencia model, even in regions away from back-to-back kinematics. For ^{12}C(γ,pn), the strength at low missing energy away from back-to-back kinematics, was found to be due to direct knockout mechanisms, though no direct strength in these kinematics were observed for ^{12}C(γ,pp).

A detailed study of the direct two-nucleon knockout process was carried out for the low missing energy. A Monte Carlo simulation assumming direct 2N knockout from a spectating residual nucleus was used to compare calculated with measured recoil distributions. Direct two-nucleon emission dominates the observed (γ,pn) yield at low residual excitation E_x <13 MeV for E_γ up to 600 MeV including kinematics away from back-to-back emission. Although slightly poorer, the spectator model gave a reasonable description of the (γ,pp) data for E_γ=150-500 MeV, describing $(1p)^2$ absorption for E_x <13 MeV. Evidence of direct (1s)(1p) diproton

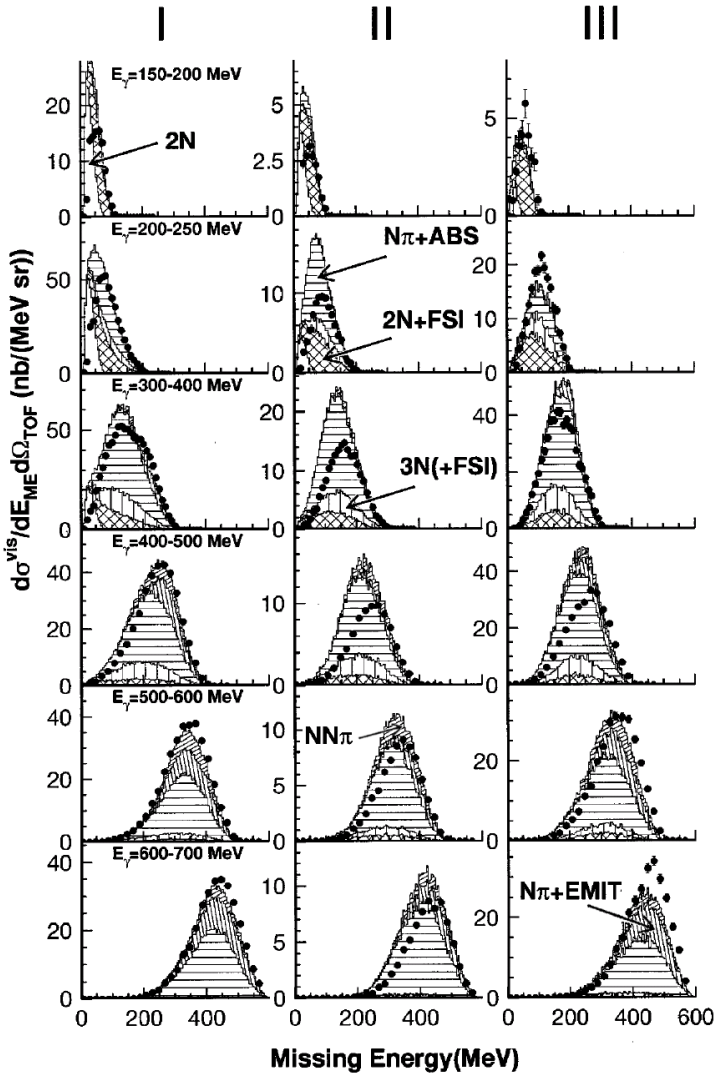

Figure 2.6: Missing energy spectra for the $^{12}C(\gamma,pp)$ reaction for the kinematic regions **I**, **II** and **III** specified in reference [24]. The Valencia model predictions are separated into direct 2N knockout (2N), direct 2N knockout with FSI (2N+FSI), direct 3N knockout with or without FSI (3N(+FSI)), initial π production with subsequent π reabsorption in the nucleus (Nπ+ABS), initial π production followed by π rescattering in the nucleus (Nπ+EMIT) and initial NNπ reactions, as indicated in the figure.

knockout was observed for E_x =13-43 MeV for E_γ up to 500 MeV. However, the detailed agreement was inferior to that observed for $(1p)^2$. Excess yield at high recoil momenta was found and the 2N absorption model could not describe the data for P_r >300 MeV. This implies greater contributions from FSI and multi-step processes at high P_r in this region. Figure 2.7 taken from reference [24] shows the recoil momentum distributions for missing energy regions (a) $E_m < 40$ MeV (E_x <13 MeV) and (b) E_m=40-70 MeV (E_x=13-43 MeV) for a wide range of photon energies together with predictions from direct 2N knockout models. Missing energy contains both the residual excitation and the reaction threshold (∼27 MeV for 2N knockout). Discrepancies between calculated and observed recoil momentum distributions were more prominent in kinematics away from back-to-back emission, where contributions from indirect processes are larger.

2.5 Calculations Using Polarised Photons

Measurements of unpolarised cross sections are sensitive only to the transverse structure function W_T (equation 2.4) which gives the average of the parallel and perpendicular nuclear response [6,9,22]. Alternatively, polarised photons give access to the difference between the parallel and perpendicular responses through the structure function $W_{TT} = W^{xx} - W^{yy}$. Theoretically, the photon asymmetry is expressed as the ratio of these structure functions:

$$\Sigma = \frac{W_{TT}}{W_T} = \frac{W^{xx} - W^{yy}}{W^{xx} + W^{yy}} \tag{2.5}$$

W_{TT} and thus Σ is sensitive to both the angular momentum contributions to nuclear currents and to interference between competing processes. The photon asymmetry provides a more sensitive observable against which models of nuclear currents contributing to two-nucleon emission can be compared. The behaviour of the cross section σ with linearly polarised photons is generally expressed through the photon asymmetry Σ as:

$$\sigma = \sigma_0(1 + \Sigma\cos(2\phi)) \tag{2.6}$$

where σ_0 is the unpolarised cross section and ϕ is the angle between the photon polarisation and the reaction plane. The beam asymmetry Σ is given by the difference

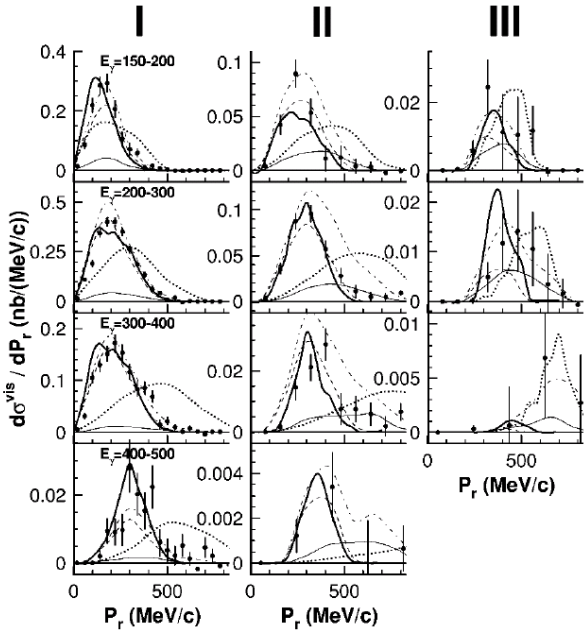

(a) E_m <40 MeV

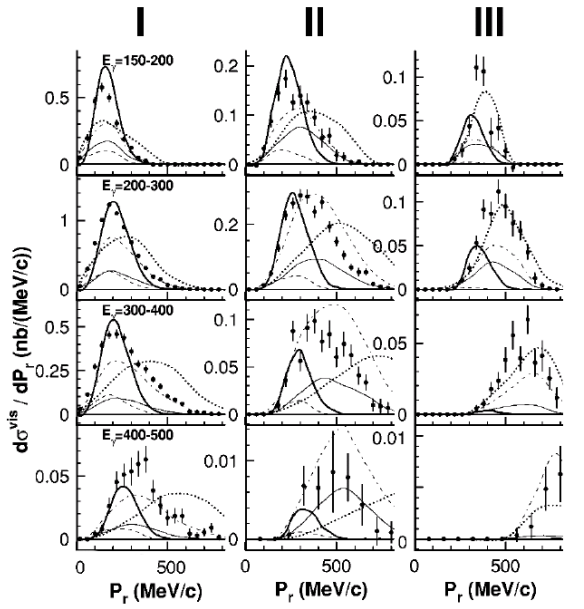

(b) E_m=40-70 MeV

Figure 2.7: Recoil momentum distributions for $^{12}C(\gamma,\mathrm{pp})$ for (a) E_m <40 MeV and (b) E_m=40-70 MeV taken from [24]. The lines on the figures show the predictions of a 2N knockout MC (thick solid), phase space model (dotted) and the predicted total (dot-dash), direct 2N knockout (dash) and 2N+FSI (thin solid) cross sections from the Valencia model. The VM predictions have been multiplied by a factor of 0.5.

over the sum of the reaction cross sections with the plane of polarisation parallel ($\sigma_{\parallel}$) and perpendicular ($\sigma_{\perp}$) to the reaction plane

$$\Sigma = \frac{\sigma_{\parallel} - \sigma_{\perp}}{\sigma_{\parallel} + \sigma_{\perp}} \tag{2.7}$$

Extensive calculations of polarisation degrees of freedom for (γ,NN) reactions on ^{12}C and ^{16}O have been carried out using the Gent model [9]. They point out that studying the cross section for excitation of the A-2 residual with different angular momentum states J_R gives information on the relative pair wave functions. Calculations were performed in quasideuteron kinematics, resulting from photon absorption on stationary initial pairs, minimising the influence of the pair COM motion. The calculations were performed for different J_R and at photon energies of 100, 200, 300 and 400 MeV. Whereas Gottfried's "zero-range" approximation restricted photoabsorption to pairs in relative S states, the Gent calculations include pairs in relative S, P and D states through partial wave terms $^{2S+1}l_j$ for l_{rel}=0, 1 and 2 respectively which are shown in table 2.1 for p^2 and sp shell knockout. The calculations indicated that the $^{12}C(\gamma,\mathrm{pp})$ asymmetries were typically larger than $^{12}C(\gamma,\mathrm{pn})$, reflecting the different mechanisms contributing to each channel. Despite the predominant role played by S-wave absorption in quasideuteron kinematics, significant deviations from higher relative angular momentum were observed in the angular cross sections and also in the photon asymmetry.

Gent calculations were also applied to ^{16}O in coplanar and symmetric kinematics. In these kinematics, both nucleons are emitted in the reaction plane with equal energies but opposite angles with respect to the beam. These kinematics complement quasideuteron kinematics and explore the fact that nucleon pairs in the medium have COM degrees of freedom in addition to their relative motion. The study tested the validity of the Gottfried model by investigating whether photoabsorption on pp-pairs in a relative $^1S_0$ state ($J_R = 0^+$) is the dominant contribution. The unfactorised calculation was applied to the unique case for a $(1p_{1/2})^2$ configuration for the residual A-2 nucleus, so that only the $J_R = 0^+$ state can contribute for the pp-case and the dominant contribution is from $^1S_0$ photoabsorption. The results are shown in figure 2.8(a). The peak in the cross section at $\theta_p = 70^\circ$ corresponds to zero recoil momentum. Except at low photon energies, Σ is close to -1 almost independent

Shell	J_R	Relative State $^{2S+1}l_j$
(1s)(1p)	0^-	$^3P_0$
	1^-	$^1S_0$
	1^-	$^3P_1$
	2^-	$^3P_2$
$(1p)^2$	0^+	$^1S_0$
	0^+	$^3P_1$
	1^+	$^3P_0$,$^3P_1$,$^3P_2$
	2^+	$^3P_1$,$^3P_2$
	2^+	$^1S_0$
	2^+	$^1D_2$

Table 2.1: Possible configurations for pp knockout from s and p shell combinations [9].

of photon energy and proton emission angle. The unfactorised model also predicts $\Sigma = -1$ indicating the photon asymmetry is insensitive to the treatment of FSI.

The effects of different angular momentum states on Σ are shown in figure 2.8(b) and 2.8(c) corresponding to $[(1p_{3/2})^2; J_R = 0^+;\ J_R = 2^+]$ and $[(1p_{3/2})(1p_{1/2}); J_R = 1^+]$ final states respectively [9]. The $1p_{3/2})^2$ configuration can be excited in $^{16}O(\gamma,pp)$ reaction through S, P and D absorption while the $(1p_{3/2})(1p_{1/2})$ configuration is unique as S-wave absorption is forbidden and only relative P wave absorption contributes, giving a positive Σ over most of the range of photon energies and proton angles. It is clear from 2.8(b) and (c) that P and D wave admixtures significantly alter the photon asymmetry Σ. The extent to which mechanisms beyond $^1S_0$ absorption contribute to the cross section depends strongly on the kinematics and nuclear structure of the A-2 fragment [9].

Calculations of the photon asymmetry for the $^{16}O(\gamma,pp)$ reaction to low lying discrete final states of the residual ^{14}N nucleus have been carried out by the Pavia group [22], also in coplanar and symmetrical kinematics. Figure 2.9 plots the calcu-

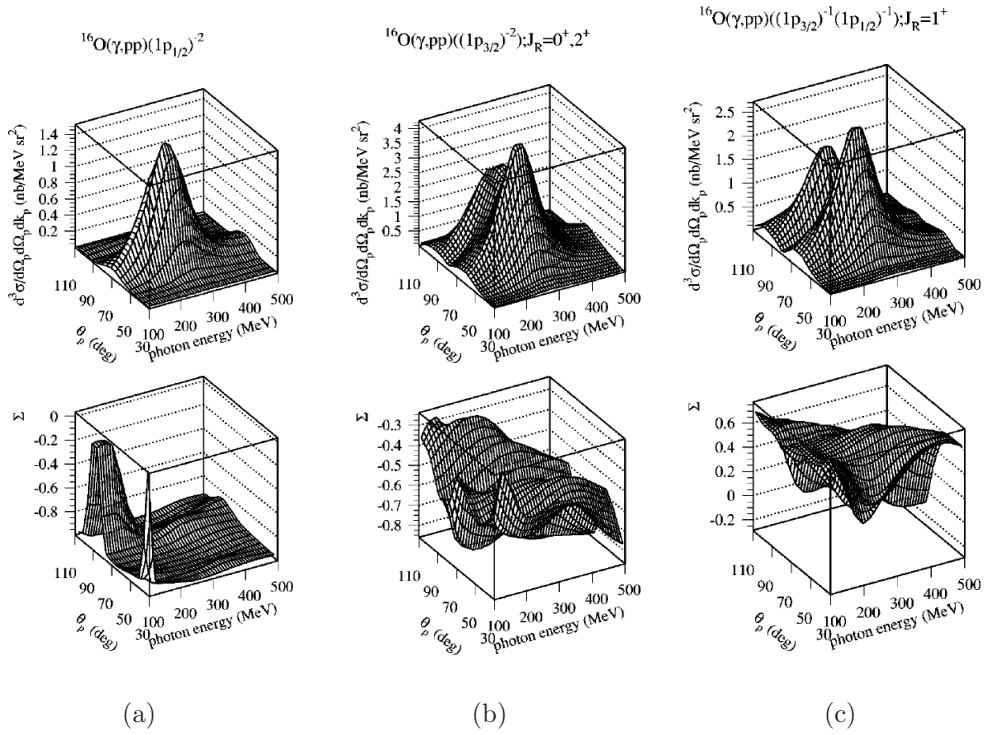

(a) (b) (c)

Figure 2.8: Calculated photon energy and proton angular dependence on the differential cross section and photon asymmetry for $^{16}O(\gamma,\mathrm{pp})$ reaction for different p-shell configurations [9]. The calculations for (a), (b) and (c) correspond to photoabsorption on pairs in different angular momentum states and is described in more detail in the text.

lated photon asymmetry for different relative states as a function of the angle of one of the emitted nucleons at E_γ=300 MeV for the $J_R = 2^+$ final state. The 2^+ state is always negative with $\Sigma \sim -1$ for pure $^1S_0$ absorption while P wave absorption brings Σ closer to zero. In agreement with the Gent calculation, the Pavia model found $\Sigma = -1$ at most energies and angles for the final 0^+ state whereas the 1^+ state is large and positive. A conclusion of the work was that the asymmetry, like the cross section is dominated by Δ currents and has little variation with photon energy. For the (γ,pp) reaction, the excitation to a Δ is suppressed for the relative $^1S_0$ state [22] due to angular momentum and parity conservation. This does not apply to diproton pairs with a larger relative angular momentum.

For $^1S_0$ absorption, the Gent calculations predict a peak at central angles in the centre-of-mass frame of the photon-nucleon pair independent of E_γ. The angular

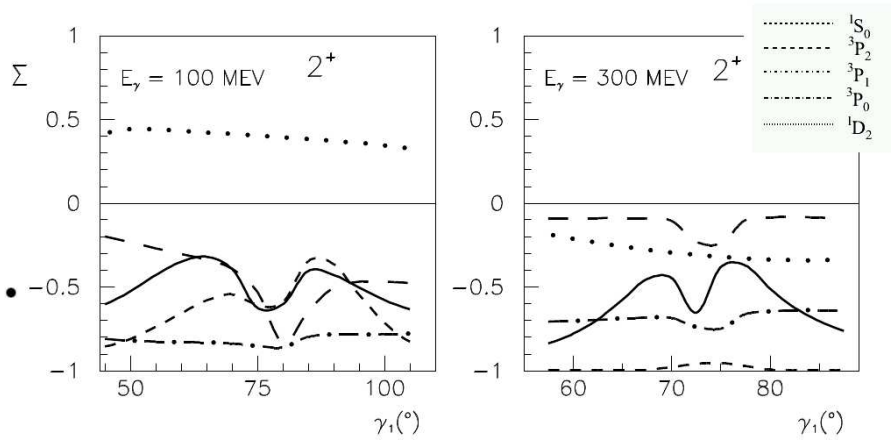

Figure 2.9: The calculated photon asymmetry for $^{16}O(\gamma,\mathrm{pp})$ reaction at E_γ=100 and 300 MeV as a function of the angle γ_1, the polar angle of higher energy proton in the centre-of-mass frame of the photon-nucleon pair. The asymmetry is sensitive to the initial relative orbital angular momentum state of the pair, with the solid line giving the incoherent sum of the individual states. Taken from [22]

dependence of Σ was largely unaffected by inclusion of FSI effects in unfactorised calculations. The asymmetry tends to zero at forwards and backwards angle. The angular distributions show little dependence on the choice of central correlation function used in the calculation. Pavia calculations in coplanar and symmetric kinematics (figure 2.9) show the angular dependence for different angular momentum states and the interference between them. Σ peaks with magnitude ~ -0.7 at $\gamma_1 \sim 75°$. Both models highlight that the photon asymmetry have a strong angular dependence. In quasideuteron kinematics, which demands absorption on a stationary pair (P=0), major deviations from S-wave absorption were observed in the angular cross section. However, the angular dependence and magnitude of the photon asymmetry was found to be far less affected when photon absorption on pairs in higher relative momentum states were included in calculations in QD kinematics. In coplanar kinematics, the addition of the slightest admixture of mechanisms going beyond $^1S_0$ absorption induce major changes in the asymmetry. This indicates that the sensitivity of the cross section and asymmetry for transition to different states is essentially due to components of the CM orbital angular momentum of the initial pair.

To summarise, both models predict that by studying the differential cross sections and photon asymmetries for excitation of the A-2 fragment with particular angular momentum J_R, information can be accessed about the nature of the initial pair wavefunction. This does not imply that the experiments require the resolution to resolve each residual state. Observables for different shell combinations, which would typically feed the residual system in a range of missing energies, would already be hugely instructive to learn about the different possible pair combinations [9]. Furthermore, the photon asymmetry is predicted to be sensitive to the various possible reaction mechanisms. For example pure contributions from either pion mechanism is predicted to produce a large positive asymmetry. However, interference between the seagull and pion-in-flight terms results in a small negative asymmetry. The extent to which S-wave absorption play a role is very much dependent on kinematics and the structure of the A-2 fragment. Therefore. studying $\Sigma_{(\gamma,pp)}$ over a wide range of kinematics will help determine which states of relative angular momentum dominate, giving insight into which terms contribute to the reaction process.

2.6 Previous Measurements with Polarised Photons

There have been several previous measurements of the photon asymmetry of (γ,NN) reactions in light nuclei. LEGS collaboration [49] measurements on ^{3}He were averaged over the photon energy range 235-305 MeV. Strong differences in Σ were observed between ^{3}He($\overrightarrow{\gamma}$,pn) and ^{3}He($\overrightarrow{\gamma}$,pp) with $\Sigma_{(\gamma,pn)}$ $\sim$-0.2 and $\Sigma_{(\gamma,pp)}$ a much smaller ~ -0.05. Calculations which include contributions from one, two and three-body photon absorption give a good description of the data. The results gave indication that one and two-body terms dominate the ($\overrightarrow{\gamma}$,pn) reaction while three-body terms dominate ($\overrightarrow{\gamma}$,pp).

Photon asymmetry measurements of the ^{4}He($\overrightarrow{\gamma}$,pn) and ^{6}Li($\overrightarrow{\gamma}$,pn) reactions have been made at the 3.5 GeV Yerevan electron synchrotron [50]. The ^{6}Li($\overrightarrow{\gamma}$,pn) data spanned a wide photon energy range 300-900 MeV and the ^{4}He data covered E_γ=450-550 MeV. The measurements were averaged over a wide range of missing energies and had limited kinematic coverage. The Σ values for both ^{4}He and ^{6}Li

have a slightly smaller magnitude than deuterium photodisintegration data, though a similar photon energy dependence was observed.

Measurements of $\Sigma_{(\gamma,pn)}$ and $\Sigma_{(\gamma,pp)}$ on ^{16}O have also been performed at LEGS in coplanar kinematics with symmetric detection angles for E_γ=245-315 MeV [51]. Two nucleon knockout reactions in these kinematics are predicted to depend strongly of Δ-currents and have little sensitivity to SRC. For E_m <50 MeV, where direct knockout is expected, a result of $\Sigma_{(\gamma,pp)}$ ∼-0.3 was obtained. This result is considerably smaller than the -1.0 expected for a pure $^1S_0$ interaction in coplanar kinematics and is interpreted as evidence for the knockout of nucleon pairs in higher relative angular momentum states. For E_m <70 MeV, the asymmetry for ($\overrightarrow{\gamma}$,pp) is a factor of ∼2 greater than $\Sigma_{(\gamma,pn)}$ supporting the conclusions of previous unpolarised works that there are fundamental differences in the two reaction channels at low E_m. However, at higher missing energies E_m >70 MeV both $\Sigma_{(\gamma,pn)}$ and $\Sigma_{(\gamma,pp)}$ have similar values of ~ -0.1. Again, this is consistent with unpolarised works on ^{12}C [24, 30, 48]. Comparison with Valencia model calculations predict that little strength from direct processes persist at high E_m and mechanisms involving intermediate pion production dominate the ($\overrightarrow{\gamma}$,NN) strength. Further ^{16}O($\overrightarrow{\gamma}$,pn) measurements corresponding to $(1p)^2$ emission in quasideuteron kinematics made over a broader photon energy range E_γ =210-330 MeV is reported in the PhD thesis of Gladyshev [51].

More recent measurements of the photon asymmetry of the ($\overrightarrow{\gamma}$,pn) and ($\overrightarrow{\gamma}$,pp) on ^{12}C covering quasideuteron kinematics were carried out in Mainz using the PiPToF detector setup [25, 52]. Data was taken in the Δ-resonance region, E_γ=160-350 MeV, and events were selected to emphasise direct two-nucleon emission. The experiment gave sufficiently good missing energy resolution to allow selection of events which emphasise emission from $(1p)^2$ (E_m <40 MeV) and (1p)(1s) orbitals (E_m=40-70 MeV).

Missing energy spectra for both ^{12}C($\overrightarrow{\gamma}$,pn) and ^{12}C($\overrightarrow{\gamma}$,pp) reactions show the perpendicular yield $Y_\perp$ generally exceeds $Y_\parallel$ indicating a negative asymmetry for both channels and for: E_γ=160-220 MeV, E_γ=220-280 MeV and E_γ=290-350 MeV [25]. Photon asymmetries constructed from these spectra are shown in figure 2.10 with $\Sigma_{(\gamma,pp)}$ showing a strong negative peak which exceeds $\Sigma_{(\gamma,pn)}$ at low E_m. This

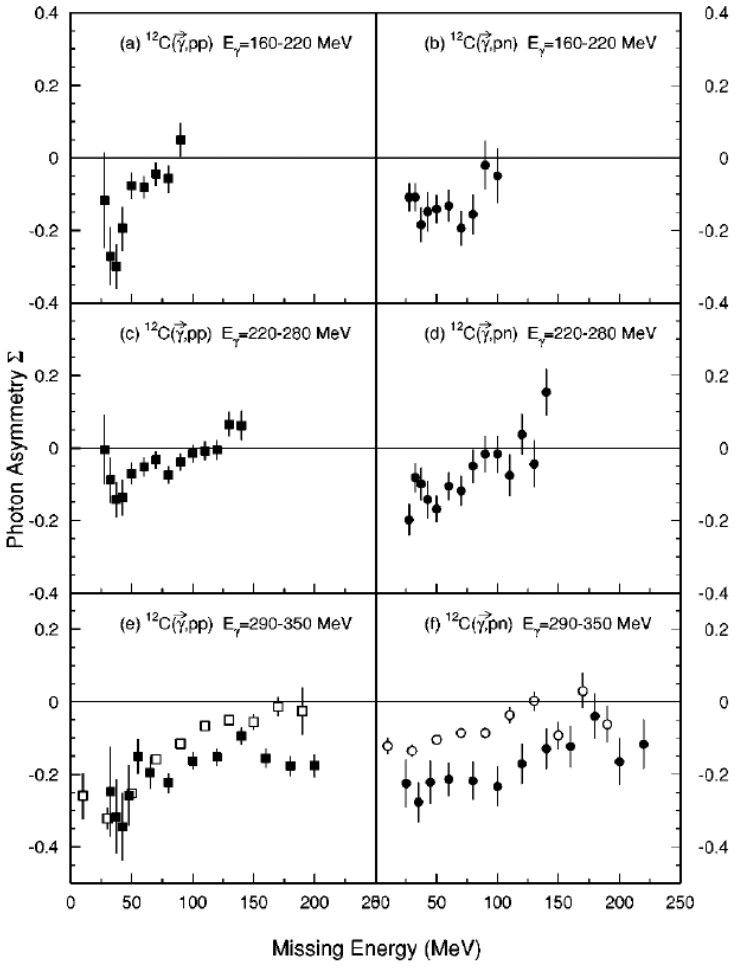

Figure 2.10: $\Sigma_{(\gamma,pp)}$ (solid squares) and $\Sigma_{(\gamma,pn)}$ (solid circles) for ^{12}C as a function of E_m for different photon energies. The open squares and circles are $\Sigma_{(\gamma,pp)}$ and $\Sigma_{(\gamma,pn)}$ for ^{16}O for E_γ=285-315 MeV [25].

reinforces the conclusion of prior unpolarised measurements that (γ,pp) is dominated by a direct knockout mechanism at low missing energy. The asymmetries remain negative but have lower magnitude at higher E_m and similarities were observed between both channels, giving indication of contributions in which more than two nucleons take part in the reaction mechanism (2N + FSI, 3N).

The photon energy dependence of Σ, emphasising direct knockout of $(1p)^2$ and (1p)(1s) nucleon pairs, is shown in figure 2.11 [25]. Despite the poor statistical accuracy of the measurements, clear differences are seen in Σ between ($\overrightarrow{\gamma}$,pp) and ($\overrightarrow{\gamma}$,pn) for the lowest missing energy region. In the higher missing energy region

sampled, the asymmetries for both channels have a similar magnitude and photon energy dependence. These reflect differences in Σ of the mechanisms which contribute to each data set. The asymmetries were compared with theoretical Gent unfactorised calculations which provided a poor overall description of the data. The calculation consistently predicted a stronger asymmetry for both channels than observed experimentally and failed to describe the fall in $\Sigma_{(\gamma,pn)}$ at low photon energy. For missing energies E_m >70 MeV, the observed asymmetries for both reactions are very similar. At low photon energies $E_\gamma < 270$ MeV, the asymmetry values are small and are thought to arise from initial photon absorption on a nucleon pair followed by FSI which wash away any asymmetry. For higher photon energies two-step processes involving initial pion production followed by reabsorption on a nucleon pair are believed to dominate. The observed asymmetries are reasonably strong for both channels with $\Sigma \sim$-0.18 at $E_\gamma = 320$ MeV. It was suggested that the observed asymmetry comes from transfer of the asymmetry from an initial quasi-free pion production reaction to the final state nucleon pair.

A limited investigation on the angular distributions of $^{12}C(\overrightarrow{\gamma}$,pp) and $^{12}C(\overrightarrow{\gamma}$,pn) have been made, plotting the differential cross section for different ToF angular bins [53]. The shape of angular distributions for ($\overrightarrow{\gamma}$,pp) showed significant differences between $\sigma_\perp$ and $\sigma_\parallel$. These are energy and angle dependent and in general $\sigma_\perp$ is stronger than $\sigma_\parallel$. For ($\overrightarrow{\gamma}$,pn), $\sigma_\perp$ is larger than $\sigma_\parallel$ for all photon energies and the differences between the two are much smaller. Gent calculations predict strong dependence of both $\sigma_\parallel$ and $\sigma_\perp$ on particle emission angle for both reactions. In general both $\sigma_\parallel$ and $\sigma_\perp$ follow similar trends for both channels, increasing or decreasing together. However, the theoretical predictions fail to give an adequate description of the experimental data. The strong variation of the calculated cross sections with particle emission angle indicates that this variable will provide a sensitive test of the calculations.

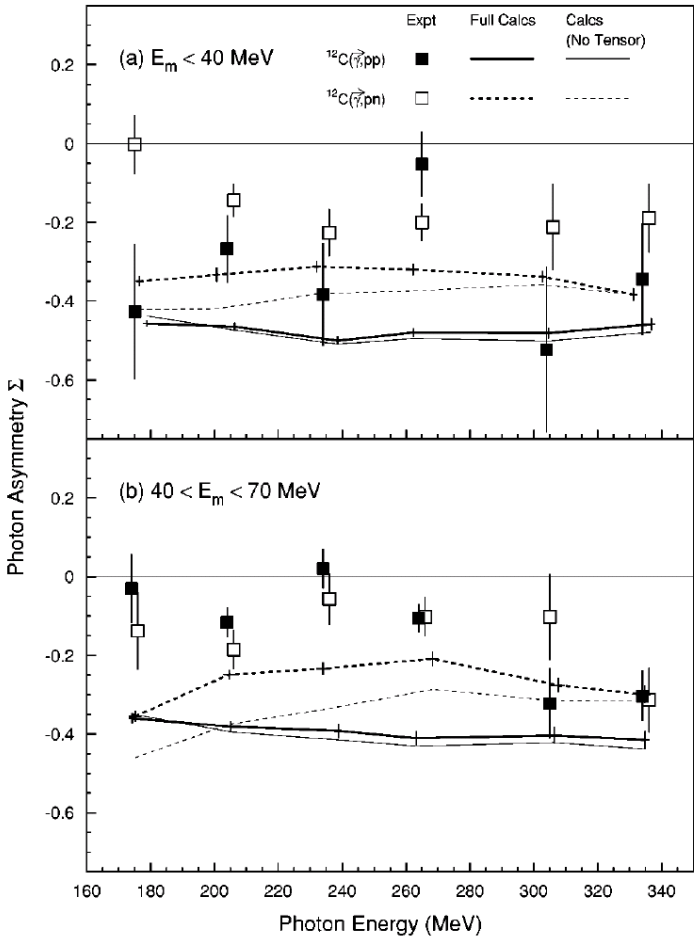

Figure 2.11: $\Sigma_{(\gamma,pp)}$ (solid squares) and $\Sigma_{(\gamma,pn)}$ (open squares) for ^{12}C as a function of E_γ and compared with two-nucleon emission calculations using the Gent model for (a) E_m <40 MeV and (b) E_m=40-70 MeV [25].

2.7 Summary and Aim of Present Work

This chapter has presented an overview of the experimental and theoretical work for studying photoinduced two-nucleon knockout reactions, with particular emphasis on the use of linearly polarised photons. Described in this thesis is a comprehensive study of the photon asymmetry of the ($\overrightarrow{\gamma}$,pp) reaction on ^{12}C over a photon energy range E_γ=200-450 MeV. Using the apparatus described in chapter 3 a substantial improvement in the statistical accuracy, angular and photon energy coverage can be made compared to previous ^{12}C measurements of Franczuk *et al.* [52] and Powrie *et al.* [25].

The photon energy dependence of Σ is studied, and direct comparisons will be made to the Powrie measurement and to the $^{12}C(\overrightarrow{\gamma}$,pn) reaction. New theoretical calculations of Σ using the Pavia model, describing direct two-nucleon knockout from ^{12}C to a discrete low lying state of the residual nucleus, would offer the most direct theoretical comparison with the measurement. Unfortunately, these calculations are ongoing and a more limited comparison of the results with theoretical predictions from the Gent model will be made. These theoretical predictions were compared with the measurement of Powrie *et al.* covering photon energies up to 350 MeV. The dependence of Σ for different missing energy regions will also be studied as a test of the spectator approximation and to gain insight into the state dependence of the initial pair wavefunction in the photoabsorption mechanism. Finally, a more thorough investigation of the angular dependence of the asymmetry will be presented.

Chapter 3

Experimental Setup

3.1 Overview

This chapter describes the various detector components and apparatus used in the study of the reaction $^{12}C(\overrightarrow{\gamma}, pp)$ carried out as part of the A2@MAMI collaboration in the A2 experimental hall of the Institut für Kernphysik, Mainz, Germany over two beamtime allocations in March and August 2008. A beam of electrons from the MAinz MIkrotron (MAMI) was directed onto a diamond radiator producing, via coherent bremsstrahlung, a beam of linearly polarised photons. The degraded electrons were momentum analysed by the Glasgow Photon Tagging Spectrometer (Tagger) and the beam of tagged photons directed to a carbon target positioned in the centre of the Crystal Ball (CB) detector.

Photonuclear reactions in the energy regime explored by MAMI produce many final state particles including protons, neutrons, pions, etas and kaons. The events of interest in this work are $^{12}C(\overrightarrow{\gamma}, pp)$, which is the main reaction being studied, and single π^0 production which is used to determine the beam polarisation. These must be separated from the events relating to the range of competing photoreactions with high efficiency. The CB, a highly segmented electromagnetic calorimeter with $\sim 4\pi$ spatial coverage is ideal for the detection of neutral mesons such as the π^0 and η through their photon decay modes. The Particle Identification Detector (PID), a barrel of thin plastic scintillators surrounding the target, provided means to identify charged species using the energy deposited in a scintillator element with coincident

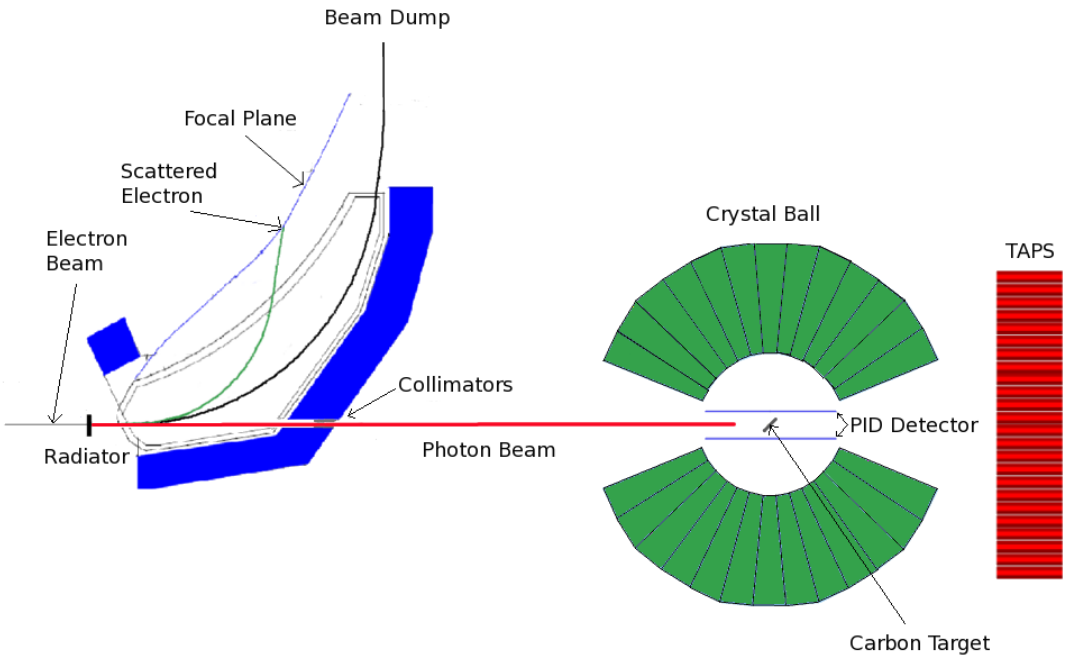

Figure 3.1: Schematic of the A2 experimental hall.

measurement of its total kinetic energy in the CB. The PID was also used for trigger timing information for events with at least one charged particle in the final state. A second electromagnetic calorimeter - the Two-Arm Photon Spectrometer (TAPS), configured as a forward wall, may provide calorimetry, identification and position information in the forward region not covered by the Crystal Ball. The arrangement of these detectors is illustrated in Figure 3.1. The TAPS data acquisition is read separately from the Crystal Ball DAQ stream and due synchronisation problems at the beginning of the experiment TAPS was not used. TAPS was also not used as $\Sigma \rightarrow 0$ as $\theta \rightarrow 0$ so little useful information was likely to be forthcoming, and there is great difficulty in normalising yields at the boundary of TAPS and the CB.

3.2 The Mainz Mikrotron

The Mainz Mikrotron [54] is a continuous wave electron accelerator (with 100% duty factor) based on a cascade of three racetrack microtrons and one higher order polytron. The accelerator in its current arrangement was completed in four stages

- from its "proof of principle" MAMI-AI through to MAMI-C, a world class accelerator facility capable of delivering an intense, highly stable beam with energies up to 1.5 GeV. Construction of the initial machine made up of a van-de-Graff injector and one race track microtron (RTM) - MAMI-AI was completed in 1979 providing a 14 MeV beam used in a series of tests to optimise the rf-structure and control of the accelerator. Addition of a second RTM and klystron in 1983 pushed MAMI-A beyond the pion production threshold, delivering a maximum beam energy of 187 MeV and beam current of 65μA. A further upgrade with MAMI-A, acting as an injector for RTM3, and replacement of the initial van-de-Graff with a linac was completed in August 1990 and named MAMI-B. This produced an exceptionally stable beam with total output energy of 855 MeV surpassing the η production threshold. The fourth generation of the Mainz Microton - MAMI-C was completed in 2006 following the installation of a double sided microtron, boosting the energy output of MAMI to 1.5 GeV. This allowed the production of strange hadrons, enabling the facility to study the quark-gluon structure of strongly interacting particles.

3.2.1 Race Track Microtrons

The electromagnetic probe has long been established as a highly successful precision tool for investigation into the internal structure of atomic nuclei and their constituents. Starting in the 1950s, inclusive electron scattering experiments used pulsed linacs with high accelerating gradient ($\sim$20 MeV/m) and the physics of the reaction were inferred solely from measurement of the scattered electron. While the results from inclusive electron scattering were impressive it was realised that isolation of specific final states would yield an abundance of additional information. Exclusive reactions requiring coincident detection of final state particles plus scattered electron placed heavier demands on the necessary beam quality delivered by accelerators. A strong demand arose in the 1970s for continuous wave, 100% duty factor beams. The finite timing resolution of any detector system means that when trying to detect two or more particles in timing coincidence there is a non zero probability that one of these particles is uncorrelated, having originated from a different nucleus. This was problematic in early pulsed accelerators were the event

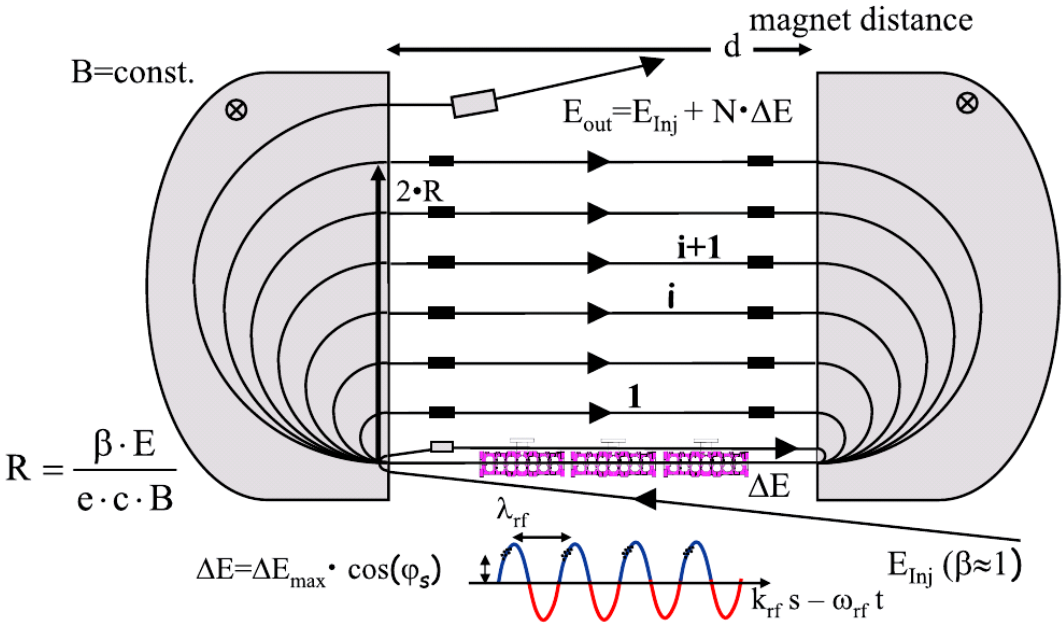

Figure 3.2: Basic setup of a racetrack microtron [54].

rate in each pulse was high. However, the probability of random events occurring can be minimised by increasing the time window in which they can occur, thus the requirement for continuous wave electron beams. The racetrack microtron design offers a compact and elegant solution which satisfies this demand.

The basic scheme of a racetrack microtron is shown in figure 3.2. An RTM in its standard design consists of a pair of 180° bending magnets facing each other with a relatively short linear accelerator placed in the field free zone [55]. Electrons are injected into the linac and are accelerated by a series of standing wave cavities powered by radio-frequency klystrons. The path of the electrons are then deflected 360° by the bending magnets, returning the beam back through the linac. The beam is recirculated through the linac multiple times via gradually increasing orbits. As the number of passes is large high energies can be reached with relatively modest accelerating gradients (∼1 MeV/m). Crucially, as the accelerating gradient is small, the RTM can run in continuous wave mode allowing a 100% duty factor beam. The design also ensures excellent energy resolution as electrons with too large a beam energy have a slightly larger orbit radius that arrive at the linac out of phase with the RF accelerating field and thus undergo smaller accelerations until this phase difference vanishes.

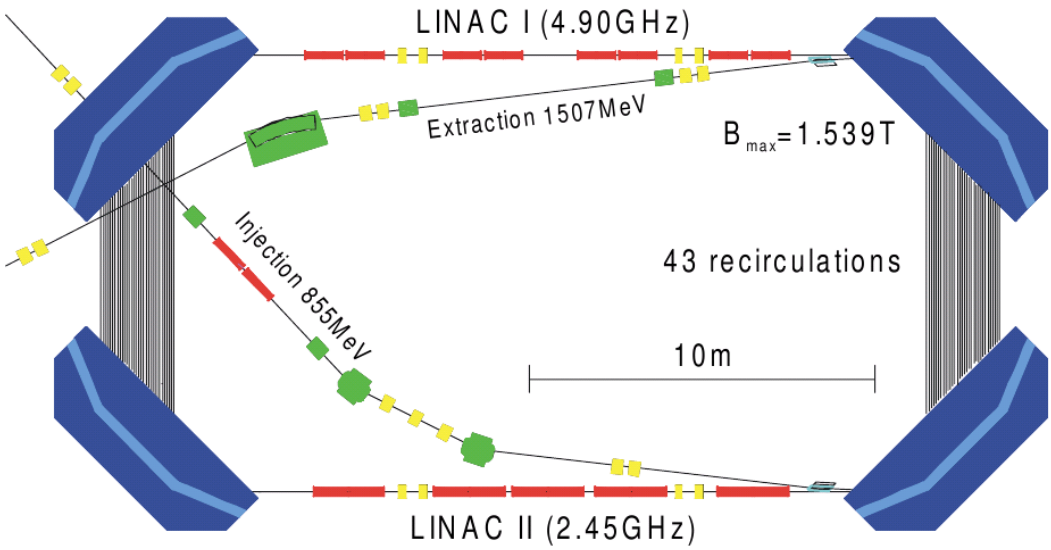

Figure 3.3: Detailed scheme of the Harmonic Double Sided Microtron for MAMI-C [56].

3.2.2 Harmonic Double Sided Microtron

The output energy of an RTM is limited to around 1 GeV with iron core magnets such as those used at MAMI. Here, one cannot generate a field much larger than 1.3 T. Once this saturation point is reached the magnetic volume required for the bending magnets scales with the third power of the output energy. To achieve the desired 1.5 GeV electron energies using a fourth RTM would require two bending magnets each with mass exceeding 2000 tonnes.

A bicyclotron design using four bending magnets offers a weight saving solution, by reducing the required deflecting angles for each magnet. The Harmonic Double Sided Microtron (HDSM) uses such a design and is the final stage of MAMI-C. Compared to a conventional RTM, the HDSM delivers twice the energy output with the same magnetic weight. The HDSM [56] illustrated in figure 3.3 has the same underlying principles as a racetrack microtron with some important modifications. The accelerator consists of two pairs of 90° bending magnets and two linacs with different frequencies, 2.45 GHz and 4.90 GHz, which provides higher longitudinal stability. Again the machine recirculates the beam through both linacs ramping up the beam energy in cw-mode until the desired output energy is attained.

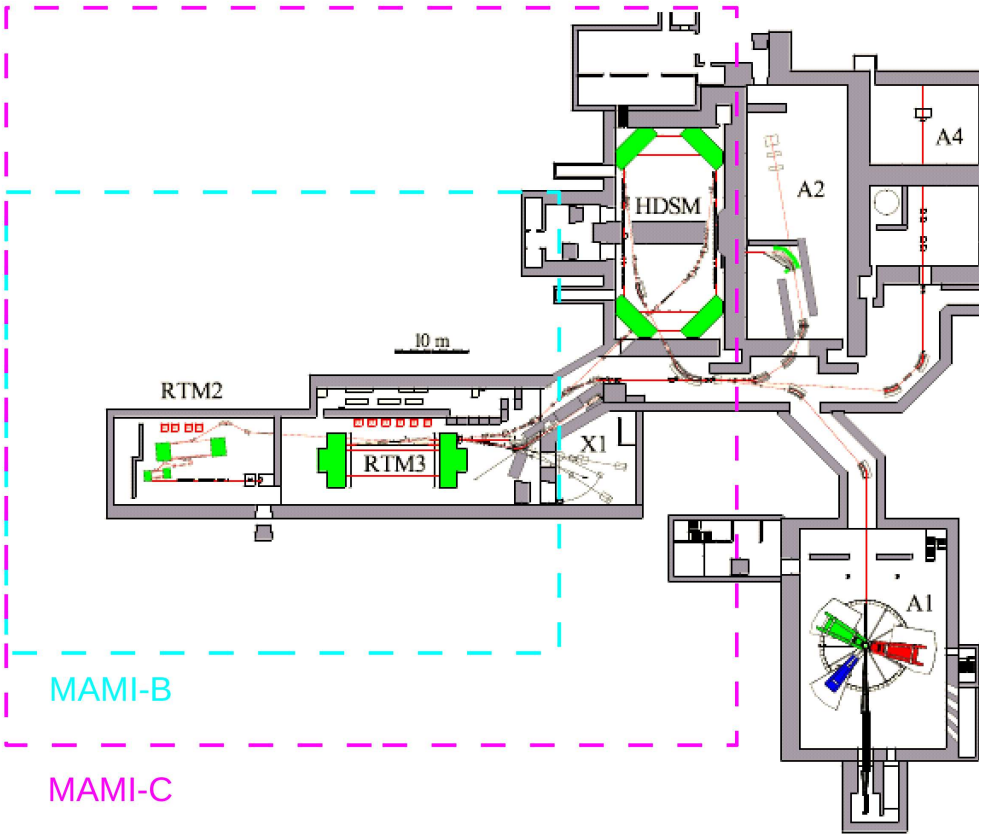

Figure 3.4: MAMI floorplan.

3.2.3 MAMI-C

A floorplan of the MAMI-C layout is provided in figure 3.4. Electrons are boiled off a GaAsP-cathode and accelerated through three successive linacs reaching an energy of 3.5 MeV. They are then injected into RTM1 where they undergo 18 recirculations boosting their energy to 14.86 MeV. These electrons are fed into RTM2 passing through the linac 52 times with an extraction energy of 180 MeV. MAMI-A acts as an injector for the final racetrack microtron - RTM3 - recirculating 90 times with output energy of 855 MeV. This beam is finally injected into the HDSM which can potentially accelerate the beam to a final energy of 1508 MeV in steps of 14-16 MeV. This depends on how many recirculations through the linacs are desired which can be adjusted by varying the position of the extraction magnet within the HDSM. The energy resolution and small beam diameter of the microtron design is inherently good and the small energy spread (1σ) of 110 keV at 1508 MeV is largely due to

		RTM1	RTM2	RTM3	HDSM
Injection Energy	MeV	3.97	14.86	180	855
Extraction Energy	MeV	14.86	180	855	1508
Number of turns		18	51	90	43
Energy Spread (1σ)	keV	1.2	2.8	13	110

Table 3.1: MAMI Beam Parameters.

synchrotron radiation. Some important MAMI parameters are summarised in table 3.1. The final MAMI-C beam can be delivered into one of three experimental halls - A1, A2 and A4 - as indicated in figure 3.4. As of September 2009, the MAMI design engineers had optimised the machine reaching an output energy of 1604 MeV.

3.3 Tagged Photon Beam

An intense beam of energy labelled photons with a well determined flux can be obtained using the established technique of bremsstrahlung tagging [57]. Typically, a mono-energetic electron beam strikes a thin radiator generating a beam of bremsstrahlung photons which are sent downstream towards a target. In the bremsstrahlung process the electrons are decelerated by the electromagnetic field of the radiator's nuclei and the emitted photons produce a continuous energy spectrum which falls off with increasing photon energy up to that of the incident electron energy. When an incident electron with energy E_0 radiates a single photon with energy E_γ the energy of the scattered electron E_{e^-} is simply:

$$E_{e^-} = E_0 - E_\gamma \tag{3.1}$$

Therefore, the energy of the radiated photon can be determined from the known incident beam energy and detection of the deflected electron using an electron spectrometer. The general concept is illustrated in figure 3.5. A photon tagging system requires a large acceptance (>95%) for the momentum analysed electrons to obtain a high overall efficiency and reduce the background from 'untagged' photons and also excellent intrinsic energy resolution. Typically in photon tagging facilities,

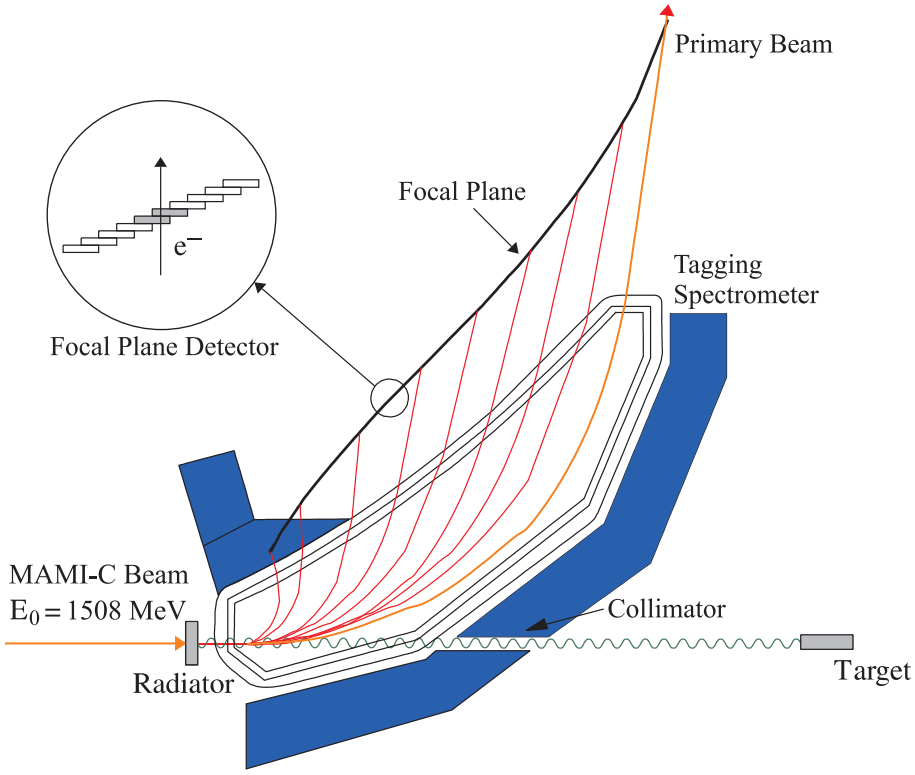

Figure 3.5: Schematic of the Glasgow Tagger. Inset is a view of the Focal Plane Detector, each Tagger channel is defined by the overlap of two neighbouring scintillators, to reduce background. There is also a small overlap of 0.05 channels between two adjacent Tagger channels. This is exploited in the Tagger calibration. [58]

the scattered electron related to the photon which induces a reaction is detected in parallel with a background of electron hits associated with photons which are lost in beam collimation and which pass through the target without interacting. Thus, a timing coincidence between the detected electrons and reaction particles is absolutely necessary to ascertain which photon is responsible for each reaction (section 4.1.2). The Tagger meets these requirements.

3.3.1 Glasgow Photon Tagging Spectrometer

The Glasgow Tagger [58] consists of a large dipole magnet [57] and a Focal Plane Detector (FPD) array [59]. The electron beam of MAMI strikes a thin radiator housed in a goniometer (section 3.4.1) delivering a beam of bremsstrahlung photons into the experimental area of A2. The scattered electrons are momentum analysed

in the field of the Tagger magnet ($\sim 2\,\mathrm{T}$) and are detected at the focal plane. The position of the electron hit along the focal plane is determined by the momentum of the scattered electron. Those with larger momenta are deflected through smaller angles before reaching the focal plane. The energy of the photon is inferred from the position of the hit on the FPD. Electrons which do not radiate are steered directly into the Faraday cup of the beam dump, thereby minimising the beam dependent background in the experimental area and allowing the total beam current to be measured. The occurrence of a photon-induced reaction in the experimental area is triggered by detection of one or more reaction products in the experimental detectors and a timing coincidence is applied to determine which Tagger hit, and hence photon energy was responsible for the observed reaction.

The number of scintillators which can be closely packed along the focal plane of the spectrometer is constrained by the physical space occupied by a single photomultiplier tube (PMT). A maximum comfortable packing density of the PMTs was reached with 353 scintillator elements and the FPD consists of 353 overlapping plastic scintillators covering a momentum range of around 5-93% of E_0. Each scintillator has length 80 mm, thickness 2 mm and variable widths ranging from 9 to 32 mm which decrease along the focal plane to ensure the energy bite of each scintillator covers roughly the same energy width. Computer modelling programs, such as RAYTRACE [60], were used to determine the electron optics of the spectrometer for all electron momenta within its acceptance range. Electrons with the same momentum but different exit angles follow slightly different paths in the spectrometer, converging at the focal plane (figure 3.5). The scintillators are arranged close to this focal plane, aligned normal to the projected electron trajectories. Each scintillator strip overlaps its neighbours by slightly over half their width to ensure that any electron which undergoes bremsstrahlung in the radiator follows a path defined by the electron optics of the spectrometer and triggers two neighbouring elements. A tagged electron hit is then defined by coincident hits in adjacent elements. The Tagger therefore has 352 coincident channels. Any hits which fail to meet this requirement are rejected as background.

With the maximum 1508 MeV MAMI-C beam, the Tagger covers an energy

range of 78 - 1400 MeV split over 352 coincident channels with an average energy width of ~ 4 MeV. However, the intrinsic resolution of the magnetic spectrometer has resolution of the order 120 keV. To accommodate an optional higher resolution detector array, the FPD was displaced from the true focal plane of the spectrometer, moving the detector system 41 mm further from the magnet along a curve parallel to the focal plane. As the intrinsic resolution of the spectrometer is far superior to the energy resolution of the FPD, this small defocusing has little effect on the total energy resolution of the tagging system.

The microscope [61] takes full advantage of the intrinsic resolution of the magnetic spectrometer. If desired, the scintillating fibre detector can be installed and adjusted along the true focal plane and covers a movable energy range of approximately 100 MeV. The microscope offers an improved energy resolution of 1 MeV per channel which is useful for experiments where a small energy range needs to be examined in more detail, such as studies of reaction thresholds. The microscope was not used in the current analysis.

The maximum flux of photons is constrained by rate limitations of the Hamamatsu R1635 PMTs which view each scintillator along the FPD, with a maximum counting rate of 1MHz per channel. The bremsstrahlung spectrum from an amorphous radiator can be approximated by a $\frac{1}{E_\gamma}$ distribution and consequently a large number of low energy photons are produced. To avoid saturation of detector elements at the extreme high electron energies and to maximise the photon flux in the region of interest, E_γ=200-450 MeV, a block of 32 Tagger channels corresponding to the lowest photon energies was switched off. Photons were tagged in the energy range 140 - 1115 MeV in this experiment.

Each individual Tagger channel has a small electronics card connected directly to its PMT. The card accommodates two discriminators and coincidence logic to enable an AND between that element and one of its two neighbours. Each discriminator has two thresholds, a low one which determines the signal time and a high one which decides if the signal is sufficiently large to originate from a residual electron. This dual threshold setup provides an individual Tagger channel with timing resolution of $\sim$0.5 ns FWHM.

Coincident signals from neighbouring cards are sent to the main Tagger electronics rack [62]. As the focal plane receives its signal before the photons generate a reaction in the experimental area, a delay in the arrival of the electron signal is required until the experimental detector is able to deliver its trigger (X-trigger). The Tagger electronics system provides a ∼500 ns delay, preserving the real-time information of the Tagger channel hit. Individual Tagger signals are fed to live-time gated scalers, through a latch to CATCH (Compass Accumulation, Transfer and Control Hardware) TDCs (Time to Digital Converters) and a logical OR of all 352 channels. The continuously updating scaler for each Tagger channel counts the number of electron hits over the live-time of the detector and can be used to determine the total of number of tagged photons in the beam. The multi-channel latch, through its bit pattern, identifies the number and location of each hit along the focal plane and the TDC determines the time difference between each hit and the X-trigger. This enables a precise offline analysis allowing identification of true or prompt events and provides a measure of the random events under the prompt peak (section 4.1.2).

3.3.2 Beam Monitoring and Tagging Efficiency

The Tagger provides an intense beam of energy labelled photons with a well determined photon flux. Numerous "Tagging Efficiency" measurements were taken during data collection using a lead glass detector to count the number of photons which reach the target compared with those created by bremsstrahlung. These measurements also provide means to calculate photon polarisation and contain information on beam diagnostics.

In principle the number of photons able to induce reactions in the experimental area equals the number of electrons counted along the FPD. In practice the photon flux is reduced somewhat by collimation, ensuring the beam radius does not exceed that of the experimental target. This loss of photon flux must be measured for precise cross section measurements. Electrons which undergo bremsstrahlung emit photons with a characteristic angle in radians of $\theta_c = \frac{m_e}{E_e}$. For 1508 MeV this corresponds to θ_c ∼0.4 mrad resulting in beam radius of ∼1 mm, 2.5m downstream of the radiator.

To constrain the beam spot to within the target dimensions, the photon beam passes through a 1.5 mm diameter lead collimator before leaving the Tagger. The beam spot and shape is observed online by using an in-beam scintillator/CCD camera after the photon beam passes through the experimental region. The position of the electron beam on the radiator was optimised ensuring the intense cone of forward focused bremsstrahlung photons pass through the centre of the collimator.

Collimation absorbs many of the photons whose electrons are counted along the Tagger FPD. A "Tagging Efficiency" measurement determines the percentage of photons tagged by a particular channel which survive collimation and reach the target. At low beam intensities the total photon flux can be measured using a large volume lead glass detector, which is moved into the beam line for tagging efficiency measurements. At small currents random coincidences are negligible and the large volume Cerenkov detector has ∼100% detection efficiency for photons. If counted in coincidence with FPD hits, the probability of a bremsstrahlung photon impinging on the experimental target can be determined. The tagging efficiency for each focal plane channel is defined:

$$\epsilon_{tagg} = \frac{N_\gamma}{N_e} \tag{3.2}$$

where N_γ is the number of photons counted after collimation and N_e is the number of 'tagged' electrons detected in the Tagger channel. The lead-glass detector would be damaged if it was in-beam during experimental running conditions and it is removed from the beam line during normal running. An in-beam ionisation chamber monitors the overall photon flux during experimental running.

3.4 Coherent Bremsstrahlung and Linearly Polarised Photons

A photon beam with strong linear polarisation can be produced using the technique of coherent bremsstrahlung [63,64] where the electron beam scatters coherently from a suitably aligned crystal radiator. The kinematics of bremsstrahlung, discussed in more detail in appendix A, heavily constrains the momentum transfer $\mathbf{q}$ from electrons to atoms in the radiator and defines a region known as the "momentum

pancake". With an amorphous radiator, an electron scatters from a single atom producing incoherent bremsstrahlung and the momentum transfer may lie anywhere inside the pancake. This gives a uniform azimuthal distribution of the polarisation vector and overall an unpolarised beam. However, if a radiator such as diamond with a regular lattice structure is chosen, the azimuthal asymmetry is broken as the reciprocal lattice vectors of the crystal restrict the magnitude and direction of the momentum transfer.

By carefully aligning the diamond with respect to the incident electron beam it is possible to isolate the momentum transfer to a single lattice vector. The Laue condition $\mathbf{q} = \mathbf{g}$ (where $\mathbf{g}$ is the reciprocal lattice vector of the crystal) implies that the recoil momentum is taken up by the crystal as a whole and the photon energy spectrum has a characteristic "coherent peak" structure which enhances the radiation of polarised photons at certain energies. Bremsstrahlung from crystalline radiators is composed of a coherent part sitting on incoherent background and it is common practice to plot the enhancement E, which is the photon energy spectrum obtained with diamond divided by that of an amorphous radiator, making an assumption that the incoherent background is well approximated by an amorphous radiator. This eliminates any channel to channel fluctuations caused by variations in the widths and efficiencies of each Tagger channel and removes the $\sim 1/E_\gamma$ shape, highlighting the coherent contributions. Figure 3.6, from the coherent bremsstrahlung facility at CLAS, Jlab [65], shows a typical enhancement spectrum with the different coherent peaks and the relevant reciprocal lattice vectors they came from. It is the relative ratio of each point to the baseline, where there is no contribution from coherent bremsstrahlung (around 0.1×10^{-3} in figure 3.6), that is important in the enhancement and not the magnitude of intensity ratio $\frac{I_{\text{coh}}}{I_{\text{inc}}}$. The absolute magnitude of the enhancement ($\times 10^{-3}$) is not an indication that the coherent yield is much smaller than the incoherent yield. Instead, a large amount of amorphous data has been used to divide out the incoherent background from the diamond bremsstrahlung distribution. Figure 5.3 in chapter 5 illustrates the relative yield of coherent and incoherent events after suitable normalisation. The photon polarisation can then be deduced using coherent bremsstrahlung theory. This is discussed in more detail in

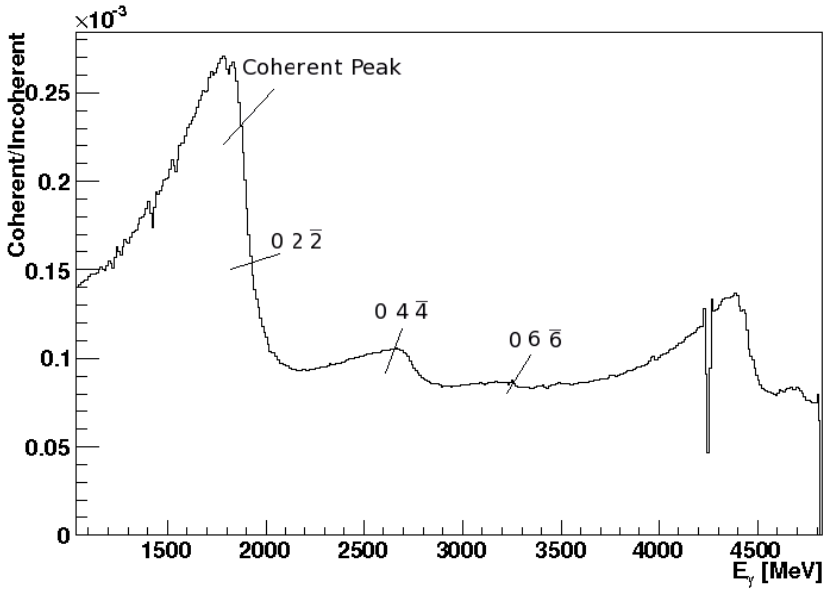

Figure 3.6: Typical enhancement spectrum showing the bremsstrahlung contribution from diamond after the incoherent background is divided out. The coherent peak structure is clear in the enhancement with the relevant reciprocal lattice vectors indicated [65].

chapter 5.

The photons in the coherent peak have a high degree of linear polarisation. Highest polarisation is achieved by selecting the [0 2 2] or [0 2 $\overline{2}$] lattice vectors [63] with maximum polarisation in the plane ($\mathbf{g}$,$\mathbf{p}_0$) where $\mathbf{p}_0$ is the momentum of the incident electron. Competing reciprocal lattice vectors which may cause interference must be removed from the momentum pancake. The orientation of the diamond is controlled by a precision goniometer which allows sensitive adjustments of the diamond with respect to the incident beam. Section 3.4.2 outlines the experimental alignment process.

A 100 μm diamond radiator was used to produce polarised photons in this experiment due to its small lattice constant and relatively high Debye temperature ($\sim$3340 K). This ensures that the mean thermal displacement of atoms in the crystal is small leaving the diamond lattice structure relatively unaffected by thermal effects [66]. A low Debye temperature indicates the increasing influence of thermal motion in smearing out the periodicity of the lattice and reduces the fraction of

atoms which radiate coherently.

A crystal with a low mosaic-structure provides a cleaner spectrum of polarised photons. Any spread in axis direction will smear out the coherent peak [66]. Similarly a thin radiator is desirable to minimise the angular divergence of the beam. When electrons pass through the diamond radiator there is a spread in the direction of the electrons with respect to the crystal orientation due to multiple scattering effects, crystal defects in the lattice and divergence of the incident electron beam. To enhance the coherent spectrum this angular variation should be smaller than the characteristic opening angle for coherent bremsstrahlung:

$$\theta_{br} = \frac{mc^2}{E_0} \tag{3.3}$$

The angular variation of the beam smears the edge position of the peak, broadening the coherent peak structure and reducing the maximum degree of polarisation.

3.4.1 Goniometer

The A2 goniometer, positioned at the entrance of the tagging spectrometer, is responsible for controlling the orientation of the diamond. A **100**[1] diamond is mounted in the centre of the five-axis precision goniometer. The goniometer is maintained in vacuum conditions and all five axes can be driven by computer controlled motors allowing shift workers to change the type of radiator being used as well as the orientation of the linearly polarised beam. Three drives are used to rotate the diamond around a vertical axis, a horizontal axis and an azimuthal axis (figure 3.7 (a)-(b)). The diamond is considered to be in its zero position when its three basis vectors (**001**,**010**,**100**) are parallel to the horizontal, vertical and beam respectively.

The goniometer also houses a selection of amorphous radiators such as copper and nickel and also a blank setting used to optimise delivery of the beam from accelerator to experimental hall. These additional radiator settings which surround the central diamond can be selected by driving the two remaining goniometer axes rotationally and horizontally. The setup of the goniometer wheel is illustrated in figure 3.7(d).

[1] meaning the **100** axis is perpendicular to the face of the diamond

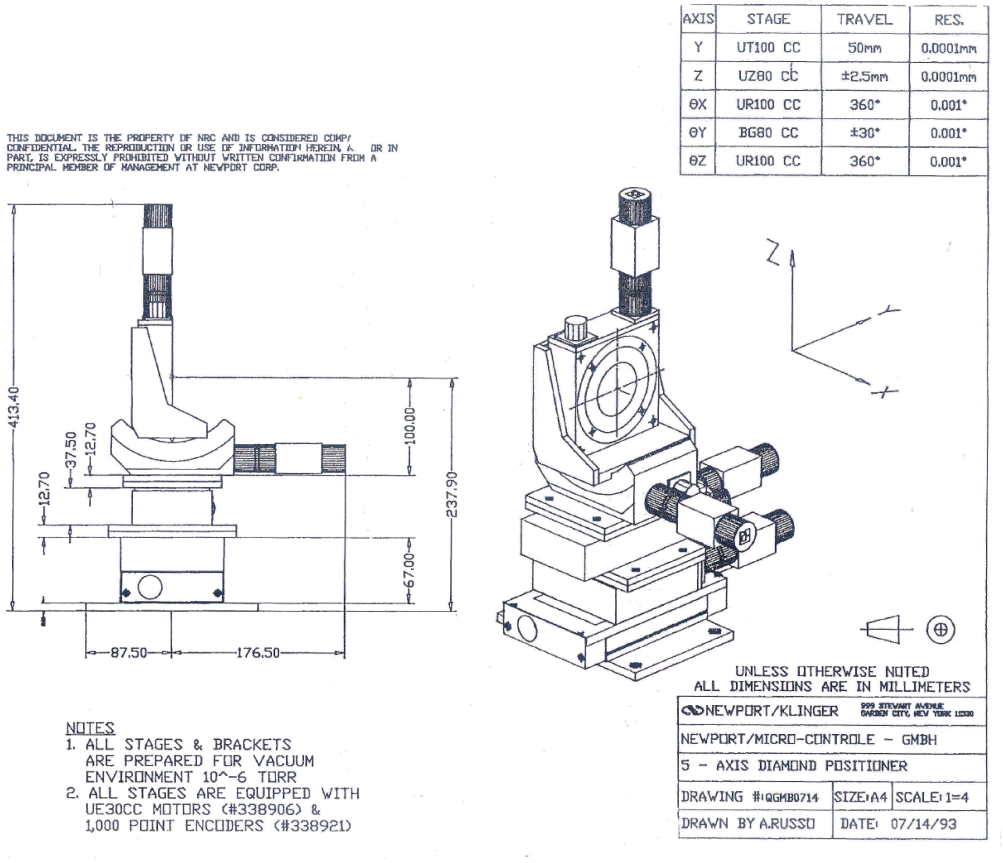

(a) A schematic diagram of the goniometer

(b) A technical drawing showing axes

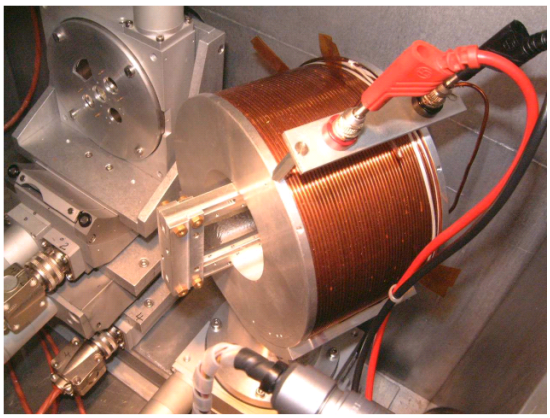

(c) The goniometer with the Moeller coil

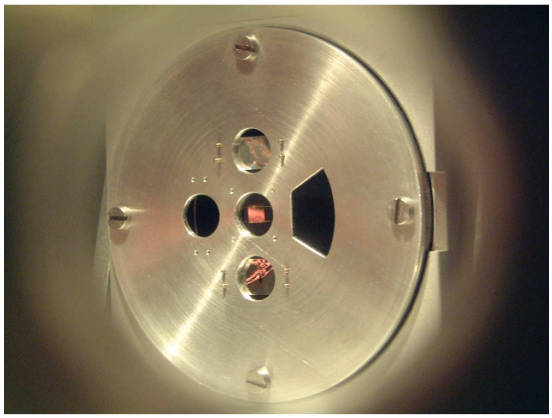

(d) The radiator choices, diamond in the centre with, clockwise from right, blank, nickel, blank and iron

Figure 3.7: The A2 goniometer [67].

3.4.2 Setup and Alignment

Before aligning the diamond to produce a polarised photon beam in the correct energy range and desired orientation it is necessary to measure an appropriate set of angular offsets between the crystal axes and electron beam. This alignment process uses techniques outlined in references [64, 68]. A series of hv (horizontal-vertical) scans are performed, were the crystal axes are swept axes around a cone of angular radius θ_r by stepping sinusoidally and cosinusoidally on the crystal vertical and horizontal axes respectively. The hv scan records the number of Tagger scaler counts as a function of photon energy for each point G_v and G_h in the scan. The *Stonehenge plot* highlights the behaviour of photon energy intensity (with energy increasing radially outwards) as a function of angle and is illustrated in the polar diagram in figure 3.8. Regions of high intensity form sets of curves which show the coherent contributions from different sets of crystal planes as their angle with respect to the beam are varied. The angular offsets of the diamond are inferred from where the curves with maximum intensity meet at $E_\gamma = 0$, indicating the [0 2 2] and [0 2 $\overline{2}$] reciprocal lattice vectors are parallel to the beam axis. Figure 3.8(a) shows a *Stonehenge plot* following a hv-scan to calculate the offsets of the 100 μm diamond crystal used in the experiment. Figure 3.8(b) is the corresponding *Stonehenge plot* with the diamond perfectly aligned with the beam. The position of the coherent edge and hence the polarisation peak and also the plane of polarisation can then be obtained by suitable rotations about the horizontal and vertical axes as described in [68].

3.4.3 Photon Polarisation

An analytical calculation of coherent bremsstrahlung and its polarisation (known as Analytic Bremsstrahlung or *anb* for short) [69] was performed prior to the experiment to determine the optimum setup parameters for a polarised photon beam covering E_γ = 200-400 MeV. Distributions of coherent and incoherent bremsstrahlung produced by electrons incident on a crystalline radiator are calculated by *anb* using realistic descriptions of beam parameters such as energy, beam divergence and

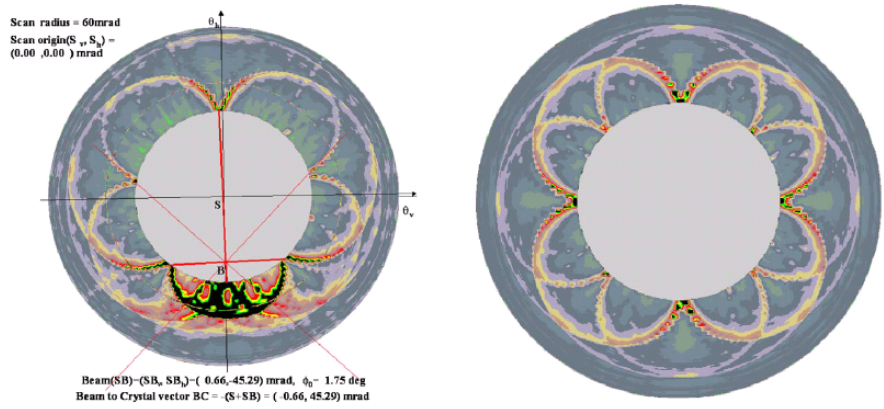

(a) (b)

Figure 3.8: Stonehenge plots: The photon energy is plotted radially from the centre of the polar diagram and the angle indicates the azimuthal angle at which the photon energy intensity was sampled. (a) An initial hv scan to calculate the crystal offsets with respect to the beam. (b) hv scan after crystal alignment using the scan results in (a). The four-fold symmetry indicates successful alignment [68].

photon collimation. The calculation also aims to give a proper account of physical processes which occur in the radiator such as thermal motion of atoms and multiple scattering effects. Coherent bremsstrahlung theory [63] is used to calculate the degree of photon polarisation from enhancement and *anb* is therefore a valuable tool in predicting approximate polarisations for different experimental conditions. This is discussed in more detail in section 5.

Enhancement spectra constructed for different input parameters are shown in the upper half of figure 3.9. The panel on the right side lists the various parameters which can be adjusted in the calculation. The analytical calculation provides a fast calculation to monitor the effects of collimation, beam divergence and electron energy on the photon polarisation. Previous work [70] has clearly shown the relative intensities of coherent to incoherent bremsstrahlung are greatly enhanced by tight collimation of the photon beam. The enhancement spectra are shown for two MAMI beam energies - 1203.8 and 1508 MeV and with collimators of diameter 1.5 and 2 mm. The calculated polarisation for each setup is shown in the lower half of figure 3.9. Clearly, highest polarisation is achieved with larger electron energy, shown in figure 3.9 by the solid and dashed blue lines (solid lines illustrate the

first energy region: E_γ=200-300 MeV and dashed: E_γ=300-400 MeV). The green and red lines are calculations based on a 1203.8 MeV beam. The green curves have slightly larger polarisations owing to tighter collimation applied (1.5 mm diameter rather than 2 mm) but falls short of the polarisation achieved with 1508 MeV incident beam. However, the calculation suggests possible interference between the two reciprocal lattice vectors [0 2 2($\overline{2}$)] and [0 4 4($\overline{4}$)] at the coherent edge of the first setting (∼300 MeV). This effect is largest for the full 1508 MeV beam. On balance, a configuration using 1203.8 MeV electron beam with 1.5 mm diameter collimator was selected for data taking in March 2008. Additional beamtime was acquired in August 2008, used a 1508 MeV incident electron beam with the same collimation. A final consideration on the polarised beam, the optimum plane of polarisation is discussed in section 3.6.1.

3.5 Targets

Graphite and high density polythene (CH_2) discs were used as targets for the present experiment. Some details of the 3 targets used are given in Table 3.2. Both graphite discs served for the measurement of $^{12}C(\overrightarrow{\gamma}, pp)$ and the CH_2 target permitted measurement of both $^{12}C(\overrightarrow{\gamma}, pp)$ and proton energy calibration via the reaction $p(\gamma, \pi^0)p$ (section 4.4.3).

An important consideration was target thickness. By using a thick target, more nuclei/cm^2 are experienced by the photon beam resulting in an increased yield of $^{12}C(\overrightarrow{\gamma}, pp)$ events. However, the benefit of higher count rates from thicker targets are offset by poorer energy resolution in the measurement caused by uncertainty in the path length each nucleon traverses in the target. There is also an increased probability that one of the ejected nucleons is absorbed in the target and never detected. Thus a compromise between target thickness and energy resolution is necessary. For the first polarisation setting, E_γ=200-300 MeV, a thinner 2.5 mm graphite target was used. Two additional targets, a 4 mm ^{12}C and 5.97 mm CH_2 target were used for the higher energy range since the ejected nucleons inherit larger momenta from the photons.

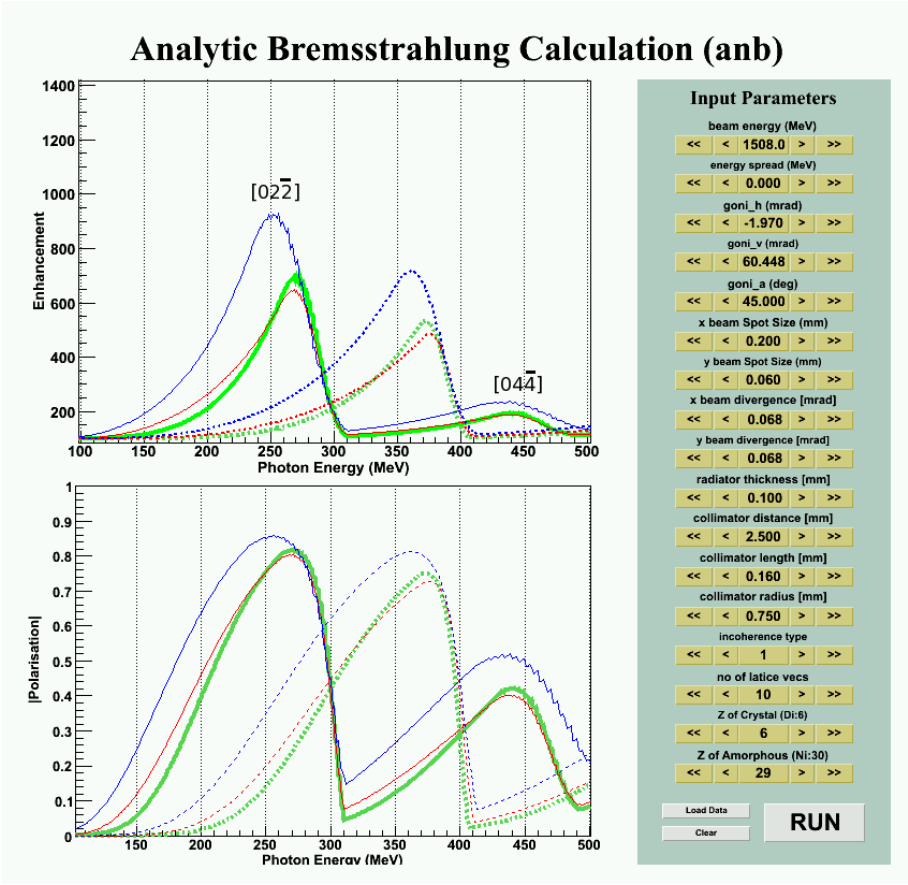

Figure 3.9: Analytical bremsstrahlung calculations: Simulation investigating the optimum beam energy and photon collimation for the current experiment. Solid lines indicate the first goniometer setting covering 200-300 MeV. Dashed lines cover approximately 300 - 400 MeV. Blue lines indicate the full 1508 MeV MAMI beam with 1.5 mm diameter collimator. Red and Green both use a 1203.8 MeV electron beam with 2 and 1.5 mm diameter collimators respectively. Top: Calculated enhancement spectrum. Bottom: Photon polarisation inferred from the enhancement

.

Material	Thickness (mm)	Diameter (mm)
Graphite ^{12}C	4.05	23.02
Graphite ^{12}C	2.51	23.03
HD Polythene CH_2	5.97	22.95

Table 3.2: Table indicating the thickness and diameter of each target used during the experiment.

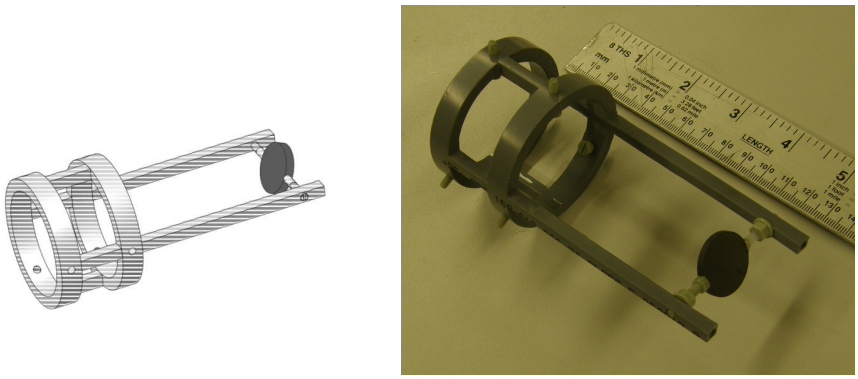

(a) (b)

Figure 3.10: (a) AutoCAD drawing of plastic target holder with target disc attached. (b) Photograph of target holder before installation in the Crystal Ball.

A further consideration was the angle at which the target is aligned with respect to the incident photon beam. A shallow angle results in a larger effective thickness whilst reducing the amount of materials the protons must traverse before reaching the Crystal Ball. Conversely, too steep an angle introduces a large uncertainty in the polar angle of the ejected nucleon, as the z-vertex of the reaction can occur over a larger range. The targets were mounted at 45° to the beam for the present experiment. The targets were held in place by a thin plastic target holder (figure 3.10(a)) designed to minimise the material from target to Crystal Ball and positioned in an evacuated carbon fibre tube in the centre of the CB. A thin (100μm) kapton window sealed the downstream end of the pipe. A photograph of the target before installation in the CB is shown in figure 3.10(b).

3.6 The Crystal Ball

The Crystal Ball is a highly segmented total energy electromagnetic calorimeter, covering 94% of 4π sr and is the main particle detector in the A2 hall. The CB was initially designed in the 1970's as a means of detecting high energy photons from the decays of hadrons produced in e^+e^- collisions at the Stanford Linear Accelerator (SLAC) [71]. To facilitate these measurements, a large photon acceptance spectrometer with full solid angle coverage, excellent angular and energy resolution was required. The detector was proposed a few months before the discovery of the

J/ψ particle in 1974 (jointly by SLAC and Brookhaven National Laboratory) and played a crucial role in making some of the first and most accurate measurements of J/ψ and its excited states [72]. The CB continued its program of meson spectroscopy specifically the study of b-quarks at the Deutches Elecktronen-Synchrotron (DESY) between 1982-1987 and after a period of storage at SLAC it was used to facilitate the study of strange and non-strange baryon resonances at Brookhaven National Laboratory (1995 to 2002). In November of that year, the Crystal Ball was shipped to Mainz and the MAMI facility, complete with a major upgrade of the detectors electronics, before undergoing an experimental program covering a wide range of physics with MAMI-B. A second round of experiments, post MAMI and Tagger upgrades is now underway.

3.6.1 Crystal Ball Design

The geometry of the Crystal Ball [73] is based on the structure of an icosahedron. Each of the 20 triangular faces of the polyhedron is divided into 4 minor triangles, which in turn are segmented into 9 smaller triangular faces (figure 3.11(a)). These smaller triangles represent the base of a truncated triangular pyramid NaI(Tl) crystal. When stacked together in this way, a near spherical shell of 720 elements is achieved. Removal of 24 crystals at opposite ends of the sphere provides an entrance and exit tunnel for the beam and gives space for target holding structures and additional sub-detectors.

Each of the remaining 672 crystals (figure 3.12) face the interaction point (target centre) and have a length of 40.6 cm, corresponding to 15.7 radiation lengths. The triangular side lengths are 5.1 cm and 12.7 cm on the internal and external surfaces respectively with the sphere having an inner radius of 25.3 cm and an outer radius of 66.0 cm. To ensure optical isolation each crystal is wrapped in reflective paper and aluminised mylar. Scintillation light travels through a 5cm air gap and a glass window where it is viewed by the crystals own PMT.

NaI(Tl) is hygroscopic and therefore attracts water molecules from moisture in the atmosphere which in turn destroys the crystal. Therefore, the crystals are hermetically sealed and stacked in two separate hemispheres made of 1.6 mm thick

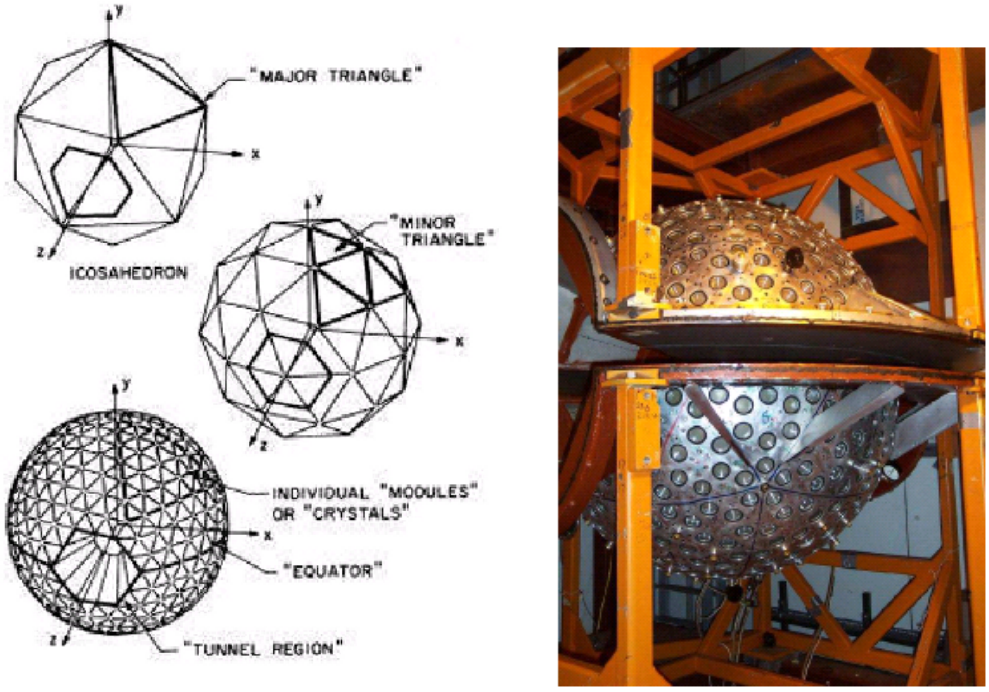

(a) (b)

Figure 3.11: (a) Crystal Ball geometry. (b) Photograph of the Crystal Ball in its frame. Taken from [74].

stainless steel. The dead region between both hemispheres, consisting of 2x1.6 mm stainless steel and air, is known as the equatorial plane. This dead region plus the entrance and exit windows account for the 6% loss in angular coverage of the CB. The mechanical separation of the two hemispheres also allows easy access for mounting and maintaining targets and detectors in the tunnel region.

The equatorial plane influenced the choice of plane of photon polarisation used in the experiment. Previous experiments in A2 defined two orthogonal polarisation planes, *para* with the **E**-field vector oscillating in the lab horizontal plane and normal to the beam direction and *perp* with **E** oscillating in a plane orthogonal to both *para* and the direction of photon propagation. For photoinduced reactions, with sensitivity to the direction of the **E**-field vector, reaction cross sections will be maximum in the reaction plane parallel to the **E**-field and minimum perpendicular to it. Using the previous polarisation setup, cross section maxima or minima would coincide with the dead region of the CB. Protons typically deposit energy in one or

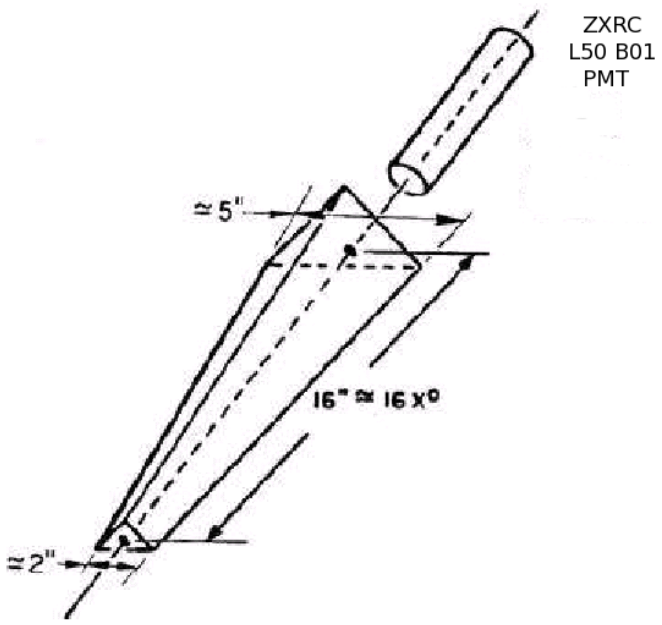

Figure 3.12: Illustration of a single NaI(Tl) Crystal. Taken from [74].

two crystals and a systematic uncertainty may arise in the measurement of $\Sigma_{(\overrightarrow{\gamma},pp)}$ with this setup. To avoid this, new planes of polarisation were defined by rotating the previous polarisation planes by 45° about the photon beam axis (z-axis). The notation *para* and *perp* will be maintained throughout this thesis although they refer to polarisation planes rotated ±45° about the equatorial plane of the CB.

Photons deposit energy in the NaI(Tl) via the electromagnetic (EM) showers which develop when it enters the crystal. Typically the energy deposited by each photon is contained in a cluster of 13 crystals with more or less a standard pattern. The selection of NaI(Tl) crystals, with high light output and the high degree of crystal segmentation ensured almost perfect photon detection efficiency (∼99%) with excellent energy and angular resolution. The energy and direction of particles in the Crystal Ball are reconstructed from the cluster of crystals in the resulting shower. Some detector properties of the Crystal Ball detailing experimental resolution are outlined in Table 3.6.1.

Charged hadrons such as pions, kaons and protons can be identified through a dE/dx technique, using a thin barrel scintillator which surrounds the target. Energy

Table 2.3: Principle Characteristics of Crystal Ball

Angular Acceptance	
Azimuthal coverage	$0^\circ \leq \phi \leq 360^\circ$
Polar coverage	$20^\circ \leq \theta \leq 160^\circ$
Angular Resolution	
Azimuthal resolution	$\frac{2^\circ}{\sin\theta}$
Polar resolution	$\sim 2 - 3^\circ$
Photon Energy Resolution	
$\frac{\sigma}{E_\gamma}$	$\sim \frac{1.7\%}{E_\gamma}\ (\mathrm{GeV})^{0.4}$

deposited by charged hadrons tend to involve only a few crystals and poorer angular resolution results. The thickness of the crystal was sufficient to stop 240 MeV charged pions, 341 MeV kaons and 425 MeV protons. This is discussed in more detail in the following section.

3.6.2 Particle Identification Detector

The Particle Identification Detector (PID) provides means to identify charged particles in the Crystal Ball. Ideally particle identification would be achieved by time-of-flight methods. However, the flight length from target to crystal is too short and the timing resolution of NaI too poor to apply this technique. The PID is a dE/dx detector which is used in conjunction with the CB to determine charged species via a ΔE-E technique. Located in the tunnel region and surrounding the target, it is composed of 24 EJ204 scintillators arranged to form a 10 cm diameter barrel. Each of the scintillators is 31 cm long, 13 mm wide and 2 mm thick and the cross section of each element is a right angled trapezium, which ensures gaps between elements are minimised. Wrapping each element in foil ensures optical isolation and the entire detector was covered in black Tedlar (PVF) to provide light-proofing. Scintillation light induced in each scintillator travels through a light guide were it is viewed by a PMT at one end of the PID. Figure 3.13 shows an image of the PID in the Crystal Ball using a Geant4 simulation.

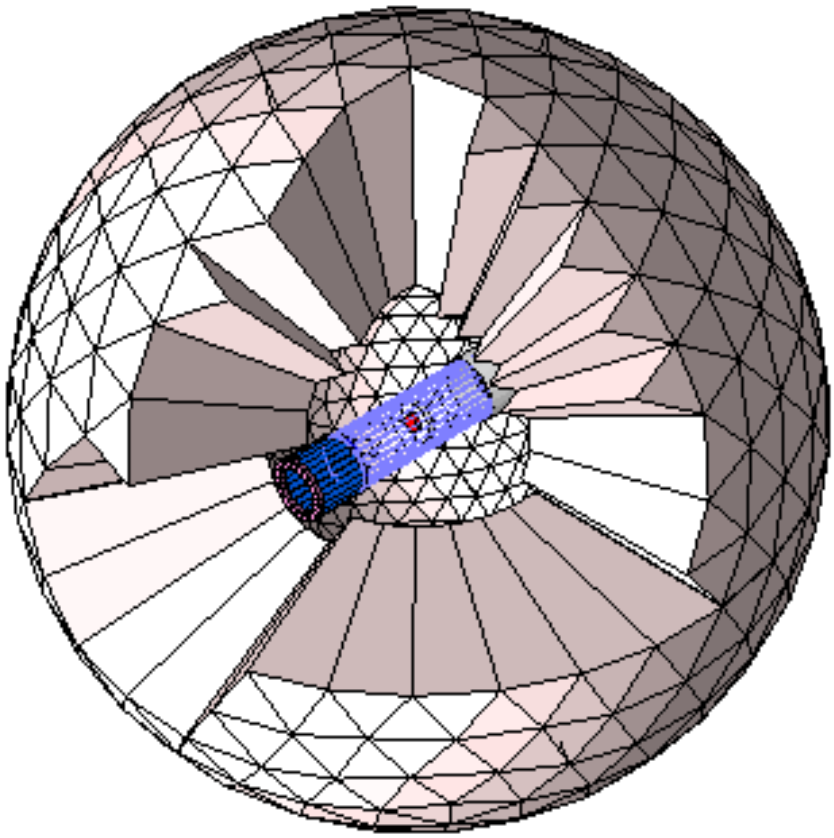

Figure 3.13: Geant4 image of the PID in the tunnel region of the Crystal Ball [75].

The differential energy loss of a particle as it traverses the PID is compared with the total energy that particle deposits in the Crystal Ball. The energy deposit in a PID element energy is typically small compared to CB total energy deposit ($\sim$400 keV for a minimum ionising particle). Charged species with equal kinetic energy but different mass deposit measurably different energies in the scintillator with lighter particles depositing smaller fractions of their total energy in the scintillator than more massive particles. The PID takes advantage of this to differentiate between charged species by applying cuts to ΔE-E plots (figure 4.8). The cylindrical design of the PID around the target gives almost full 360° azimuthal coverage and the length of the scintillators ensured polar angle coverage $\theta = 20° - 160°$, matching that of the Crystal Ball.

3.7 Data Acquisition and Trigger Systems

Analogue signals from all detector elements were digitised and read by the A2 data acquisition system (DAQ) to build events into a format which can be used for data analysis. In most cases, physical information is extracted by splitting the analogue signals from the PMTs into two parts, feeding the signal to a charge-to-digital converter (QDC) and also via a discriminator to a TDC. Where energy is required the analogue signal is fed to a QDC which integrates a sample of the pulse returning an integer proportional to the energy deposited in the detector element. Where timing is required the analogue signal is fed to a discriminator which can provide a start/stop signal for a TDC. These signals are also fed into the logic circuitry which forms the experimental trigger. The TDC start was prompted by the experimental trigger while the stop came from the relevant detector signal. The timing of a particular signal is then relative to the other detectors. Triggering electronics determines whether or not a particular 'event' should be read to file.

3.7.1 Crystal Ball Electronics

A simplified view of the CB electronics is provided in figure 3.14 [76]. Crystal Ball PMTs were connected to Uppsala designed active fan-in fan-out units in groups of sixteen channels **(1)**. This produces 3 matched outputs: with one sent via delay to a multi-sampling Flash ADC (FADC) **(2)**, the second, via discriminators to a CATCH TDC **(4)** with the final branch used for triggering electronics **(3)**, sending the analogue sum of all the 16 inputs to provide a sum of all energy deposit in the Crystal Ball.

The discriminators receive the summed amplitude signal of the 16 crystal group and decides whether the signal continues on its path by applying a low and high threshold. The low threshold (2 MeV) provides timing for the CB total energy trigger and the start of the TDCs **(6)** and scalers **(7)** dependent on whether this threshold has been met. The high threshold is set at 10 MeV to provide the CB total energy deposit threshold. The cluster multiplicity **(5)** records the index of 16 crystal groups whose energy sum is above the high discriminator threshold. The

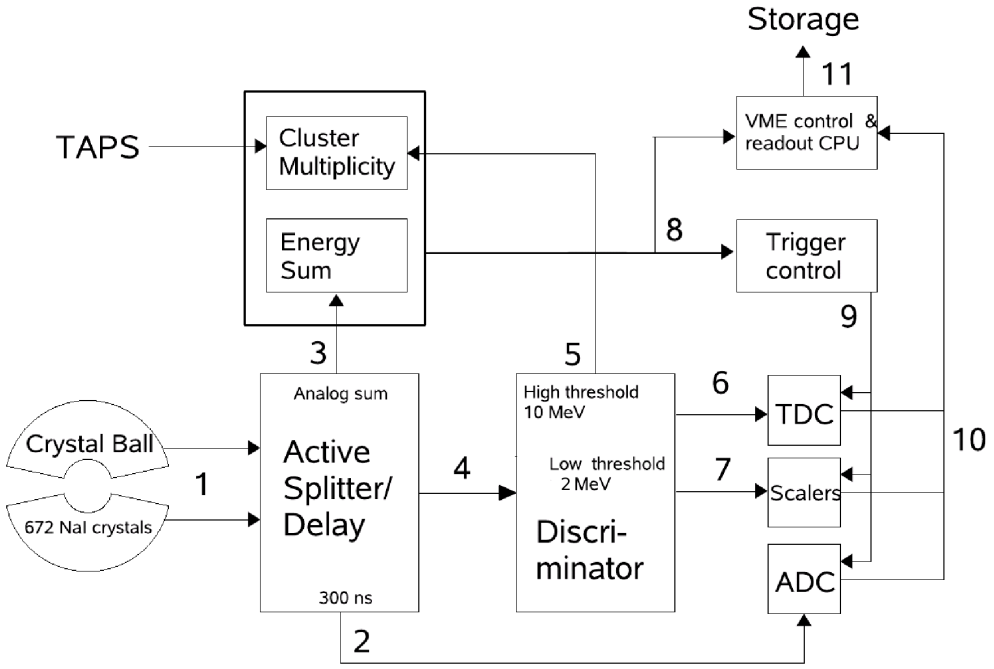

Figure 3.14: Simplified view of the Crystal Ball electronics [78]. See text for details.

triggering box **(8)** makes the final decision. If it is positive, it sends a stop signal to the TDCs, ADCs and scalers which allows the digitisation of the signal and sends it to the storage computer **(9)-(11)**. A more detailed description of the CB electronics can be found in reference [77] and the PhD thesis of D. Krambrich [78].

3.7.2 Flash ADCs

The FADCs sample the signal pulse shape at a frequency of 40MHz. In principle, the full sample of the pulse can be digitised and stored in the data stream but to reduce readout time only integrated pulse amplitudes were stored. Three regions of the signal were sampled, over the pedestal, signal and tail region of the pulse. A measure of the residual charge in the ADC (the pedestal) was made for every event and was dynamically subtracted from the signal. This improves the attainable energy resolution of the crystals.

3.7.3 CATCH TDCs

Standard TDCs as used in the previous incarnation of the Tagger [59] were started / stopped by a hit in the FPD channel and stopped / started by a logic pulse from triggering electronics. After the MAMI-C energy upgrade, the Tagger, PID and Crystal Ball all determine detector timing using CATCH TDCs which work differently. The CATCH TDCs are continuous sampling, multi-hit units with no start/stop. Each TDC essentially acts as a free running clock, oscillating at ∼10GHz with a channel to time conversion of 117ps/channel. They are synchronised by a CERN-standard trigger control system (TCS) with one reference TDC channel connected to the trigger. When an event passes each level of the triggering electronics, a logic pulse is sent to the reference TDC which stores the oscillator value. Each time a TDC registers a hit, the corresponding oscillator count is stored in a buffer. The timing of the hit with respect to the trigger signal is then accessed by subtracting the number stored in the reference TDC from the oscillator count and using the channel to time conversion given by the 10GHz [79].

3.7.4 Triggering Electronics

While the DAQ is reading out an event, the electronics are dead to any further hits in the detector. This is known as experimental dead time which can be minimised by placing constraints on acceptable events by making the triggering electronics as selective as possible for each experiment. The trigger was determined by two LeCroy LRS 4805 logic units as described in reference [77]. For an event to be read out and stored on file, it must satisfy various conditions. These conditions can be modified in various ways to optimise the trigger for a specific experiment. For this experiment the first trigger condition was satisfied if the energy sum of all 672 elements in the Ball passed an energy threshold of 50 MeV. A second condition was satisfied only when the number of clusters in the CB, known as multiplicity, exceeded or equalled 2. If both conditions were satisfied, the QDC and TDCs were gated, read out and the triggering electronics reset.

Chapter 4

Calibration and Data Analysis

The previous chapter detailed the experimental apparatus and setup used during the experiment in the A2 hall at MAMI. However, before any analysis can be undertaken it is necessary to calibrate the various detector subsystems to convert the output into a meaningful physical format (time, energy, position). This chapter describes the conversion of raw data stored by the experimental data acquisition into real physical information on the interaction, from which photon asymmetries can be derived. The experimental setup consists of several detectors systems with many instrumentation channels and the calibration work was divided out between various members of the collaboration. This section outlines the method of calibration for each detector, with particular emphasis on the proton energy correction performed by the author which is crucial to the analysis of (γ,pp). Calibrations which were performed by colleagues are referenced below.

The first stage in the analysis uses calibrations to convert raw QDC and TDC values into energies (MeV) and times (ns) respectively. Cluster finding algorithms were then used to group together detector hits in the Crystal Ball originating from the same particles. Using information from the PID and Crystal Ball, particle identification can be carried out on an event-by-event basis and one can then undertake a detailed study on a particular reaction channel with a more advanced analysis.

4.1 Photon Tagger Calibration

4.1.1 Tagger Energy Calibration

The energy of tagged photons are determined from the incident MAMI electron beam and measurement of the recoiling electron in the Tagger, as defined by equation 3.1. Unlike the near monoenergetic MAMI electron beam, the energy of radiated photon beam covers a continuous range of energies up to that of the incident electron. Therefore, a reliable measurement of photon energy is dependent on accurate knowledge of the incident electron beam, defined by the total number of beam recirculations in the HDSM and the measured energy of the scattered electron. Accurate determination of the MAMI electron beam is outlined in reference [54], ray tracing the electron beam through the known magnetic fields of the MAMI magnets. The experiment ran with incident beam energies of 1203.8 MeV in March 2008 and 1508.0 MeV in August 2008, with an uncertainty in beam energy of $\sim$110 keV.

The energy of the scattered electron is derived from the hit position along the FPD and the calibration from Tagger channel space to electron energy is described in detail by McGeorge *et al.* [58]. To calibrate, a few low intensity MAMI beams with energies smaller than those used during experimental running, were scanned across several FPD elements by slowly varying the Tagger field about the value required to dump the beam. A 1.057 T and 1.834 T field is required to dump the main MAMI beam energies of 885 MeV and 1508 MeV respectively. By making small steps in field strength, it is possible to measure the field values for which the beam hits the small overlap between neighbouring channels. This gives the hit position to an accuracy of $\sim \pm 0.05$ channel. Interpolation of channel number against field strength gives the (fractional) channel hit for the correct field. This relates Tagger channel to electron energy for a specific field. Such calibration measurements have been carried out for seven MAMI energy beams for a field of 1.834 T with the resulting calibration shown in figure 4.1(a). To guide the interpolation between these seven points a computer program TagCal [80] was written to calculate the calibration on the basis of a uniform Tagger field constructed on the basis of a field map measured along the main beam trajectory. The uniform field is scaled by the measured Tagger

field, obtained by an NMR probe permanently installed inside the Tagger magnet. Using the known relative positions and angles of the scintillators along the focal plane, TagCal applies a χ^2-minimisation routine to interpolate between the points in figure 4.1(a), mapping tagged electron energy as a function of Tagger channel. The calculated calibration is shown by the solid line in figure 4.1(a).

Figure 4.1(b) plots the energy difference between the measured and calibrated electron energy for a calibration based on E_0=1508 MeV and 1.834T field. The deviation between calculated and measured energy is ∼1.5 MeV over most of the energy range although the discrepancy increases to ∼4 MeV at the lowest photon energies. These differences arise due to large scale field non-uniformity which exist in the Tagger which relate to pole shim mounting screws which cause field dips. This is investigated in more detail in reference [58]. A phenomenological correction was used to correct for these field non-uniformities.

4.1.2 Tagger Timing Alignment and Random Subtractions

For each experimental trigger, the scattered electron related to the photon which induces the reaction in the target is detected together with an additional background of uncorrelated electron hits at other places along the FPD. This background is associated with photons which pass through the target without interaction, photons stopped by beam collimation and Møller scattering on the radiator. Consequently, there is some ambiguity about which electron hit corresponds to the photon that interacts.

The relative timing of the electron hit with respect to the experimental trigger can be used to reject some of the random uncorrelated background. The time recorded by each focal plane TDC corresponds to the time difference between the hit in the Tagger element and the experimental trigger. The channel to time conversion for the Tagger TDCs is set by the TDC modules which have been established from previous calibrations as 0.18 ns/channel [59]. There is a definite time difference associated with the time of photon propagation from radiator to target plus the time taken for the reaction particles to make an experimental trigger. This produces a strong prompt peak. Conversely, electrons unrelated to the photon that induces a

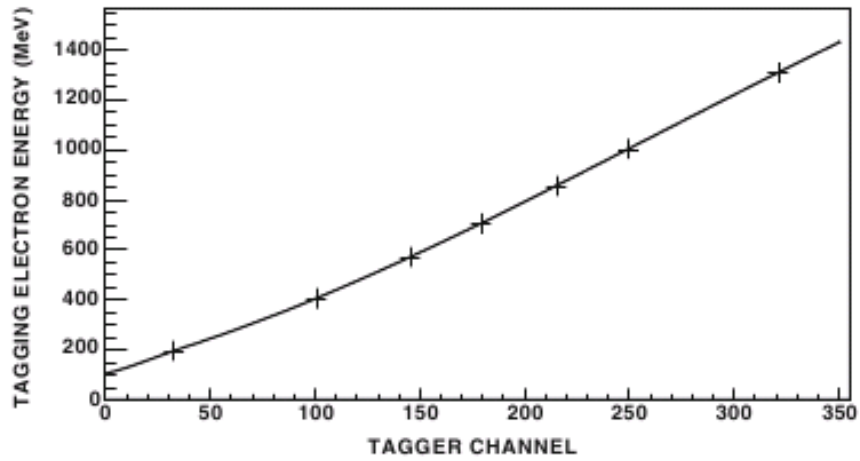

(a)

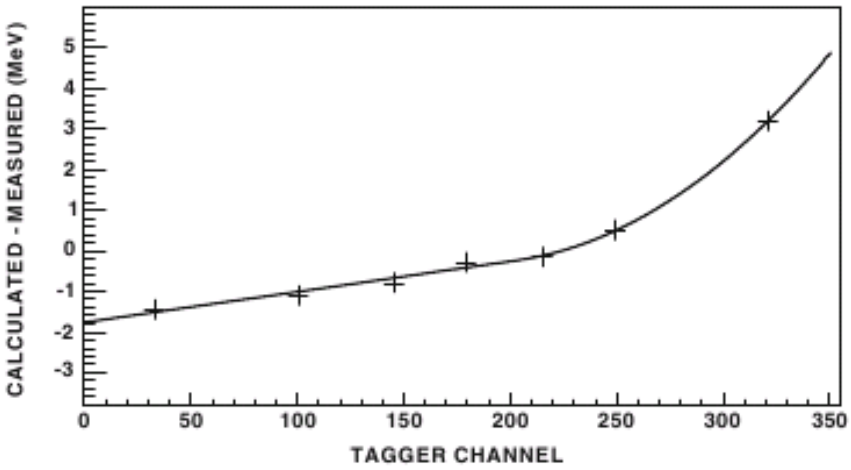

(b)

Figure 4.1: (a) Tagger energy calibration taken from [58] for the main MAMI beam energy 1508 MeV, using MAMI energies 195.2, 405.3, 570.3, 705.3, 855.3, 1002.3 and 1307.8 MeV. The solid line shows calculated calibration assuming a uniform field. (b) Difference between calculated and measured electron energy. The line here shows a smooth fit to the seven measured points and indicates the small correction to the calculated calibration because of large-scale field non-uniformity.

reaction form a flat 'random' background covering the event window.

It is advantageous to align each individual Tagger TDC such that the prompt peak of each element are coincident (figure 4.2). Uniform cuts can then be applied to the combined timing spectrum, TimeOR, defining a single prompt region. This

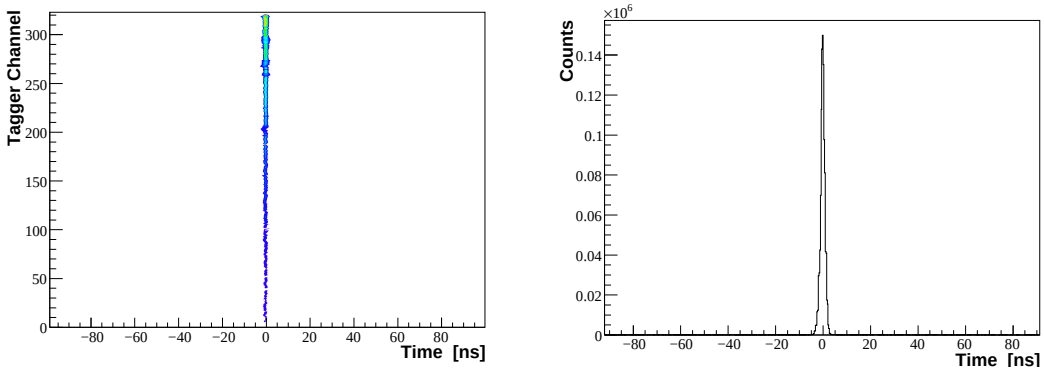

(a) (b)

Figure 4.2: (a) Tagger timing alignment. (b) Projection of (a) for all Tagger channels.

procedure was carried out during tagging efficiency runs (section 3.3.2) where the Crystal Ball was removed from the DAQ and the experimental trigger was made by a ∼100% efficient Pb glass detector. Due to the low intensity beam current the number of random coincidences along the FPD is negligible and the prompt peak dominates. This simplified the alignment process, fitting a Gaussian distribution to the prompt peak of each channel and applying an offset to shift the mean for each channel to some arbitrary time (∼0 ns here). Figure 4.2(a) plots Tagger time against channel number after alignment, showing a peak about 0 ns for all Tagger channels. Figure 4.2(b) is the combined spectra for all channels and highlights the dominant prompt peak and near absence of random coincidences.

Figure 4.3 plots the time difference (Tagger time - trigger time) under experimental conditions, where the Crystal Ball makes the trigger, summed for all 352 Tagger channels. The coincident peak has a FWHM = 6.5 ns. It is evident that there are random contributions either side of the prompt peak. It is not possible to distinguish between individual real and random events in this region. However, the effect of random coincidences can be subtracted out from the selected data by evaluating the contribution from random regions away from the prompt peak after suitable scaling. The background is corrected by sampling two regions: (1) the prompt region containing the peak plus background (shaded in red in figure 4.3) and (2) the random background on either side of the prompt peak (shaded in green

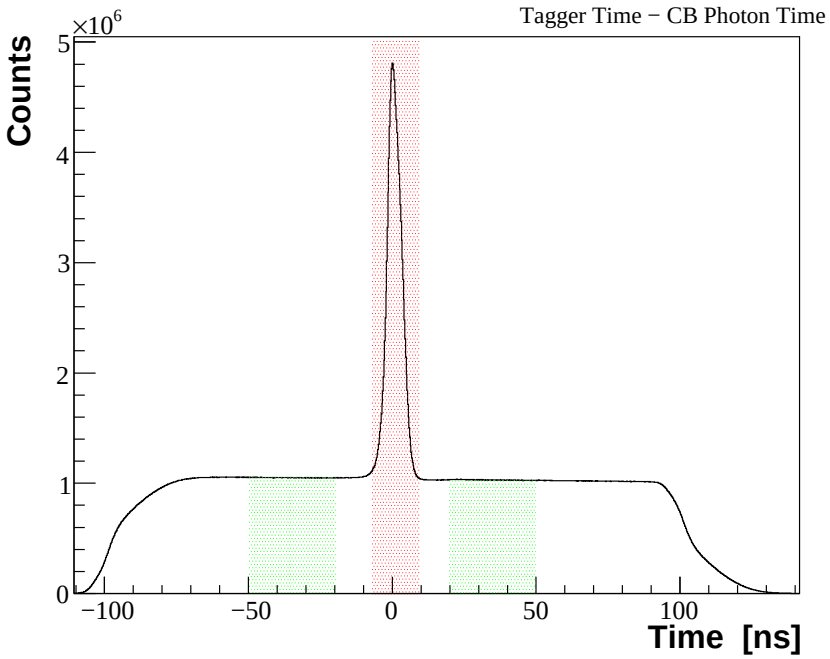

Figure 4.3: Tagger timeOR of all 352 Tagger channels for production data. The shaded red region (-7-8 ns) indicated events defined as prompt events. The shaded green regions were used to sample the background under the prompt peak.

in figure 4.3). The random region sampled can be scaled by the relative widths of the prompt and random windows (0.25 in this case) giving a sample equivalent to the background under the prompt peak. This random sample was then subtracted from the prompt region for all observables dependent on photon energy.

4.1.3 Tagging Efficiency

Tagging efficiency measurements, described in section 3.3.2, were made several times during data collection. Accurate determination of the photon flux incident on the target is essential when normalising reaction yield to evaluate cross sections. Photon asymmetry measurements depend on the different yields from two orthogonal photon polarisation planes and the magnitude of the tagging efficiency does not feature in this ratio. Nevertheless, tagging efficiency measurements are useful for coherent bremsstrahlung as it has a photon trigger (the photon has a ∼100% detection probability in the Pb glass) and also for beam diagnostic purposes. The photon trigger gives a Tagger hits spectrum which is reaction independent and these spectra can

be used to determine photon polarisation. Using the Crystal Ball as a trigger introduces reaction cross section into the Tagger hits spectrum which must be accounted for before the photon polarisation is calculated. This is discussed in more detail in chapter 5.

To account for activation, the build up of background radiation along the Tagger FPD, background measurements of Tagger scaler counts were made immediately before and after each block of tagging efficiency measurements. Equation 3.2 is modified to correct this background, N^{bg}, for each Tagger channel n:

$$\epsilon^{n}_{tagg} = \frac{N_\gamma}{N_e - N_{bg}} \tag{4.1}$$

Early tagging efficiency measurements as a function of Tagger channel (effectively photon energy) for adjacent runs covering the first coherent peak, E_γ =200-300 MeV for *para* and *perp* orientations are shown in figure 4.4(a). The sharp change in ϵ_{tagg} around channel 280 and also the edge around channel 230, is due to coherent bremsstrahlung from the diamond radiator. Coherent bremsstrahlung is more strongly forward focused than normal bremsstrahlung and polarised photons are more likely to reach the target after beam collimation. There is therefore, a large increase in tagging efficiency for polarised photons. A tagging efficiency measurement using an amorphous radiator (copper) is plotted in figure 4.4(b), showing near uniform behaviour with photon energy.

4.2 Crystal Ball Calibration

4.2.1 Photon Cluster Algorithm

In a segmented calorimeter such as the Crystal Ball, a single energetic particle will generally produce a shower of secondary particles spreading the energy deposit over several neighbouring crystals. Such a group is known as a cluster and different particles produce cluster signatures with different spatial extents and distributions of energy deposition. A clustering algorithm is therefore required to group adjacent energy deposits which stem from the same shower and thus same particle.

Energetic photons are detected from their electromagnetic showers in the crystals

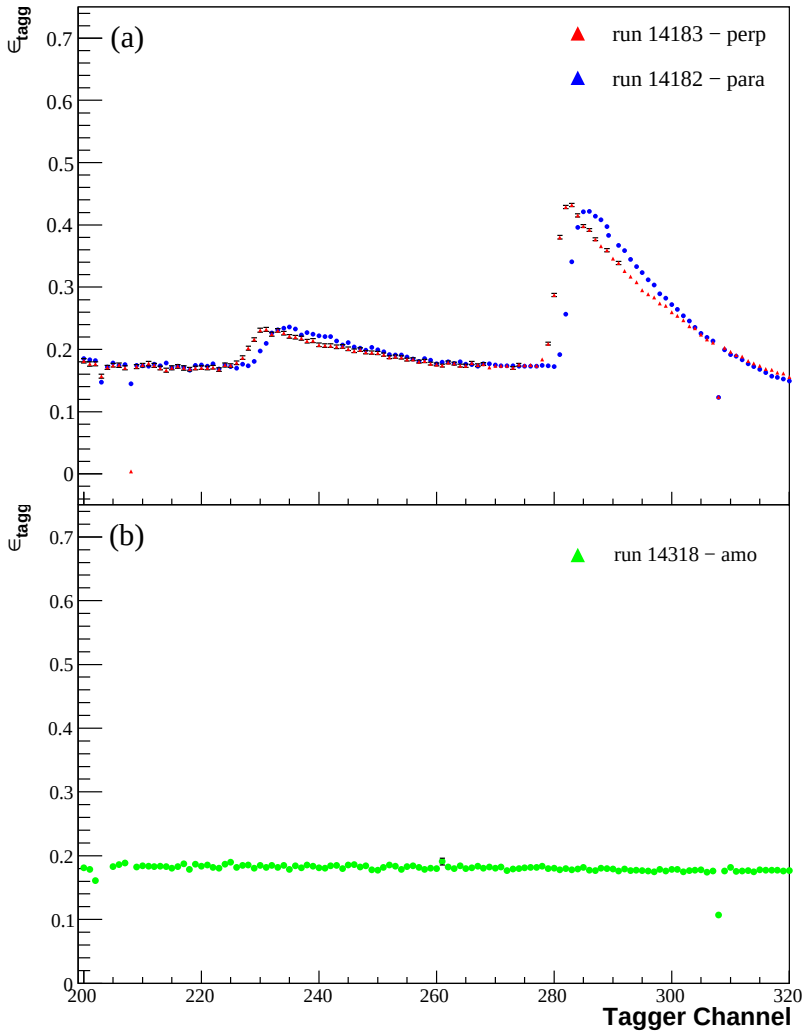

Figure 4.4: Tagging efficiency as a function of Tagger channel. (a) The blue points show data taken for *para* and red points *perp*. The sharp change in ϵ_{tagg} is due to coherent bremsstrahlung. (b) Tagging efficiency measurement with a copper radiator.

and typically (∼98% of the time) deposit their energy within a cluster of 13 NaI crystals. On the other hand, the energy deposit for protons is constrained to only a few crystal elements. The clustering algorithm first identifies the crystal with maximum energy deposit and assumes it to be the central element of the cluster. The algorithm then scans its 12 neighbouring crystals (figure 4.5) for any further energy deposit. Any energy deposit in adjacent crystals are added to the central crystal energy and the total energy in a cluster is $E_{tot} = \sum_i E_i$, where E_i is the energy

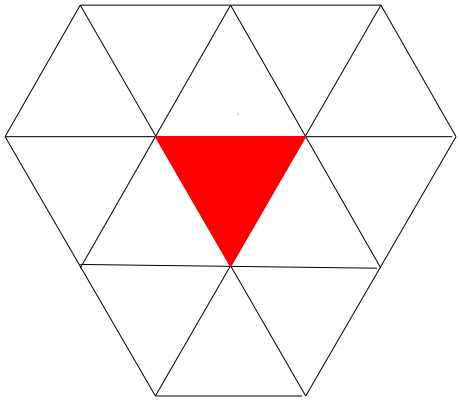

Figure 4.5: An NaI cluster. Each triangle represents the face of an NaI crystal. The algorithm searches for the crystal with the highest energy deposit - shaded in red - and sums that energy with any energy deposited in the 12 neighbouring crystals.

deposited in the i^{th} crystal. Clusters with an energy sum less than a threshold of 15 MeV were rejected as background. The position of the particle was calculated as the weighted mean position of the cluster hits:

$$\mathbf{r_m} = \frac{\sum_i \mathbf{r_i}\sqrt{E_i}}{\sum_i \sqrt{E_i}} \tag{4.2}$$

where $\mathbf{r_i}$ defines the (x,y,z) co-ordinate of the i-th crystal.

4.2.2 Crystal Ball Photon Energy Calibration

The Crystal Ball energy calibration converts the QDC value of each crystal element into an energy in MeV. A linear relationship was assumed between QDC channel and energy as the light output response of NaI(Tl) for photons is linear with energy for the photon energies used in this experiment [81]. Possible energy dependent corrections such as shower loss effects were found to have small effects in this range. An initial relative energy calibration was performed by colleagues from the University of Mainz [82], adjusting the PMT bases for each crystal to align the 4.438 MeV γ-decay of $^{12}C^*$ using a $^{241}Am/^{9}Be$ source. The decay photons deposit their energy in only a few crystals and this initial calibration provides sufficient alignment to set hardware thresholds for each crystal to similar levels.

However, these low energy photons are not typical of the photons produced in photoinduced reactions such as those produced in meson decay which generally have

energies greater than 40 MeV. Such energetic photons form a cluster of crystal hits in the CB. Thus a further, more detailed calibration is required. The $\pi^0 \rightarrow \gamma\gamma$ decay, stemming from the kinematically overdetermined $\gamma p \rightarrow p\pi^0$ reaction, provides an excellent source of calibration for high energy photons. The measured energy of the π^0 decay photons were compared to its expected energy, calculated from the known beam energy and pion emission angle. As the intention was to calibrate on a crystal-by-crystal basis, only events in which at least 70% of the photon's energy was deposited in the central crystal of a cluster were used in the analysis. The CB gain (MeV/channel constant) for each crystal was then rescaled to align the π^0 peak to its invariant mass of 135 MeV. As adjusting the gain for one crystal affects the results for neighbouring elements an iterative procedure was applied until the conversion constants converged. This high energy calibration was performed by colleagues from UCLA [83]. The proton energy response of the crystals is different and is discussed later.

An additional timing calibration was also carried out by UCLA collaborators who aligned the timing of each NaI TDCs with respect to a reference crystal. The CATCH TDCs used with the Crystal Ball have a constant channel to time conversion factor of 117ps/channel (section 3.7.1). Figure 4.6 shows the Crystal Ball time alignment results for the August data set. The structure seen in figure 4.6 is due to protons, which take longer to make an experimental trigger. The crystal elements with this structure are the more forward crystals in the CB which are more likely to detect protons. A separate timing alignment implementing the PID was used to identify events with protons in the final state and is discussed below.

4.2.3 Particle Identification Detector Calibrations

The PID identifies charged particles via a ΔE-E analysis using the correlation of energy deposited in a PID element with the total energy deposited in the CB. It is therefore important to carry out a position calibration to correlate the azimuthal angle (ϕ) of each PID element with the charged particles cluster in the CB. An energy calibration then must be performed prior to charged particle identification. Both calibrations were carried out by colleagues from the University of Edinburgh [84]. A

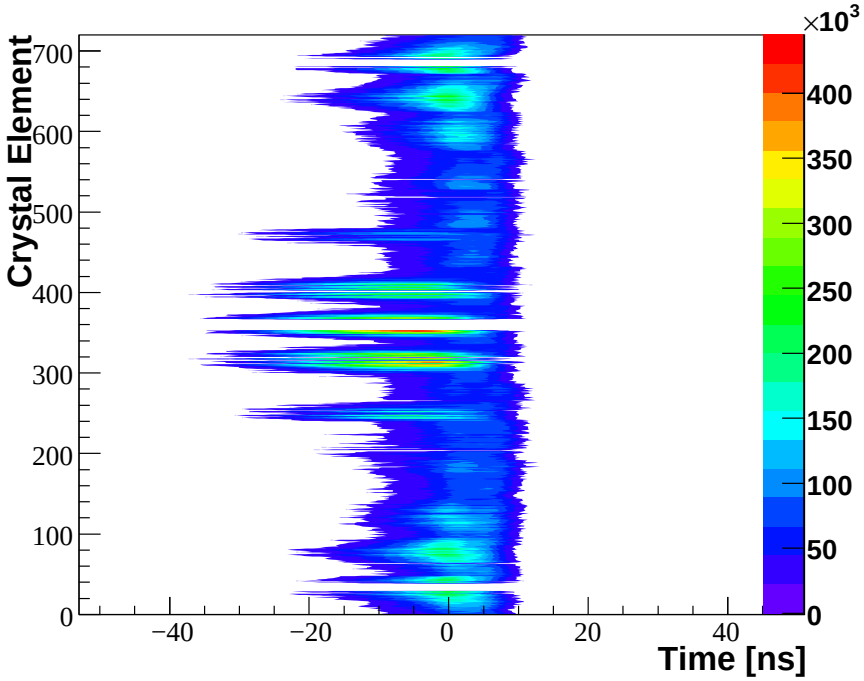

Figure 4.6: Aligned Crystal Ball TDCs.

first approximation of the azimuthal coverage of each PID element is accessed from a 2D plot of PID channel hit versus CB azimuth for events with at least one hit in the PID (figure 4.7(a)). Projecting the azimuthal distribution in the CB for a single PID element (figure 4.7(b)) reveals the true coincidence. The strong peak in figure 4.7(b) is a result of charged particles passing through PID element 3 before detection in the CB. The width of the peak relates to the azimuthal coverage of the PID element. The weaker peak ∼180° from the larger peak comes from events such as p(γ,π^+n), which deposits an additional signal in the CB but no signal in the PID.

An energy calibration of the PID was then carried out by comparing the results from experiment with simulated data using Geant4 (section 4.4.1). The simulation models the response of the CB and PID to protons, charged pions and electrons. The total energy E of each particle detected in the CB is plotted against ΔE, the energy deposited in the thin scintillators of the PID. Figure 4.8(a) shows the resultant 2D plot obtained from experimental data, showing the characteristic curves related to charged particles with different masses. The two intense regions highlighted correspond to protons and charged pions. Figure 4.8(b) projects ΔE for E=55-

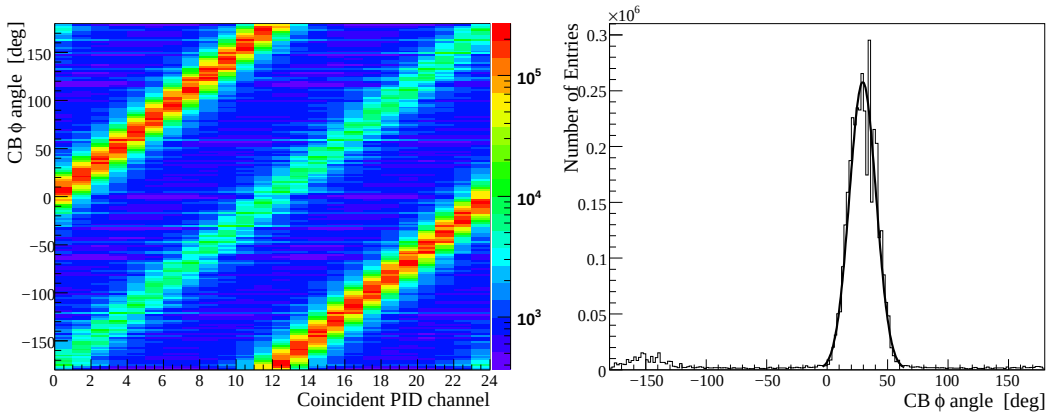

(a) (b)

Figure 4.7: For events with at least one hit in the PID. (a) PID channel which registers a hit against the ϕ angle of the coincident hit of the particle in the Crystal Ball. (b) A single PID channel projection from (a). Solid line is a Gaussian distribution fitted to the data.

65 MeV and shows reasonably clean separation between the lower energy pion peak, centred on ∼0.5 MeV, and the proton peak at ∼2.1 MeV. Gaussian distributions were fitted to both peaks for each CB energy projection and an identical process was repeated with the simulated data. The PID QDC gains for each element were adjusted to align the experimental mean of the proton and pion peak for each E projection to that observed in the simulation.

The particle identification process initially assumes that all detected clusters in the CB are photons. An algorithm then searches for an azimuthal correlation between the CB cluster and any PID hit. If the azimuthal correlation is within ±7.5° of the centre of a PID element, that particle is labelled as charged and is identified from the ΔE-E plot in figure 4.8(a). Particles were identified as protons if they fell within the red polygon cut in 4.8(a) and as charged pions if they are enclosed by the pink polygon cut. There is also an intense region due to electrons below the pion ridge deposit only a small amount of energy (<0.5 MeV) in the PID.

Unlike the slow timing response of NaI crystals which have a typical rise time of ∼250 ns [85], the pulse signals from the PID are very sharp with an intrinsic timing resolution of ∼0.5 ns. Each PID element has an associated CATCH TDC with a

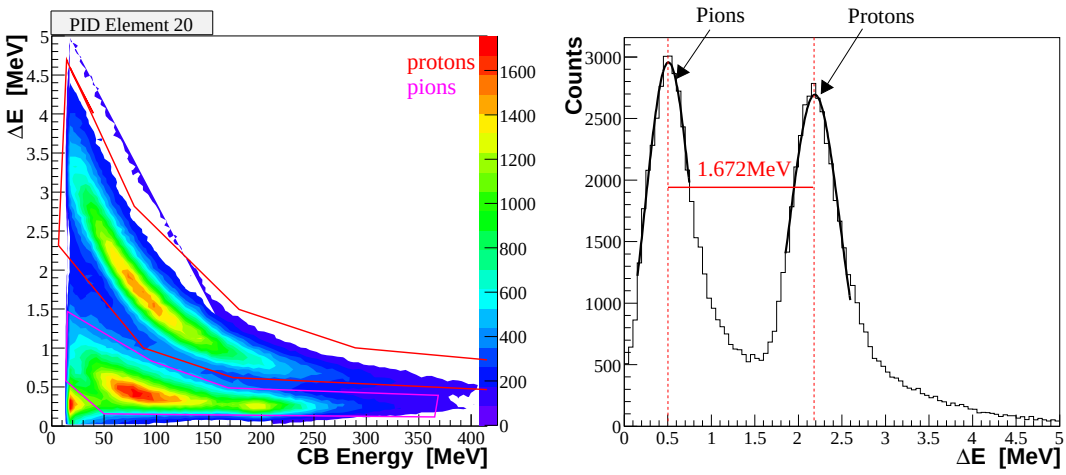

(a) (b)

Figure 4.8: (a) ΔE vs E plot for PID channel 20. Points within the red (pink) polygon are identified as protons (charged pions). (b) Projection of (a) for E=55-65 MeV. The smooth curves represent Gaussian distributions fitted to the pion and proton peak. The dotted line identifies the mean value of ΔE for each peak.

constant channel-to-time conversion factor. In a similar process to the Tagger and CB time alignments, the timing peak for each PID element was aligned to the same relative time. For reactions with a charged particle in the final state such as (γ,pp), the PID with its superior timing resolution was used to make a timing coincidence with the Tagger. Figure 4.9 plots Tagger time minus PID time. This gives a sharp coincident peak with FWHM=2.3 ns compared to FWHM=6.5 ns when using CB time to generate a timing coincidence.

4.3 Selection of π^0s

To measure the photon polarisation (section 5) and to apply a full proton energy correction (section 4.4) one must be able to identify neutral pions with a high detection efficiency. The π^0 is the lightest bound meson and as such cannot decay via the strong force. Instead, the π^0 decays via the electromagnetic interaction into two photons, $\pi^0 \rightarrow \gamma\gamma$, with a branching ratio of 99% [86]. This decay occurs with a mean lifetime of in 8.4×10^{-17}s and all information about the π^0 must be inferred from the detection of the decay photons. The invariant mass of all detected photon

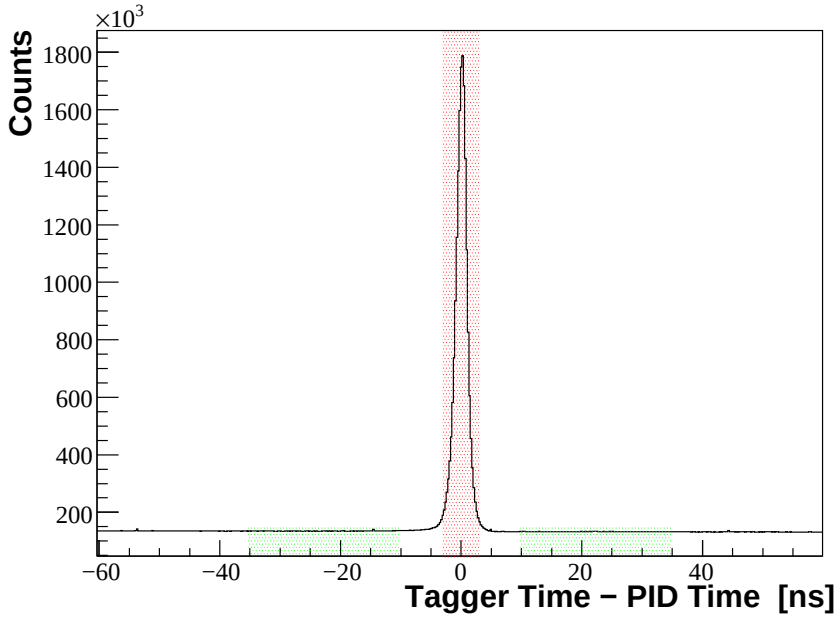

Figure 4.9: Event timing using the PID to select prompt events (prompt region shaded red). The shaded green regions were used to sample the background under the prompt peak.

pairs was reconstructed using the following relation:

$$m_{\gamma\gamma} = \sqrt{2E_1E_2(1-\cos\psi)} \tag{4.3}$$

where $E_1(E_2)$ labels the energy of photon 1(2) and ψ is the opening angle between them (appendix B).

The reconstructed invariant mass for all events with two clusters in the CB which were identified as photons is shown in figure 4.10. The strong peak around 135 MeV is due to $\pi^0 \to \gamma\gamma$ decay. There is also a clear η peak from the $\eta \to \gamma\gamma$ decay (with a branching ratio of 39.4%) which is centred around 450 MeV. The measured invariant mass of the η is offset from its particle data group (pdg) mass of 548 MeV [86] due to energy dependent photon shower losses. At higher energies, the photon cluster algorithm fails to identify all crystals which scintillate following an electromagnetic shower. To align the η peak with its known mass, an energy dependent global energy scale factor, which multiplies the measured energy by this factor, is applied. Typical scaling factors of 1.05 are used [87].

The 4-momentum of the pion in the lab frame is measured from the two detected

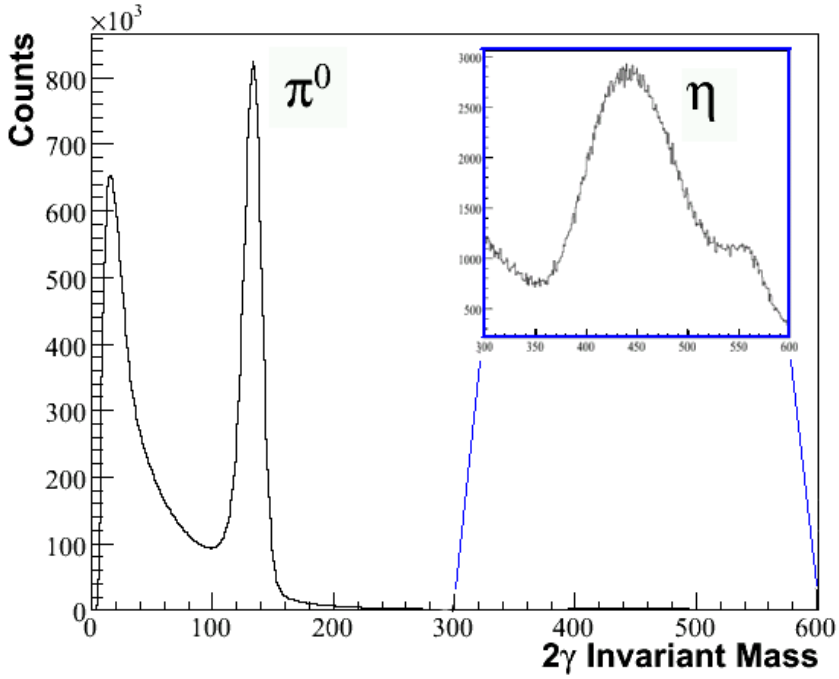

Figure 4.10: Invariant mass $M_{\gamma\gamma}$ for events where two photons are detected in the Crystal Ball. A clear π^0 peak around 135 MeV. A distinct η peak (inset) is visible upon closer inspection of the region $M_{\gamma\gamma}$=300-600 MeV.

photons:

$$p_\pi^\mu = p_1^\mu + p_2^\mu \tag{4.4}$$

where p_1^μ and p_2^μ are the 4-momenta of the decay photons.

$$p_1^\mu = (E_1, \mathbf{p}_1) \tag{4.5}$$

Here **p** is the reconstructed 3-momentum of the detected photon and E its energy.

4.4 Proton Energy Correction

Charged particles such as protons lose energy, primarily through ionisation and atomic excitations as they travel through the target, air, plastic scintillators, steel casing and any additional material in its path before it reaches the Crystal Ball. This energy loss must be determined for a wide range of proton energies and emission angles. A correction based on this calculation was applied to protons detected in the

Crystal Ball. Geant4 [88] provides a platform to simulate the passage of particles through matter and it was used to model and correct for energy loss in the CB. Section 4.4.1 describes the Geant4 A2 simulation (G4A2) used in the analysis and section 4.4.2 outlines the technique used to extract and apply the correction. The energy loss modelled by the simulation, calculates the difference in energy between the proton at the reaction vertex T_p^v and its energy at the crystal face T_p^c:

$$\mathrm{E_{loss}} = T_p^v - T_p^c \tag{4.6}$$

A secondary correction was also necessary to account for light attenuation losses in the NaI crystals which are not taken into account by the simulation. This correction depends only on proton energy and can be extracted using the overdetermined kinematics of the p(γ, π^0)p reaction. This light loss can be expressed as the difference in energy at the crystal face T_p^c and that measured from the QDC pulse height T_p^m:

$$\text{light attenuation} = T_p^c - T_p^m \tag{4.7}$$

Figure 4.11 illustrates both effects. The angular distribution of protons for p(γ, π^0)p is more forward focused than the distribution of protons for $^{12}C(\gamma,\mathrm{pp})$ which has a more uniform angular distribution. Therefore, a one step correction based solely on p(γ, π^0)p would be insufficient for protons detected at backwards angles. Thus, to calculate the proton energy upon ejection from the nucleus, T_p^v, from that measured in the CB, T_p^m, both effects must be corrected for separately.

4.4.1 Geant4 A2 Simulation

A realistic Monte Carlo simulation of the A2 experiment modelling the CB, TAPS, PID and different targets (Cryogenic and Solid) was written by colleagues from the University of Edinburgh [75]. Geant4 (G4) provides facilities for handling the physical layout of the experiment and for tracking the passage of particles, their interactions and various decay processes, through all materials and detectors in its path. Figure 4.12 shows a visualisation of the Crystal Ball and TAPS detector in the G4A2 simulation. The software can also record the response of each detector to various particles travelling through its volume, approximating the response of

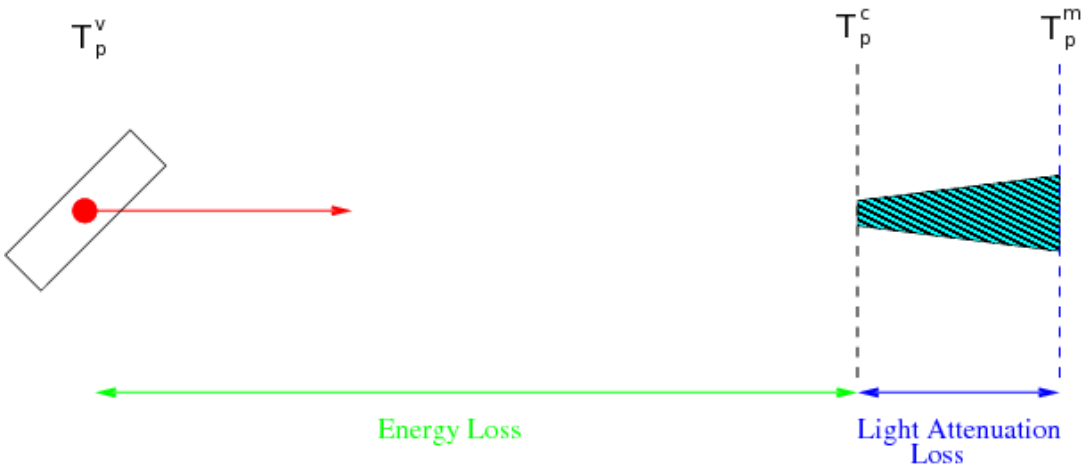

Figure 4.11: Schematic of proton energy loss from ejection to detection in the Crystal Ball. A proton is knocked out a nucleus with energy T_p^v, after losing energy along its path it arrives at the crystal face with energy T_p^c. Additional losses in signal amplitude are due to light attenuation in the NaI crystal. A final energy T_p^m is measured by the CB PMTs.

a real detector. This provides an invaluable tool for calculating the acceptance of any detector system for a particular reaction, given a file of pre-generated events matching the kinematic distributions of the various particles involved.

The G4A2 simulation was used in this analysis to model the passage of protons through the various detectors and materials in the Crystal Ball, mapping proton energy loss as a function of energy and angle. Approximately 100 million protons were generated with random energies, uniformly in the range, T=30-300 MeV, from within the carbon target. Geant4 uses various physics models including several electromagnetic and hadronic packages to compute the energy lost by each particle from reaction vertex to detection. T is equivalent to T_p^v, the energy of the proton when ejected from the nucleus and the ultimate aim of the energy correction is to translate from detected energy to T_p^v. The simulation processes each proton on an event-by-event basis and produces output in the form of a ROOT Tree [89] containing information including the detector elements struck and the energy deposited in each element. The simulated data can then be analysed using the same code as real data and analysis of the output is discussed below.

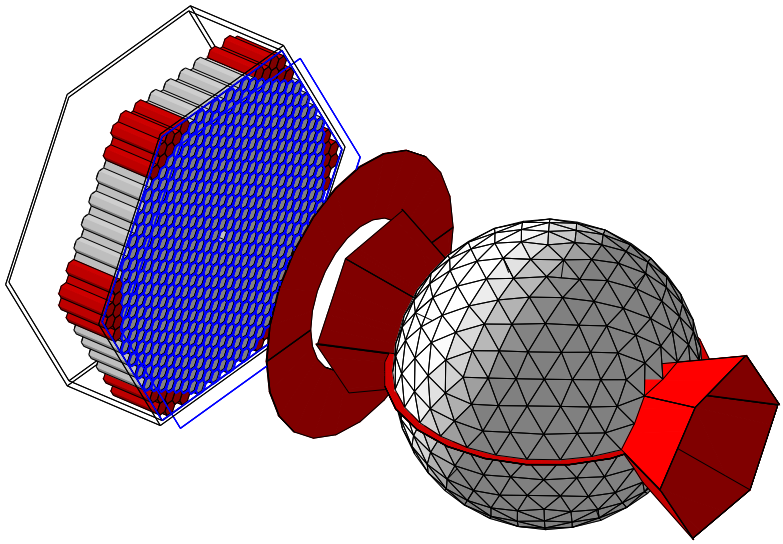

Figure 4.12: A picture of the CB-TAPS setup from A2 simulation [75].

4.4.2 Energy Loss

The energy loss of protons as they travel through the detector system varies with energy and also emission angle θ due to discrete components such as support structures surrounding the target. There is also some dependence on the azimuthal angle, despite the detector system being azimuthally symmetric. This is a consequence of the azimuthal asymmetry of the target. A proton ejected from a carbon nucleus at $\theta = 45°$ may move along the entire length of the target before detection or escape the target promptly, depending on ϕ. Therefore, to map out the required energy loss correction the magnitude of the correction as a function of energy, θ and ϕ must be determined. In the analysis code, each NaI crystal is given an index X from 0 - 719 (the 48 additional indices correspond to *blank* crystals required to complete the full 4π icosahedron geometry) and analysis of energy loss as a function of X implicitly contains information on both θ and ϕ.

It is important to define a correction factor $f_E^{cor}(T_p^c)(X)$:

$$f_E^{cor}(T_p^c)(X) = \frac{T_p^v - T_p^c}{T_p^c} \tag{4.8}$$

where X is the index of the crystal with largest energy deposit. The magnitude of f_E^{cor} for a given crystal gives a measure of the fractional energy lost by a proton with initial energy T_p^v as it travels from target to crystal X. Figure 4.13(a) shows the variation in f_E^{cor} with T_p^c, the energy of the proton at the crystal face, for X=110. The fractional energy loss for protons is largest for low energy protons ($< 50\,\text{MeV}$) with up to 100% of the energy measured at the crystal face, T_p^c, also being lost as it travels from target to CB. The fractional loss tails off with energy, with protons with energies greater than 100 MeV depositing less than 10% of their measured energy on the way to crystal 110. The spread in f_E^{cor} for each crystal is due to the stochastic nature of the Monte Carlo. Figure 4.13(b) projects f_E^{cor} from figure 4.13(a) for T_p^c=120-130 MeV. A Gaussian fit is applied to each projection and the value of f_E^{cor} for each T_p^c range was taken as the mean of the fit. For crystal 110, $f_E^{cor} \sim 0.05$ for T_p^c=120-130 MeV, corresponding to an energy loss of $\sim$6 MeV. Figure 4.13(c) shows the energy dependence of the correction, plotting the mean of each fit to f_E^{cor} against T_p^c.

This process was repeated for all 720 crystals and the magnitude of f_E^{cor} for all energies and crystals was stored in a lookup table. For real data, when a proton deposits energy T_p^c in a given crystal, the lookup table was accessed and f_E^{cor} was determined by interpolation. The energy of the proton T_p^v can then be calculated via:

$$T_p^v = T_p^c + f_E^{cor} T_p^c \tag{4.9}$$

As a consistency check, this technique was applied to the simulated data. Figure 4.14 shows the distribution of T_p^v minus the measured energy in the simulation (with and without the correction). The blue line corresponds to energy difference before any energy loss correction is applied. There is a clear offset in the peak due to energy loss. When the correction is applied the peak shifts to 0 MeV with a FWHM of $\sim$4 MeV. This gives an indication of the accuracy of the energy loss reconstruction.

This technique was successful for all but those crystals adjacent to the beam

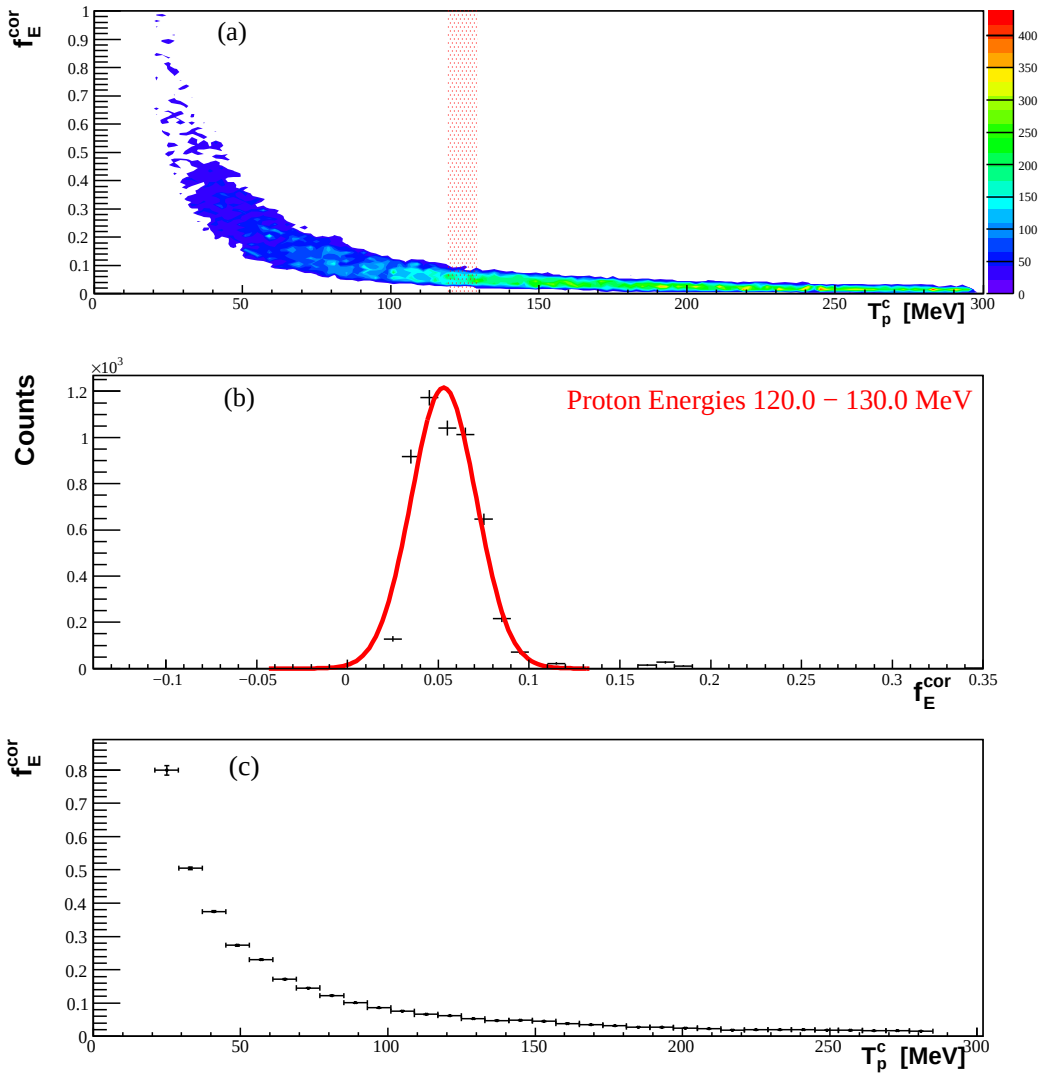

Figure 4.13: Simulated proton energy loss for crystal 110. (a) Proton fractional energy loss f_E^{cor} as a function of measured energy. The shaded red region projects f_E^{cor} for (b) T_p^c=120-130 MeV. The distribution is fitted with a Gaussian function. (c) The mean fit of each energy projection is plotted showing the energy dependence of f_E^{cor}.

entrance and exit tunnels. Figure 4.15 shows the variation in f_E^{cor} with T_p^c for one such crystal, X=40. The distribution observed for edge crystals have two distinct energy loss bands. This indicates that some protons fail to deposit all of their energy in the NaI crystals. If the energy deposited in the crystal is less than its true energy at the crystal, f_E^{cor} is shifted to larger values and a misleading correction factor

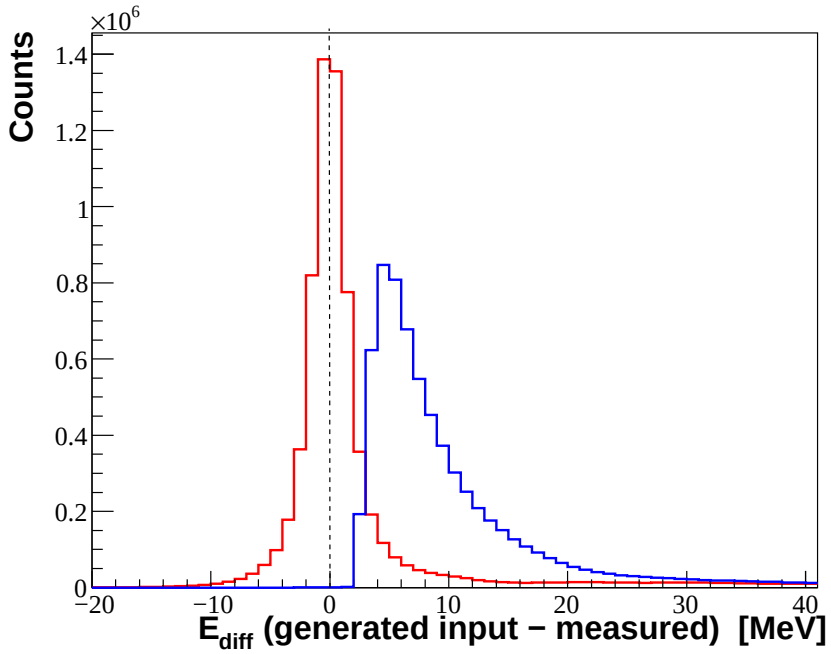

Figure 4.14: A test of the energy loss correction obtained using Geant4. E_{diff} (Generated - Measured Energy) summed over all NaI crystals. Energy difference before correction is applied in blue and after correction in red.

is obtained. The remaining energy would likely be deposited in the forward wall (TAPS) and using this information f_E^{cor} could be adjusted accordingly. However, as TAPS was not included in the data stream the 8 most forward NaI crystals were removed from the analysis.

4.4.3 Light Attenuation Correction

In an ideal situation, the experimentally measured energy would be equivalent to the simulated data, i.e. $T_p^m \equiv T_p^c$. Unfortunately, this is not the case and due to the light response of NaI crystals to protons a secondary correction was required. This correction includes light attenuation losses in the crystal and also a scaling factor converting the energy calibration which is tuned to measure photon energies from their electromagnetic showers, to a calibration more suitable for protons (which generally deposit their energy in a few crystals). A correction which converts T_p^m to T_p^c is therefore required before applying the energy loss correction. This correction

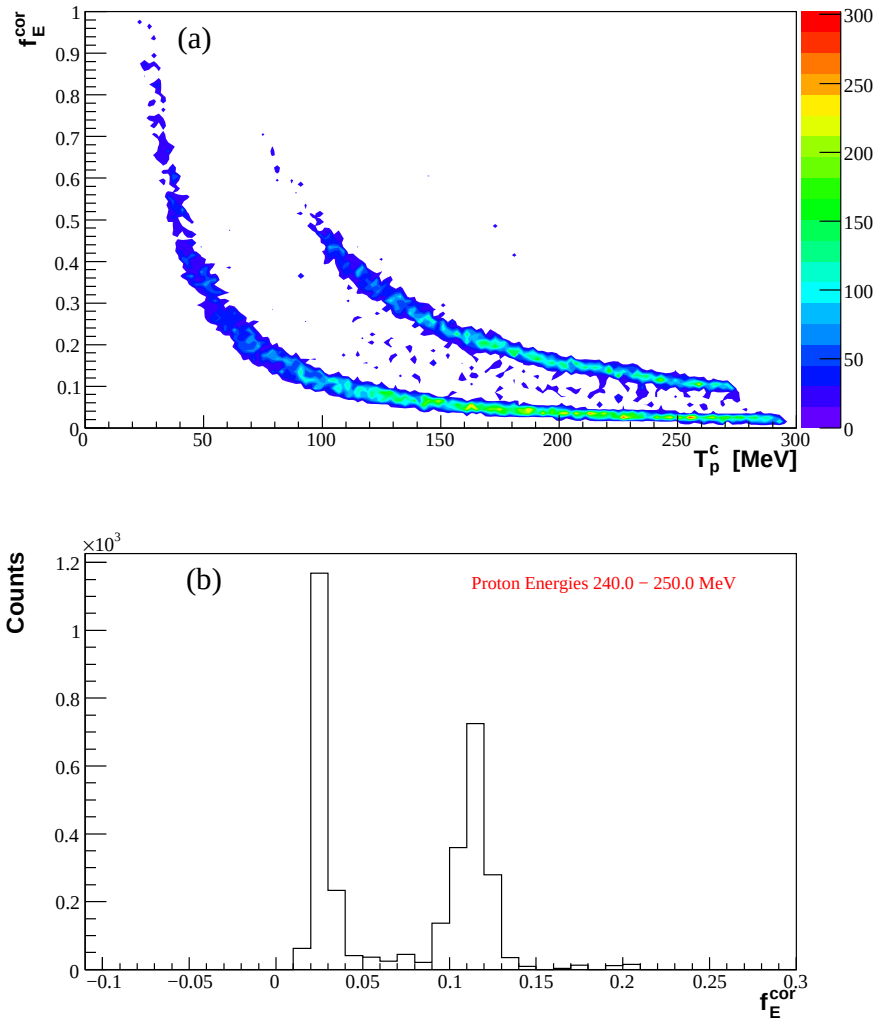

Figure 4.15: (a) Proton fractional energy loss f_E^{cor} as a function of T_p^c for X=40 at the edge of the Crystal Ball. The shaded red region defines the f_E^{cor} projection for (b) T_p^c = 240-250 MeV.

can be extracted from the kinematically overdetermined $\gamma p \rightarrow p\pi^0$ reaction. Events with detection of only a proton and π^0 in the final state were first selected. By conservation of momentum and energy, the 4-vector of the recoiling proton can be completely determined from the incident photon energy, known target mass and the detected pion:

$$(E_p, \mathbf{p}_p) = (E_\gamma, \mathbf{p}_\gamma) + (m_p, 0) - (E_\pi, \mathbf{p}_\pi) \tag{4.10}$$

where E_p and $\mathbf{p}_p$ are the energy and momentum of the recoiling proton, E_γ and $\mathbf{p}_\gamma$ the photon energy, m_p the proton mass and E_π and $\mathbf{p}_\pi$ the energy and momentum of the pion.

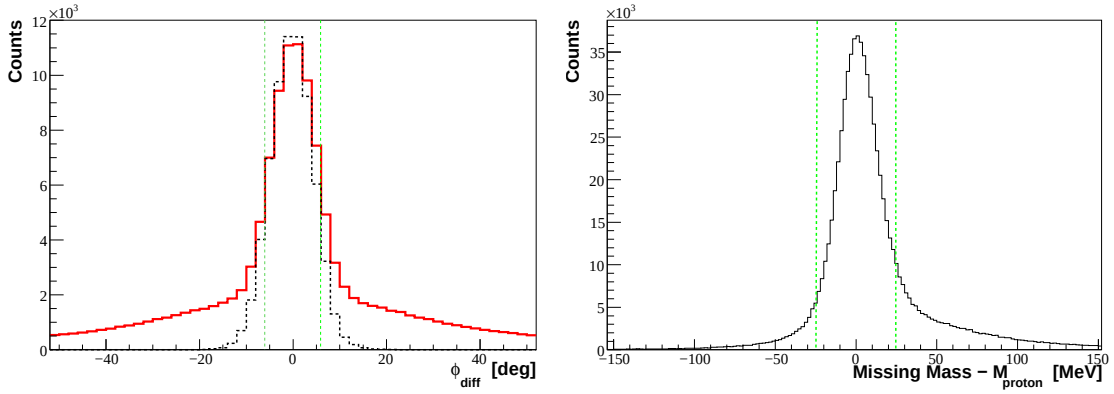

(a) (b)

Figure 4.16: (a) The angular difference between detected and reconstructed proton momentum from the $(\gamma, p\pi^0)$ reaction. In blue - data taken with hydrogen target. In red- CH2 target. (b) The missing mass derived from the reconstructed 4-vector minus proton mass for the CH_2 target. Dashed green lines indicate data cuts applied to both histograms.

To ensure consistency between the proton reconstructed from $\gamma p \rightarrow p\pi^0$ and the detected proton two conditions had to be met. Firstly, a constraint was applied to the opening angle, ϕ_{diff}, between the reconstructed and measured momentum vectors (figure 4.16(a)). An identical analysis on data with a pure proton target gives a clean peak centred on zero. However, things are complicated somewhat by the initial Fermi motion of protons in carbon nuclei and also $^{12}C(\gamma, p\pi^0 X)$ reactions. In the latter, other particles X are emitted (e^-,π^0, additional nucleons and various other particles) which carry off some energy which may not be detected in the CB. Both smear ϕ_{diff} and bias the reconstructed 4-vector and are therefore unreliable events to use when deriving a secondary corrections. A 2σ cut, $-6° < \phi_{diff} < 6°$ was applied to reduce the aforementioned background. A second test ensured the *missing mass*, the invariant mass of the reconstructed four-vector, was consistent with the proton mass. Figure 4.16(b) plots the missing mass of the 4-vector, reconstructed from $\gamma p \rightarrow p\pi^0$, minus the proton mass. A Gaussian function was fitted to the distribution and a 2σ cut was applied to reduce the background in the final sample.

The energy of the reconstructed proton in the lab frame $E_p = E_\gamma - E_\pi$ is equivalent to T_p^v in the simulation. To obtain a correction for light response effects

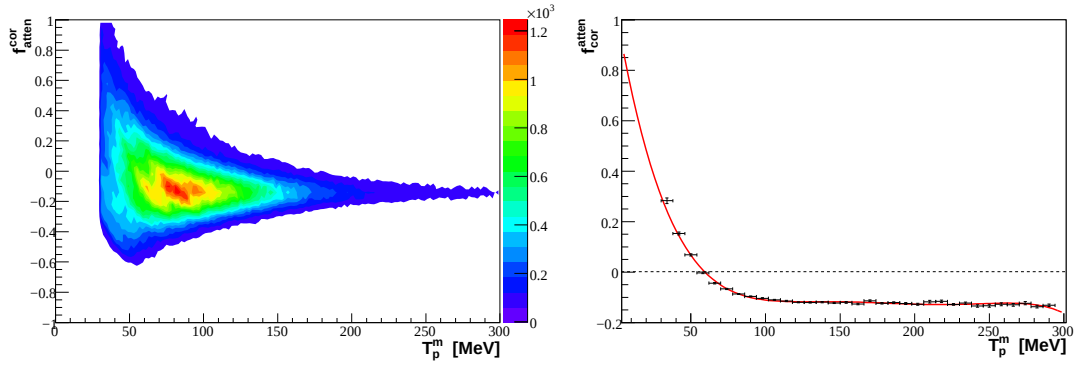

(a) (b)

Figure 4.17: Light response correction as a function of measured proton energy integrated over all CB crystals.

one can use a slight modification of the energy loss correction discussed in section 4.4.2 to convert from T_p^v to T_p^c. Any secondary energy loss can then be determined from knowledge of T_p^c and T_p^m. Modifying equation 4.8, one can define $f_E^{gencor}(T_p^v)(X) = \frac{T_p^v - T_p^c}{T_p^v}$ which models energy loss as a function of T_p^v rather than T_p^c. Following a similar recipe to section 4.4.2, T_p^c can be accessed from f_E^{gencor} and T_p^v:

$$T_p^c = T_p^v - f_E^{gencor} T_p^v \tag{4.11}$$

Figure 4.17(a) plots the normalised energy difference $f_{atten}^{cor} = \frac{T_p^c - T_p^m}{T_p^m}$ as a function of T_p^m and figure 4.17(b) plots the mean value of f_{atten}^{cor} for each T_p^m projection of 4.17(a). A phenomenological correction, approximated by a fifth order polynomial was applied to figure 4.17(b) to map the energy dependence of the secondary correction:

$$f_{atten}^{cor} = \mathrm{b}_0 + \mathrm{b}_1\mathbf{x} + \mathrm{b}_2\mathbf{x}^2 + \mathrm{b}_3\mathbf{x}^3 + \mathbf{b}_4\mathbf{x}^4 + \mathrm{b}_5\mathbf{x}^5 \tag{4.12}$$

where $\mathrm{x} = T_p^m$, $\mathrm{b}_0 = 1.11$, $\mathrm{b}_1 = -3.84 \times 10^{-2}$, $\mathrm{b}_2 = -4.58 \times 10^{-4}$, $\mathrm{b}_3 = -2.63 \times 10^{-6}$, $\mathrm{b}_4 = 7.24 \times 10^{-9}$ and $\mathrm{b}_5 = -7.72 \times 10^{-12}$ with $\chi^2/\text{n.d.f.} \approx 3.5$.

Each time a proton was detected in the CB with measured energy, T_p^m, f_{atten}^{cor} was extracted from from equation 4.12. T_p^m can then be converted to T_p^c and the energy loss correction described in section 4.4.2 can be applied to determine the proton energy at the reaction vertex, T_p^v.

It is clear from figure 4.17(b) that for T_p^m <50 MeV, that some additional en-

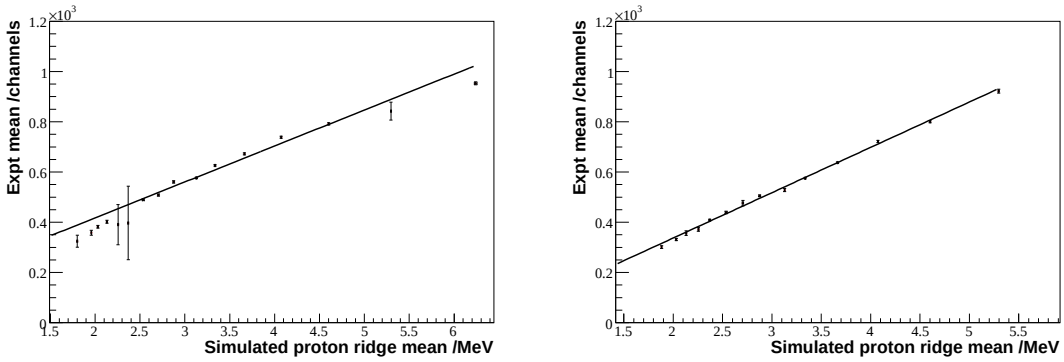

(a) (b)

Figure 4.18: PID calibration showing the simulated proton ridge mean against the mean value (in channel) of the ridge for real data. (a) pre- and (b) post-light attenuation correction [90].

ergy loss is occurring in the NaI crystals which must be corrected for. Above T_p^m=100 MeV, f_{atten}^{cor} tails off and is essentially independent of energy. If the Crystal Ball was calibrated specifically for protons, f_{atten}^{cor} would tend to zero at high energies. However, $f_{atten}^{cor} \rightarrow\sim$-0.1 indicating that $T_p^m > T_p^c$ for high T_p^m.

More recent PID calibrations performed by colleagues at the University of Edinburgh make use of this attenuation correction [90]. PID ΔE-E plots (figure 4.8(a)) were constructed for real and simulated data. Energy projections were made for both histograms and a Gaussian function was fitted to the real and simulated proton peak (figure 4.8(b)). Figure 4.18(a) plots the experimental mean energy deposited in PID channel 0 (in QDC channel) against simulated energy deposit, before any light loss correction is applied. Figure 4.18(b) is the equivalent graph with light attenuation corrections applied before the ΔE-E plot is constructed. The gradient of the line in each plot gives the energy calibration constant in MeV/channel for that PID element. Applying the light attenuation correction to protons in the Crystal Ball clearly improves the linear relationship between measured and simulated energy deposit in the PID implying the attenuation correction is successful.

A final check of the energy loss procedure was carried out by comparing the energy of the reconstructed proton T_p^r with the measured proton energy after both corrections have been applied. Figure 4.19 plots the energy difference, $T_p^r - T_p^m$,

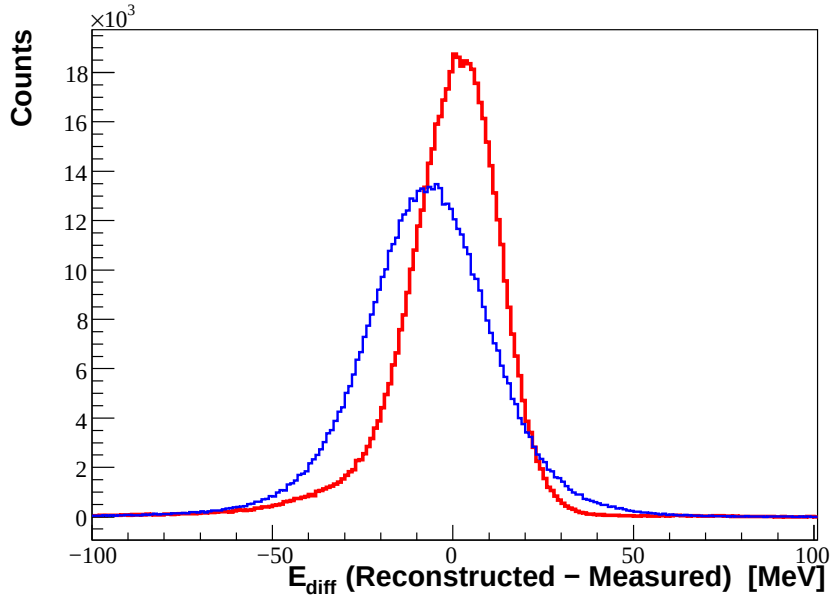

Figure 4.19: Energy difference between reconstructed and measured proton energy. In blue - Energy difference with no correction applied. In red - Energy difference with both corrections applied.

integrated over all energies and emission angles, with and without the energy loss corrections. The corrections shift the initial broad blue peak to ∼0 MeV and changes the width of the distribution from σ ∼17.0 MeV to σ ∼10.7 MeV.

4.5 Summary

Once the processes described in this chapter have been completed, the data are considered to be calibrated and in a format which can now be used for initial particle identification and the construction of physics 4-vectors. These particle 4-vectors allow for a more detailed physics analysis of events of interest within the data. The final aspect of calibration is the determination of photon polarisation and is discussed in the following chapter. The results of the (γ,pp) data analysis using the initial particle identification and event selection discussed in this chapter are presented in chapter 6.

Chapter 5

Photon Polarisation

An advantage of measuring a photon asymmetry as opposed to a cross section is that systematic errors from detector acceptance cancel. The dominant systematic error is then that on P, the degree of polarisation of the photon beam. This chapter begins by outlining the functional form of Σ, and the method used to extract it from data. The remainder of the chapter discusses two methods used to extract the beam polarisation as a function of beam energy. The first method, based on a comparison between an enhancement plot of the Tagger scaler spectra and an analytic bremsstrahlung calculation is discussed along with its limitations in obtaining accurate measurements of photon polarisation. The second method details a more reliable method using coherent π^0 photoproduction from ^{12}C as photon polarimeter. Finally, a comparison will be made between the two methods of measuring P along with estimation of the systematic uncertainties involved in the measurement.

5.1 Extraction of a Photon Asymmetry Σ

The behaviour of a cross section with linear polarisation of the photon beam is usually expressed through the beam asymmetry Σ as:

$$\frac{d\sigma}{d\Omega} = \sigma_0(1 + P\Sigma\cos(2\phi)) \tag{5.1}$$

where σ_0 is the unpolarised cross section, P the photon polarisation and ϕ the azimuthal angle between the photon polarisation and the reaction plane. One can

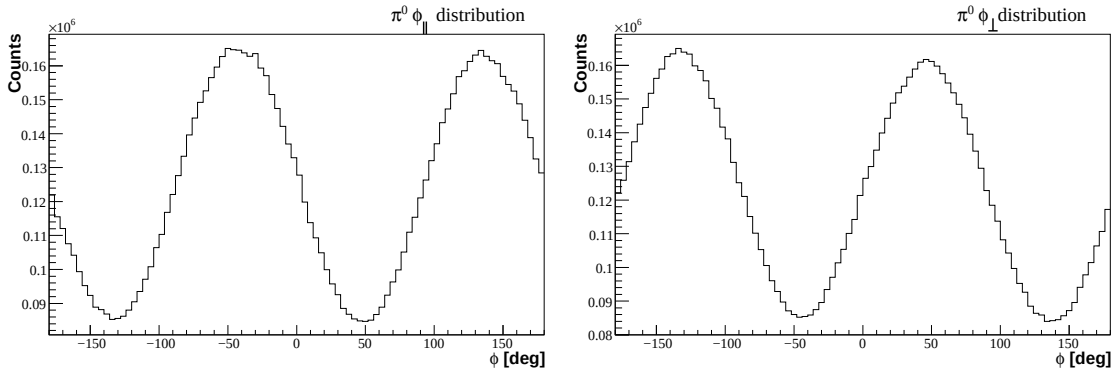

(a) *para* (b) *perp*

Figure 5.1: π^0 azimuthal distribution for (a) *para* and (b) *perp* polarised photon beams over the entire θ acceptance of the CB for E_γ=200-300 MeV and 2.5 mm graphite target. The Crystal Ball has a near uniform ϕ acceptance for π^0s and $\cos(2\phi)$ distributions are evident in the raw distributions. There is a 90° phase shift between the polarisation planes.

exploit the $\cos(2\phi)$ dependence of the polarised cross section to extract Σ assumming the photon polarisation is well determined. One method of extracting Σ involves taking the ratio of azimuthal distributions from polarised and unpolarised data and fitting with some known function of $\cos(2\phi)$. However, this method is not optimal as the coherent peak has an enhancement $\gtrsim$4 above the unpolarised yield and the resulting statistical uncertainty in the measurement is dominated by the poorer statistics of the amorphous data set.

A better method, is to form an asymmetry of the ϕ distribution of two orthogonal polarised data sets, labelled $\parallel$ and $\perp$ as defined in section 3.6.1 and again fitting with a known function of $\cos(2\phi)$. The azimuthal distribution of π^0s using linearly polarised photons incident on a carbon target is plotted in figure 5.1 for (a) *para* and (b) *perp*. The distribution has the following functional form:

$$N(\phi)_{\parallel,\perp} \sim A(\phi)F_{\parallel,\perp}(1 + P_{\parallel,\perp}\Sigma\cos(2\phi)) \tag{5.2}$$

where $A(\phi)$ is the detector acceptance as a function of ϕ which can be difficult to simulate accurately, particularly for multi-particle final states and thus can be source of large statistical uncertainty. It is evident from figure 5.1 that the acceptance is pretty flat for detection of π^0s in the Crystal Ball. This is not the case for

protons. $F_{\parallel,\perp}$ and $P_{\parallel,\perp}$ are the photon flux and linear polarisation for *para* and *perp* respectively. However, as the detector acceptance $A(\phi)$ is independent of photon polarisation, taking ratios or asymmetries has the advantage of removing any detector acceptance issues, eliminating its associated systematic uncertainty from the measurement. Ideally, the photon flux is well defined and the data can be scaled appropriately to ensure $F_\parallel = F_\perp = F$ and the polarisation is stable over the beamtime for both polarisation planes $P_\parallel = P_\perp = P$ reducing the asymmetry to:

$$\frac{N(\phi)_\parallel - N(\phi)_\perp}{N(\phi)_\parallel + N(\phi)_\perp} = P\Sigma\cos(2\phi) \tag{5.3}$$

However, in general the photon flux is not known well enough to appropriately scale the data sets and the polarisations $P_\parallel$ and $P_\perp$ are not necessarily equivalent. In addition, there is likely to be a systematic offset, ϕ_0, which is required to make the $\cos(2\phi)$ distribution consistent with the data. This offset is geometric and depends on the initial alignment of the diamond in the goniometer and only needs determined once, using a reaction channel with high statistics. The resulting expression for the azimuthal asymmetry of reaction particles is more complicated than the ideal scenario. Defining some ratios, $F_R = F_\parallel/F_\perp$, $P_R = P_\parallel/P_\perp$ and $\overline{P} = \overline{P_\parallel + P_\perp}$ and substituting for $F_{\parallel,\perp}$ and $P_{\parallel,\perp}$, the asymmetry can be expressed:

$$\frac{N(\phi)_\parallel - N(\phi)_\perp}{N(\phi)_\parallel + N(\phi)_\perp} = \frac{F_R - 1 + \frac{F_R P_R + 1}{P_R + 1} 2\overline{P}\Sigma\cos(2(\phi - \phi_0))}{F_R + 1 + \frac{F_R P_R - 1}{P_R + 1} 2\overline{P}\Sigma\cos(2(\phi - \phi_0))} \tag{5.4}$$

This distribution was fitted with a function with four free parameters A, B, C and D:

$$\frac{N(\phi)_\parallel - N(\phi)_\perp}{N(\phi)_\parallel + N(\phi)_\perp} = \frac{A - 1 + \frac{AB+1}{B+1} 2C\cos(2(\phi - D)}{A + 1 + \frac{AB-1}{B+1} 2C\cos(2(\phi - D))} \tag{5.5}$$

where $A = F_R$, $B = P_R$, $C = \overline{P}\Sigma$ and $D = \phi_0$. The systematic offset ϕ_0 for the March beamtime was determined by fitting equation 5.5 to the high statistic π^0 production channel and is shown in figure 5.2. The value of ϕ_0 extracted from the fit was $46.84° \pm 0.04°$. The ratios $\frac{F_\parallel}{F_\perp}$ and $\frac{P_\parallel}{P_\perp}$, which vary with photon energy, are also indicated on figure 5.2, with the average value of both over the photon energy range E_γ=200-300 MeV equal to unity.

A significant advantage of fitting azimuthal asymmetries with equation 5.5 is that it allows extraction of Σ without explicit knowledge of the photon flux. Instead, the

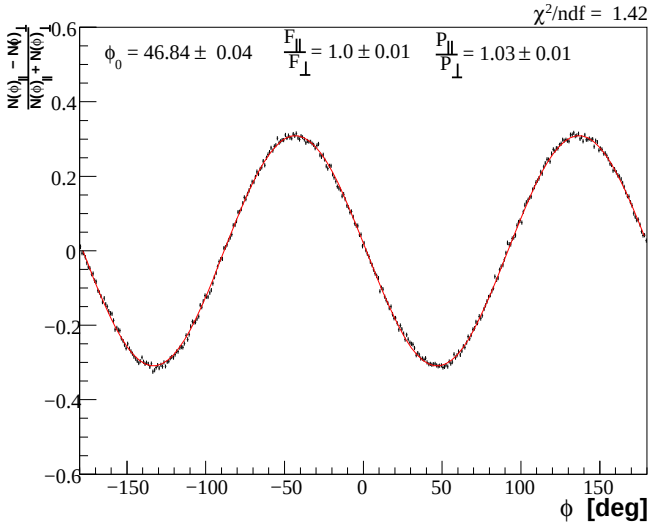

Figure 5.2: Azimuthal asymmetry for π^0s averaged over full coherent peak E_γ=200-300 MeV and over all angles. The distribution was fitted with equation 5.5 to extract the phase offset ϕ_0.

ratio of the fluxes and photon polarisation can be extracted from the fit. An accurate extraction of Σ by fitting an azimuthal asymmetry with equation 5.5 depends on knowledge of the degree of linear polarisation (averaged over the two polarisation directions) and the remainder of this section is dedicated to the extraction of P.

5.2 Determining the Photon Polarisation

5.2.1 Coherent Bremsstrahlung Comparison

The degree of linear polarisation can be determined from the analytic bremsstrahlung calculation discussed in section 3.4.3. To do so, it is necessary to determine the position of the coherent edge and understand the relationship between photon energy and polarisation for each edge position. The position of the coherent edge is determined by making an enhancement plot of Tagger scaler spectra, dividing the Tagger scaler distribution with polarised photons by that taken with a reference amorphous Cu radiator. Automated enhancement plots are made for every scaler read, the time taken to fill a predefined buffer which is typically every 2 minutes. Figure 5.3(a) plots typical scaler distributions along the Tagger focal plane for polarised (red)

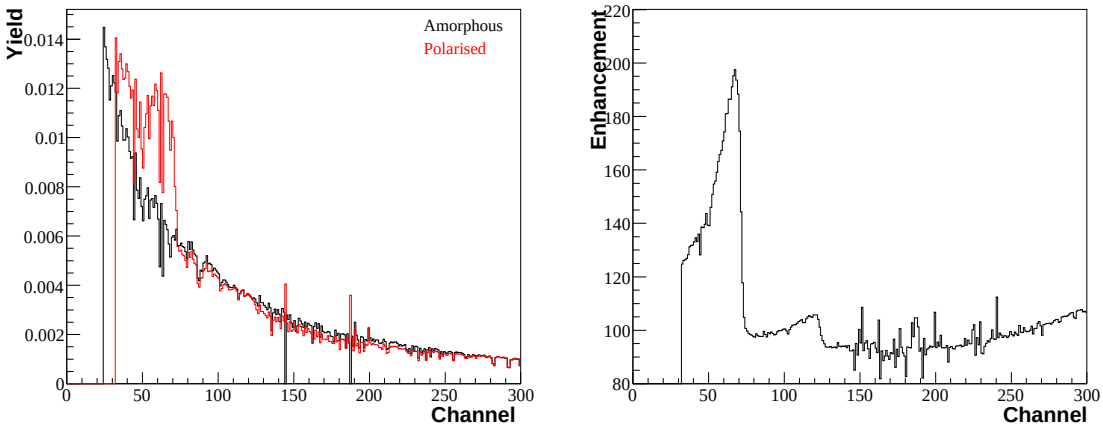

(a) (b)

Figure 5.3: (a) Tagger scaler spectra for polarised (red) and unpolarised (black) photons. (b) The corresponding enhancement plot which reveals a clear coherent edge.

and unpolarised photons (black). The coherent bremsstrahlung spectrum from a crystalline radiator is composed of a coherent part sitting on incoherent background and it is difficult to determine the coherent edge from raw scaler distributions. An enhancement plot, shown in figure 5.3(b), overcomes this problem by dividing out the incoherent background from the diamond bremsstrahlung spectrum, revealing a distinct coherent edge. The position of the edge is very sensitive to both the alignment of the electron beam and the orientation of the diamond radiator and any slight variation in either will affect the polarisation of the photon beam.

The polarisation can then be deduced from the enhancement using *anb*. In coherent bremsstrahlung theory [63], intensities and polarisation are described in terms of fractional energies, $x = \frac{E_\gamma}{E_{beam}}$. The intensity for a single, isolated, coherent peak (g) is represented as the sum of coherent (I^c) and incoherent (I^i) contributions and the polarisation is described as a function of x and the discontinuity energy x_g^d as follows:

$$P_g = -\Phi(x)/(1 + I^i/I^c) \tag{5.6}$$

where

$$\Phi(x) = \frac{2Q_g^2x^2}{(1-x)}\left[1 + (1-x)^2 - \frac{4Q_g^2x^2}{1-x}\left(\frac{1-x}{Q_gx} - 1\right)\right]^{-1} \quad ; \quad Q_g = \frac{1-x_g^d}{x_g^d} \tag{5.7}$$

$\Phi(x)$ defines the upper limit of polarisation which is set by the coherent edge energy and I^i/I^c represents the relative intensities of the incoherent and coherent contributions. Tight collimation decreases the incoherent contributions I^i relative to I^c and P increases towards its upper limit. In reality, the intensity distribution is smeared due to factors such as beam divergence, spread in beam momentum and crystal thickness and the upper intensity spectrum $\phi(x)$ is a sum of many $\Phi(x)$ contributions over a range of discontinuities $(x_d \pm \Delta x_d)$. The parameters of *anb* must be adjusted to take such factors into account whilst also attempting to model collimation and the angular spread of the generated photons in order to predict the I^i/I^c ratio.

The test of this is how well the calculated enhancement agrees with the experimental enhancement and the agreement between the polarisation derived from the calculation and that measured by some independent method, either a polarimeter or a reaction with a well defined analysing power. The data from this experiment offers an excellent opportunity to examine these issues. In section 5.3.1 the experimental enhancement is compared with that derived from the calculation while in the following section coherent pion photoproduction is discussed as a photon polarimeter which will test the analytic bremsstrahlung calculation of P.

5.2.2 Coherent π^0 Photoproduction as a Polarimeter

Pion photoproduction on the nucleon occurs when the photon couples to the electromagnetic current of a nucleon causing it to radiate a pion. The reaction can proceed via 4 channels:

$$\gamma + p \rightarrow p + \pi^0 \tag{5.8}$$

$$\gamma + n \rightarrow n + \pi^0 \tag{5.9}$$

$$\gamma + p \rightarrow n + \pi^+ \tag{5.10}$$

$$\gamma + n \rightarrow p + \pi^- \tag{5.11}$$

Pion photoproduction off nuclei takes place on individual nucleons embedded in the nuclear environment and has special theoretical interest incorporating three basic fields of research [6]: the elementary production mechanism on the nucleon,

the nuclear dynamics and pion-nucleus interaction. The nuclear process can occur coherently with the same initial and final nuclear state, $A(\gamma,\pi)A$, and incoherently when the final state differs, $A(\gamma,\pi)A^*$. Due to charge conservation only neutral pion production can occur coherently. This process occurs with equal probability on protons and neutrons [91] and as the initial and final nuclear states are equivalent the π^0 can be produced coherently from all A nucleons and the resulting differential cross section scales with A^2.

For spin-0 nuclei such as ^{12}C, parity and angular momentum conservation imply that coherent photoproduction must proceed exclusively via magnetic transitions [70]. In the energy range of the present experiment the pion is emitted as a p-wave following M1 excitation of the Δ resonance. Additionally for spin-saturated nuclei, all spin-dependent terms in the cross section cancel and the differential cross section in the π-nucleus centre-of-mass system reads:

$$\frac{d\sigma}{d\Omega} = \frac{1}{2}\frac{|\mathbf{q}|}{|\mathbf{k}|}A^2F^2_{\mathrm{coh}}(|\mathbf{t}|^2)|2M_{1+}+M_{1-}|^2\sin^2(\theta) \tag{5.12}$$

where $|2M_{1+}+M_{1-}|^2\sin^2(\theta)$ is the π^0 cross section which is independent of the nucleon spin orientation and $F(|\mathbf{t}|^2)$ denotes the nuclear matter form factor as a function of nuclear momentum transfer $\mathbf{t}=\mathbf{q}-\mathbf{k}$. The different shapes of the coherent $F_{\mathrm{coh}}(t)$ and incoherent form factors $F_{\mathrm{inc}}(t)$ can be exploited to separate coherent and incoherent (γ,π^0) contributions.

Coherent π^0 photoproduction with linearly polarised photons served as a photon polarimeter reaction for this experiment. As both the ^{12}C target and π^0 are spin zero and because the π^0 is pseudoscaler, there are only three vectors available: $\overrightarrow{\epsilon}, \overrightarrow{k}$ and $\overrightarrow{q}$ which correspond to the polarisation vector and momentum of the photon and the momentum of the pion respectively. There is only one way to form a pseudoscalar operator from these vectors is $\overrightarrow{\epsilon}.\overrightarrow{k}\times\overrightarrow{q}$ [92].

Therefore, when the polarisation vector is parallel to the reaction plane defined by the pion and photon $\overrightarrow{k}\times\overrightarrow{q}$, the transition matrix element is zero such that:

$$\frac{d\sigma_{\parallel}}{d\Omega} = 0 \tag{5.13}$$

and the asymmetry for linearly polarised photons is:

$$\Sigma = \frac{\frac{d\sigma_{\parallel}}{d\Omega} - \frac{d\sigma_{\perp}}{d\Omega}}{\frac{d\sigma_{\parallel}}{d\Omega} + \frac{d\sigma_{\perp}}{d\Omega}} = -1 \tag{5.14}$$

where $\frac{d\sigma_{\perp}}{d\Omega}$ is the differential cross section with the photon polarisation perpendicular to the reaction plane. Therefore, the azimuthal distribution $\frac{N(\phi)_{\parallel} - N(\phi)_{\perp}}{N(\phi)_{\parallel} + N(\phi)_{\perp}}$ of the π^0 for $^{12}C(\gamma,\pi^0)^{12}C$ events exhibits a $\cos(2\phi)$ distribution with a magnitude equal to the degree of photon polarisation.

5.2.3 Selection of Coherent Events

Several different processes contribute to neutral pion photoproduction. Coherent π^0 photoproduction competes with a background of incoherent processes (leaving the residual nucleus in a discrete excited state), quasifree processes (where a proton or a neutron is knocked out of the nucleus with the π^0) and double pion photoproduction. To extract the photon beam polarisation using $^{12}C(\gamma,\pi^0)^{12}C$, it is therefore essential to isolate the coherent yield from the non-coherent background. This can be achieved via a missing energy analysis which exploits the different threshold energies required for each background process and makes explicit use of the incident photon energy determined by the Tagger and the π^0 4-vector detected in the CB. Table 5.1 outlines the additional energy required for each non-coherent process in carbon.

Process	Extra Energy Required [MeV]
Nuclear Excitation	4.4, 15.0,...
Proton Knockout	16.0
Neutron Knockout	12.5
Double π^0 production	134.98

Table 5.1: Extra energy required (in MeV) for non-coherent processes in carbon.

The pion missing energy ΔE_{π} is defined:

$$\Delta E_{\pi} = E_{\pi}^{cm}(E_{\gamma}) - E_{\pi}^{cm}(\gamma_1\gamma_2) \tag{5.15}$$

where $E_\pi^{cm}(E_\gamma)$ is the energy of the π^0 in the pion-nucleus centre-of-mass frame. Using the incident photon energy and assumming a coherent process:

$$E_\pi^{cm}(E_\gamma) = \frac{s + m_\pi^2 - M^2}{2\sqrt{s}} \tag{5.16}$$

where E_γ is the incident photon energy, m_π the pion mass, M the mass of the nucleus and s the invariant mass of the photon and the target nucleus.

$E_\pi^{cm}(\gamma_1\gamma_2)$ is the detected π^0 energy, Lorentz transformed to the pion-nucleus centre-of-mass frame. The energy of the pion in the lab frame, E_π can be accessed most simply from:

$$E_\pi = E_1 + E_2 \tag{5.17}$$

where E_1 and E_2 are the detected energies of photon 1 and 2 respectively. This method does not use all the information from the detector system and one can achieve better energy resolution if the available angular information is also used [93]. The energy of the π^0 can instead be defined:

$$E_\pi = \sqrt{\frac{2m_\pi^2}{(1 - X^2)(1 - \cos\psi)}} \tag{5.18}$$

where ψ is the opening angle between the two decay photons, m_π the pion mass and X is an energy sharing parameter, defined:

$$X = \frac{E_1 - E_2}{E_1 + E_2} \tag{5.19}$$

The Lorentz transformation of E_π into the pion-nucleus centre-of-mass frame is given by:

$$E_\pi^{cm}(\gamma_1\gamma_2) = \gamma(E_\pi - \beta(E_1\cos\theta_1 + E_2\cos\theta_2)) \tag{5.20}$$

where θ_1 and θ_2 are the polar angles of the decay photons, E_π the pion energy in the lab frame and β is known from the incident photon energy and the mass of the recoiling nucleus:

$$\beta = \frac{E_\gamma}{E_\gamma + M} \tag{5.21}$$

A detailed derivation of equations 5.15 to 5.21 is provided in Appendix B.

For coherent π^0 photoproduction, the detected pion energy, $E_\pi^{cm}(\gamma_1\gamma_2)$ equals the calculated energy, $E_\pi^{cm}(E_\gamma)$, and ΔE_π=0 MeV. The competing incoherent and

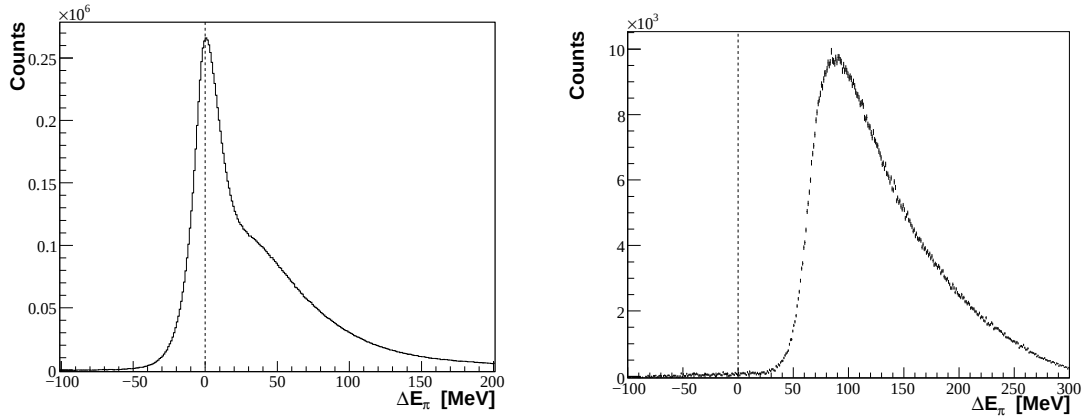

(a) (b)

Figure 5.4: (a) Pion missing energy ΔE_π for ^{12}C data. (b) Pion missing energy for quasifree π^0 photoproduction on ^{12}C.

quasifree processes require additional energy either to eject a nucleon from the nucleus or to leave the recoiling nucleus in a discrete excited state. Thus, less energy is available to the π^0 and ΔE_π for non-coherent background processes shifts towards larger missing energies.

The only events selected were those with two photon clusters detected in the Crystal Ball which reconstruct to a π^0 (section 4.3) with an additional constraint that there were no hits in the PID detector. Figure 5.4(a) shows the pion missing energy integrated over all pion angles for E_γ=135-500 MeV. There is a clear peak centred on $\Delta E_\pi = 0$ MeV due to coherent photoproduction. However, the coherent peak sits on a substantial background which reduces the measured magnitude of Σ and as a consequence P. Therefore, further event selection was required to minimise the ratio of incoherent to coherent events.

Figure 5.4(b) shows the equivalent missing energy spectrum for quasifree events where a proton is detected in coincidence with a π^0. There is a threshold in the missing energy spectrum and the quasifree contribution under the coherent peak can be separated by applying a tight cut on ΔE_π far below the threshold for quasifree events.

Given the small energy gap of 4.4 MeV between the first excited state and the ground state of ^{12}C, it is more difficult to cleanly separate coherent and incoherent

events, particularly at higher photon energies where the absolute resolution of the detector worsens [74]. However, one can use the known features of the coherent and incoherent cross sections to minimise the ratio of incoherent to coherent processes. $F_{\mathrm{coh}}(t)$ peaks at t=0 whereas the peak in $F_{\mathrm{inc}}(t)$ is shifted to higher t. For a given photon energy, the nuclear momentum transfer t increases as θ_π increases and there is often a region at low θ_π where the coherent cross section is much larger than the incoherent cross section, which vary much more slowly with pion emission angle [94, 95]. By placing constraints on θ_π it is possible to select regions where the coherent process dominates.

Figure 5.5 plots pion missing energy for different regions of π^0 emission angles: $\theta_\pi = 0-45°$, $45-90°$, $90-135°$ and $135-180°$. The relative incoherent to coherent contributions evident in figure 5.4 are substantially reduced when a cut is applied to the most forward focused pions, $\theta_\pi = 0-45°$. This ratio increases with larger emission angles, with the incoherent processes dominating at backwards angles.

The asymmetry of the azimuthal distribution of the π^0, $P\Sigma = \frac{N(\phi_\parallel)-N(\phi_\perp)}{N(\phi_\parallel)+N(\phi_\perp)}$ as a function of θ_π gives an indication of where the incoherent background under the coherent peak becomes non-negligible. Figure 5.6 plots this variation in $P\Sigma$, for ΔE_π <0 MeV and E_γ=200-300 MeV. The magnitude of $P\Sigma$ is largest and remains relatively stable at the most forward angles, $\theta_\pi = 10-50°$. For $\theta_\pi > 50°$ there is clear dilution in the asymmetry due to the increased strength of the incoherent background under the coherent peak. The largest dilution comes at backwards angles. With the absence of a forward detector (TAPS) in the data stream, difficulties were found in constructing clean π^0 invariant masses at the most forward angles, $\theta_\pi < 10°$ which causes dilution in $P\Sigma$ in this region. A cut of $\theta_\pi = 10-50°$ was applied to the data to minimise dilution due to incoherent processes. A tighter cut $\theta_\pi = 20-40°$, selecting the region of figure 5.6 with the absolute maximum magnitude of PΣ, was also investigated. This cut introduced no systematic offset in the magnitude of PΣ against photon energy compared to $\theta_\pi = 10-50°$ and the initial cut was retained to maximise the statistical accuracy of the measurement.

Further minimisation of the relative ratio of incoherent to coherent events was achieved by constraining the allowed ΔE_π for a 'coherent' event. The azimuthal

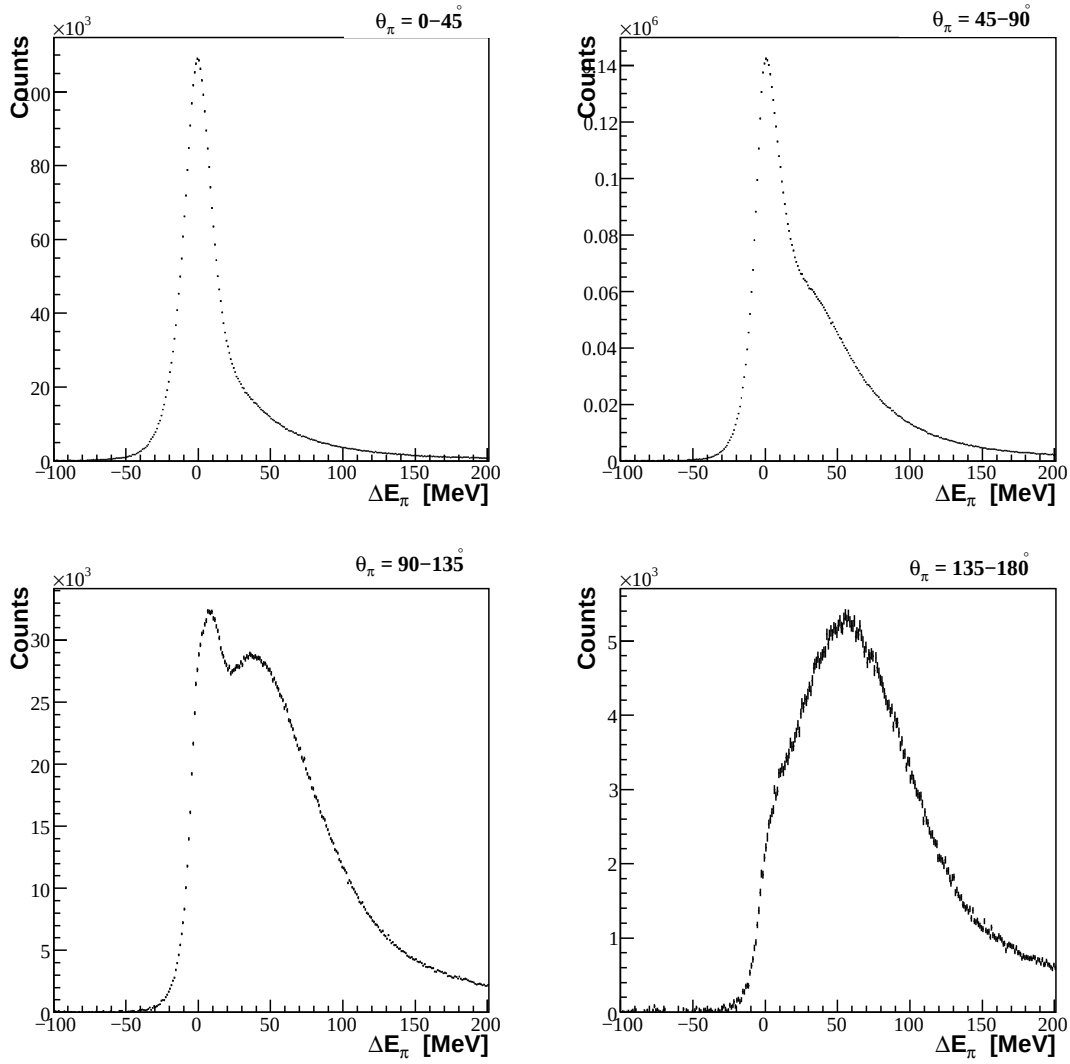

Figure 5.5: Pion missing energy spectra for the four polar angle regions, θ_π, indicated in the figure.

asymmetry of the π^0 against ΔE_π is plotted in figure 5.7 for $\theta_\pi = 10° - 50°$. An additional constraint, $\Delta E_\pi \leq 0\,\text{MeV}$ was applied to the data and any event which met the aforementioned conditions was accepted as a coherently emitted π^0. A tighter cut of $\Delta E_\pi \leq$ -15 MeV was also investigated. This had little appreciable effect on the magnitude of $P\Sigma$ other than reducing the statistical accuracy of the measurement. Figure 5.7(b) applies an identical analysis for E_γ=300-450 MeV. For higher E_γ, no dominant coherent region is evident and $P\Sigma$ decreases quickly with ΔE_π. With increasing photon energy, the resolution of ΔE_π decreases [94] and there is a significant increase in the ratio of incoherent to coherent contributions. It is

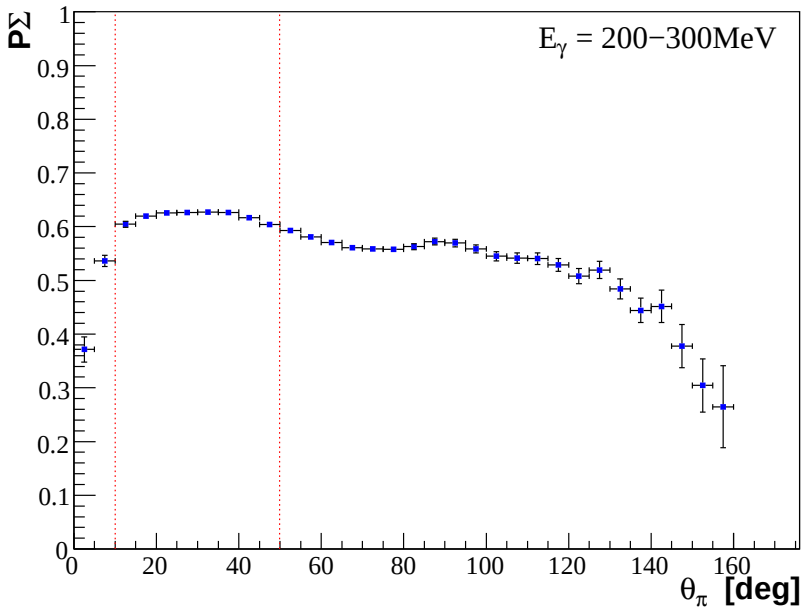

Figure 5.6: $P\Sigma$ against θ_π for $\Delta E_\pi \leq 0\,\text{MeV}$. The dilution in $P\Sigma$ around 50° indicates the increasing strength of non-coherent processes. Dashed red lines indicate the cuts applied to the data $\theta_\pi = 10° - 50°$.

therefore more difficult to separate coherent contributions. As a consequence, there is likely to be considerable dilution in the measured photon polarisation when using $^{12}C(\gamma,\pi^0)^{12}C$ as a polarimeter at higher photon energies.

5.3 Analytic Calculation of Photon Polarisation

In this section the prescription outlined in section 5.2.1 is used to calculate the photon polarisation for the two beamtimes when $^{12}C(\gamma, pp)$ data was taken. The coherent peak setting for the March beamtime covered a photon energy range E_γ=200-300 MeV and E_γ=300-450 MeV in August.

5.3.1 March Beamtime

Figure 5.8(a) plots the variation in the position of the coherent edge of the 022 peak for the March data set. The edge, defined as the part of the sharp slope of the peak with the largest negative gradient, was determined by fitting a polynomial in the

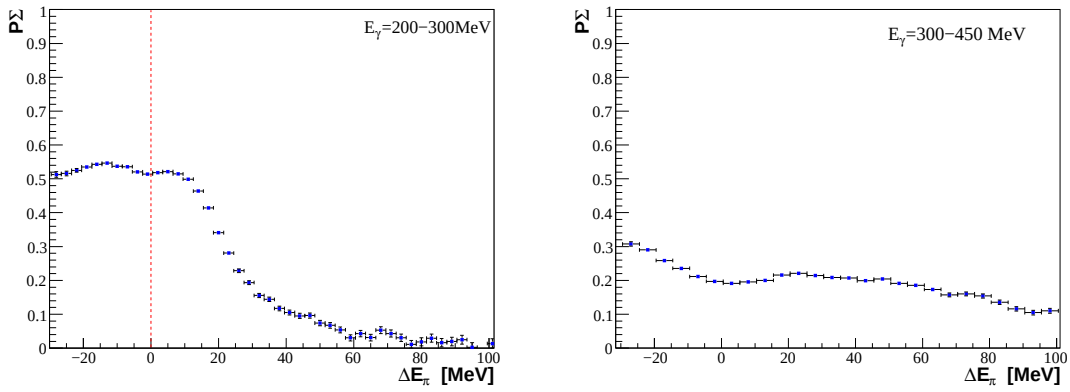

(a) (b)

Figure 5.7: $P\Sigma$ against ΔE_π for $\theta_\pi = 10 - 50°$ and (a) E_γ=200-300 MeV and (b) E_γ=300-450 MeV.

region of the channel with the largest enhancement and finding the point of the fit with the steepest slope. This process was automated and a fit was made to each Tagger scaler enhancement and the coherent edge (in channel and photon energy) was recorded throughout the beamtime. The coherent edge showed significant instability during data collection with the peak constantly shifting. This is emphasised in figure 5.8(b) which plots the edge energy distribution during data collection. The instability results in considerable smearing of the photon polarisation.

Using Tagger scaler distributions is ideal for monitoring the coherent peak during experimental running as the high counting rates involved allow reliable enhancement spectra to be formed on a regular basis. However, scaler counts only give information on the bremsstrahlung distribution pre-collimation before much of the incoherent background is removed. The degree of polarisation is larger at the target and a collimated enhancement from which the polarisation is deduced, is greater than that obtained from Tagger scalers. An enhancement based on TDC hits, which make an experimental trigger and thus survive beam collimation, was obtained by taking random background subtracted TDC spectra for both polarised and unpolarised photons, and dividing the amorphous distribution from the polarised data set. Figure 5.8(c) compares the enhancement spectrum pre- and post-collimation, extracted from data where the edge remains stable (indicated by the dashed red lines of figure

5.8(a)). The plot emphasises the benefits of beam collimation for increasing the degree of polarisation as the magnitude of the enhancement is a factor of ∼2 larger after collimation. Figure 5.8(d) plots TDC enhancement against photon energy for each edge energy, determined from the automated fit to the scaler edge in 5.8(c). There is a clear correlation between the derived edge energy (from the fit) and that seen in the TDC enhancement. This gives confidence that the automated fit is a reliable tool for tracking the edge position during data collection.

Figure 5.9 plots the experimental enhancement for each edge energy recorded during data collection (taken from x-projections of figure 5.8(d)). The parameters of *anb* were adjusted to provide a reasonable agreement with experiment. To test whether the instability of the coherent peak was related to θ_g, the effective small angle between the electron beam and the $02\bar{2}$ lattice vector which defines the coherent edge energy, only θ_g was adjusted in the calculation. Varying θ_g was successful in predicting the general trend of the enhancement, with the magnitude of E (and also P) increasing as the coherent edge shifts to lower fractional energies ($x = \frac{E_\gamma}{E_{beam}}$). However, the overall shape of the enhancement was not well described and modification of beam divergence and collimation geometry were also required to achieve better agreement between calculation and experiment. The calculated photon polarisation for each enhancement fit are shown in the bottom half of figure 5.9.

Although the calculation fails to accurately reproduce the measured enhancement, giving unreliable photon polarisations where calculation and experiment disagree, figure 5.9 serves to model the variation in photon polarisation under the first coherent peak. It also stresses the importance of the coherent edge energy in defining the upper limit of $\Phi(x)$ in equation 5.7. Figure 5.9 clearly shows the upper limit of the polarisation decreases when the coherent edge shifts to higher photon energies. The substantial smearing of the coherent peak evident here makes extraction of a reliable photon polarisation extremely difficult. One method to extract the mean polarisation over the data set involves accurately fitting each enhancement from figure 5.9 and applying a weighted sum of the calculated polarisations using the frequency distribution of 5.8(b). However, a considerable systematic uncertainty in polarisation is likely to entail using this method. A more elegant solution is offered

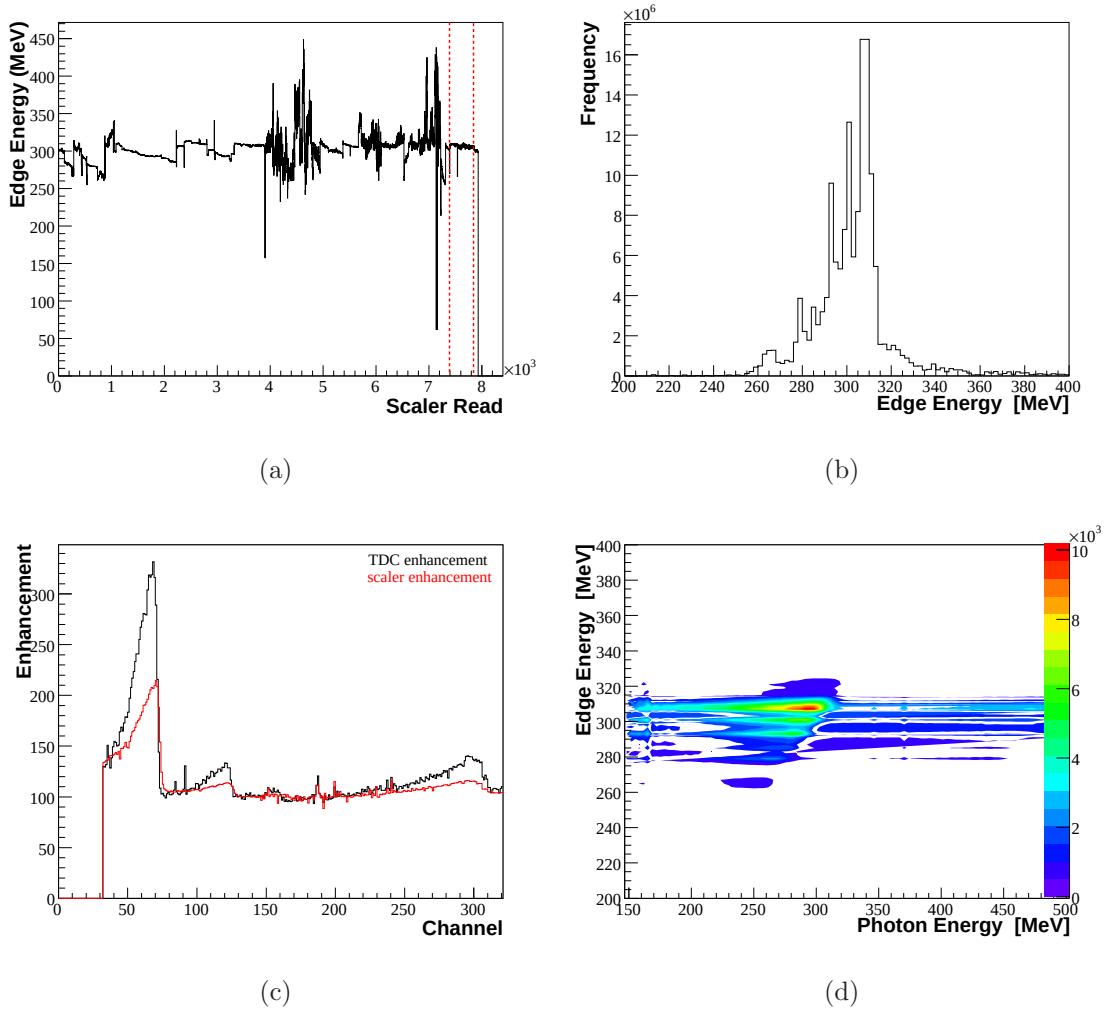

Figure 5.8: (a) Position of fitted edge position as a function of the number of the scaler buffer read. The dashed red lines indicates a region of stability in edge position. (b) Frequency plot of edge position highlighting the energy spread of the edge position. (c) Comparison of the enhancements obtained from scalers (red) and TDC hits (black) showing the increase in enhancement due to collimation. (d) 3D histogram plotting TDC enhancement (z-axis) against photon energy (x-axis) for each edge position calculated from the fit to the scaler enhancement (y-axis).

through the $^{12}C(\overrightarrow{\gamma},\pi^0)$ reaction.

The coherent peak and hence the polarisation remains stable in the region indicated by the red vertical lines in figure 5.8(a). This is an ideal region to compare the calculated polarisation with the measured pion asymmetry, providing a test of how reliable the $^{12}C(\overrightarrow{\gamma},\pi^0)$ measurement is for determining the average polarisa-

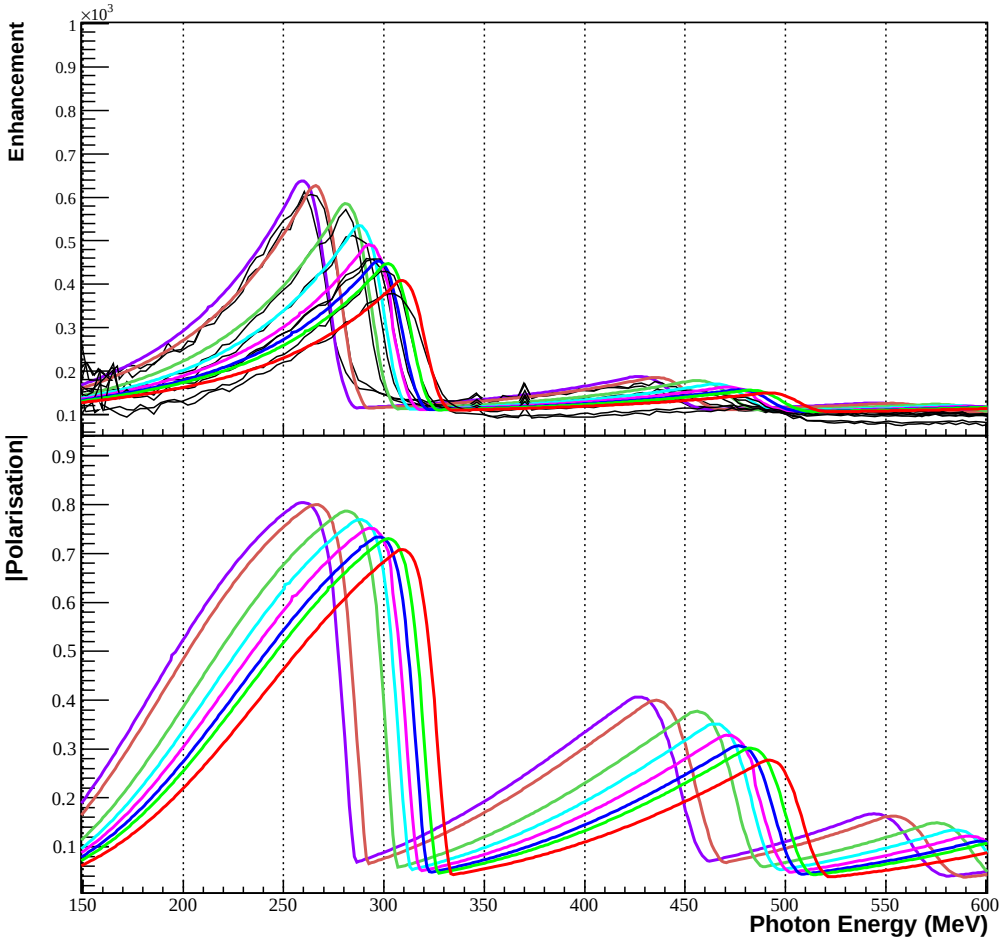

Figure 5.9: Enhancement spectra obtained from x-projections of figure 5.8(d). The measured enhancements were compared to *anb* calculations and the resultant photon polarisation calculations are shown in the lower half of the diagram.

tion over the data set. Figure 5.10 plots the experimental enhancement obtained for (a) *perp* and (b) *para* in this region. For *perp*, a calculated enhancement which agrees reasonably well with the data is overlaid. However for *para*, despite the stability in the coherent edge, the calculation struggles to describe the tail region of the experimental enhancement. However, the stable coherent edge position for both orientations suggests the electron beam was particularly stable for this data subset and the effects noted for *para* are most likely due to some process occurring in the diamond. Crucially, as the parameters of *anb* have been tuned to give a good description of the edge, a reliable definition of $\Phi(x)$, the upper limit of the polarisation,

is obtained. In the tail region, the calculated polarisation is deduced from I^i/I^c. If the enhancement and data disagree by a small amount in this region, the effective change in polarisation is fairly small, if the coherent edge is well approximated. The polarisation calculated from the generated enhancement is shown by the red curve in figure 5.10(c) *perp* and (d) *para*.

Despite the approximate agreement between calculation and experiment for *perp* there are some systematic differences across the coherent peak particularly about the peak where *anb* overestimates the enhancement. The deviations between calculation and data worsens for *para*. Clearly if the enhancement is smaller than the calculation predicts, the calculated polarisation should be modified on the basis of that. A correction can be derived based on the difference between measured and calculated enhancement [96]. In the data, the enhancement is $E = I_{\text{meas}}/I_{\text{amorphous}} = (I^i + I^c)/I_{\text{amorphous}}$ where the assumption is made that the incoherent contribution is well approximated by an amorphous radiator. Substituting $\frac{I^i}{I^c}$ in terms of E in equation 5.6 gives:

$$P_g = -\Phi(x)(1 - 1/E) \tag{5.22}$$

and differentiating with respect to E gives:

$$\frac{\delta P_g}{\delta E} = -\Phi(x)/E^2 \tag{5.23}$$

For a small change, ΔE in E the corresponding fractional change in P_g is given by:

$$\frac{\Delta P_g}{P_g} = \frac{1}{E-1}\frac{\Delta E}{E} \tag{5.24}$$

Hence if the calculated enhancement underpredicts the data by some small amount ΔE a correction based on equation 5.24 was applied to the calculated polarisation. The corrected polarisation for *perp* is illustrated by the blue data points in figure 5.10(c). The equivalent polarisation for *para* is shown by the black data points in figure 5.10(d). The systematic uncertainty in the modified polarisation for *para* is larger than for *perp* as *anb* gives a rather poor description of the *para* enhancement and the discrepancy between calculation and experiment is relatively large.

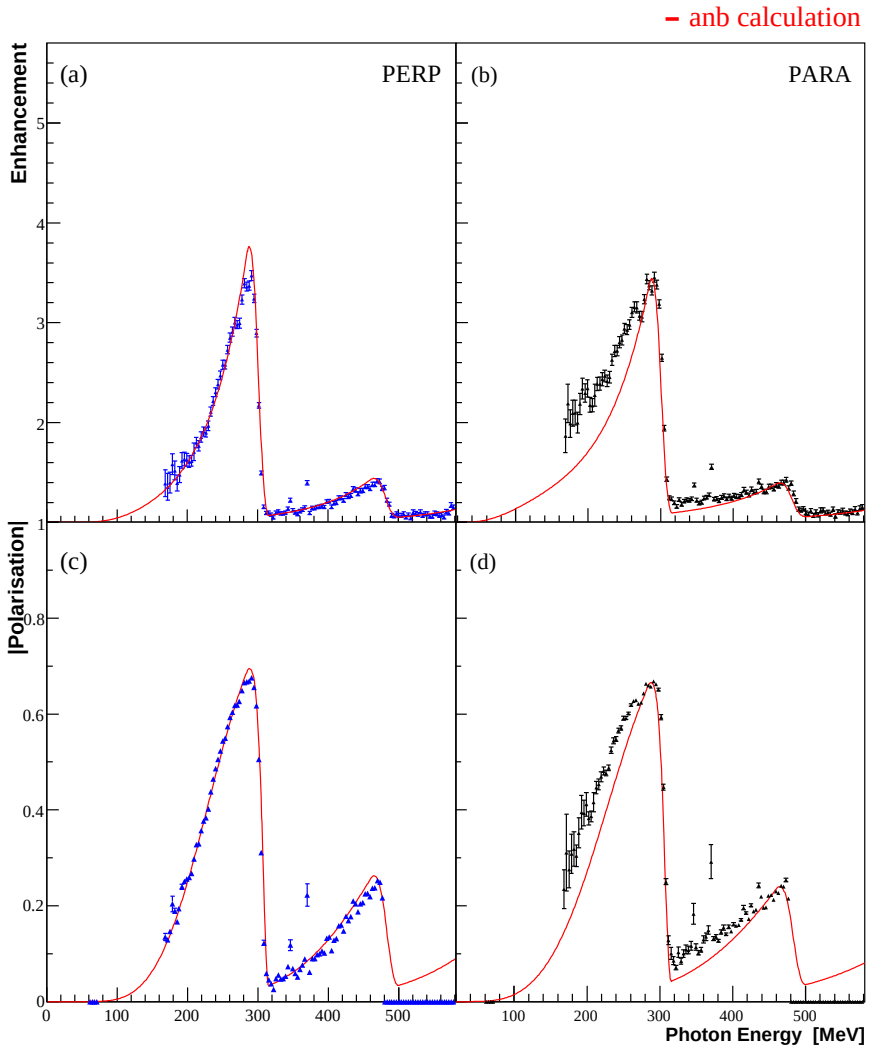

Figure 5.10: (a) Enhancement spectrum for *perp* data together with the *anb* calculation (red line). (b) As (a) for *perp* and the corresponding *anb* calculation. (c) Calculated *anb* polarisation values (red line) for *perp* setting. The data points are adjusted polarisation values obtained from equation 5.24 which account for deviations of the enhancement data from the *anb* calculation shown in (a). (d) Calculated *anb* polarisation values adjusted for *para* setting and adjusted values obtained from equation 5.24.

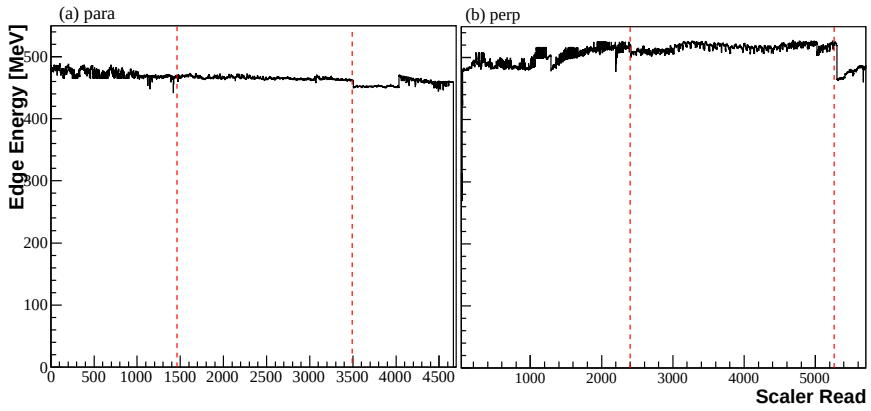

Figure 5.11: Coherent edge energy for (a) para and (b) perp orientations for each scaler read.

5.3.2 August Beamtime

Figure 5.11 shows the variation the coherent edge for the higher energy coherent peak taken in August 2008. The edge position remains relatively stable throughout the beamtime which is far more typical of previous polarised photon experiments carried out in A2. The edge energy of the *perp* orientation is systematically larger than *para* throughout the data set.

Enhancement spectra were constructed for *para* and *perp* for data where the edge remains most stable, shown by the red dashed cuts in figure 5.11. The enhancements are plotted in figure 5.12(a) with the calculated polarisation in figure 5.12(b). The calculation struggles to describe the coherent edge for both *para* and *perp*, meaning $\Phi(x)$ is poorly defined. As a consequence, the calculated polarisation is less trustworthy than figure 5.10. The enhancement spectra for both diamond settings, exhibits considerable smearing, which is most evident at the coherent edge and *anb* fails to calculate an enhancement which describes either orientation. The coherent edge remains relatively stable throughout the beamtime and the observed smearing in the edge is unlikely to arise from small changes in θ_g. This is supported by enhancement spectra derived from Tagger scalers which are read into the data stream every 2 minutes that also exhibit similar smearing around the edge.

Some of the physical quantities required as input for the calculation such as beam

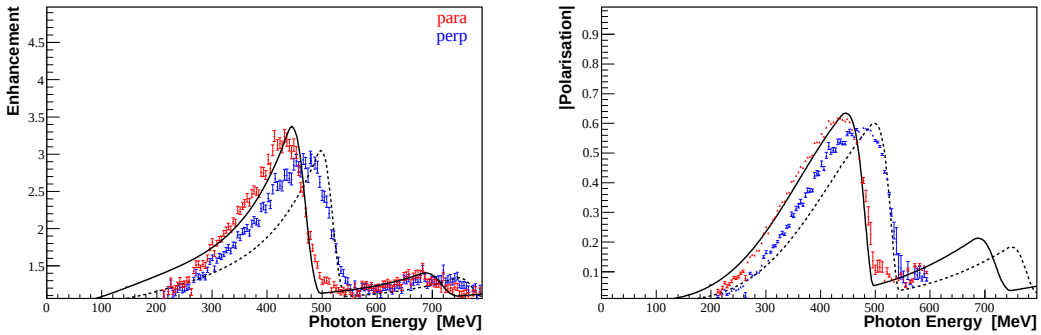

(a) (b)

Figure 5.12: (a) Enhancement spectrum for *para* data (red points) together with *anb* calculation (solid line). The blue points and dashed line corresponds to the experimental enhancement and calculation for *perp*. (b) The solid and dashed lines are the calculated polarisation derived from the corresponding line in (a). The polarisation values adjusted by equation 5.24 are shown for *para* (red) and *perp* (blue).

spot size and beam divergence tend to be poorly defined or unknown. The calculation must attempt to model the collimation and angular spread of the bremsstrahlung photons and several approximations are made in order to predict the experimental enhancement and thus photon polarisation. The following section attempts to quantify these parameters by fitting the enhancement spectrum, using coherent bremsstrahlung theory to guide the fit [96].

5.3.3 A Fittable Function

In the following, fractional energies $x = \frac{E_\gamma}{E_0}$ are used and only the reciprocal lattice vectors $g = 02\overline{2}$, $04\overline{4}$,...,$0G\overline{G}$ with discontinuities x_2^d, x_4^d,..., x_G^d are included. In principle, the area under the main coherent peak generally has three contributors; one from the $02\overline{2}$ vector, one from the $04\overline{4}$ vector which may be zero depending on how tightly the beam is collimated and incoherent contributions from the crystal.

The coherent contribution from each vector, and the corresponding polarisation,

are well determined analytically, and for $x < x_g^d$ has the following form [63]:

$$I_g(x, x_g^d) = C_g(x, x_g^d) \times I_g^0 \chi_g(x, x_g^d) \quad (5.25)$$

$$P_g(x) = -\phi_g(x) / \left[1 + \frac{I_i(x)}{I_g(x, x_g^d)}\right] \quad (5.26)$$

where $\phi_g(x)$ is defined by equation 5.7, I_g^0 is a constant for lattice vector g which determines the amplitude of $I_g(x, x_g^d)$, $I_i(x)$ is the incoherent contributions and $\chi_g(x)$ is defined in terms of Q_g as follows:

$$\chi_g(x, x_g^d) = xQ_g^2/(1-x)\Big[1 + (1-x)^2 - \frac{4Q_g^2 x^2}{1-x}\Big(\frac{1-x}{Q_g x} - 1\Big)\Big] \quad (5.27)$$

For each lattice vector g, the upper cutoff x_g^d is related to the edge of the momentum pancake. There is also a lower cut off x_g^c which is related to the photon beam collimation, $x_g^c = x_g^d/[1 + \theta_r^2(1 - x_g^d)]$ where θ_r^2 is the relative angle which can be worked out approximately from the beam energy and collimation:

$$\theta_r = E_0(\text{MeV}) \times 0.001 \times \frac{C_{\text{diam}}}{C_{\text{distance}}} \quad (5.28)$$

where C_{diam} and C_{distance} are the collimator radius and the distance from radiator respectively. The cumulative distribution function $C_g(x, x_g^d)$ discussed in [96] describes this lower cut off and also accounts for the smearing of the 2D beam spot across the collimator. The total coherent contribution for the vectors g=02$\overline{2}$,04$\overline{4}$,...,0$G\overline{G}$ can be expressed:

$$I_{\text{coh}}(x) = \sum_{g=2,4,..}^{G} I_g(x, x_g^d) \quad (5.29)$$

This function generates distributions that are different from the observed data because the discontinuities x_g^d are too sharp. In reality, the discontinuity is smeared due to the spread in θ_g, the angle between the beam and the crystal lattice. When restricted to g=02$\overline{2}$, 04$\overline{4}$, ..., 0$G\overline{G}$ the angular dependence of θ_g is:

$$\theta_g = \frac{k}{gE_0[\frac{1}{x_g^d} - 1]} \quad (5.30)$$

where $k = m_e a/4\sqrt{2\pi}$=26.5601 MeV and the diamond lattice constant a = 923.7 (dimensionless units). Rearranging to express the discontinuities x_g^d in terms of θ_g:

$$x_g^d = \frac{1}{\frac{k}{gE_0\theta_g} + 1} \quad (5.31)$$

This allows us to substitute for x_g^d in equation 5.27 and equation 5.29 becomes a function of x,G and θ_g:

$$I_{\rm coh}(x, G, \theta_g) = \sum_{g=2,4,..}^{G} I_g(x, x_g^d, \theta_g) \tag{5.32}$$

The total $\Phi_{tot}(x)$ function, representing the upper limit of the polarisation, is given by the mean of the individual $\Phi_g(x, x_g^d)$ contributions weighted by their respective strengths:

$$\Phi_{tot}(x, G, \theta_g) = \frac{\sum_{g=2,4,..}^{G} [\Phi_g(x, g, \theta_g) \times I_g(x, g, \theta_g)]}{\sum_{g=2,4,..}^{G} I_g(x, g, \theta_g)} \tag{5.33}$$

The total coherent intensity $I^s_{\rm coh}(x, G, \theta_g)$ and $\phi^s_{\rm tot}(x, G, \theta_g)$ can now be smeared over a range of θ_g to closer represent reality. A Gaussian in θ_g was used to describe the smearing and integrating over $\theta_g \pm 3\sigma$ gives:

$$I^s_{\rm coh}(x, G, \theta_g) = \frac{\int_{\theta_g-3\sigma}^{\theta_g+3\sigma} \left\{ e^{\frac{(\theta'_g-\theta_g)^2}{2\sigma^2}} I_{\rm coh}(x,G,\theta'_g) \right\} d\theta'_g}{\int_{\theta_g-3\sigma}^{\theta_g+3\sigma} e^{\frac{(\theta'_g-\theta_g)^2}{2\sigma^2}} d\theta'_g} \tag{5.34}$$

$$\Phi^s_{\rm tot}(x, G, \theta_g) = \frac{\int_{\theta_g-3\sigma}^{\theta_g+3\sigma} \left\{ e^{\frac{(\theta'_g-\theta_g)^2}{2\sigma^2}} \Phi_{\rm tot}(x,G,\theta'_g) \right\} d\theta'_g}{\int_{\theta_g-3\sigma}^{\theta_g+3\sigma} e^{\frac{(\theta'_g-\theta_g)^2}{2\sigma^2}} d\theta'_g} \tag{5.35}$$

The total intensity spectrum from a diamond radiator also includes incoherent contributions from the crystal:

$$I_{\rm total}(x, \theta_g) = I_{\rm i}(x) + I_{\rm coh}(x, \theta_g) \tag{5.36}$$

The data can be represented as an enhancement spectrum by dividing $I_{\rm total}(x, \theta_g)$ by the incoherent spectrum obtained from an amorphous radiator $I_{\rm amo}(x)$ and is normalised to have an intensity of $\sim$1 as a baseline. Hence anything above 1 is the enhancement of coherent over incoherent contributions to the spectrum. Assumming the incoherent contribution $I_{\rm inc}$ has the same shape as the incoherent spectrum from an amorphous radiator, the enhancement and the polarisation based on this

enhancement is reduced to:

$$E^s_{\rm tot}(x, G, \theta_g) = \frac{[I_{\rm inc} + I^s_{\rm coh}(x, G, \theta_g)]}{I_{\rm inc}} \tag{5.37}$$

$$P_g = -\Phi^s_{\rm tot}(x, G, \theta_g) \left[1 - \frac{1}{E^s_{\rm tot}(x, G, \theta_g)}\right] \tag{5.38}$$

Equation 5.37 can be used to generate and fit an enhancement spectrum with equation 5.38 calculating the corresponding polarisation as a function of x. The parameters which determine the form of $E^s_{\rm tot}(x, G, \theta_g)$ distribution are:

- θ_g - Angle between the beam and crystal planes defined by the 022 vector
- σ - Gaussian smearing of θ_g to account for beam divergence, movement of the incident electron beam and multiple scattering
- θ_r - Relative angle of collimation
- σ_r - Smearing factor for collimation around θ_r via cumulative distribution function $C_g(x, g, \theta_g)$
- E^0_2,E^0_4,...,E^0_G - Enhancements of the discrete peaks

Figure 5.13 uses the prescription outlined above to fit the experimental enhancement for (a) *para* and (b) *perp*. The fit gives a good description of both the coherent edge and tail region of the enhancements. The lower half of each plot shows the polarisation derived from the fit using equation 5.38 and also the modified polarisation corrected for the difference between the data and calculated enhancement using equation 5.24. For *perp*, where the fit does not do so well in describing the data (E_γ=420-480 MeV), the effective change in photon polarisation is small, <2%.

5.4 Comparison of Calculated and Measured Polarisation

The mean polarisation $\bar{P}$ for the first coherent peak was extracted from the asymmetry of the ϕ-distributions obtained for *para* and *perp* after applying the data cuts

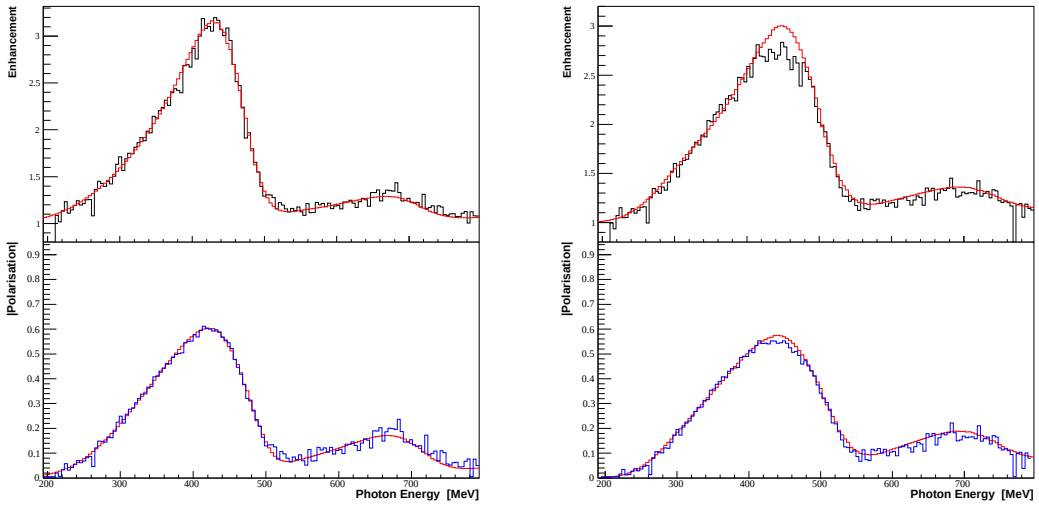

(a) para (b) perp

Figure 5.13: Fit to experimental enhancements and the calculated polarisation for (a) *para* and (b) *perp* for the August data set. The upper plot shows the experimental enhancement (black) and the fit to the distribution. The lower half plots the photon polarisation from the fit (red) with adjustments due to discrepancies between the fit and data (blue) using equation 5.24.

specified in section 5.2.3. Assuming clean selection of coherent events $\Sigma = -1$, fitting equation 5.4 to the asymmetry reveals $|\bar{P}|$ from the fit parameter $C = \bar{P}\Sigma$. One can then extract the photon energy dependence of $\bar{P}$ by plotting the π^0 azimuthal distribution against photon energy (figure 5.14). The energy dependence of $\bar{P}$ was extracted, by projecting ϕ distributions for each Tagger channel and forming the asymmetry of the orthogonal data sets. Figure 5.18 plots this energy dependence for the full March data set.

A comparison was made between calculated and measured photon polarisation, testing the validity of the $^{12}C(\overrightarrow{\gamma}, \pi^0)$ extraction of polarisation. Any dilution in the $^{12}C(\overrightarrow{\gamma}, \pi^0)$ sample will reduce the observed asymmetry and the pion measurement therefore sets a lower limit on $\bar{P}$. The mean polarisation from the calculation $\bar{P}^c$ is the weighted sum of $P^c_{\parallel}$ and $P^c_{\perp}$:

$$\bar{P}^c = \frac{N_{\parallel}}{N_{\parallel} + N_{\perp}} P^c_{\parallel} + \frac{N_{\perp}}{N_{\parallel} + N_{\perp}} P^c_{\perp} \tag{5.39}$$

where $N_{\parallel}$ and $N_{\perp}$ are the photon fluxes for *para* and *perp* respectively. The photon

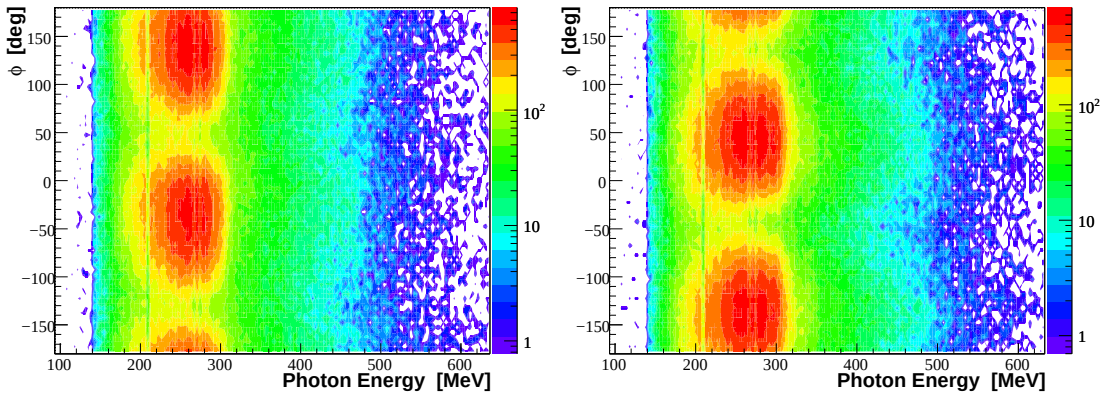

(a) (b)

Figure 5.14: Azimuthal distribution of π^0s against photon energy for (a) *para* and (b) *perp*.

flux is not well determined and instead the relative ratio $N_{\parallel}/N_{\perp}$ is used to construct the weighted sum. This ratio is extracted from the $\cos(2\phi)$ fits with the functional form of equation 5.5. Substituting $x = N_{\parallel}/N_{\perp}$ into equation 5.39 gives:

$$\bar{P}^c = \frac{x}{x+1}P^c_{\parallel} + \frac{1}{x+1}P^c_{\perp} \tag{5.40}$$

Figure 5.15 plots this ratio against photon energy for the region with edge stability indicated in figure 5.8(a). The polarisation $\bar{P}^c$ calculated from *anb* and adjusted according to equation 5.24, is compared with the $^{12}C(\overrightarrow{\gamma}, \pi^0)$ measurement. This is shown in figure 5.16(a), with the difference between the measurements is plotted in figure 5.16(b). There is excellent agreement between the two methods for photon energies up to E_γ ~310 MeV. The difference between $\bar{P}^c$ and P_π is consistent with zero over the photon energy range sampled. Therefore, the polarisation based on P_π can be trusted to give a measure of the average photon polarisation for the March data set covering E_γ=200-310 MeV.

A similar comparison was made for the higher energy photon range, E_γ=300-450 MeV. The polarisation calculated from fits to the experimental enhancement is compared to the pion measurement in figure 5.17(a) and figure 5.17(b) plots the difference between the methods. On average, the polarisation measured using the $^{12}C(\gamma, \pi^0)$ reaction as a polarimeter underpredicts the calculation. This is largely due to difficulties in cleanly separating coherent and incoherent (γ, π^0) contributions

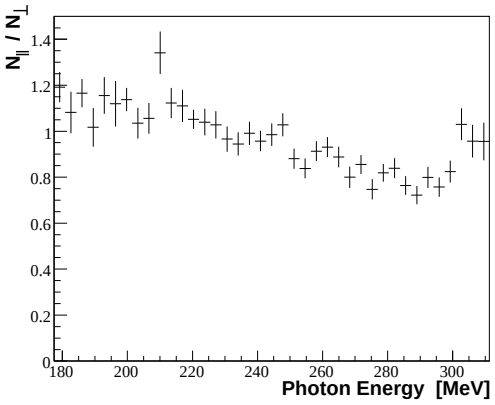

Figure 5.15: The ratio of photon fluxes $N_{\parallel}/N_{\perp}$ as a function of photon energy in the range E_{γ} = 180-320 MeV. Each point on the plot corresponds to a single Tagger channel.

at higher photon energies.

The polarisation obtained using the $^{12}C(\gamma,\pi^0)$ reaction is used for the $^{12}C(\gamma$,pp) analysis. For E_{γ}=200-310 MeV, the average systematic uncertainty was estimated by fitting a straight line to the difference plot in figure 5.16(b). This gives a near horizontal line with a y-offset of ∼0.8%. However, the difference between calculated and measured polarisation varies by $\pm \sim 3\%$ either side of $P_{\rm diff} = 0$, and we take this value as a conservative estimate of the absolute systematic uncertainty in P. For the higher energy setting, the dilution factor due to the background in the $^{12}C(\gamma,\pi^0)$ signal is unknown and we compare with the coherent bremsstrahlung calculation to get a handle on the systematic uncertainty. Here, the reasons for the spread of the coherent peak are not well understood. Nevertheless, the bremsstrahlung calculation gives a polarisation which is consistently larger than or equal to the π^0 measurement which would be expected. The largest discrepancy is 10% and on this basis it is prudent to allocate an absolute systematic uncertainty of 10% to the polarisation for E_{γ} >350 MeV.

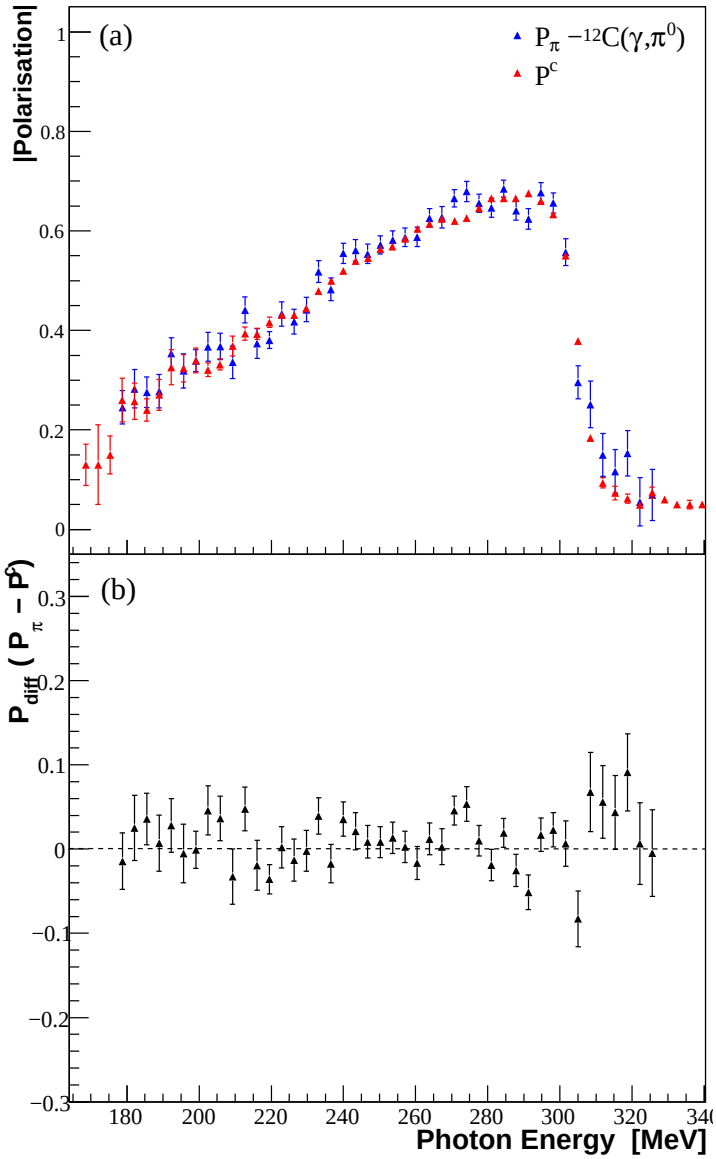

Figure 5.16: (a) Comparison of calculated polarisation P^c using *anb* (red points) and measured polarisation P_π using coherent pion photoproduction (blue points) for E_γ=200-310 MeV. (b) The difference between P_π and P^c.

5.5 Summary

Figure 5.18 plots the average photon polarisation for (a) March and (b) August taken from P_π. The average polarisation, derived from the $^{12}C(\overrightarrow{\gamma},\pi^0)$ analysis, shows considerable smearing compared to figure 5.16(a), highlighting the instability in the coherent edge energy during the beamtime. The measurement accounts for

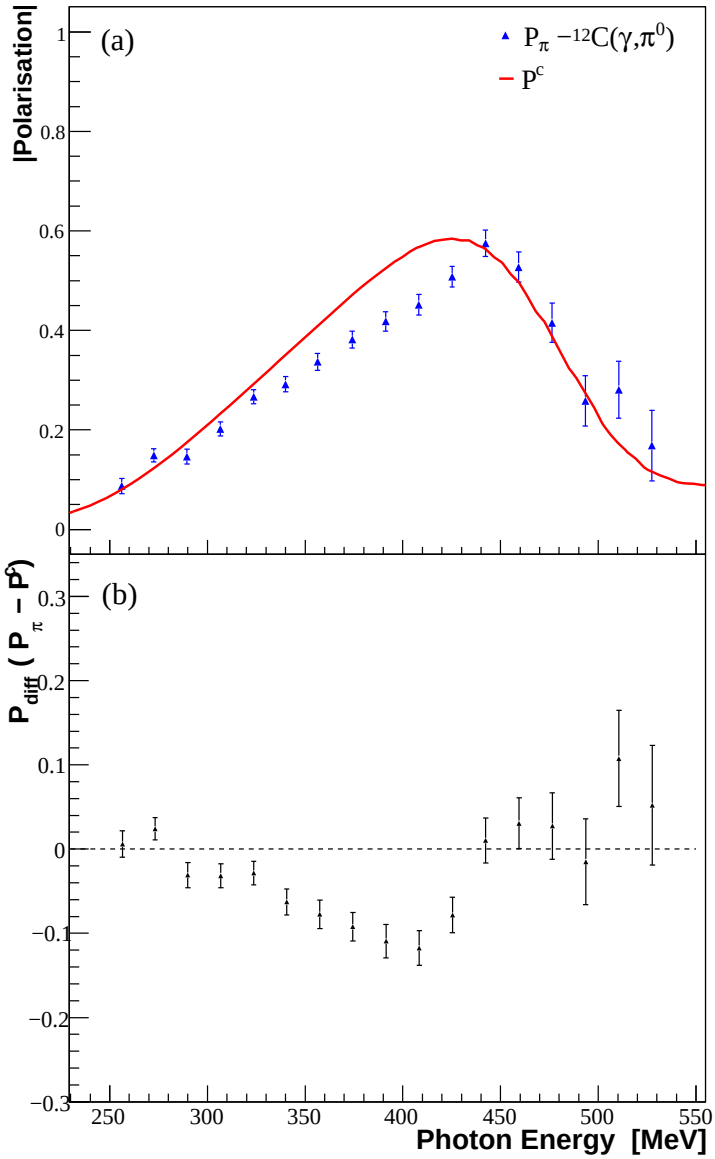

Figure 5.17: (a) Comparison of calculated polarisation (red line) using the prescription outlined in section 5.3.3 and the measured polarisation P_π for E_γ=300-500 MeV. (b) The difference between calculated and measured polarisation.

drifts in polarisation during data collection and gives the average photon polarisation for each Tagger channel. There is some additional smearing in the edge energy when the average polarisation is measured over the full August data set compared to figure 5.17(a). However, the polarisation in the tail region remains largely unaffected. The dashed vertical lines indicate the cuts applied to the data for the $^{12}C(\gamma,pp)$ analysis. Above E_γ ~450 MeV the $^{12}C(\gamma,pp)$ cross section is negligible and this data is not

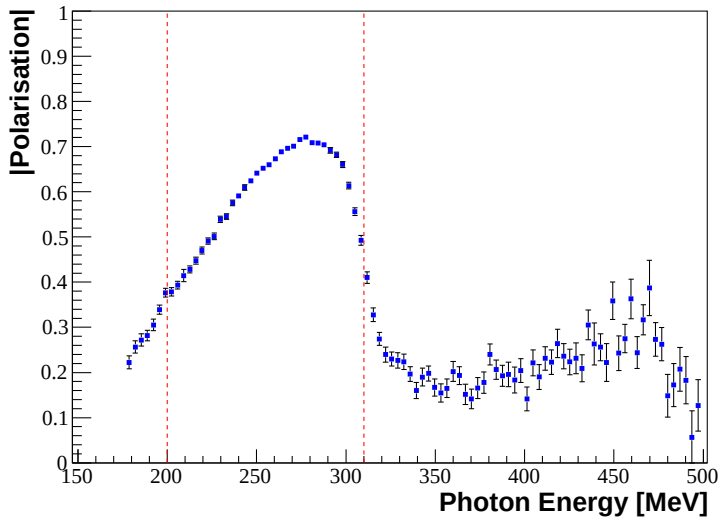

(a)

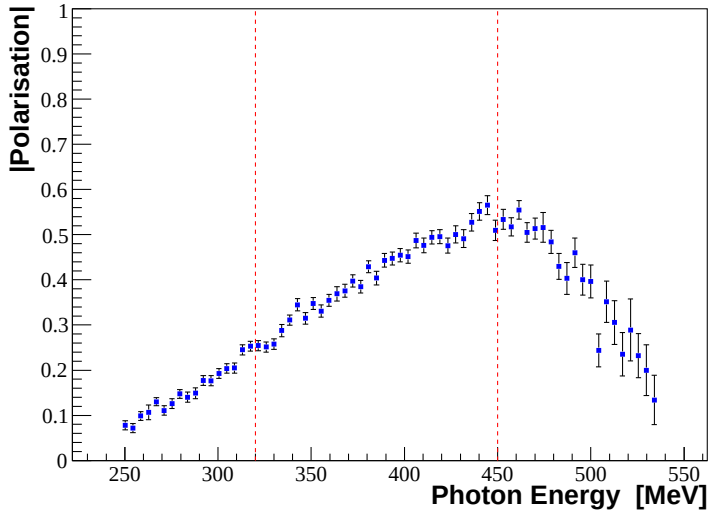

(b)

Figure 5.18: Photon polarisation against photon energy measured through the beam asymmetry of coherent π^0 photoproduction for (a) March beamtime and (b) August beamtime in the region of the first coherent peak. The dashed red lines indicate the cuts applied to the data for the $^{12}C(\gamma,\mathrm{pp})$ analysis.

used [24].

Now each detector system has been calibrated and the photon polarisation extracted, a more refined data analysis can be performed on the $^{12}C(\overrightarrow{\gamma},\mathrm{pp})$ reaction. The following chapter discusses the event selection for this reaction channel and presents the results of this work.

Chapter 6

Results and Discussion

In this chapter the results of this work are presented. The chapter begins with an outline of the cuts applied to the data to kinematically select regions were direct two-nucleon emission dominates. The presented photon asymmetries provide an observable, independent from the unpolarised cross section, with which photonuclear reaction models can be compared. By analysing the data for different missing energy regions, E_m, it is possible to separate out two nucleon knockout contributions from different shells. The photon asymmetry Σ is presented as a function of missing energy. For different E_m regions, the dependence of Σ on photon energy and for the first time proton emission angle is examined to gain a deeper understanding of the reaction processes. Comparisons are made with previous $^{12}C(\overrightarrow{\gamma}$,NN) measurements and also with theoretical predictions, based on the work of the Gent group as described in section 2.3.3. The figures illustrating these results show only statistical error bars as the sources of systematic uncertainty in the measurements have only a small effect on the photon asymmetries presented. The final section of this chapter justifies the previous statement by discussing the sources of systematic uncertainty and quantifying how these alter Σ. The results presented in this section are tabulated in appendix D.

6.1 Event Selection

In the study of (γ,NN), illustrated in figure 1.1, two kinematic variables are useful; the recoil momentum $\mathbf{P}_r$ and the missing energy E_m. The momentum of the recoiling system

$$\mathbf{P}_r = \mathbf{P}_\gamma - \mathbf{P}_1 - \mathbf{P}_2 \tag{6.1}$$

is obtained from the measured momenta of the absorbed photon (P_γ) and the two emitted nucleons (P_1 and P_2). For direct 2N knockout, in the absence of final state interactions between the ejected nucleons and the nuclear potential of the residual nucleus, the recoil momentum is opposite to the initial momentum P_{pair} of the nucleon pair in the target nucleus, $P_{\text{pair}} + P_r = 0$. Pair distributions have been calculated and compared with measured P_r distributions [24, 29, 30] and these studies have enabled the possibility of distinguishing between different absorption mechanisms and identification of the presence of more complex reaction mechanisms which involve FSI, shifting P_r to larger values.

The missing energy is defined:

$$E_m = E_\gamma - T_1 - T_2 - T_r = E_s + E_x \tag{6.2}$$

where T_1, T_2 and T_r are the kinetic energies of the two outgoing nucleons and residual nucleus respectively. E_s is the separation energy at threshold for two-nucleon emission (27 MeV for the reaction studied) and E_x is the excitation energy of the residual nucleus. The kinetic energy of the residual nucleus is typically small and is accessed through the recoil momentum P_r:

$$T_r = \frac{P_r^2}{2M_r} \tag{6.3}$$

where M_r is the mass of the residual ^{10}Be nucleus. Strictly, this should also include any excitation energy of the residual nucleus, but this can be neglected to first order. The missing energy gives information about the energy associated with the excitation of the residual (A-2) system or other undetected particles and therefore shows sensitivity to the underlying mechanism involved. In ^{12}C, the E_m <40 MeV region corresponds to absorption on $(1p)^2$ nucleon pairs, while E_m=40-70 MeV emphasises

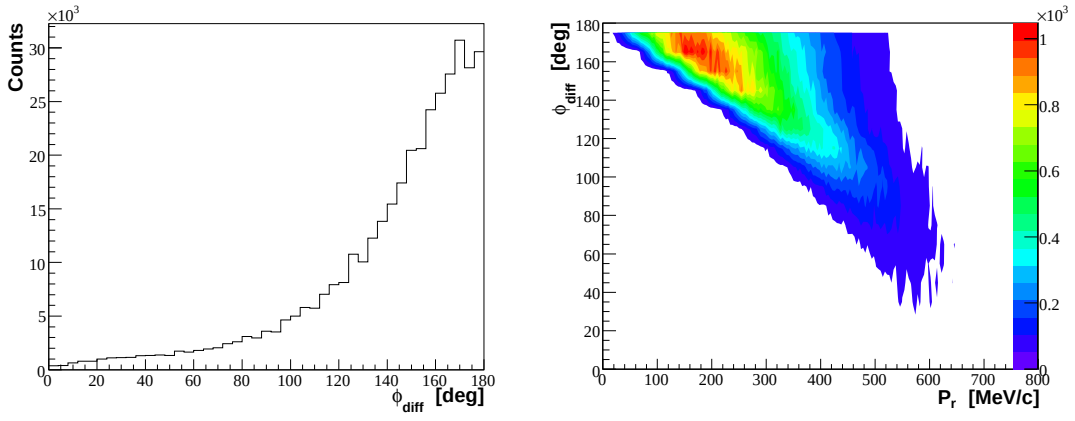

(a) (b)

Figure 6.1: (a) Proton pair opening angle (b) Correlation between the opening angle and the total relative momentum of the pair.

absorption on (1s)(1p) pairs. No attempt is made to extract the $(1s)^2$ strength as its contribution is expected to be weak and spread over a wide range of E_m [29].

Figure 6.1(a) plots the absolute opening angle of the proton pair ϕ_{diff} for all E_m and over the photon energy range E_γ=200-310 MeV. The (γ,pp) yield is largest in back-to-back kinematics with a significant reduction in strength as ϕ_{diff} decreases. Figure 6.1(b) shows the correlation between ϕ_{diff} and P_r. The concentration of strength at low $P_r < 300$ MeV/c corresponds to mostly back-to-back emission. At higher P_r, pairs are ejected from the nucleus with smaller ϕ_{diff}, with the deviations from back-to-back emission increasing with P_r. The more extreme opening angles sample very high momentum components in the pair momentum distribution and as the probability of large P_r is small, the reaction strength is significantly reduced in these kinematics. However for larger values of recoil momentum, there are increased contributions from more complex mechanisms involving FSI which make it difficult to separate direct 2N-knockout events from multi-step processes.

Previous measurements of $\Sigma_{(\gamma,pp)}$ on ^{12}C had limited azimuthal coverage and extracted the photon asymmetry from $\Sigma = (1/P)(Y_\parallel - Y_\perp)/(Y_\parallel + Y_\perp)$. The full 2π azimuthal coverage of the Crystal Ball allows Σ to be extracted more reliably from the $\cos(2\phi)$ azimuthal asymmetry via equation 5.4 where ϕ is the momentum weighted average azimuthal angle of the reaction plane defined by equation 6.4. If

the photon is absorbed on a stationary nucleon pair the nucleons are ejected exactly back-to-back and ϕ is well determined. Matters are complicated somewhat by initial Fermi motion of the nucleons and the pair momentum component perpendicular to the incident photon cause the outgoing pair to be non-coplanar. Figure 1.1 illustrates photon absorption on a pair with momentum P_{pair}. The initial momentum of each nucleon must be taken into account, allowing construction of the average azimuth of the two protons, to construct the azimuthal distribution of the reaction plane before extracting Σ. Using equation 6.4 to define ϕ gives weight to the proton with the largest momentum component perpendicular to the photon beam.

$$\phi = \frac{|p_1 \sin\theta_1|\phi_1 + |p_2 \sin\theta_2|\phi_2}{|p_1 \sin\theta_1| + |p_2 \sin\theta_2|} \tag{6.4}$$

where $p_{1(2)}$, $\theta_{1(2)}$ and $\phi_{1(2)}$ are the momentum, polar and azimuthal angle of proton 1 (2) respectively.

6.2 Missing Energy

A missing energy resolution better than ∼20 MeV FWHM is required to identify direct emission of proton pairs from 1p orbitals [97]. Figure 4.19 gives the single proton energy resolution integrated over all proton angles and energies for the γp $\rightarrow$ pπ^0 reaction, giving a resolution ∼25 MeV FWHM. Folding two of these spectra gives an estimate of the total missing energy resolution for (γ,pp) of ∼35 MeV, which is less sensitive to nuclear structure aspects of the reaction. Therefore some contribution from (1s)(1p) proton pairs is expected for E_m <40 MeV.

Events with only two protons in the final state were selected from the ΔE-E cuts described in section 4.2.3 and energy loss corrections were applied to both (section 4.4). The corresponding missing energy distributions for ^{12}C(γ,pp) are shown in figure 6.2 for (a) E_γ=200-310 MeV and (b) E_γ=320-450 MeV. The observed yields are consistent with previous measurements [29, 30, 48] with no discernible structure found at threshold indicating that the residual nucleus is not often left in or near its ground state. This is in contrast to ^{12}C(γ,pn) which shows a concentration of strength at low E_m. Most of the ^{12}C(γ,pp) yield is found at higher missing energies

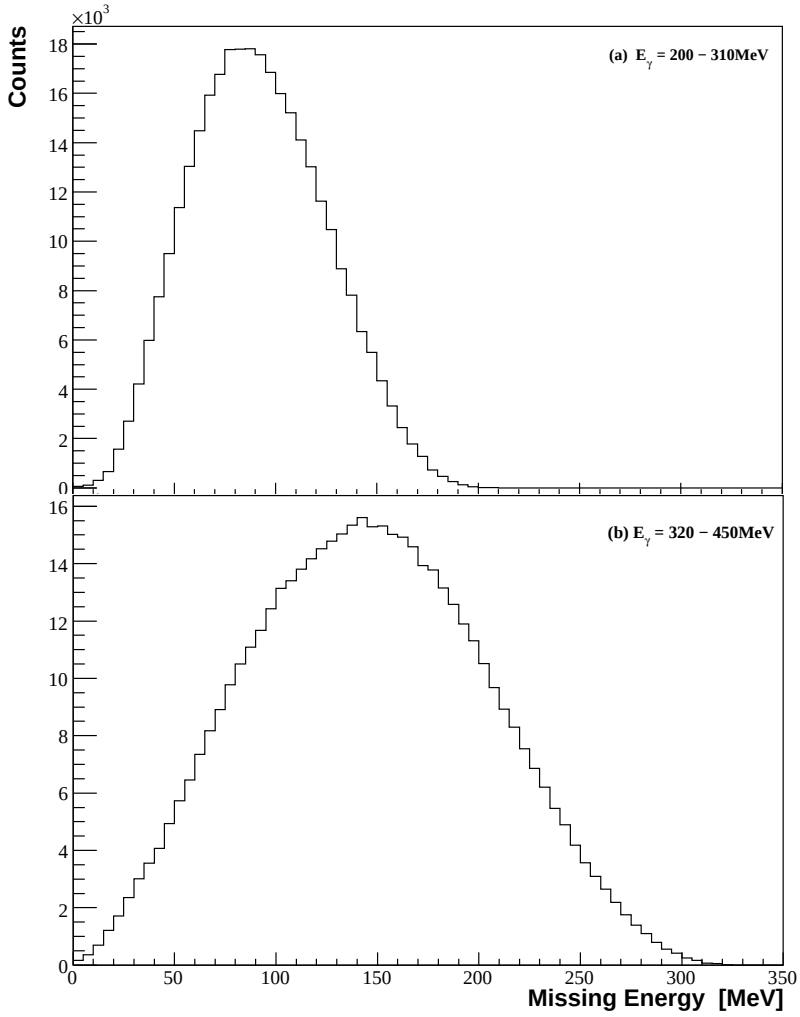

Figure 6.2: Missing energy distributions for the $^{12}C(\gamma,\mathrm{pp})$ reaction for (a) E_γ=200-310 MeV and (b) E_γ=320-450 MeV.

where much of the strength comes from initial pion production, multi nucleon knock-out and mechanisms with FSI. At higher E_m the spectra for both photon energy ranges fall off smoothly as there is an E_γ-dependent phase space limit.

The asymmetry of the (γ,pp) reaction as a function of missing energy is shown in figure 6.3. No angular cuts or constraints on recoil momentum are placed on the data and Σ is averaged over the two photon energy ranges outlined above. For E_γ=200-310 MeV (figure 6.3(a)) the results are compared with the $^{12}C(\gamma,\mathrm{pp})$ measurement using the PiPToF setup at Mainz and covering E_γ=220-280 MeV [25]. The asymmetry is most negative at low E_m ∼40 MeV where emission of $(1\mathrm{p})^2$ proton pairs is

expected in both photon energy ranges. The dip at low E_m for E_γ=200-310 MeV is consistent with that observed with previous data although the peak is wider in the current data, probably due to the poorer E_m resolution of the experiment. At low E_m the magnitude of $\Sigma_{(\gamma,pp)}$ at the peak tends to be greater than $\Sigma_{(\gamma,pn)}$ [51, 52]. This supports the conclusion of previous works that the (γ,pp) reaction proceeds via direct knockout mechanisms for E <40 MeV. If a large part of the (γ,pp) strength came from initial (γ,pn) absorption followed by a charge exchange FSI, the magnitude of $\Sigma_{(\gamma,pp)}$ would be expected to lie closer to zero than $\Sigma_{(\gamma,pn)}$ as the asymmetry of the initial absorption process would be smeared by FSI effects which are likely to scatter the outgoing nucleons. This tends to support the conclusion by Watts *et al.* [24] that different one- and two-body currents are important in the (γ,pp) and (γ,pn) reactions at low E_m.

At higher E_m, $\Sigma_{(\gamma,pp)}$ remains negative but decreases in magnitude as E_m increases. For E_γ=200-310 MeV and E_m >100 MeV, $\Sigma_{(\gamma,pp)}$ is consistent with zero. The missing energy dependence is similar in $\Sigma_{(\gamma,pn)}$ (figure 2.10), possibly indicating that similar reaction mechanisms are responsible at higher E_m. In this region, Valencia model calculations predict increasing contributions from 2N (and 3N) knockout with FSI and initial pion production followed by subsequent reabsorption in the nucleus for E_γ=200-300 MeV [24, 98]. Multi-step mechanisms dilute any asymmetry present in the initial process and a fall in Σ with increasing E_m is likely when more complex mechanisms dominate the reaction cross section.

The photon asymmetry shows a similar missing energy dependence for both photon energy ranges. The peak has a slightly larger magnitude for E_γ=320-450 MeV which may reflect the increasing contribution from Δ currents in this region. The observed asymmetry at high E_m in the Δ region is similar to (γ,pn) [51, 25]. The conclusion drawn from these works was that the observed asymmetries stem from the large asymmetry of an initial (γ, πN) process. This possibility is discussed in more detail in section 6.5.

The work of Watts *et al.* [24] provides assistance on which cuts can be applied to the data to emphasise direct knockout mechanisms. For E_m <40 MeV, a Monte Carlo simulation of the direct 2N knockout process gave a reasonable description

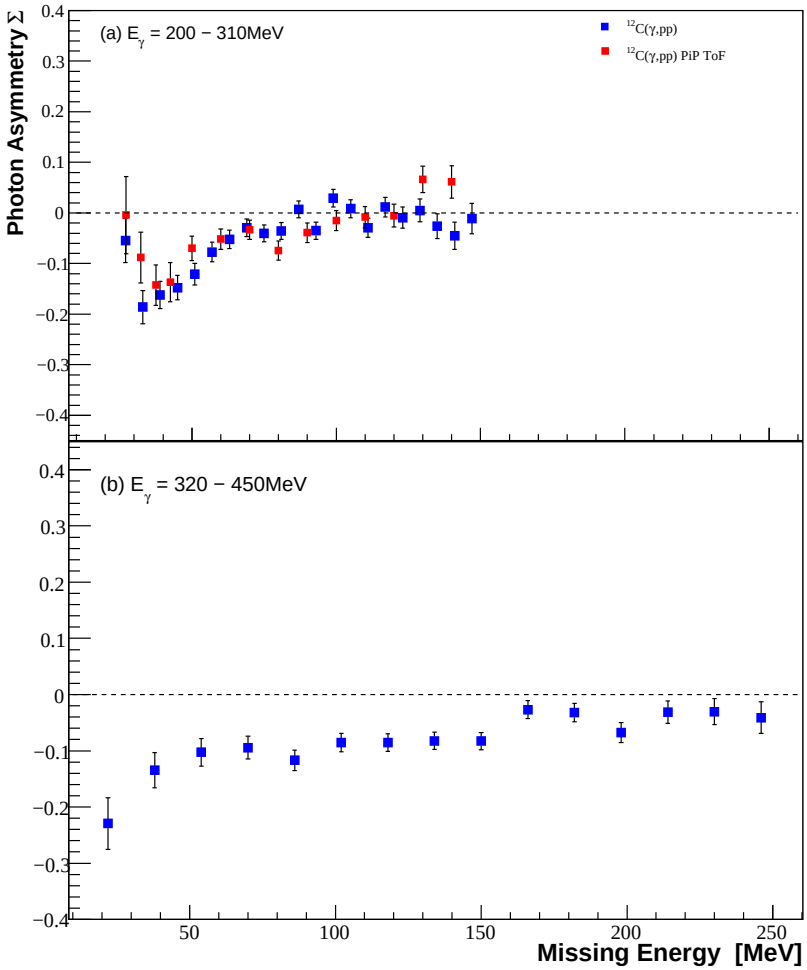

Figure 6.3: $\Sigma_{(\gamma,pp)}$ (blue squares) for ^{12}C plotted as a function of missing energy for (a) E_γ=200-310 MeV and (b) E_γ=320-450 MeV. The red squares are $\Sigma_{(\gamma,pp)}$ for ^{12}C, E_γ=220-280 MeV [25].

of measured recoil momentum distributions in back-to-back kinematics, although the model predicted some strength at low P_r which was not visible in the data (figure 2.7(a)). Away from back-to-back kinematics, the description provided by the model was slightly poorer. In the photon energies covered by this experiment, the model failed to account for some strength observed for P_r >400 MeV/c, although the direct knockout Monte Carlo (MC) accounted for most of the measured strength in this region. For E_m=40-70 MeV (figure 2.7(b)), the MC does not provide a good description of the data for P_r >300 MeV/c in back-to-back kinematics. This trend

was accentuated in kinematics away from back-to-back. The regions where the model fails to account for the observed strength in the data is an indication of strength from other processes.

In view of the above, the missing energy dependence of Σ was studied for two regions of recoil momentum, P_r <300 MeV/c and P_r >300 MeV/c, with the results shown in figure 6.4. There is a clear enhancement in Σ for P_r <300 MeV for all missing energies in both photon energy ranges sampled. It is worth noting for P_r <300 MeV/c that Σ remains strong right down to the lowest E_m events in E_γ=200-310 MeV and is in fact largest in magnitude here for the higher photon energy range. This is a strong signature of the direct process. In the lower photon energy range, the strong negative asymmetry observed for P_r <300 MeV/c in the missing energy region E_m=50-100 MeV vanishes or becomes slightly positive when events with high recoil momentum are sampled. This is consistent with Valencia calculations that for P_r >300 MeV/c and E_m=40-70 MeV some of the measured (γ,pp) yield comes from processes other than direct 2N knockout. At lower missing energy E_m <50 MeV, Σ remains significantly negative for both P_r ranges studied, although there is some dilution for P_r >300 MeV/c. This is to be expected as the direct 2N knockout MC outlined in reference [24] accounts for most of the observed (γ,pp) strength up to P_r ~500 MeV/c. For E_γ=320-450 MeV, the missing energy dependence for the two recoil momentum regions follows a similar trend to E_γ=200-310 MeV. There is a larger dilution for low E_m when events with high recoil momentum are sampled which may indicate increased strength from indirect processes at higher E_γ. At higher E_m, Σ is again reduced for P_r >300 MeV/c compared to P_r <300 MeV/c although a negative asymmetry ($\Sigma \sim -0.1$) remains.

In general, for E_m <70 MeV, a cut on low recoil momentum P_r <300 MeV/c, emphasises the direct knockout process. At higher P_r, the data is more sensitive to indirect knockout mechanisms with additional contributions from FSI which reduce the observed asymmetries. This is examined in more detail in the following section.

Figure 6.5 plots the E_m dependence of the photon asymmetry for (a) E_γ = 200-310 MeV and (b) E_γ = 320-450 MeV for different pair opening angles: ϕ_{diff}=160-180° and 140-160°. The aim of using equation 6.4 to define the azimuth of the reaction

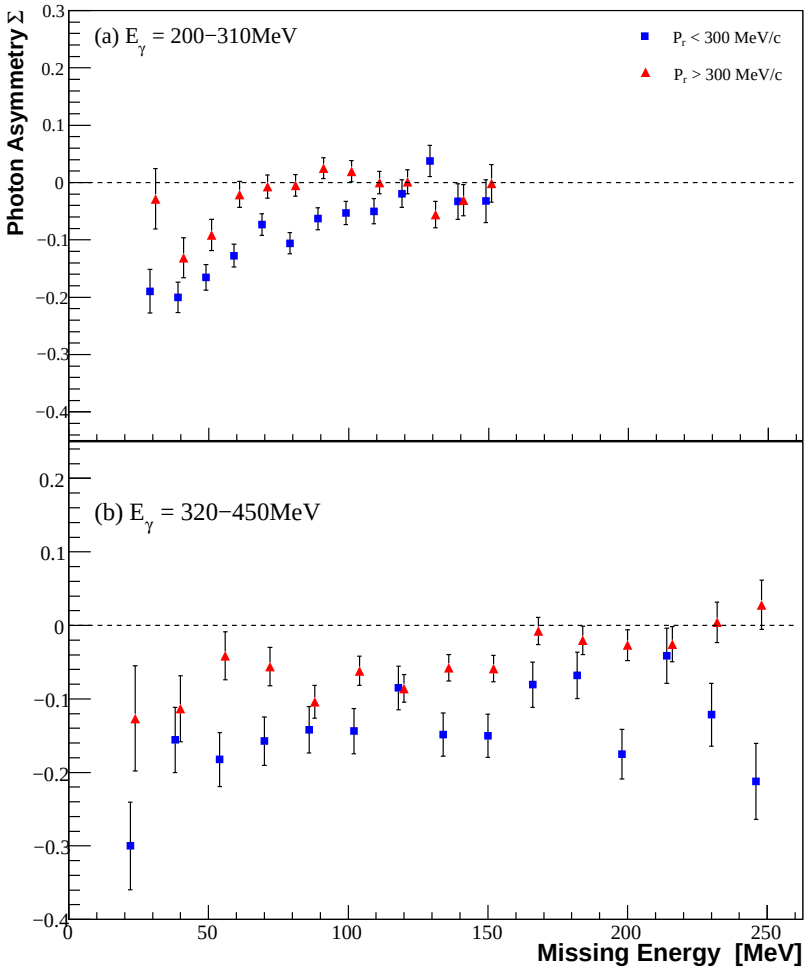

Figure 6.4: $\Sigma_{(\gamma,pp)}$ for ^{12}C plotted as a function of missing energy for the photon energy range (a) 200-310 MeV and (b) 320-450 MeV. The blue squares correspond to P_r <300 MeV/c and red triangles, P_r >300 MeV/c. The red points are offset by 2 MeV for clarity.

plane with respect to the **E**-field of the incident photon was to recover non-coplanar events and extract an asymmetry equal to that measured in back-to-back kinematics. Unfortunately, the asymmetry measured for non-coplanar events ($\phi_{\text{diff}} = 140 - 160°$) is clearly diluted compared to $\phi_{\text{diff}} = 160 - 180°$. This may indicate that the correct azimuth of the reaction plane has not been accessed for $\phi_{\text{diff}} = 140 - 160°$ diluting the extracted asymmetry. The differences in Σ between $\phi_{\text{diff}} = 160 - 180°$ and $\phi_{\text{diff}} = 140 - 160°$ is largest in the low photon energy region. However, away from

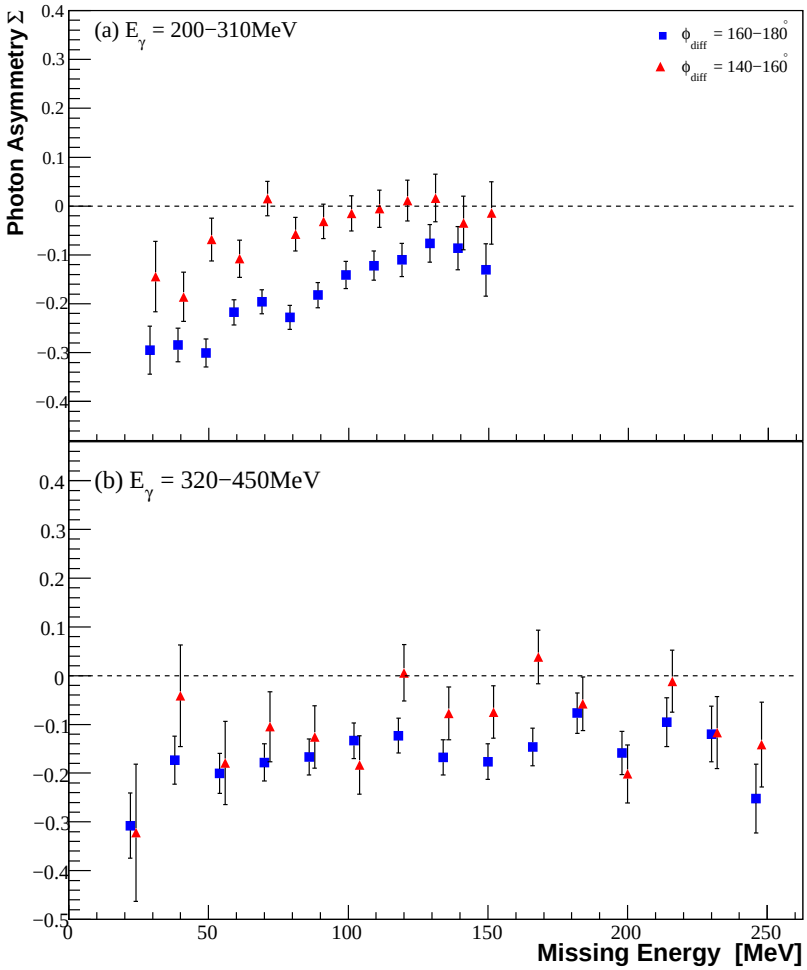

Figure 6.5: The missing energy dependence of $\Sigma_{(\gamma,pp)}$ for (a) 200-310 MeV and (b) 320-450 MeV. The blue squares and red triangles correspond to different pair opening angles: $\phi_{\text{diff}} = 160 - 180°$ and $140 - 160°$ respectively.

back-to-back kinematics the relative ratio of direct to indirect processes is greatly reduced (figure 2.7) and the larger contributions from indirect processes may be responsible for the reduced asymmetry for $\phi_{\text{diff}} = 140 - 160°$. These differences are larger than expected from slightly larger P_r which is correlated with different ϕ_{diff} ranges. A detailed simulation is required to determine which is primarily responsible for reducing Σ. In order to obtain the largest Σ magnitudes which are characteristic of direct processes, the measured photon asymmetries presented below are restricted to pairs with opening angles in the range $\phi_{\text{diff}} = 160 - 180°$.

6.3 Photon Energy Dependence of Asymmetry

In this section, the photon energy dependence of Σ is explored for two missing energy regions: E_m <40 MeV where photon absorption on $(1p)^2$ proton pairs dominate with the residual nucleus spectating and E_m=40-70 MeV where direct two nucleon emission is from (1s)(1p) shells. Additionally, the results of the present work are compared with previous measurements of $\Sigma_{(\gamma,NN)}$ on ^{12}C [25]. To assist the interpretation of the experimental results, previous theoretical calculations from the Gent model are provided. Newer calculations from the Pavia group covering the full kinematic coverage of the present experiment are underway but are not available at the time of writing.

Figure 6.6 plots the photon energy dependence of Σ for the $^{12}C(\overrightarrow{\gamma}$,pp) for (a) E_m <40 MeV and (b) E_m=40-70 MeV, averaged over the full angular range of the experiment. Although the degree of polarisation is relatively large ($\sim$ 40%) for photon energies in the range E_γ = 450-500 MeV, the measured photon asymmetries do not extend into this region as the (γ,pp) cross section is negligible.

The negative $^{12}C(\overrightarrow{\gamma}$,pp) asymmetries observed for E_m <40 MeV and E_m=40-70 MeV over the entire photon energy range investigated can be attributed to a larger contribution from magnetic rather than electric multipoles. A large contribution from electric multipoles yields a positive value of Σ [99]. From a simplistic point of view if the reaction has electric dominance, one of the ejected protons will be attracted along the direction of the electric field vector of the photon. For low initial pair momentum, the second proton will be emitted in the opposite direction. Therefore, the reaction cross section will be larger when the electric vector is parallel to the reaction plane and the photon asymmetry will be positive. In the photon energy range covered by the present experiment, the cross section is dominated by the magnetic dipole interaction ($\gamma N \rightarrow \Delta$) which results in an intermediate ΔN state. Following a $\Delta \rightarrow \pi N$ decay and reabsorption of the pion, both nucleons are emitted. A large magnetic contribution from this process will lead to a large cross section when the magnetic vector is in the reaction plane (when the electric vector is perpendicular to the reaction plane). Consequently $d\sigma_\perp > d\sigma_\parallel$ and the photon asymmetry is negative. Negative asymmetries are observed in $\Sigma_{(\gamma,pp)}$ and $\Sigma_{(\gamma,pn)}$ for

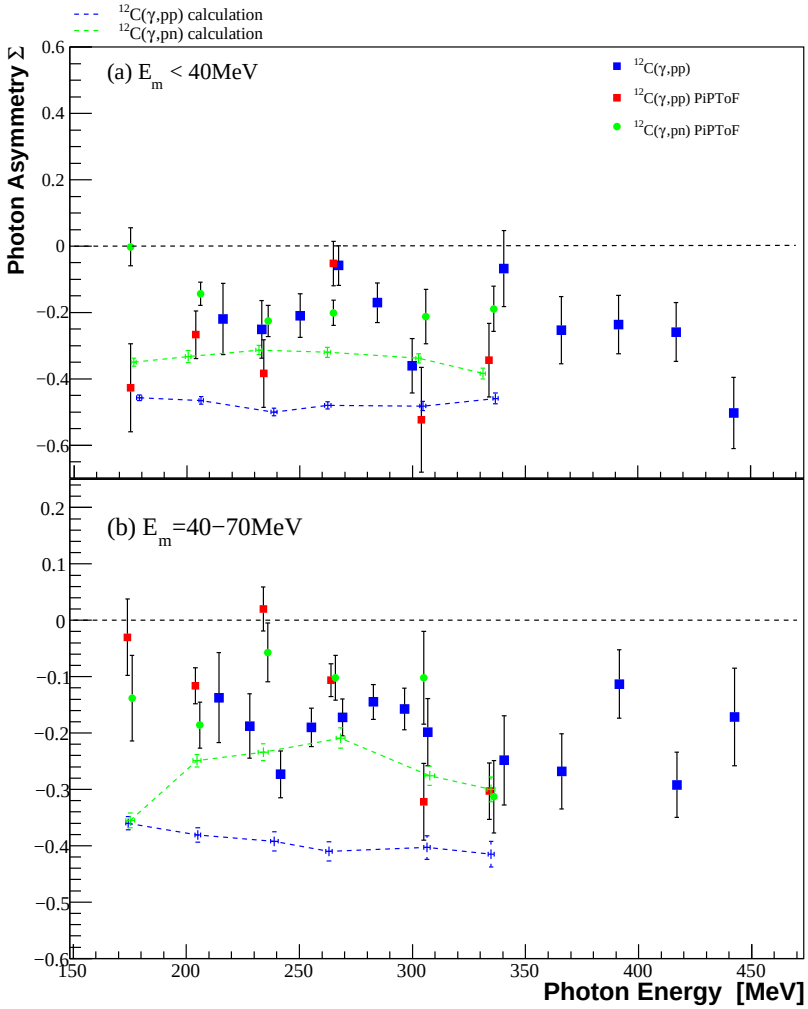

Figure 6.6: Photon energy dependence of Σ for (a) E_m <40 MeV and (b) E_m=40-70 MeV. Present $\Sigma_{(\gamma,pp)}$ results are shown by blue squares and previous PiPToF measurements by red squares ($\Sigma_{(\gamma,pp)}$) and green circles ($\Sigma_{(\gamma,pn)}$). Theoretical predictions from the Gent direct knockout model are indicated by dashed lines for $^{12}C(\gamma$,pp) (blue) and $^{12}C(\gamma$,pp)(green) for (a) $(1p)^2$ and (b) (1s)(1p) photon absorption.

E_m <40 MeV and E_m=40-70 MeV both of which, on average, have slightly larger strength at higher photon energies (E_γ >300 MeV), perhaps reflecting increased strength from Δ processes.

For E_m <40 MeV (figure 6.6(a)), there is reasonable agreement between the present measurement and previous $\Sigma_{(\gamma,pp)}$ PiPToF measurements. Below photon energies of 250 MeV, $\Sigma_{(\gamma,pp)}$ is relatively large at ~ -0.2. Both measurements show

the photon asymmetry drops in magnitude around E_γ ∼260 MeV, with the present measurement showing a distinct fall in the magnitude of Σ perhaps indicating the observation in the PiPToF measurement is not simply a result of statistical fluctuations. The reason for this drop in magnitude is unclear although it may be related to the decreased M2 multipole strength which falls to $\sim 0\mu$b in exactly this energy region [99]. Interestingly, $\Sigma_{(\gamma,pn)}$ does not follow this trend, possibly reflecting the different reaction mechanisms which contribute to (γ,NN) at these photon energies, particularly the influence of charged meson exchange. The $^{12}C(\overrightarrow{\gamma}$,pp) asymmetry becomes significantly more negative again above photon energies of ∼280 MeV ($\Sigma \sim -0.3$) probably indicating a change in reaction mechanism most likely due to the increased influence of processes involving intermediate Δ excitation [46].

For the lower E_m region and at photon energies below Δ excitation energies, $\Sigma_{(\gamma,pp)}$ is generally larger than $\Sigma_{(\gamma,pn)}$ supporting the conclusions of previous works that intrinsically different mechanisms contribute to each channel. This also suggests that contributions from initial (γ,pn) absorption followed by charge exchange FSI are small. Theoretical calculations [22] and previous works on (γ,pN) reactions provides some guidance on the relevance of the various reaction mechanisms in this region. At intermediate energies and low missing energy (γ,pn) reactions proceed via meson exchange and Δ currents, with MEC contributions decreasing as E_γ approaches Δ energies. Gent theoretical calculations including the two dominant MEC terms, pion-in-flight and seagull, plus the Δ currents provide a reasonable representation of (γ,pn) angular distributions [47]. The calculations reported significant interference between the two dominant MEC terms. This interference was also present in Pavia calculations of Σ for the $^{16}O(\gamma$,pn) reaction [22]. Pure contributions from seagull and pion-in-flight currents generally gave positive Σ. However, their interference effects resulted in a small negative asymmetry. The combination of Δ and meson exchange terms also gave a negative asymmetry for intermediate energies, similar to the present experiment. The calculations also found that at larger values of photon energy, above ∼300 MeV the asymmetry is dominated by Δ currents. SRC and one-body currents only slightly affected the calculated cross sections and asymmetries. The calculations for the two reaction channels get closer to each other in this region.

For (γ,pp) reactions, MEC are suppressed and only Δ currents and one body terms contribute. Therefore, one would expect similar amplitudes for $\Sigma_{(\gamma,pp)}$ and $\Sigma_{(\gamma,pn)}$ at higher photon energies where Δ currents dominate both channels. For E_γ >300 MeV there is reasonable agreement in Σ between both experimental channels although it is necessary to see if this behaviour in $\Sigma_{(\gamma,pn)}$ continues up to E_γ ~450 MeV before a more definitive interpretation can be drawn.

Figure 6.6(b) shows the photon energy dependence of Σ for E_m=40-70 MeV. The measurement has better statistical accuracy due to the larger cross section involved and shows smoother behaviour with photon energy than the previous $\Sigma_{(\gamma,pp)}$ results of Powrie *et al.* [25]. Below the Δ resonance the asymmetry shows some photon energy dependence which differs from the previous measurements. There is a local peak with $\Sigma \sim -0.3$ around E_γ=240 MeV followed by a slight drop in magnitude around E_γ=270 MeV. This is similar but not as marked as that observed for E_m <40 MeV. Again there is an increase in magnitude above photon energies of 300 MeV where Δ currents are expected to dominate. In general, the asymmetry has similar magnitude in both E_m regions perhaps due to the cuts placed on P_r and ϕ_{diff} which emphasise direct knockout processes in both regions. In the higher E_m region, the measurement has a larger magnitude than the PiPToF $\Sigma_{(\gamma,pp)}$ measurement. The PiPToF measurement analysed (γ,pp) events if the angle between the measured nucleon momentum in ToF and that calculated from the measured proton momentum in PiP was within the range $\Theta_{diff} = 0 - 30°$. These kinematics sample back-to-back ejected nucleons with recoil momentum distributions up to $\mathbf{P}_r$ ~500 MeV [30, 24]. No cuts were placed on this variable and the PiPToF results for E_m=40-70 MeV also sample more complicated mechanisms which dilute the asymmetry associated with the direct absorption processes. The photon asymmetry is on average larger than $\Sigma_{(\gamma,pn)}$ [52] for photon energies less than 300 MeV reinforcing the conclusion of Watts *et al.* that for P_r <300 MeV/c and E_m=40-70 MeV, much of the reaction strength comes from direct two-nucleon knockout. Above E_γ = 300 MeV, $\Sigma_{(\gamma,pp)}$ and $\Sigma_{(\gamma,pn)}$ have similar magnitudes although further measurements of $\Sigma_{(\gamma,pn)}$ are necessary to see if this trend continues up to E_γ=450 MeV. This will help establish whether both reactions proceed through similar mechanisms in this region.

For coplanar kinematics in the factorised plane wave approximation, where it is assumed that the proton pair are in a relative S state, the photon asymmetry, $\Sigma \sim -1.0$. The present analysis with $\phi_{\rm diff}$ constrained to 160-180° satisfies this kinematic requirement but obtains $\Sigma_{(\gamma,pp)}$ much smaller in magnitude than -1.0. This is further evidence of the involvement of proton pairs in higher angular momentum states (P and D) and reinforces the need for theoretical models to include these contributions in their calculations. Similar conclusions were reached by Lindgren [100] and Powrie *et al.* [25]. Theoretical work by the Gent group [9] reported that inclusion of higher relative states in their (γ,pp) calculations significantly reduced the magnitude of the photon asymmetry compared to that calculated from pure $^1S_0$ photon absorption.

To assist in interpreting the measured photon asymmetry for $^{12}C(\overrightarrow{\gamma}$,pp) and any differences with $\Sigma_{(\gamma,pn)}$, a comparison is made with the results of Gent calculations [9]. The calculations were averaged over the acceptance of the PiPToF detectors using a Monte Carlo technique [101] and cover a photon energy range E_γ=180-340 MeV. Calculations for the low missing energy region are based on direct knockout of a $(1p_{3/2})$ pair and $(1p_{3/2})(1s_{1/2})$ knockout for the higher missing energy region. Overall, the calculations overpredict the magnitude of Σ for both channels and provide a poor description of its energy dependence.

In the low E_m region the calculation does predict that the $\Sigma_{(\gamma,pp)}$ has a larger amplitude than $\Sigma_{(\gamma,pn)}$ although it overpredicts the magnitude for both channels. The E_γ dependence of the calculated photon asymmetry is fairly flat for both reaction channels, despite the fact that Δ current contributions are strongly energy dependent. In particular the calculations do not reproduce the reduction in $\Sigma_{(\gamma,pp)}$ which seems to be a feature at photon energies at $E_\gamma \sim$260 MeV. For the higher missing energy region, the calculated asymmetry is again generally larger than the experimental data although the present measurement brings $\Sigma_{(\gamma,pp)}$ closer to theory for $E_\gamma <$300 MeV. It may be relevant that the calculations employ the spectator approach which neglects multiple scattering processes involving the outgoing pair with other nucleons. It is possible that the experimental data are affected by multiple scattering, particularly in the missing energy region E_m=40-70 MeV, which may

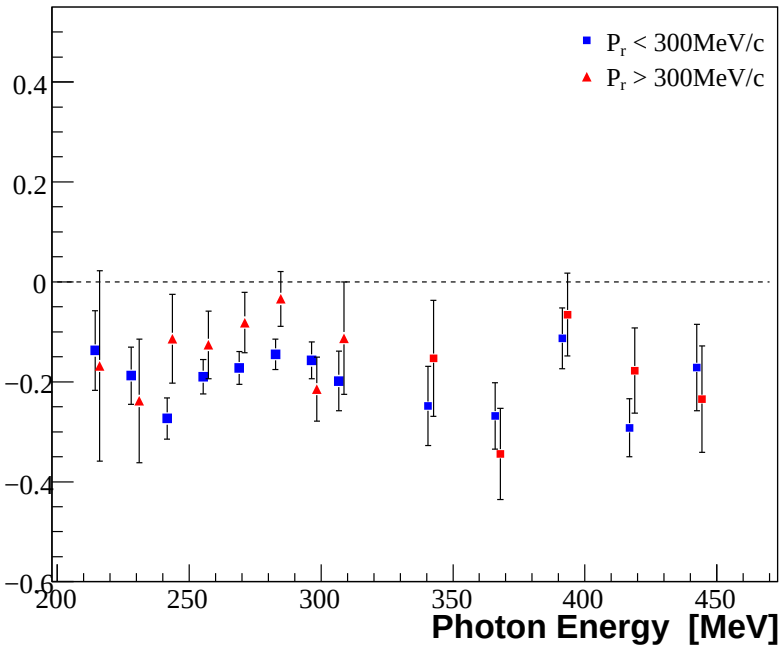

Figure 6.7: Photon energy dependence of $\Sigma_{(\gamma,pp)}$ for E_m=40-70 MeV and $\phi_{\text{diff}} = 160 - 180°$. Two kinematic regions are sampled: P_r <300 MeV/c (blue) and P_r >300 MeV/c (red). The red points are offset by 2 MeV for clarity.

dilute the intrinsic asymmetry of the contributing mechanisms.

Figure 6.7 plots the photon energy dependence of $\Sigma_{(\gamma,pp)}$ for E_m=40-70 MeV for P_r <300 MeV/c and P_r >300 MeV/c. A cut of $\phi_{\text{diff}} = 160 - 180°$ is placed on the data. In general the photon asymmetry is enhanced for low recoil momentum compared to P_r >300 MeV/c with the enhancement most obvious for E_γ <300 MeV. Valencia model calculations predict the dominance of the direct knockout mechanism at low missing energies (E_m <50 MeV) in back-to-back kinematics up to photon energies E_γ ∼400 MeV. At higher E_m, contributions from more complex mechanisms involving FSI and initial pion production compete with the direct process, diluting any asymmetry. At high P_r the direct 2N knockout cross section decreases as it demands absorption on a nucleon-pair with very large initial momentum which has a small probability in the pair momentum distribution. Therefore, the relative ratio of direct to multistep processes decreases at high P_r and increased dilution of Σ follows.

Interestingly for higher recoil momentum, the measured asymmetry has a more similar magnitude and behaviour to that measured by Powrie for E_γ <300 MeV, which in general had a smaller magnitude than $\Sigma_{(\gamma,pn)}$. This behaviour was seen as an indication that some of the (γ,pp) strength in these kinematics comes from initial pn absorption followed by charge exchange FSI. Final state interactions are likely to distort the outgoing nucleons which could reduce any asymmetry present from the initial absorption. The present work suggests the data are more sensitive to multiple scattering processes which tends to shift P_r to higher values. In this missing energy region, the direct knockout process is emphasised by placing a cut of P_r <300 MeV/c. The poor statistics for E_m <40 MeV makes a similar comparison impractical. However, it is likely that the reduction in Σ for P_r >300 MeV/c in this region will be significantly smaller than E_m=40-70 MeV as direct 2N knockout models describe most of the observed strength in data up to P_r ∼500 MeV/c [30,24].

6.4 Angular Distributions

Previous experimental work has shown that both $^{12}C(\gamma,pp)$ and $^{12}C(\gamma,pn)$ cross sections have a strong angular dependence [47]. Theoretical calculations also predict that Σ will also have a strong angular dependence [9]. In principle studies of angular distributions will provide a sensitive test for calculations of two-nucleon emission and it therefore of interest to study the angular dependence of the present data.

The angular dependencies of Σ for ($\overrightarrow{\gamma}$,NN) reactions are studied as a function of θ_p^{COM}, the polar angle of the ejected nucleons in the centre-of-mass (COM) frame of the photon and nucleon pair. This is the same reference frame used in Gent theoretical calculations [9]. The diagram on the right side of figure 6.8 illustrates the (γ,pp) reaction in this frame. In the lab frame the photon is absorbed on a pair with some initial momentum $\mathbf{P}_{\text{pair}}$ and the ejected pair are non coplanar (figure 1.1). In the COM frame the photon and pair have equal and opposite momentum. To conserve energy and momentum the nucleons are ejected exactly back-to-back, defining a plane.

Figure 6.9 presents the angular dependence of Σ for E_m <40 MeV for (a) E_γ=200-

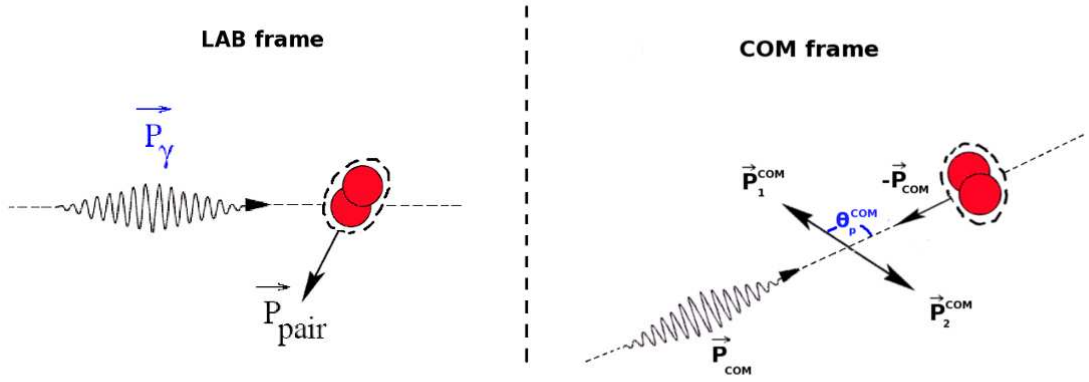

Figure 6.8: Photon absorption on a pair with initial momentum $\mathbf{P}_{\text{pair}}$ in the LAB frame (left) transformed into the centre-of-mass frame of the initial photon and nucleon pair. In this frame, the nucleon pair are ejected back-to-back with $\mathbf{P}_1 = \mathbf{P}_2$.

310 MeV and (b) E_γ=320-450 MeV. The photon asymmetry shows a strong angular dependence, peaking around $\theta_p^{COM} \sim 80°$ for both photon energy ranges studied. The magnitude at the peak for E_γ=200-310 MeV, $\Sigma \sim -0.5$, exceeds that for the higher energy setting, $\Sigma \sim -0.4$. The photon asymmetry quickly drops in magnitude as the angle changes for both photon energy ranges with $\Sigma \sim 0$ at $\theta_p^{COM} \sim 50°$ and $\theta_p^{COM} \sim 120°$.

To assist in the interpretation, the results have been compared to Gent theoretical calculations for E_γ=300 MeV and E_γ=400 MeV in quasideuteron kinematics. Figure 6.9 shows the incoherent sum of absorption on pairs with relative angular momentum states of $J_R = 0^+$ and $J_R = 2^+$. The calculations include outgoing nucleon distortions, isobaric currents and ground state correlations. The model predicts a peak in Σ at central angles around $\theta_p^{COM} = 60 - 100°$ which had little dependence on photon energy. The magnitude of Σ showed a strong dependence on the relative angular momentum of the initial pair although the incoherent sum of the two states studied ($J_R = 0^+$ and $J_R = 2^+$) had little effect on the shape of the distribution [9]. The shape of the angular distributions for $\Sigma_{(\gamma,pp)}$ and $\Sigma_{(\gamma,pn)}$ were found to be rather

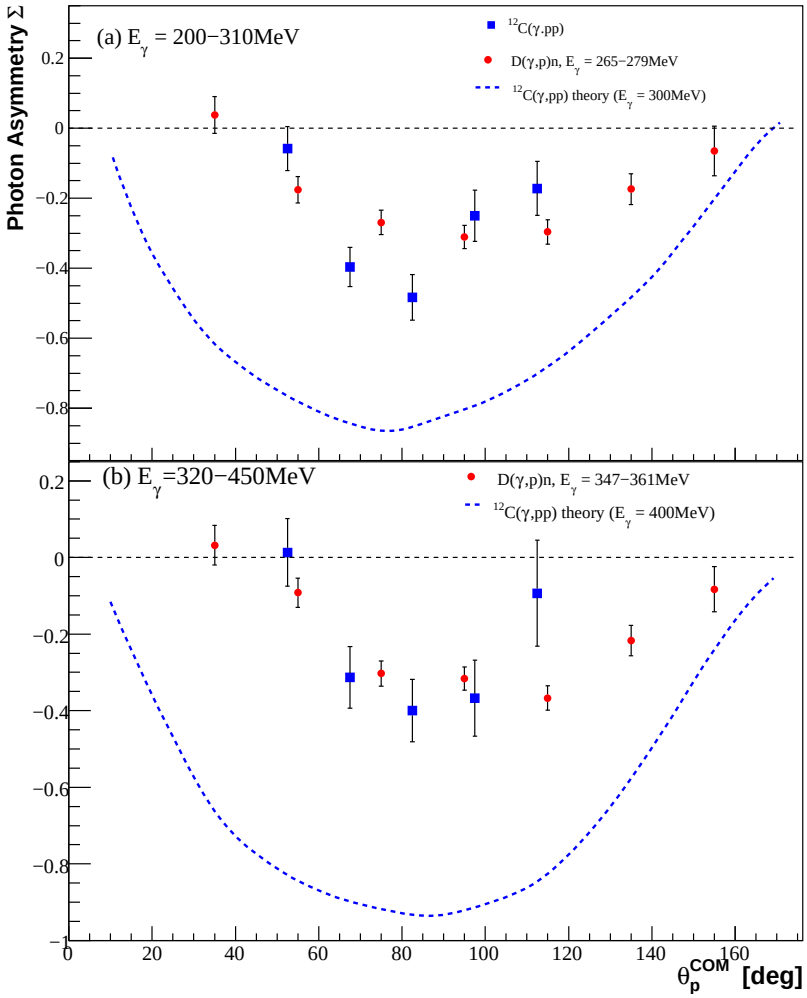

Figure 6.9: Photon asymmetry for (γ,pp) (blue) as a function of θ_p^{COM} for E_m <40 MeV and for the photon energy ranges indicated. Also shown is Σ for $d(\gamma,p)n$ (red) as a function of proton polar angle for two photon energy ranges indicated [102] and Gent theoretical calculations (dashed lines).

similar although $\Sigma_{(\gamma,pp)}$ typically had a larger magnitude. The Gent calculations overpredict the magnitude of the photon asymmetry for both photon energy ranges suggesting the need for P and D absorption to be incorporated into the models. Additionally, the asymmetries presented fall to Σ ∼0 either side of the peak faster than the theory predicts and also that observed in the deuteron measurement. This may be further evidence of the involvement of pairs in relative P and D states and it is necessary to examine how photoabsorption on pairs in higher momentum states

affect the shape of the $\Sigma_{(\gamma,pp)}$ angular distribution. Furthermore, this measurement is likely to include photoabsorption on proton pairs, leaving the residual nucleus in a total angular momentum state other than $J_R = 0^+$ and $J_R = 2^+$. Inclusion of additional states may bring the theory closer to the results presented here.

The calculations for ($\overrightarrow{\gamma}$,pn) were compared with d($\overrightarrow{\gamma}$,p)n data to test whether S-wave absorption automatically implies deuteron like behaviour [9]. For E_γ ∼100 MeV there was little resemblance between the ^{12}C calculations and deuteron photodisintegration results. At these energies, one-body photoabsortpion plays an important role for d($\overrightarrow{\gamma}$,p)n whereas the Gent calculation highlights the importance of MEC. Into the Δ-region, the (γ,pn) calculated distributions for E_γ=300 MeV and E_γ=400 MeV are similar to the deuteron data, indicating similar mechanisms contribute to both reactions. Surprisingly, the (γ,pp) measurements presented are also remarkably similar to d($\overrightarrow{\gamma}$,p)n results [102], with the comparison shown in figure 6.9. For E_γ=200-310 MeV, $\Sigma_{(\gamma,pp)}$ has a similar shape but a larger magnitude at the peak than the deuteron data. In the higher photon energy range, $\Sigma_{(\gamma,pp)}$ is closer $\Sigma_{d(\gamma,p)n}$, suggesting similar mechanisms involving the Δ dominate.

In the higher missing energy region, E_m=40-70 MeV, the angular variation of Σ is similar to that observed for low E_m although the magnitude is somewhat reduced for E_γ=200-310 MeV (figure 6.10). Here the angular distribution is flatter than for E_m <40 MeV and the smaller magnitude at the peak, $\Sigma \sim -0.24$ is perhaps due to increased contributions from FSI and other processes. The asymmetry drops to zero slower on either side of the peak. The asymmetry has increased magnitude in the higher photon energy data and there is better agreement between E_m=40-70 MeV and E_m <40 MeV. However, the statistics are poorer and there is little data at backwards angles, although Σ doesn't appear to drop off as quickly in this region.

Before any definite conclusions can be drawn from the angular distributions, a detailed comparison between the results presented and theory must be carried out. More detailed calculations involving pairs in higher relative angular momentum states over a range of photon energies and emission angles are ongoing and the data presented would offer a stringent test of the model.

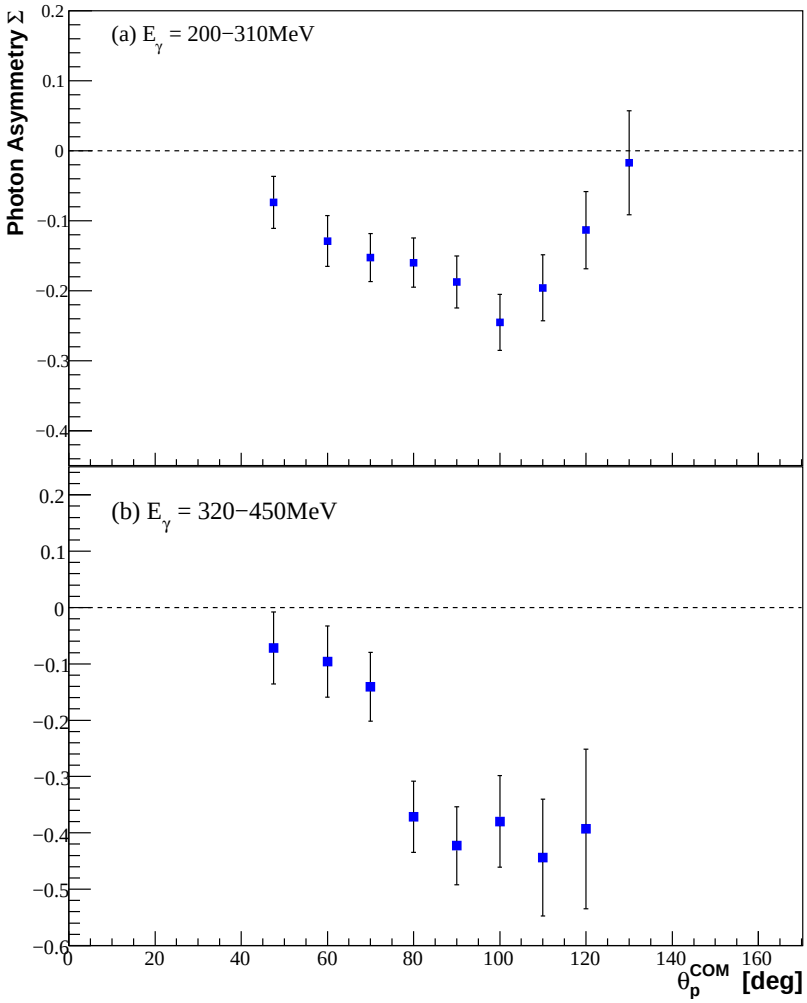

Figure 6.10: Photon asymmetry for (γ,pp) (blue) as a function of θ_p^{COM} for E_m =40-70 MeV and for the photon energy ranges indicated.

6.5 E_m >100 MeV

For E_m >70 MeV, multistep processes are predicted to dominate the reaction cross section [24, 30, 48]. At low photon energies (E_γ <250 MeV), comparison of missing energy spectra with Valencia model calculations [31] indicates that contributions from initial photon absorption on a nucleon pair followed by FSI, 3N absorption and pion production with absorption in the nucleus all have similar strengths for E_m=70-100 MeV. There will also be some relatively small contributions from direct knockout in this region owing to the poor missing energy resolution (∼35 MeV) of the experiment. Beyond E_m=100 MeV the observed reaction strength is dominated

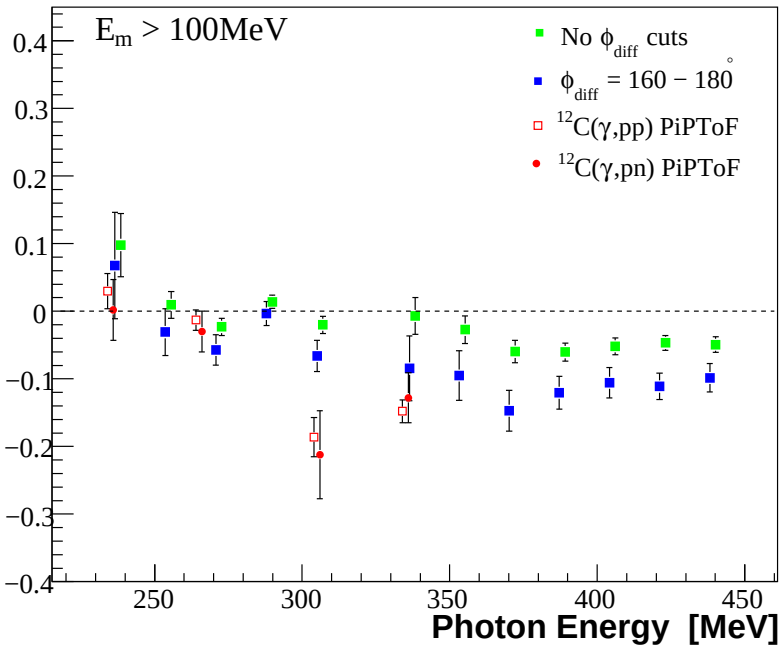

Figure 6.11: Σ for $^{12}C(\gamma,pp)$ with (blue squares) and without (green squares) angular cuts, as a function of E_γ, for E_m >100 MeV compared with data from $^{12}C(\gamma,NN)$ [25].

by pion production. This mechanism dominates further above E_γ=300 MeV. In both reaction channels the most significant process involves pion reabsorption on a pair of nucleons, although pion rescattering also contributes.

The angular correlation between the emitted nucleons in two-step processes is much weaker than in direct two-nucleon emission and the photon energy dependence at high E_m was studied with and without angular cuts applied to the data. No cuts on P_r were applied to the data. Figure 6.11 shows the photon energy dependence of Σ averaged over the total angular acceptance of the CB, and for $\phi_{\text{diff}} = 160 - 180°$. The results are compared with Σ for $^{12}C(\gamma,pp)$ and $^{12}C(\gamma,pn)$ reactions for E_m > 100 MeV taken with the PiPToF setup in A2 [25]. The PiPToF measurements were made with no angular cuts placed on their data.

With and without angular cuts, Σ shows a similar energy dependence to that observed by Powrie *et al.* for $(\overrightarrow{\gamma},NN)$ reactions at high E_m. The asymmetry is consistent with zero for E_γ <300 MeV but increases at higher energies. This may

reflect the change from 2N absorption followed by FSI, to pion production followed by pion reabsorption as the Δ resonance is approached. The observed negative asymmetry in the Δ region may arise from the large asymmetry of the initial pion production process. Previous measurements have shown that pion production on the proton has large negative asymmetries: $\Sigma \sim -0.35$ for p($\overrightarrow{\gamma}, \pi^+$)n and $\Sigma \sim -0.45$ for p($\overrightarrow{\gamma}, \pi^0$)p at E_γ $\sim$300 MeV [103]. The transfer of a large part of the initial asymmetry is possible as the measured $d(\pi^+$,pp) cross section is strongly peaked at forward-backwards angles [104]. In addition to some reduction in Σ due to FSI, the asymmetry of the initial process may be diluted in complex nuclei by the Fermi motion of the nucleons involved. When no angular cuts are applied to the data, the asymmetry for E_γ >300 MeV is significantly smaller than that observed in the PiPToF measurements. This may reflect the larger angular coverage explored by this measurement. For events where proton pairs are ejected at smaller ϕ_{diff}, the asymmetry of the initial process is likely to be washed away. The present experiment had full azimuthal coverage unlike the PiPToF measurement and more pairs away from back-to-back kinematics are sampled, thus giving an asymmetry with a smaller magnitude than seen previously. When back-to-back cuts are imposed on the data, Σ has a larger magnitude in the Δ-region which is closer to the PiPToF results above E_γ=300 MeV. These kinematics sample the peak of the $d(\pi^+$,pp) cross section and it is more likely that the initial asymmetry of the initial pion production is preserved. The results at high E_m are consistent with such an explanation although detailed modelling would be needed to substantiate this.

6.6 Systematic Uncertainties

In the measurement of a reaction cross section the main source of systematic uncertainty comes from the uncertainty in the physical position of the detector systems, their detector efficiencies, uncertainty in target density and for experiments with polarised photons, the uncertainty in photon polarisation. For asymmetries, most of the above systematic errors cancel, leaving the uncertainty in the polarisation as the major source systematic uncertainty.

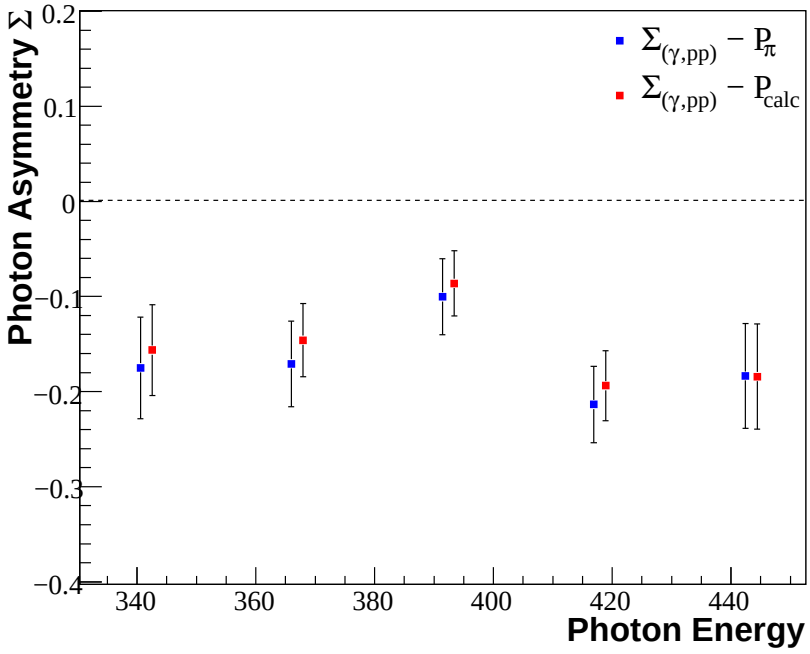

Figure 6.12: The photon energy dependence of $\Sigma_{(\gamma,pp)}$ for E_m=40-70 MeV using the measured polarisation from (γ,π^0) (blue) and the polarisation derived from a fit to the enhancement spectra shown in figure 5.13 (red).

The systematic uncertainty in the photon asymmetry due to the systematic uncertainty in the photon polarisation can be estimated by performing the $^{12}C(\overrightarrow{\gamma}$,pp) analysis using both the calculated polarisation (figure 5.17) and the polarisation derived from $^{12}C(\overrightarrow{\gamma},\pi^0)$. Figure 6.12 plots the photon energy dependence of $\Sigma_{(\gamma,pp)}$in the range E_γ=320-450 MeV for E_m=40-70 MeV. In this region, the uncertainty in photon polarisation is large, with the largest discrepancy between calculation and measurement of the order 10%. On average, the larger polarisation obtained from the coherent bremsstrahlung calculation (figure 5.13), reduces the magnitude of Σ by only ∼0.02. Figure 6.12 is indicative of the systematic uncertainty in P for all plots as a function of E_γ. For the lower photon energy range, the absolute uncertainty in the photon polarisation is smaller, with ΔP ∼3%. The corresponding uncertainty in Σ due to ΔP for E_γ <300 MeV is thus less than 0.02.

A systematic uncertainty may also arise due to particle misidentification in the PID and an estimate of this uncertainty was made by studying Σ with tighter cuts

around the proton ridges observed in the ΔE-E plots (figure 4.8). The contamination of the signal, most probably due to charged pions falling within the proton cut, was found to be fairly small affecting the magnitude of Σ by <0.01. A further systematic uncertainty may be introduced due to misidentification of the azimuth of the reaction plane using the prescription of equation 6.4. A measure of the associated uncertainty was estimated by analysing the data for $\phi_{diff} = 160 - 180°$ and $170 - 180°$. For the latter, the pair are ejected more back-to-back and the azimuth of the reaction is better defined than for $\phi_{diff} = 160 - 170°$. The tighter cut applied ϕ_{diff} increased the magnitude of Σ by ∼0.01. This difference in Σ is small compared to the difference between $\Sigma_{(\gamma,pp)}^{\phi_{diff}=160-180°}$ and $\Sigma_{(\gamma,pp)}^{\phi_{diff}=140-160°}$, suggesting that most of the dilution in Σ at smaller ϕ_{diff} is probably due to increased contributions from indirect processes.

Overall the absolute systematic uncertainty in the measured asymmetries are estimated to be no more than 0.03 for E_γ <320 MeV and no more than 0.05 for E_γ >320 MeV. The systematic uncertainty in the measurement of Σ is dominated by the uncertainty in the photon polarisation. As the systematic uncertainties due to the uncertainty in polarisation, illustrated in figure 6.12, are relatively small compared to the statistical accuracy of the measurement, it is assumed that the statistical uncertainty dominates the measurement and the results plotted in this chapter are presented with statistical error bars only.

Chapter 7

Conclusions and Further Work

Measurements of the photon asymmetry, using linearly polarised photons, of two-nucleon knockout reactions are predicted to be sensitive to details of photonuclear reaction mechanisms. In particular, they are expected to be sensitive to interference between contributions from one- and two-body currents. In this thesis, the most extensive study to date of the $^{12}C(\overrightarrow{\gamma}$,pp) reaction using linearly polarised photons has been presented. The work has extended previous studies of ($\overrightarrow{\gamma}$,NN) reactions, measuring Σ for photon energies up to 450 MeV with $\sim$94% solid angle coverage. To examine which processes govern the (γ,pp) reaction a study has been made of how Σ varies with photon energy for different missing energy regions which emphasise absorption of pairs from different shell configurations. Additionally, the first measurements of the angular dependence of $\Sigma_{(\gamma,pp)}$ have been presented. To aide the interpretation of the experimental results, a comparison was made to previous $^{12}C(\overrightarrow{\gamma}$,NN) measurements and theoretical predictions based on the Gent model of direct two-nucleon knockout.

7.1 Conclusions

The photon asymmetry for $^{12}C(\overrightarrow{\gamma}$,pp) presented was found to be mostly negative. Generally, with increasing E_m, the magnitude of Σ dropped towards 0 with the asymmetry showing a similar missing energy dependence for both photon energy ranges sampled. The asymmetry is most negative for E_m <40 MeV where most of

the reaction strength comes from direct knockout processes. For E_m=40-70 MeV, the observed asymmetry is reduced compared to E_m <40 MeV giving indication of larger contributions from FSI and multi-step processes. However, applying a cut to recoil momentum, P_r <300 MeV/c, emphasises direct knockout processes in the higher missing energy region and Σ for E_m <40 MeV and E_m=40-70 MeV are closer in magnitude.

At low missing energies, the photon energy dependence of the asymmetry of $\Sigma_{(\gamma,pp)}$ has a similar or larger magnitude to $\Sigma_{(\gamma,pn)}$ indicating the dominant process is direct knockout with only small contributions from FSI. The observed asymmetries have a rather flat photon energy dependence although $\Sigma_{(\gamma,pp)}$ is most negative for E_γ >300 MeV. The similarities in Σ for both channels suggest the common mechanism responsible for two-nucleon knockout at low E_m and at the photon energies studied is absorption on Δ-currents. The photon energy range of the measurement is limited as the cross section decreases at high photon energies and it is unfeasible to study Σ much beyond E_γ=450 MeV. Looking at more extreme kinematics, sampling high initial pair momentum where the ejected pair come out with smaller ϕ_{diff} was not very productive as it was found to dilute the magnitude of Σ. The largest signal came from the direct process and the asymmetry decreases with $\mathbf{P}_r$. The asymmetry for $^{12}C(\overrightarrow{\gamma}$,pp) was shown to have a strong angular dependence for both missing energy and photon energy regions investigated. These results offer a sensitive test of theoretical calculations and a comparison will be provided by new calculations using an unfactorised model of direct 2N knockout developed by the Pavia group which are ongoing [105].

Calculations using the Gent model predicted asymmetries which are much less negative than the Gottfried picture of photoabsorption on pairs in a relative S state, giving an additional signature of Δ-mechanisms which proceed through relative P states. However, the model overpredicts the magnitude of Σ which is on average a factor of $\sim$2 more negative than the experiment. In the work of Powrie *et al.* [25], the discrepancy between theory and experiment was most apparent in the photon energy dependence of $d\sigma_\parallel$ and $d\sigma_\perp$, which predicted too large a peak in $d\sigma_\perp$. This suggests that the Gent calculations overpredict the strength of the Δ-resonance.

For higher missing energy, E_m >100 MeV, photon asymmetries close to zero were observed for photon energies less than ∼300 MeV. A significantly more negative Σ was measured at higher photon energies. The magnitude of Σ was amplified for E_γ >300 MeV by selecting pairs which were detected back-to-back. At high E_m, the energy dependence of $\Sigma_{(\gamma,pp)}$ was found to be comparable to $\Sigma_{(\gamma,pn)}$. Below E_γ=300 MeV, the results give indication that a significant contribution of the reaction strength comes from initial NN absorption followed by FSI. Above 300 MeV, the larger asymmetry suggests initial $(\gamma, N\pi)$ processes followed by subsequent pion reabsorption play an important role in the observed (γ,NN) strength at higher missing energies.

7.2 Further Work

The major drawback of the current experiment was the poor missing energy resolution making it difficult to cleanly separate absorption from different nucleon shells. Previous work [94] has demonstrated that the Crystal Ball can detect low energy nuclear decay photons in coincidence with the high energy products of photoproduction. Looking for decay gammas in coincidence with (γ,pp) events would allow separation of inelastic events from those which leave the recoiling ^{10}Be nucleus in its ground state, thereby cleaning up the ground state signal. By selecting events with low lying gammas, it may be possible to identify a specific low lying state. However, the decay photons may also cascade from high excitations through low lying levels. For higher excitation, corresponding to (1s)(1p) absorption, a decay via one or two large energy decay gammas could be easily identified. A cascade of low energy gammas, which would be less easy to interpret, may be more likely. Nevertheless, identification of decay photons together with tagged (γ,pp) events is certainly worth investigating.

Higher resolution detectors, utilising Ge and Si detectors potentially offer an overall E_m resolution of ∼1.5 MeV [106] which is sufficient to separate low lying final states. Such an experiment would allow a high resolution study of the reaction cross section and photon asymmetry for excitation of the A-2 residual with different

angular momentum states J_R.

Another problem experienced during the experiment was with the photon polarisation. This work highlighted the need for more sensitive beam position monitoring to ensure the coherent peak remains stable during data collection. For future experiments using polarised photons a slightly wider beam collimator with diameter 2-2.5 mm would be used, which would be less sensitive to slight drifts in the MAMI electron beam. Although this will reduce the peak polarisation, more usable data will be recovered if the peak remains relatively stable during the beamtime. Further work on accurately determining the degree of linear polarisation is discussed briefly in section 7.3.

It would be interesting to look at the (γ, NN) reaction for other targets such as ^{16}O to examine how the asymmetry depends on specific state wavefunction. This will help gain a fuller understanding of the longer range exchange processes in the nuclear environment. It is also desirable to perform a higher statistics measurement of $\Sigma_{(\gamma,NN)}$ for E_γ >300 MeV. At these energies, both channels are expected to proceed mainly through Δ-currents and one would expect the photon asymmetry to be similar for (γ, pp) and (γ, pn).

A more rigorous analysis, presenting the data in the centre-of-mass (CoM) frame of the photon and the nucleon pair is desirable. This frame is the fundamental interaction frame and also the natural frame in which to compare the data with theoretical calculations. The analysis is somewhat more complicated in this frame as the angle of the incident photon varies on an event by event basis depending the magnitude and direction of P_{pair} and the momentum of the incident photon. The effective degree of linear polarisation and the plane of polarisation also changes in this frame. A discussion of the kinematics of the ($\overrightarrow{\gamma}$,NN) reaction in this frame is provided in appendix C.

7.3 Further Work on Determining Linear Polarisation

This work has demonstrated that the degree of polarisation for linearly polarised photons produced via coherent bremsstrahlung can be well determined from coherent bremsstrahlung theory if the peak remains stable. This is not always the case and often an independent measurement of polarisation is required. Coherent pion photoproduction from ^{12}C has been demonstrated as a viable photon polarimeter for photon energies up to E_γ ~320 MeV, as for purely coherent events the amplitude of the asymmetry $\bar{P}\Sigma$ is equivalent to the polarisation as Σ=-1. Beyond 320 MeV, the coherent signal is diluted due to increased contributions from incoherent processes and the pion measurement instead defines the lower limit of P. Identification of low energy decay photons in coincidence with photoproduced pions have recently been demonstrated in the Crystal Ball [94] as an excellent way to tag incoherent $A(\overrightarrow{\gamma},\pi^0)A^*$ events. Applying a similar analysis to this data but vetoing any events in which decay gammas are detected together with the π^0 is likely to give a cleaner coherent signal and the polarisation extracted through the azimuthal asymmetry will yield a polarisation closer to its true value (bringing the lower limit closer to P).

This technique can be extended to any spin zero nucleus to provide a measure of the photon polarisation. Whilst offering an excellent method of determining the photon polarisation for the first coherent peak in this experiment, using $A(\overrightarrow{\gamma},\pi^0)A$ reactions as a polarimeter is very limited. It is only feasible at intermediate photon energies up to E_γ ~400 MeV (above which the cross section decreases rapidly) and the method is very much target dependent. Much of the experimental programmes at tagged photon facilities such as A2, CLAS at JLab [107] and CBELSA in Bonn [108] are dedicated to the study of baryon spectroscopy. For these experiments ^1H and ^2H targets are more common and polarised photons at higher energies are required. A similar approach, using a high statistic hadronic interaction in the target with a well defined asymmetry such as single pion production can be utilised as a polarimeter. This method is again experiment specific and absolutely requires good calibration

and small systematic uncertainty to accurately monitor the photon polarisation.

Alternative methods of polarimetry based on pair production ($\gamma \rightarrow e^+e^-$) offer a reaction independent method for measuring the polarisation [109]. The plane of the e^+e^- pair depends on the polarisation vector of the incident photon. The polarised cross section, σ_P, can be expressed in terms of the unpolarised cross section, σ_0, via:

$$\sigma_p = \sigma_0 \left(1 + P_L A \cos(2\phi)\right) \tag{7.1}$$

where A is the analysing power of a particular experimental setup and P_L is the photon polarisation. A pair polarimeter designed for this purpose at the Yerevan synchrotron yielded analysing powers of 0.25-0.28 [110]. The main advantage of a polarimeter based on pair production is that is well described by QED. However, it is experimentally difficult to measure due to the small characteristic opening angle of the pair, $\theta = \frac{m_e c^2}{E_\gamma}$. This demands high position resolution detectors such as Si microstrip or pixel detectors. Such a polarimeter still needs to be built and requires thorough calibration and simulation before reliable polarisations can be extracted using this technique.

Appendix A

Polarised Photon Production

A beam of linearly polarised photons with a high degree of linear polarisation and intensity can be produced by coherent bremsstrahlung. In the bremsstrahlung process, a charged particle is decelerated when moving in the Coulomb field of an atom, with the emission of a real photon and some small momentum transfer to a third body. In this appendix, there is focus on bremsstrahlung resulting from the deceleration of a relativistic electron in the field of an atomic nucleus ($e+N \rightarrow N^{'}+e^{'}+\gamma$). Coherent bremsstrahlung occurs when the momentum transfer to the atom(s) is restricted to a unique value because the electron is moving in a regularly spaced lattice structure. From energy and momentum conservation (in natural units $\hbar = c = 1$):

$$\mathbf{p} = \mathbf{q} + \mathbf{p}^{'} + \mathbf{k} \tag{A.1}$$

$$E_0 = E^{'} + k \tag{A.2}$$

where the momenta are represented by $\mathbf{p}$ and $\mathbf{p}^{'}$ for the initial and final respectively, $\mathbf{k}$ for the photon and $\mathbf{q}$ is the momentum transferred to the crystal. The initial and final energy of the electron are denoted by E and $E^{'}$ respective and the photon energy is denoted k. The energy transfer to the crystal, T, is neglected in equation A.2 as it is negligible compared to $E^{'}$ and k owing to the large nuclear mass.

The bremsstrahlung process is azimuthally symmetric around the direction of $\mathbf{p}$ and it is natural to split the momentum transfer to the nucleus into its longitudinal (q_l) and transverse (q_t) components with respect to $\mathbf{p}$. This is illustrated by figure

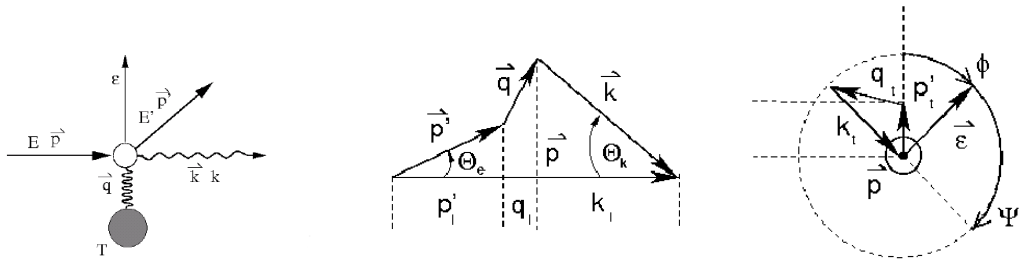

(a) (b) (c)

Figure A.1: (a) Kinematics of bremsstrahlung. (b) Momentum decomposition into longitudinal components. (c) Momentum decomposition in transverse components.

A.1. It is possible to calculate the limits on the recoil momentum imparted to the nucleus which defines an allowed region in momentum space [63, 64] and is defined by the relationships:

$$\delta \leq q_l \lesssim 2\delta \tag{A.3}$$

$$0 \leq q_t \lesssim 2x \tag{A.4}$$

where:

$$\delta = \frac{1}{2E}\frac{x}{1-x} \tag{A.5}$$

denotes the minimum recoil for fixed $x(=\frac{k}{E})$ which is obtained for forward emission of electron and photon. Although, δ increases strongly as x approaches 1, it corresponds to a small momentum transfer compared to $p_l^{'}$ and k_l. The allowed momentum region, often referred to as the momentum pancake due to its small longitudinal component compared to its large transverse extent, sweeps through momentum space as x increases and is shown by figure A.2.

The differential cross section for bremsstrahlung for a photon with energy k is proportional to $(1/\mathrm{k})\cos^2\psi$, where ψ is the azimuthal angle of the polarisation vector around **p** with respect to the plane (**p**,**q**). Therefore, the cross section peaks when the polarisation vector lies in the plane of the incident electron momentum and the momentum transfer [63]. In an amorphous radiator the momentum transfer to the nucleus can lie anywhere in the azimuthally symmetric momentum *pancake* and the resulting photon energy distribution has a smooth 1/k dependence. On average, an unpolarised photon beam is produced by scattering off an amorphous radiator.

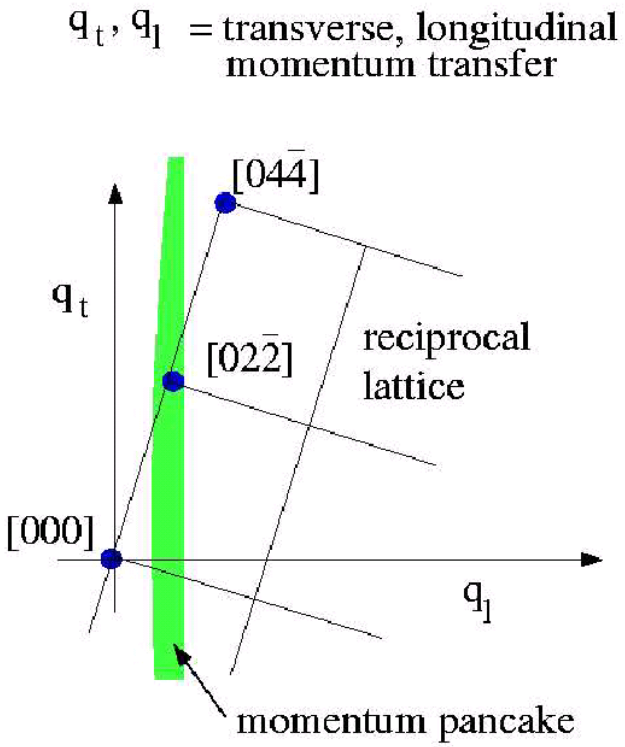

Figure A.2: Representation of the reciprocal lattice and the allowed momentum pancake in momentum space. By aligning the crystalline radiator, it is possible to restrict a single reciprocal lattice vector within the momentum pancake [63].

With a crystalline radiator, the momentum transfer is to the lattice rather than an individual nucleus, and q is constrained to be equal to one of the lattices reciprocal lattice vectors described by:

$$\mathbf{g} = \sum_{k=1}^{3} h_k \mathbf{b}_k \tag{A.6}$$

where $\mathbf{g}$ is a reciprocal lattice vector, $\mathbf{b}_k$ is a reciprocal lattice basis vector and h_k corresponds to the set of Miller indices [h_1,h_2,h_3].

The crystal can then be aligned to ensure that only one reciprocal lattice vector lies within the momentum pancake (figure A.2). The recoil momentum is further constrained to $\mathbf{g}$ and the azimuthal symmetry around $\mathbf{p}$ is broken and the photon polarisation lies in the plane ($\mathbf{p}$,$\mathbf{g}$). As x increases, the minimum longitudinal transfer $q_l^{\max}$ shifts to higher values until the $\mathbf{g}$ drops out of the *pancake*. This leads to a discontinuity in the coherent bremsstrahlung spectrum which is denoted as the

coherent edge in chapter 5. A detailed discussion of coherent bremsstrahlung and the kinematics involved is provided by Timm [63].

Appendix B

Pion Kinematics

B.1 Pion Decay

For the $\pi^0 \longrightarrow \gamma\gamma$ decay, the invariant mass of the two photons should equal the rest mass of the π^0. The invariant mass can be simply calculated:

$$m^2 = E^2 - \mathbf{p}^2 \tag{B.1}$$

$$\begin{aligned} m_{\gamma\gamma}^2 &= (E_1 + E_2)^2 - (\mathbf{p}_1 + \mathbf{p}_2)^2 \\ &= E_1^2 + E_2^2 + 2E_1E_2 - (p_1^2 + p_2^2 + 2p_1p_2cos\psi) \\ &= 2E_1E_2(1 - cos\psi) \end{aligned} \tag{B.2}$$

where E_1 and E_2 are the energies of both photons and ψ is the opening angle between the pair. For a photon pair arising from a pion decay $m_{\gamma\gamma} = m_\pi$. The opening angle between the pair is then:

$$\sin\frac{\psi}{2} = \frac{m_\pi}{2\sqrt{E_1E_2}} \tag{B.3}$$

B.2 Pion Energy

For coherent π^0 photoproduction from a nucleus, if the incident photon energy E_γ and the mass of the nuclear target M is known, then the energy of the pion can be calculated. The following derivation is taken from reference [74]. The total energy

in the lab frame of the incoming photon and target nucleus ($\sqrt{s}$) can be calculated:

$$\begin{aligned} s &= (E_\gamma + E_A)^2 - (\mathbf{p}_\gamma + \mathbf{p}_A)^2 \\ &= (E_\gamma + M)^2 - E_\gamma^2 \\ &= E_\gamma^2 + 2E_\gamma M + M^2 - E_\gamma^2 \\ &= 2E_\gamma M + M^2 \end{aligned} \tag{B.4}$$

This is equivalent to the total energy available in the centre-of-mass frame of the pion and target recoil:

$$\begin{aligned} s &= (E_\pi^{\mathrm{cm}} + E_A^{\mathrm{cm}})^2 - (\mathbf{p}_\pi^{\mathrm{cm}} + \mathbf{p}_A^{\mathrm{cm}})^2 \\ &= (E_\pi^{\mathrm{cm}} + E_A^{\mathrm{cm}})^2 \\ \sqrt{s} &= E_\pi^{\mathrm{cm}} + E_A^{\mathrm{cm}} \end{aligned} \tag{B.5}$$

The difference in the invariant masses of the recoil nucleus and pion is:

$$\begin{aligned} M^2 - m_\pi^2 &= (E_A^{\mathrm{cm}2} - \mathbf{p}^{\mathrm{cm}2}) - (E_\pi^{\mathrm{cm}2} - \mathbf{p}^{\mathrm{cm}2}) \\ &= E_A^{\mathrm{cm}2} - E_\pi^{\mathrm{cm}2} \\ &= (E_A^{\mathrm{cm}} + E_\pi^{\mathrm{cm}})(E_A^{\mathrm{cm}} - E_\pi^{\mathrm{cm}}) \\ &= \sqrt{s}(E_A^{\mathrm{cm}} - E_\pi^{\mathrm{cm}}) \end{aligned} \tag{B.6}$$

The difference between the recoil energy and the pion energy can be accessed by rearranging equation B.6:

$$E_A^{\mathrm{cm}} - E_\pi^{\mathrm{cm}} = \frac{M^2 - m_\pi^2}{\sqrt{s}} \tag{B.7}$$

Subtracting B.5 from B.7 gives:

$$\begin{aligned} 2E_\pi^{\mathrm{cm}} &= \sqrt{s} - \frac{M^2 - m_\pi^2}{\sqrt{s}} \\ E_\pi^{\mathrm{cm}} &= \frac{s - M^2 + m_\pi^2}{2\sqrt{s}} \end{aligned} \tag{B.8}$$

The energy of a coherently produced π^0 in the pion-nucleus centre-of-frame can then be derived by substituting B.4 into B.8:

$$E_\pi^{\mathrm{cm}} = \frac{2E_\gamma M + m_\pi^2}{2\sqrt{E_\gamma M + M^2}} \tag{B.9}$$

B.3 Pion Missing Energy

The pion missing energy used to separate coherent and incoherent events in chapter 5 is defined as:

$$\Delta E_\pi = E_\pi^{\rm cm}(E_\gamma) - E_\pi^{\rm cm}(\gamma_1\gamma_2) \tag{B.10}$$

where $E_\pi^{cm}(E_\gamma)$ is defined as in equation B.9. $E_\pi^{cm}(\gamma_1\gamma_2)$ is the detected pion energy transformed into the pion-nucleus centre of mass frame:

$$E_\pi^{\rm cm}(\gamma_1\gamma_2) = \gamma(E_\pi - \beta p_{z\pi}) \tag{B.11}$$

where E_π is the detected pion energy and $p_{z\pi}$ is the component of the pion momentum along the beam direction.

$$\beta = \frac{E_\gamma}{E_\gamma + M} \tag{B.12}$$

$$\gamma = \frac{1}{\sqrt{1-\beta^2}} \tag{B.13}$$

From momentum conservation $p_{z\pi}$ is the sum of the components of the two decay photons momentum along the beam direction:

$$\begin{aligned} p_{z\pi} &= p_{z1} + p_{z2} \\ &= E_1\cos\theta_1 + E_2\cos\theta_2 \end{aligned} \tag{B.14}$$

The detected photon energy in the lab frame is simply:

$$E_\pi = E_1 + E_2 \tag{B.15}$$

However, this does not use any of the angular information recorded by the detectors. Defining the energy sharing parameter X as:

$$\begin{aligned} X &= \frac{E_1 - E_2}{E_1 + E_2} \\ &= \frac{E_1 - E_2}{E_\pi} \end{aligned} \tag{B.16}$$

From this, E_1 and E_2 are:

$$E_1 = \frac{E_\pi}{2}(1+X) \tag{B.17}$$

$$E_2 = \frac{E_\pi}{2}(1-X) \tag{B.18}$$

The product of E_1 and E_2 gives:

$$E_1 E_2 = \frac{E_\pi^2}{4}(1 - X^2) \tag{B.19}$$

Rearranging B.19 gives:

$$E_\pi^2 = \frac{4E_1 E_2}{1 - X^2} \tag{B.20}$$

Combining with B.2 gives:

$$\begin{aligned} E_\pi^2 &= \frac{4}{1 - X^2}\frac{m_\pi^2}{2(1 - \cos\psi)} \\ E_\pi &= \sqrt{\frac{2m_\pi^2}{(1 - X^2)(1 - \cos\psi)}} \end{aligned} \tag{B.21}$$

The detected pion energy transformed to the pion-nucleus centre of mass frame can then be calculated:

$$E_\pi^{cm}(\gamma_1\gamma_2) = \gamma\left(\sqrt{\frac{2m_\pi^2}{(1 - X^2)(1 - \cos\psi)}} - \beta(E_1\cos\theta_1 + E_2\cos\theta_2)\right) \tag{B.22}$$

Appendix C

(γ,pp) Kinematics

In the lab frame, a photon with momentum $\mathbf{P}_\gamma$ is absorbed by a correlated nucleon pair in the nucleus with total momentum $\mathbf{P}_r$ and both nucleons are ejected from the nucleus. The initial interaction is illustrated in figure C.1(a). To transform this system to the centre-of-mass frame of the photon and nucleon pair, the magnitude and direction of the boost vector β_c must be derived. The boost vector can be derived from:

$$\beta_c = \frac{P_{\rm tot}}{E_{\rm tot}} \tag{C.1}$$

$$P_{\rm tot} = \sqrt{P_\gamma^2 + P_r^2 - 2P_r P_\gamma \cos\theta_r} \tag{C.2}$$

$$E_{\rm tot} = P_\gamma + \sqrt{P_r^2 + 4M_n^2} \tag{C.3}$$

where $P_{\rm tot}$ and $E_{\rm tot}$ are the total momentum and energy of the initial system and M_n=938 MeV is the proton mass. The individual momenta and angles are defined in figure C.1(a).

The angle β_c makes with respect to the incident photon can be obtained simply via:

$$\cos\theta_c = \frac{P_\gamma - P_r\cos\theta_r}{\sqrt{P_\gamma^2 + P_r^2 - 2P_\gamma P_r\cos\theta_r}} \tag{C.4}$$

Figure C.2 plots the magnitude of β_c for typical pair momentum P_r in the range 50-350 MeV and for photon energies E_γ=200, 300 and 400 MeV. The calculations consider events when the pair move towards and away from the incident photon. In general, the boost vector typically falls within the range β_c=0.1-0.2 although values

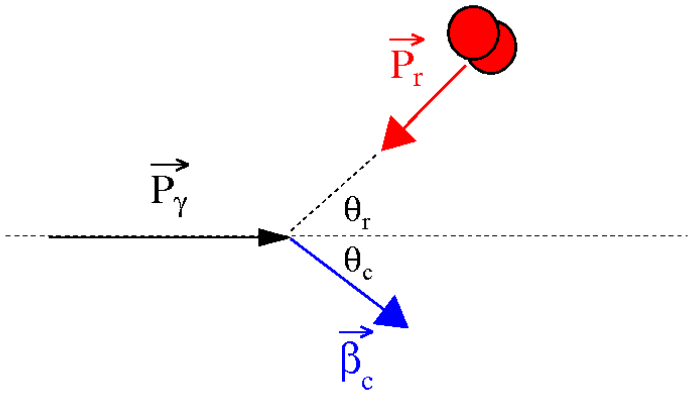

(a)

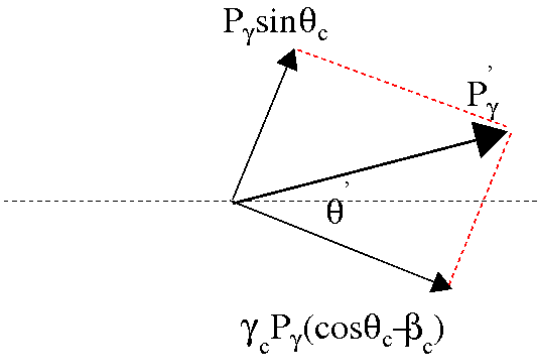

(b)

Figure C.1: (a) Photon absorption on a nucleon-pair with momentum P_r moving at angle θ_r with respect to the incident photon in the lab frame. (b) Photon in the COM frame of photon and proton pair.

up to 0.3 are observed at high P_r when the pair is moving in the same direction as the photon.

The components of P_γ parallel and perpendicular to $\vec{\beta_c}$ are:

$$P_\gamma^{\parallel} = P_\gamma \cos\theta_c \tag{C.5}$$

$$P_\gamma^{\perp} = P_\gamma \sin\theta_c \tag{C.6}$$

In the centre-of-mass frame of the pair and photon, the components $P_\gamma^{'\parallel}$ and $P_\gamma^{'\perp}$ along β_c (figure C.1) are given by:

$$P_\gamma^{'\parallel} = \gamma_c(P_\gamma \cos\theta_c - \beta_c P_\gamma) \tag{C.7}$$

$$P_\gamma^{'\perp} = P_\gamma \sin\theta_c \tag{C.8}$$

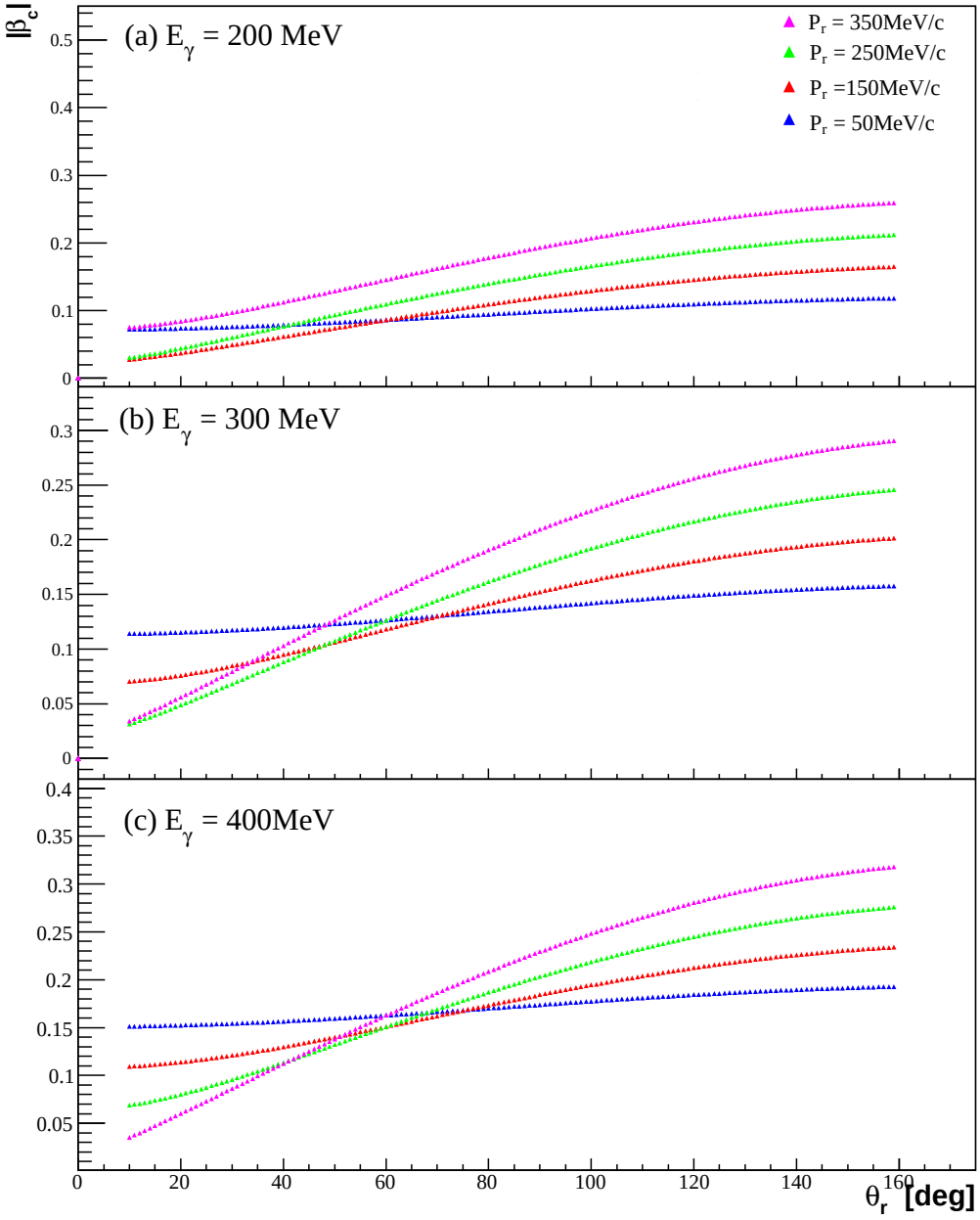

Figure C.2: The magnitude of β_c as a function of P_r, P_γ and θ_r as defined in figure C.1. The blue, red, green and pink markers correspond to P_r = 50, 150, 250 and 350 MeV/c respectively. For (a) P_γ=200 MeV/c, (b) P_γ=300 MeV/c and (c) P_γ=400 MeV/c.

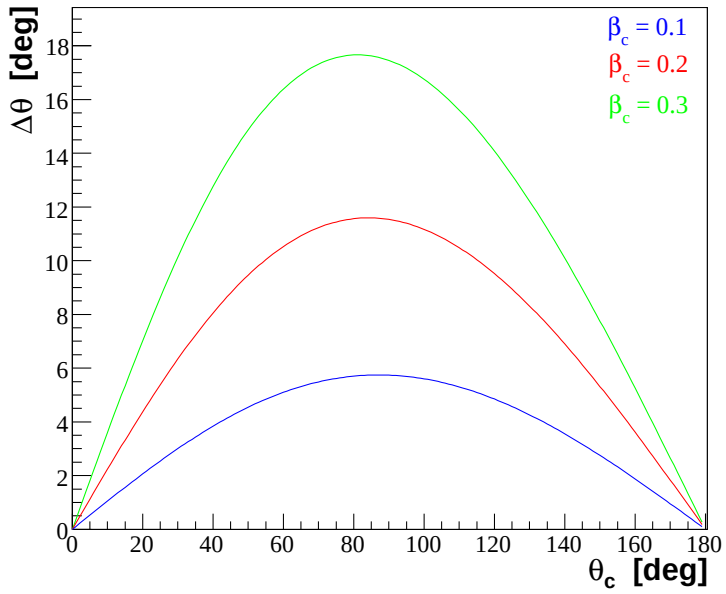

Figure C.3: $\Delta\theta$ as a function of θ_c the angle of the boost vector with respect to z_{lab} as defined in figure C.1 for β_c=0.1 (blue), 0.2 (red) and 0.3 (green).

where $\gamma_c^2 = 1/(1-\beta_c^2)$. The energy of the photon in the COM frame is:

$$P_\gamma^{'} = \gamma_c(P_\gamma - \beta_c P\gamma\cos\theta_c) = \gamma_c P_\gamma(1-\beta_c\cos\theta_c) \tag{C.9}$$

The angle of the transformed photon with respect to $\vec{\beta_c}$ can be accessed:

$$\cos\theta^{'} = \frac{\gamma_c P_\gamma(\cos\theta_c - \beta_c)}{P_\gamma^{'}} = \frac{\cos\theta_c - \beta_c}{1-\beta_c\cos\theta_c} \tag{C.10}$$

The incident angle of the COM photon with respect to the photon beam in the lab frame is simply $\Delta\theta = \theta^{'} - \theta_c$. Figure C.3 plots $\Delta\theta$ for typical magnitudes of β_c and for $\theta_c = 0 - 180°$. The maximum $\Delta\theta \sim 18°$ is relatively small and occurs at large β_c (=0.3), perpendicular to $\vec{P_\gamma}$.

For the measured azimuthal asymmetry to equal the intrinsic asymmetry of the reaction in the COM frame, certain conditions must be satisfied. Firstly, Σ must change relatively slowly with photon energy, as the energy difference between the lab and COM photon, as governed by equation C.9, can be relatively large depending on the magnitude and direction of β_c. Figure C.4 plots the ratio $\frac{E_\gamma^{CM}}{E_\gamma}$ for typical values of β_c. For ($\overrightarrow{\gamma}$,NN) reactions, the theoretical calculations for Σ shown in figure 6.6 show a rather flat energy dependence. Furthermore, one requires the azimuthal

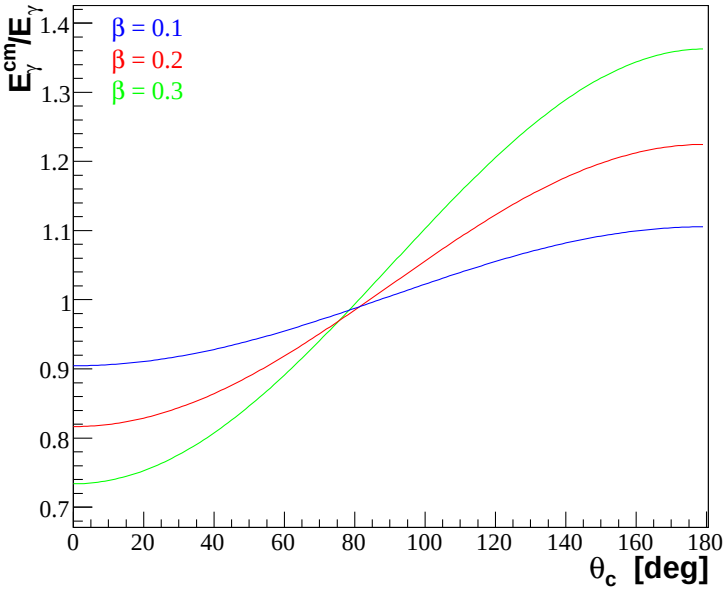

Figure C.4: Ratio $\frac{E_\gamma^{CM}}{E_\gamma}$ as a function of θ_c for β_c=0.1 (blue), 0.2 (red) and 0.3 (green).

angle of the outgoing particle(s) in the lab frame to be similar to that in the COM system and also that the polarisation vector transforms into a similar azimuth in the CoM system. For the small $\Delta\theta$ calculated here, these conditions are satisfied to second order and any smearing in the measured asymmetry is small [111].

Appendix D

Tables of Results

E_m [MeV]	$\Sigma \pm \Delta\Sigma$(stat)		
	All P_r	P_r <300 MeV	P_r >300 MeV
24 - 34	-0.130±0.031	-0.189±0.038	-0.031±0.052
34 - 44	-0.177±0.021	-0.200±0.027	-0.131±0.035
44 - 54	-0.136±0.017	-0.165±0.022	-0.091±0.027
54 - 64	-0.076±0.015	-0.127±0.02	-0.020±0.023
64 - 74	-0.050±0.014	-0.073±0.019	-0.006±0.02
74 - 84	-0.043±0.013	-0.106±0.018	-0.005±0.019
84 - 94	-0.018±0.013	-0.063±0.019	0.025±0.018
94 - 104	-0.005±0.013	-0.053±0.02	0.02±0.019
104 - 114	-0.011±0.014	-0.050±0.021	0±0.019
114 - 124	-0.006±0.015	-0.019±0.023	0.001±0.02
124 - 134	-0.013±0.017	0.038±0.027	-0.055±0.023
134 - 144	-0.036±0.020	-0.033±0.031	-0.03±0.027
144 - 154	-0.011±0.024	-0.032±0.0372	-0.001±0.033

Table D.1: Missing energy dependence of Σ for E_γ=200-310 MeV for all recoil momentum P_r, P_r <300 MeV/c and P_r >300 MeV/c. The results are plotted in figures 6.3(a) and 6.4(a).

E_m [MeV]	$\Sigma \pm \Delta\Sigma$(stat)		
	All P_r	P_r <300 MeV	P_r >300 MeV
14-30	-0.229±0.046	-0.300±0.060	-0.127±0.072
30-46	-0.134 ±0.032	-0.156±0.044	-0.113±0.045
46-62	-0.103±0.025	-0.182±0.037	-0.041±0.033
62-78	-0.094±0.020	-0.157±0.033	-0.056±0.026
78-94	-0.117±0.018	-0.142±0.031	-0.104±0.022
94-110	-0.085±0.017	-0.144±0.031	-0.062±0.020
110-126	-0.085±0.016	-0.085±0.030	-0.086±0.019
126-142	-0.082±0.015	-0.148±0.029	-0.058±0.018
142-158	-0.083±0.015	-0.150±0.029	-0.059±0.018
158-174	-0.027±0.016	-0.081±0.031	-0.008±0.018
174-190	-0.03±0.016	-0.068±0.032	-0.020±0.019
190-206	-0.067±0.018	-0.175±0.034	-0.027±0.021
206-222	-0.031±0.02	-0.041±0.037	-0.026±0.024
222-238	-0.030±0.023	-0.121±0.043	0.004±0.028
238-254	-0.041±0.028	-0.212±0.052	0.028±0.033

Table D.2: Missing energy dependence of Σ for E_γ=320-450 MeV for all recoil momentum P_r, P_r <300 MeV/c and P_r >300 MeV/c. The results are plotted in figures 6.3(b) and 6.4(b).

E_γ [MeV]	P_{ave}	$\Sigma \pm \Delta\Sigma$(stat) (P_r <300 MeV/c)
207.5-224.6	0.44	-0.219±0.108
224.6-241.7	0.54	-0.251±0.087
241.7-258.8	0.63	-0.209±0.065
258.8-275.9	0.69	-0.058±0.060
275.9-293.0	0.71	-0.170±0.060
293.0-310.2	0.64	-0.361±0.082
327.9-353.2	0.33	-0.068±0.115
353.2-378.7	0.39	-0.253±0.102
378.7-404.1	0.46	-0.237±0.088
404.1-429.6	0.53	-0.259±0.088
429.6-455.2	0.55	-0.503±0.107

Table D.3: Photon energy dependence of Σ for E_m <40 MeV, $\phi_{diff} = 160 - 180°$ and P_r <300 MeV/c. Shown in figure 6.6.

E_γ [MeV]	P_{ave}	$\Sigma \pm \Delta\Sigma$(stat)	
		P_r <300 MeV	P_r >300 MeV
207.5-221.2	0.43	-0.137±0.080	-0.170±0.190
221.2-234.8	0.51	-0.188±0.057	-0.332±0.123
234.8-248.5	0.59	-0.273±0.041	-0.114±0.089
248.5-262.2	0.65	-0.190±0.034	-0.126±0.068
262.2-275.9	0.69	-0.172±0.033	-0.081±0.061
275.9-289.6	0.71	-0.145±0.031	-0.034±0.055
289.6-303.3	0.67	-0.157±0.037	-0.215±0.064
303.3-317.1	0.55	-0.198±0.060	-0.113±0.112
327.9-353.2	0.33	-0.248±0.079	-0.153±0.116
353.2-378.7	0.39	-0.268±0.067	-0.344±0.091
378.7-404.1	0.46	-0.113±0.061	-0.066±0.083
404.1-429.6	0.53	-0.292±0.058	-0.178±0.085
429.6-455.2	0.55	-0.171±0.087	-0.235±0.107

Table D.4: Photon energy dependence of Σ for E_m=40-70 MeV for $\phi_{diff} = 160-180°$ and P_r <300 MeV/c and P_r >300 MeV/c. Shown in figure 6.7.

θ_p^{COM} [deg]	$\Sigma \pm \Delta\Sigma$(stat)	
	E_γ=200-310 MeV	E_γ=320-450 MeV
45-60	-0.058±0.063	0.013±0.088
60-75	-0.396±0.056	-0.313±0.080
75-90	-0.483±0.065	-0.400±0.082
90-105	-0.250±0.073	-0.367±0.099
105-120	-0.172±0.077	-0.093±0.138

Table D.5: Angular dependence of Σ for E_m <40 MeV for P_r <300 MeV/c and the photon energy ranges indicated. Shown in figure 6.9.

θ_p^{COM}	$\Sigma \pm \Delta\Sigma$(stat)	
	E_γ=200-310 MeV	E_γ=320-450 MeV
40-55	-0.074±0.037	-0.072±0.064
55-65	-0.129±0.036	-0.096±0.063
65-75	-0.153±0.034	-0.141±0.061
75-85	-0.160±0.035	-0.372±0.063
85-95	-0.187±0.037	-0.423±0.069
95-105	-0.245±0.040	-0.380±0.082
105-115	-0.196±0.047	-0.444±0.104
115-125	-0.113±0.055	-0.393±0.142
125-135	-0.017±0.074	

Table D.6: Angular dependence of Σ for E_m=40-70 MeV for P_r <300 MeV/c and the photon energy ranges indicated. Illustrated in figure 6.10.

E_γ [MeV]	$\Sigma \pm \Delta\Sigma$(stat)	
	$\phi_{diff} = 0 - 180°$	$\phi_{diff} = 160 - 180°$
228.0-248.5	0.098±0.047	0.068±0.079
245.0-265.6	0.009±0.020	-0.031±0.034
262.2-282.7	-0.023±0.013	-0.057±0.023
279.3-299.9	0.014±0.010	-0.004±0.018
296.5-317.1	-0.020±0.013	-0.066±0.023
327.9-344.8	-0.007±0.027	-0.085pm0.048
344.8-361.6	-0.027±0.020	-0.095pm0.037
361.6-378.7	-0.060±0.017	-0.147pm0.030
378.7-395.6	-0.060±0.013	-0.121pm0.024
395.6-412.6	-0.052±0.012	-0.106pm0.022
412.6-429.6	-0.047±0.011	-0.111pm0.019
429.6-446.7	-0.049±0.012	-0.098pm0.021

Table D.7: Photon energy dependence of Σ for E_m >100 MeV for $\phi_{diff} = 0 - 180°$ and $\phi_{diff} = 160 - 180°$ Illustrated in figure 6.11.

Bibliography

[1] Vijay R. Pandharipande, Ingo Sick, and Peter K. A. deWitt Huberts. Independent Particle Motion and Correlations in Fermion Systems. *Rev. Mod. Phys.*, 69(3):981–991, Jul 1997.

[2] J. Pearson. *Nuclear Physics*. A. Hilger, Bristol, 1986.

[3] Otto Haxel, J. Hans D. Jensen, and Hans E. Suess. On the "Magic Numbers" in Nuclear Structure. *Phys. Rev.*, 75(11):1766, Jun 1949.

[4] Maria Goeppert Mayer. On Closed Shells in Nuclei. *Phys. Rev.*, 75(12):1969–1970, Jun 1949.

[5] M. Q. Barton and J. H. Smith. Proton-Neutron Coincidences in the High-Energy Photodisintegration of Lithium. *Phys. Rev.*, 95(2):573–574, Jul 1954.

[6] S. Boffi. *Electromagnetic response of atomic nuclei*. Oxford University Press, USA, 1996.

[7] Kurt Gottfried. On the determination of the nuclear pair correlation function from the high energy photo-effect. *Nuclear Physics*, 5:557 – 587, 1958.

[8] J. S. Levinger. The high energy nuclear photoeffect. *Phys. Rev.*, 84(1):43–51, Oct 1951.

[9] J. Ryckebusch et al. Polarization degrees of freedom in photoinduced two-nucleon knockout from finite nuclei. *Phys. Rev. C*, 57(3):1319–1336, Mar 1998.

[10] C. Giusti, F. D. Pacati, and M. Radici. Two-proton emission induced by real and virtual photons. *Nuclear Physics A*, 546(3):607 – 621, 1992.

[11] H. Müther and A. Polls. Two-body correlations in nuclear systems. *Progress in Particle and Nuclear Physics*, 45(1):243 – 334, 2000.

[12] K. Shimizu and L.Y. Glozman. On the origin of the short range NN interaction. *Phys. Lett. B*, 477:59, 2000.

[13] L. Lapikas. Quasi-elastic Electron Scattering off Nuclei. *Nuclear Physics A*, 553:297 – 308, 1993.

[14] T. Neff and H. Feldmeier. Tensor correlations in the unitary correlation operator method. *Nuclear Physics, Section A*, 713(3-4):311–371, 2003.

[15] K.S. Krane. Introductory nuclear physics. 1987.

[16] R. Machleidt, K. Holinde, and C. Elster. The bonn meson-exchange model for the nucleon–nucleon interaction. *Physics Reports*, 149(1):1–89, 1987.

[17] R.B. Wiringa, V.G.J. Stoks, and R. Schiavilla. Accurate nucleon-nucleon potential with charge-independence breaking. *Physical Review C*, 51(1):38–51, 1995.

[18] V.G.J Stoks et al. Construction of high-quality NN potential models. *Physical Review C*, 49(6):2950–2962, 1994.

[19] R. Machleidt, F. Sammarruca, and Y. Song. Nonlocal nature of the nuclear force and its impact on nuclear structure. *Physical Review C*, 53(4):1483–1487, 1996.

[20] R. Machleidt. High-precision, charge-dependent Bonn nucleon-nucleon potential. *Physical Review C*, 63(2):24001, 2001.

[21] A. Nagl, V. Devanathan, and H. Uberall. *Nuclear pion photoproduction.* Springer-Verlag, 1991.

[22] C. Giusti and F. D. Pacati. Photon-induced two-nucleon knockout reactions to discrete final states. *Nuclear Physics A*, 641(3):297 – 320, 1998.

[23] M. Vanderhaeghen et al. On meson-exchange and Δ-isobar currents in the two-nucleon photoabsorption mechanism. *Nuclear Physics A*, 580(4):551 – 576, 1994.

[24] D.P Watts et al. The $^{12}C(\gamma, NN)$ reaction studied over a wide kinematic range. *Phys. Rev. C*, 62(1):014616, Jun 2000.

[25] C.J.Y. Powrie et al. Polarized photon measurements of the $^{12}C(\overrightarrow{\gamma}, pp)$ and $^{12}C(\overrightarrow{\gamma}, pn)$ reactions for $E_\gamma = 160 - 350$ MeV. *Phys. Rev. C*, 64(3):034602, Aug 2001.

[26] K. Gottfried. On the Determination of the Nuclear Pair Correlation Function from the High Energy Photo-effect. *Nucl. Phys*, 5:557–587, 1958.

[27] R. Jastrow. Many-body problem with strong forces. *Phys. Rev.*, 98(5):1479–1484, Jun 1955.

[28] L Boato and M M Giannini. Two-nucleon photoemission and nuclear correlations. *Journal of Physics G: Nuclear and Particle Physics*, 15(10):1605, 1989.

[29] J. C. McGeorge et al. $(\gamma, 2N)$ reaction in ^{12}C. *Phys. Rev. C*, 51(4):1967–1976, Apr 1995.

[30] P. D. Harty et al. The contribution of 2N photon absorption in $^{12}C(\gamma, 2N)$ reactions for E_γ = 150-400 MeV. *Physics Letters B*, 380(3-4):247 – 252, 1996.

[31] R. C. Carrasco and E. Oset. Interaction of real photons with nuclei from 100 to 500 MeV. *Nuclear Physics A*, 536(3-4):445 – 508, 1992.

[32] C. Giusti and FD Pacati. Two-proton emission induced by electron scattering. *Nuclear Physics, Section A*, 535(3-4):573–591, 1991.

[33] J. Ryckebush et al. Do proton-neutron pairs behave like quasideuterons in the photoabsorption process? *Physics Letters B*, 291(3):213 – 217, 1992.

[34] J. Ryckebusch et al. Effects of the final-state interaction in (γ, pn) and (γ, pp) processes. *Nuclear Physics A*, 568(4):828 – 854, 1994.

[35] W.J.W. Geurts et al. Two-nucleon spectral function of ^{16}o at high momenta. *Phys. Rev. C*, 54(3):1144–1157, Sep 1996.

[36] R.V. Reid. Local phenomenological nucleon-nucleon potentials,. *Annals of Physics*, 50(3):411 – 448, 1968.

[37] P.C. Stein et al. Dependence on atomic number of the nuclear photoeffect at high energies. *Phys. Rev.*, 119(1):348–351, Jul 1960.

[38] J. Garvey et al. Correlated neutron-proton pairs from the photodisintegration of oxygen. *Nuclear Physics*, 70(2):241 – 263, 1965.

[39] I.L. Smith et al. The quasi-deuteron photodisintegration process in lithium, carbon and calcium. *Nuclear Physics B*, 1(8):483 – 493, 1967.

[40] R.M. Weinstein et al. Photoproton-proton coincidences from various nuclei. *Phys. Rev.*, 99(5):1621–1622, Sep 1955.

[41] J. Arends et al. *Nuclear Physics A*, 526(3):479, 1991.

[42] M. Kanazawa et al. *Phys. Rev. C*, 35(5):1828–1843, May 1987.

[43] I. Anthony et al. A tagged photon spectrometer for the mainz 180 MeV microtron. *Nuclear Physics A*, 446(1-2):321 – 321, 1985.

[44] S.N. Dancer et al. Investigation of the $^{12}C(\gamma, pn)$ Reaction Using Tagged Photons. *Phys. Rev. Lett.*, 61(10):1170–1173, Sep 1988.

[45] I.J.D. MacGregor et al. The $^{16}O(\gamma, 2N)$ reaction measured with tagged photons. *Nuclear Physics A*, 533(2):269 – 291, 1991.

[46] I.J.D. MacGregor et al. Mechanisms in the $^{12}C(\gamma, pn)$ and (γ, pp) Reactions. *Phys. Rev. Lett.*, 80(2):245–248, Jan 1998.

[47] T.T.H. Yau et al. The angular distribution of the $^{12}C(\gamma, pn)$ reaction for E_γ=120-150 MeV. *The European Physical Journal A*, 1(3):241–244, 1998.

[48] T. Lamparter et al. On photonuclear reaction mechanisms at intermediate energies. *Zeitschrift fur Physik A Hadrons and Nuclei*, 355(1):1–3, 1996.

[49] D.J. Tedeschi et al. Exclusive Photodisintegration of ^{3}He with Polarized Photons. *Physical review letters*, 73(3):408–411, 1994.

[50] F.V. Adamian et al. Comparative study of the $d(\gamma, pn)$, $^6Li(\gamma, pn)X$ and $^4He(\gamma, pn)X$ processes by linear polarized photons in the energy range 0.3-0.9 GeV. *Journal of Physics G: Nuclear and Particle Physics*, 17(11):1657, 1991.

[51] V. Gladyshev et al. $^{16}O(\gamma, pp)$ and $^{16}O(\gamma, pn)$ Spin Asymmetry and Cross Section Measurements. In *APS Meeting Abstracts*, page 2308, 1998.

[52] S. Franczuk et al. $^{12}C(\gamma, pn)$ photon asymmetry for E_γ= 180-340 MeV. *Physics Letters B*, 450(4):332–338, 1999.

[53] I.J.D. MacGregor. Proceedings on the 5^{th} international workshop on electromagnetically induced two-hadron emission. Lund, 2001, Ed. P. Grabmayr et al. pp264-268 ISBN 91-631-1612-X. http://www.pit.physik.uni-tuebingen.de/grabmayr/CD-Lund2001/HTML/Contributions.html .

[54] A. Jankowiak. The Mainz Microtron MAMI: Past and future. *Eur. Phys. J.*, A28S1:149–160, 2006.

[55] Y.M. Tsipenyuk and S.P. Kapitza. *The microtron: development and applications*. Taylor & Francis, London; New York, 2002.

[56] A. Jankowiak et al. Status Report on the Harmonic Double-sided Microtron of MAMI C. page 3 p, 2006.

[57] I. Anthony et al. Design of a tagged photon spectrometer for use with the Mainz 840 MeV microtron. *Nuclear Instruments and Methods in Physics Research Section A*, 301(2), 1991.

[58] J.C. McGeorge et al. Upgrade of the Glasgow photon tagging spectrometer for Mainz MAMI-C. *The European Physical Journal A-Hadrons and Nuclei*, 37(1):129–137, 2008.

[59] S.J. Hall et al. A focal plane system for the 855 MeV tagged photon spectrometer at MAMI-B. *Nuclear Instruments and Methods in Physics Research-Section A*, 368(3):698–708, 1996.

[60] S.B. Kowalski and H.A. Enge. The ion-optical program raytrace. *Nuclear Instruments and Methods in Physics Research Section A: Accelerators, Spectrometers, Detectors and Associated Equipment*, 258(3):407, 1987.

[61] A. Reiter et al. A microscope for the Glasgow photon tagging spectrometer in Mainz. *The European Physical Journal A*, 30(2):461–467, 2006.

[62] J.R.M Annand. The Glasgow/Mainz Bremsstrahlung Tagger Operations Manual.

[63] U. Timm. Coherent bremsstrahlung of electrons in crystals. *Fortschritte der Physik*, 17(12), 1969.

[64] D. Lohmann et al. Linearly polarized photons at MAMI (Mainz). *Nuclear Instruments and Methods in Physics Research-Section A*, 343(2):494–507, 1994.

[65] R. Johnstone. Private Communication.

[66] J.D. Kellie et al. The selection and performance of diamond radiators used in coherent bremsstrahlung experiments. *Nuclear Inst. and Methods in Physics Research, A*, 545(1-2):164–180, 2005.

[67] E. Downie. *Ph.D. Thesis*. PhD thesis, University of Glasgow, 206.

[68] K. Livingston. The Stonehenge Technique. A new method of aligning crystals for linearly polarized photon production from coherent bremsstrahlung, 2009.

[69] F.A. Natter et al. Monte Carlo simulation and analytical calculation of coherent bremsstrahlung and its polarisation. *Nuclear Inst. and Methods in Physics Research, B*, 211(4):465–486, 2003.

[70] F. Rambo et al. Enhancement of the linear polarization of coherent bremsstrahlung by collimation of the photon beam. *Physical Review C*, 58(1):489–501, 1998.

[71] E.D. Bloom and C.W. Peck. Physics with the Crystal Ball detector. *Annual Review of Nuclear and Particle Science*, 33(1):143–198, 1983.

[72] M. Oreglia et al. A study of the reaction $\psi' \rightarrow \gamma\gamma J/\psi$. *Physical Review D*, 25:2259.

[73] B.M.K Nefkens. Crystal Ball Internal Report. Technical report, UCLA, 1995.

[74] Claire Tarbert. *Coherent Pion Photoproduction on Nuclei*. PhD thesis, University of Edinburgh, 2007.

[75] D. Glazier. A Geant4 simulation for the CrystalBall@MAMI Setup. Private Communication.

[76] F. Pheron. *In preparation. Ph.D. Thesis*. PhD thesis, University of Basel, 2010.

[77] J.R.M. Annand and D. Krambrich. DAQ for CB@MAMI. Technical Report. Technical report, 2002.

[78] D. Krambrich. *Ph.D. Thesis*. PhD thesis, University of Mainz, 2006.

[79] H. Fischer et al. The COMPASS data acquisition system. *IEEE Transactions on Nuclear Science*, 49(2 Part 1):443–447, 2002.

[80] I. Anthony. Tagcal. Private Communication.

[81] J.B. Birks and F.W.K. Firk. The theory and practice of scintillation counting. *Physics Today*, 18:60, 1965.

[82] M. Unverzagt. *Ph.D. Thesis*. PhD thesis, University of Mainz, 2007.

[83] S. Prakhov. Private Communication.

[84] T. Jude. *Ph.D. Thesis*. PhD thesis, University of Edinburgh, 2010.

[85] G.F. Knoll. Radiation Detection and Measurement, 1989. *Edition John Wiley & Sons USA*.

[86] W. M. Yao et al. *J. Phys. G: Nucl. Part. Phys 33, 1*, 2006.

[87] J.R.M. Annand. Data Analysis within an AcquRoot Framework. *University of Glasgow*, 2005.

[88] S. Agostinelli et al. GEANT4 a simulation toolkit. *Nuclear Inst. and Methods in Physics Research, A*, 506(3):250–303, 2003.

[89] R. Brun, F. Rademakers, et al. ROOT-an object oriented data analysis framework. *Nuclear Instruments and Methods in Physics Research-Section A*, 389(1):81–86, 1997.

[90] P. Hall-Barrientos. Calibration of the PID detector. Private Communication.

[91] D. Drechsel et al. A unitary isobar model for pion photo-and electroproduction on the proton up to 1 GeV. *Nuclear Physics, Section A*, 645(1):145–174, 1999.

[92] V. Bellini et al. Coherent π^0 photo-production on ^{4}He at intermediate energies with polarized photons. *Nuclear Physics, Section A*, 646(1):55–66, 1999.

[93] G.J. Miller and R.O. Owens. The treatment of data from a neutral meson spectrometer. *Nuclear Instruments and Methods in Physics Research A*, 390:257–266, 1997.

[94] CM Tarbert et al. Incoherent Neutral Pion Photoproduction on ^{12}C. *Physical Review Letters*, 100(13):132301, 2008.

[95] T. Takaki, T. Suzuki, and JH Koch. Photoproduction of neutral pions to discrete nuclear states. *Nuclear Physics, Section A*, 443(4):570–588, 1985.

[96] K. Livingston. Determining the Degree of Polarization for Linearly Polarized Photons at CLAS, June 2010.

[97] I. J. D. MacGregor and D.P. Watts. Mainz PAC proposal A2/2-98. Experimental Proposal, January 1998.

[98] L. Machenil et al. Absorption mechanisms in photon induced two-body knockout. *Physics Letters B*, 316(1):17 – 22, 1993.

[99] P. Wilhelm, J. A. Niskanen, and H. Arenhövel. Signatures from polarization observables for photon absorption on a $^1S_0$ proton pair. *Nuclear Physics A*, 597(4):613 – 622, 1996.

[100] R. Lindgren. Report no. bnl-65187, http://www.legs.bnl.gov. January 1988.

[101] D. G. Ireland, I. J. D. MacGregor, and J. Ryckebusch. Interpretation of two-nucleon photoemission data. *Phys. Rev. C*, 59(6):3297–3303, Jun 1999.

[102] S. Wartenberg et al. Photon Asymmetry of Deuteron Photodisintegration Between 160 and 410 MeV. *Few-Body Systems*, 26(2):213–226, 1999.

[103] F. A. Berends and A. Donnachie. *Nuclear Physics B*, 54(2), 1967.

[104] H.J. Weyer. Pion absorption in light nuclei. *Physics Reports*, 195(6):295 – 367, 1990.

[105] C. Giusti. Private Communication.

[106] P. Grabmayr. Experimental Proposal A2/4-94 MAMI PAC. A high resolution $^{16}O(\gamma, pp)^{14}C$ experiment, January 1997.

[107] B. A. Mecking et al. The CEBAF large acceptance spectrometer (CLAS). *Nuclear Instruments and Methods in Physics Research Section A: Accelerators, Spectrometers, Detectors and Associated Equipment*, 503(3):513 – 553, 2003.

[108] V. Crede. Baryon spectroscopy with the CB-ELSA detector at ELSA. *The European Physical Journal A-Hadrons and Nuclei*, 18(2):163–165, 2003.

[109] K. Livingston. Eurotag conference, June 2008.

[110] F. Adamyan et al. A photon beam polarimeter based on nuclear e+e- pair production in an amorphous target. *Nuclear Instruments and Methods in Physics Research Section A: Accelerators, Spectrometers, Detectors and Associated Equipment*, 546(3):376 – 384, 2005.

[111] R.O. Owens. Private Communication.